



Universiteit  
Leiden  
The Netherlands

## **Caging ruthenium complexes with non-toxic ligands for photoactivated chemotherapy**

Cuello Garibo, J.A.

### **Citation**

Cuello Garibo, J. A. (2017, December 19). *Caging ruthenium complexes with non-toxic ligands for photoactivated chemotherapy*. Retrieved from <https://hdl.handle.net/1887/58688>

Version: Not Applicable (or Unknown)

License: [Licence agreement concerning inclusion of doctoral thesis in the Institutional Repository of the University of Leiden](#)

Downloaded from: <https://hdl.handle.net/1887/58688>

**Note:** To cite this publication please use the final published version (if applicable).

Cover Page



Universiteit Leiden



The handle <http://hdl.handle.net/1887/58688> holds various files of this Leiden University dissertation.

**Author:** Cuello Garibo J.A

**Title:** Caging ruthenium complexes with non-toxic ligands for photoactivated chemotherapy

**Issue Date:** 2017-12-19

# Caging ruthenium complexes with non-toxic ligands for photoactivated chemotherapy

PROEFSCHRIFT

ter verkrijging van  
de graad van Doctor aan de Universiteit Leiden,  
op gezag van Rector Magnificus Prof. mr. C. J. J. M. Stolker  
volgens besluit van het College voor Promoties  
te verdedigen op dinsdag 19 december 2017  
klokke 11:15 uur

door

Jordi-Amat Cuello-Garibo  
Geboren te Puçol, País Valencià, Spanje  
in 1989

## **Samenstelling Promotiecommissie**

**Promotor** Prof. dr. E. Bouwman

**Copromotor** Dr. S. Bonnet

**Overige Leden** Prof. dr. H. S. Overkleeft  
Prof. dr. J. Brouwer  
Prof. dr. E. Alessio (Università degli studi di Trieste)  
Prof. dr. T. E. Keyes (Dublin City University)

ISBN 978-94-6299-796-7

Printed by Ridderprint BV

*Perquè hi haurà un dia que no podrem més  
i llavors ho podrem tot*

*“One day we won’t be able to take it anymore  
and when that day comes we will take it all”*

Vicent Andrés Estellés

To my parents and my sister, for always being there,  
despite the 1443 km

To Shorouk, for expanding the boundaries

# TABLE OF CONTENTS

---

<b>Chapter 1</b>	<b>7</b>
Introduction	
<b>Chapter 2</b>	<b>27</b>
Influence of steric bulk and solvent on the photoreactivity of ruthenium polypyridyl complexes coordinated to L-proline	
<b>Chapter 3</b>	<b>53</b>
To cage or to be caged? The cytotoxic species in ruthenium-based photoactivated chemotherapy is not always the metal	
<b>Chapter 4</b>	<b>67</b>
Ruthenium-based PACT compounds based on an N,S protecting ligand: a delicate balance between photoactivation and thermal stability	
<b>Chapter 5</b>	<b>95</b>
Tuning the stereoselectivity, photoreactivity, and redox potential of cycloruthenated complexes by small changes in the N,S ligand	
<b>Chapter 6</b>	<b>119</b>
PACT or PDT: are ruthenium(II) complexes photosubstituting a non-toxic ligand also phototoxic under hypoxic conditions?	
<b>Chapter 7</b>	<b>139</b>
Summary, conclusions, and outlook	

Appendix I: General photochemistry methods	149
Appendix II: Cell culture and (photo)cytotoxicity studies	155
Appendix III: Supporting information for Chapter 2	159
Appendix IV: Supporting information for Chapter 3	173
Appendix V: Supporting information for Chapter 4	175
Appendix VI: Supporting information for Chapter 5	183
Appendix VII: Supporting information for Chapter 6	187
Samenvatting	193
List of publications	197
Curriculum Vitae	199
Acknowledgements	201



# 1

## Introduction

## 1.1 Cisplatin: the spearhead of metal-based chemotherapy

Cancer, also called malignant tumor or neoplasm, is a generic term for a wide group of diseases that involve an irregular growth of cells beyond their usual boundaries, which can then spread to adjoining or distant parts of the body. It is caused by alterations in oncogenes, tumor-suppressor genes, and microRNA genes. According to the World Health Organization (WHO), cancer was the second leading cause of death in 2015 with 8.8 million death.<sup>1</sup> Since the beginning of the 20<sup>th</sup> century, with the development of modern medicine, an enormous amount of resources has been dedicated to the understanding and cure of cancer. Although at first most efforts focused on the surgical removal of the tumor, chemotherapy received special attention after World War II, when the antitumor and antileukemic properties of mustine hydrochloride (the infamous mustard gas) and other poisonous gases were discovered.<sup>2-3</sup> This is how, within a program of the National Cancer Institute (US) to develop new chemotherapeutic agents, the antitumor activity of the complex *cis*-dichlorodiammineplatinum(II) (known as cisplatin, see Figure 1.1) was discovered in 1969 by Professor Barnett Rosenberg and Loretta van Camp at Michigan State University. This discovery gave birth to the first generation of metal-based chemotherapy drugs.<sup>4</sup> In 1978, cisplatin was approved by the US Food and Drug Administration for the treatment of testicular tumors and ovarian adenocarcinoma;<sup>5</sup> and with the development of carboplatin and oxaliplatin (two derivatives of cisplatin, see Figure 1.1) the use of platinum-based drugs was expanded to the treatment of other types of cancer.<sup>6-8</sup>

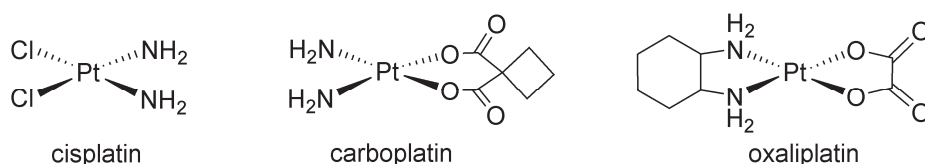


Figure 1.1. Platinum(II) complexes used in cancer chemotherapy.

Although the exact mechanism of action of platinum(II) complexes is not completely clear, the ultimate event that induces apoptosis in cancer cells is generally accepted to be the coordination of DNA to the metal center after aquation of one or two labile ligand(s). DNA binding to platinum inhibits DNA replication and transcription, ultimately leading to cell death.<sup>9-11</sup> In order to develop new platinum-based drugs that are able to bind to DNA, four classical rules are usually stated. First, the platinum complex should contain two monodentate or one bidentate labile ligand(s) that can be

replaced by water molecules; second, it should contain two (or one bidentate) kinetically inert amine ligands; third, the charge of the complex should be neutral; and fourth, it should have *cis* configuration, allowing DNA binding via two neighboring guanines on the same strand.<sup>12-13</sup> However, two important drawbacks of platinum drugs based on these principles can be mentioned: first, inherent or acquired resistances of the tumor cells to the drug are not uncommon,<sup>14-16</sup> and second, highly toxic side effects are typically experienced by the patients, for example hepato- and nephrotoxicity, which limits the long-term clinical use of these compounds in any given patient.<sup>17-19</sup>

## 1.2 Alternatives in the transition metal block: the case of ruthenium

In order to overcome the drawbacks generally associated with platinum-based drugs, a wide range of transition metal-based drugs has been investigated in the last decades, ranging from ruthenium to osmium, gallium, gold, or rhenium complexes.<sup>20-22</sup> Focusing on ruthenium, the flagship complexes in the field have been KP1019 and NAMI-A, which reached Phase I and II in clinical trials, respectively (Figure 1.2). Both compounds were developed in the late 80's and since they share certain structural similarities they have been often compared and extensively reviewed together.<sup>23-24</sup> In short, KP1019, a ruthenium(III) compound of formula [IndH][*trans*-RuCl<sub>4</sub>(Ind)<sub>2</sub>] (Ind = indazole), was developed within a series of azole-based ruthenium(III) complexes by Keppler *et al.*<sup>25-26</sup> It showed great activity against colon cancer in rat models, which allowed to undergo clinical trials. Although the conclusions of the results obtained in Phase I were positive,<sup>27-28</sup> clinical Phase II was never started due to the low solubility of the compound. The more water-soluble NKP-1339 (the sodium salt version of KP1019) has taken the leadership recently, concluding successfully Phase I.<sup>23</sup> The suggested mechanism of action involves the accumulation of the compound in transferrin receptors (which are overexpressed in certain tumor cells) and its subsequent reduction to ruthenium(II) species in the reductive environment characteristic of tumors. However, these hypotheses are controversial and the final biological target of the compound remains discussed.<sup>24</sup> Finally, it is believed that apoptosis of the cancer cells is achieved via mitochondrial damage by disruption of the redox balance, among other possible pathways.<sup>29</sup>

On the other hand, NAMI-A (Figure 1.2), a ruthenium(III) compound of formula [ImH][*trans*-RuCl<sub>4</sub>(DMSO-κS)(Im)] (Im = imidazole and DMSO = dimethyl sulfoxide) was developed by Alessio *et al.* in the early 90's, and it was preceded by its sodium salt version (NAMI).<sup>30</sup> Despite its structural similarity with KP1019, NAMI-A

did not show any cytotoxicity *in vitro* but it showed antimetastatic activity *in vivo*, especially against non-small cell lung cancer, suggesting a different mechanism of action from that of cisplatin or KP1019. Although DNA binding is possible *in vitro*, such interactions are considered of no relevance in the cell due to the non-cytotoxic but antimetastatic effect of NAMI-A. Thus, the inhibition of cellular migration and invasion by modifying the actin cytoskeleton or selectively binding to collagen are the most likely antimetastatic modes of action.<sup>31-32</sup> This good *in vivo* data resulted in clinical trials, which failed in Phase I/II since NAMI-A appeared to be less effective than gemcitabine alone, a common chemotherapy medication.<sup>33</sup>

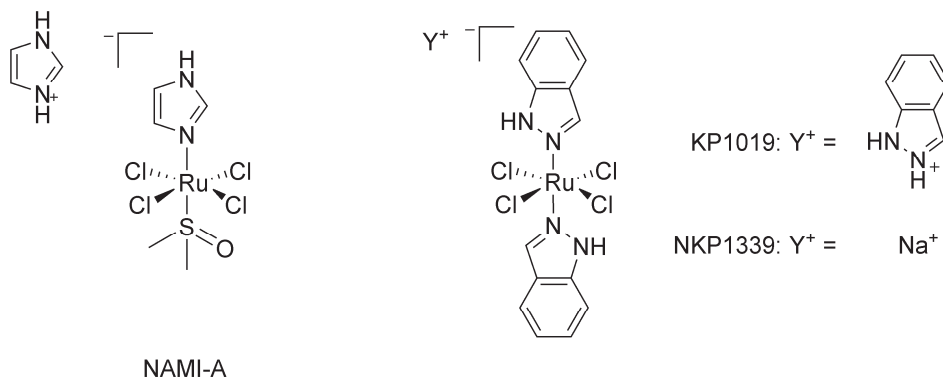


Figure 1.2. Formulae of the ruthenium(III) complexes NAMI-A and KP1019 that have undergone clinical trials for anticancer treatment.

In light of the relative success of NAMI-A and KP1019, many other ruthenium complexes have been developed as alternative antitumor drugs in the last two decades. A new group of complexes based on arene ligands was pioneered by Dyson and Sadler.<sup>34</sup> Their half-sandwich conformation leaves three free coordination sites to coordinate different kind of ligands (three monodentate ligands or one facial tridentate ligand), thus tuning its thermodynamic and kinetic properties to target different biomolecules. Furthermore, the hydrophobic arene ligand in conjunction with the hydrophilic metal center provides valuable amphiphilic properties.<sup>35</sup> One of the clinically most advanced arene complexes is RAPTA-C (Figure 1.3). This complex, which has a p-cymene and an 1,3,5-triaza-7-phosphatricyclo-[3.3.1.1]decanephosphine (PTA) as ligands, was first developed by Dyson and co-workers in 2001.<sup>36</sup> After aquation of chloride ligands and further substitution of the labile aqua ligand by biomolecules, it shows low *in vitro* cytotoxicity, but a good one *in vivo*.<sup>37</sup> Furthermore, studies have demonstrated its similarity to NAMI-A: DNA is an unlikely target, RNA and proteins are probable targets, and antimetastatic activity predominates. Scores of

structural variations, such as modification of the arene, halogen, or phosphine ligand were performed to study their influence and modulate the anticancer/antimetastatic activity of the complex. For example, RAPTA-B and RAPTA-T (Figure 1.3) inhibit metastasis growth and increase cytotoxicity, respectively.<sup>38</sup> Instead of p-cymene, they have a benzene and a toluene, respectively, coordinated to the ruthenium center.

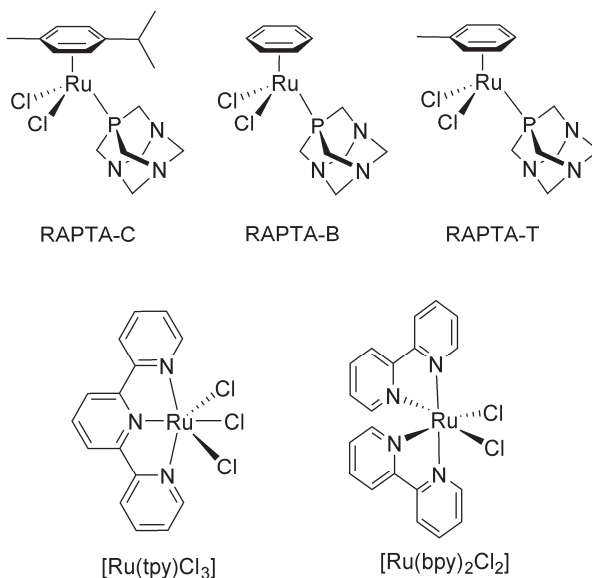


Figure 1.3. Top: Ruthenium(II)-arene complex RAPTA-C and its derivatives RAPTA-B and RAPTA-T with antimetastatic and enhanced cytotoxic activity, respectively. Below: ruthenium(II) and ruthenium(III) polypyridyl complexes studied by Reedijk and co-workers.<sup>39</sup>

Ruthenium polypyridyl complexes also caught the attention of researchers as possible cisplatin-like drugs. Like arene-based complexes, polypyridyl complexes can have coordinating sites available to interact with biomolecules after aquation of the chloride ligands. Thus, in principle, they are able to bind to DNA like cisplatin. Reedijk and co-workers studied the cytotoxicity of [Ru(tpy)Cl<sub>3</sub>] (tpy = 2,2':6',2''-terpyridine), [Ru(tpy)(bpy)Cl]Cl (bpy = 2,2'-bipyridine), and *cis*-[Ru(bpy)<sub>2</sub>Cl<sub>2</sub>] (Figure 1.3) against HeLa and murine cancer cells. The cytotoxicity of a compound is expressed with the EC<sub>50</sub> value, which is the effective concentration of compound at which 50% of the treated cells are dead, compared to untreated control cells. For [Ru(tpy)(bpy)Cl]Cl and [Ru(bpy)<sub>2</sub>Cl<sub>2</sub>], EC<sub>50</sub> values 70 times higher than that for [Ru(tpy)Cl<sub>3</sub>] were obtained.<sup>39</sup> In an attempt to increase the cytotoxicity but keep the two labile chloride ligands in *cis*, Reedijk and co-workers replaced the bpy ligands by 2-phenylazopyridine (azpy), a dissymmetric ligand which contains an azo group and is more lipophilic.<sup>40</sup> Due to the

dissymmetry of the azpy ligand,  $[\text{Ru}(\text{azpy})_2\text{Cl}_2]$  has five different regioisomers (Figure 1.4), of which  $\alpha$ ,  $\beta$ , and  $\gamma$  were studied. Cytotoxicity studies against renal cancer (A498 cells), breast cancer (MCF-7 and EVSA-T cells), non-small cell lung cancer (H226 cells), ovarian cancer (IGROV cells), melanoma (M19 cells), and colon cancer cells (WIDR cells) showed lower  $\text{EC}_{50}$  values for the  $\alpha$  and  $\gamma$  isomers than for the  $\beta$  isomer. This result suggests a stereoselective coordination to biomolecules, and thus a different mechanism of action depending on the isomer.<sup>41</sup> Cytotoxicity studies of  $[\text{Ru}(\text{tpy})(\text{N-N})(\text{L})]^{n+}$  (where N-N = 2,2'-azobispyridine, azpy, or 2-phenylpyridinylmethylene amine, and L =  $\text{Cl}^-$ ,  $\text{H}_2\text{O}$ , or  $\text{CH}_3\text{CN}$ ) showed that the presence of an azo group is required for anticancer activity and that the nature of the labile ligand L does not have a significant effect on cytotoxicity.<sup>42</sup> Furthermore, the mixed-ligand complex  $\alpha$ - $[\text{Ru}(\text{azpy})(\text{bpy})\text{Cl}_2]$  shows an intermediate cytotoxicity: higher than that of  $[\text{Ru}(\text{bpy})_2\text{Cl}_2]$  but lower than that of  $[\text{Ru}(\text{azpy})_2\text{Cl}_2]$ , reinforcing the idea that an azo group is necessary to reach a high cytotoxic effect.<sup>43</sup>

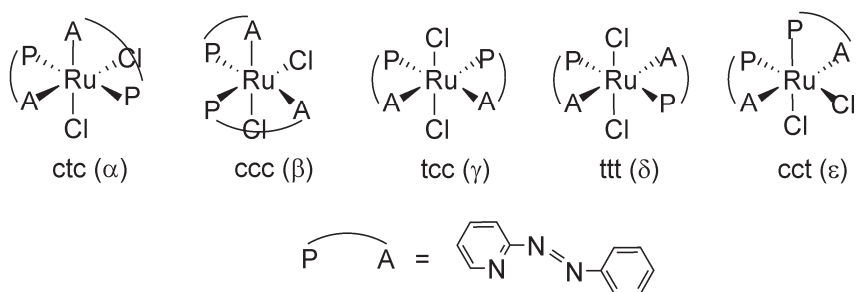


Figure 1.4. Structural representation of the five regioisomers ( $\alpha$ ,  $\beta$ ,  $\gamma$ ,  $\delta$ , and  $\epsilon$ ) of the complex  $[\text{Ru}(\text{azpy})_2\text{Cl}_2]$ . The three-letters code indicates the mutual cis (c) or trans (t) orientation of Cl, N-pyridine and N-azo donor atoms, respectively.<sup>41</sup>

### 1.3 And there was light

One of the first problems encountered with chemotherapy was the lack of selectivity towards cancer cells, inducing all kind of collateral toxicities. Different strategies to localize the administration of the drug and thus increase the selectivity have been developed over the years, from peptide targeting to specific drug delivery carriers.<sup>44-46</sup> One of these strategies consists in using visible light to activate a photosensitive drug with a precise spatial and temporal control.<sup>47</sup> In 1903, the treatment of skin cancer by application of eosin (a photosensitizer) followed by irradiation of the area was reported, establishing the relation between light, dioxygen, and the photosensitizer, and marking the scientific start of Photodynamic Therapy (PDT).<sup>48</sup> Although some work was performed in the PDT field in the following decades,<sup>49-50</sup> it was not until the early

1970's when Diamond, Dougherty, and Tomson reported, almost simultaneously, the use of PDT against malignant tumors.<sup>51-53</sup> Nowadays, several dyes are available on the market as PDT photosensitizers, most of them based on porphyrins (*e.g.* Photofrin, Verteporfin) or chlorins (*e.g.* Foscan, Figure 1.5).<sup>48, 54</sup>

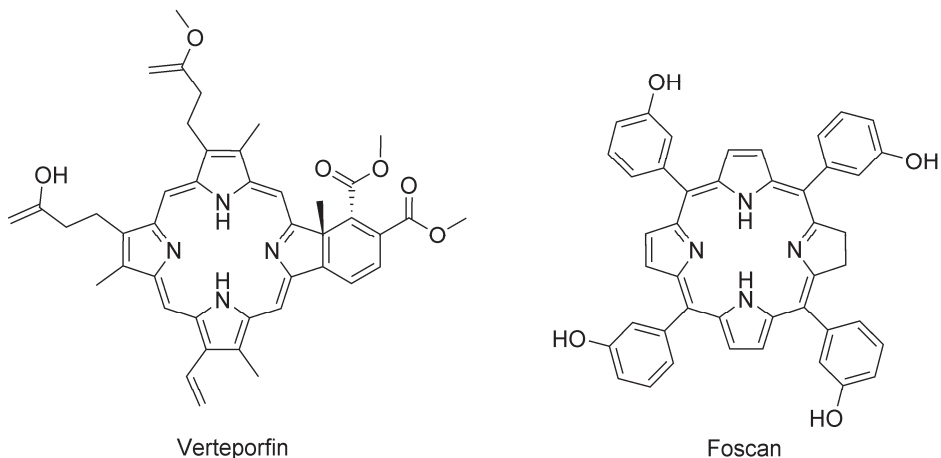


Figure 1.5. Chemical structure of Verteporfin and Foscan, two clinically used PDT photosensitizers.

In the most common form of PDT, called PDT type II, the photosensitizer is excited upon light irradiation to its singlet state and undergoes intersystem crossing (ISC) to a triplet state. As shown in Figure 1.7, in presence of ground state molecular oxygen ( $^3\text{O}_2$ ) both molecules can collide to produce a triplet-triplet annihilation (TTA) event that transfers the energy from the photosensitizer to the molecular oxygen, which is excited to its singlet state ( $^1\text{O}_2$ ).  $^1\text{O}_2$  is a very reactive species that can oxidize many biomolecules like amino acids, DNA, or lipids, thereby causing oxidative damage and inducing cell death.<sup>55-56</sup> On the other hand, PDT type I involves the generation of free radicals through an electron (or proton) transfer reaction from the excited photosensitizer to a biological substrate. The radical further reacts with tissue dioxygen, generating reactive oxygen species (ROS) and oxidative stress.<sup>48</sup> Although PDT has been successfully used in the clinic to treat different cancer types, it also has two major limitations. First, it depends on the presence of dioxygen, while many regions in tumors are hypoxic;<sup>57</sup> second, the spectral range in which the photosensitizers absorb light should be in the so-called phototherapeutic window. This region of the spectrum consists of wavelengths that penetrate biological tissues deep enough without causing radiation damage. The range in which the phototherapeutic window is generally considered optimal is between 620 and 850 nm.<sup>58</sup>

Ruthenium(II) polypyridyl complexes are  $d^6$  complexes with an octahedral geometry that can be potential photosensitizers for PDT due to their long-lived excited triplet state. In regular octahedral complexes of the type  $[\text{Ru}(\text{bpy})_3]^{2+}$ , a singlet metal-to-ligand charge transfer ( $^1\text{MLCT}$ ) state is populated upon irradiation, quickly evolving to a triplet metal-to-ligand charge transfer ( $^3\text{MLCT}$ ) state via ISC. From this microsecond-lived triplet state, energy transfer to molecular oxygen can occur to produce the reactive species  $^1\text{O}_2$  (Figure 1.7). Many examples of PDT-like ruthenium(II) complexes have been reported, of which TLD1433 has even reached clinical trials (Figure 1.6). TLD1433 is a complex having the formula  $[\text{Ru}(4,4'\text{-dmbpy})_2(\text{IP-TP})]\text{Cl}_2$  (4,4'-dmbpy = 4,4'-dimethyl-2,2'-bipyridine, IP-TP = 2-(2',2'':5'',2'''-terthiophene)-imidazo[4,5-f][1,10]phenanthroline) developed by McFarland *et al.*<sup>59</sup> Preliminary *in vitro* studies against promyelocytic leukemia cells (HL-60) showed no cytotoxicity in the dark but a high cytotoxic effect upon red light irradiation. Last year, TLD1433 went to Phase I in clinical trials for the treatment of bladder cancer.<sup>60</sup>

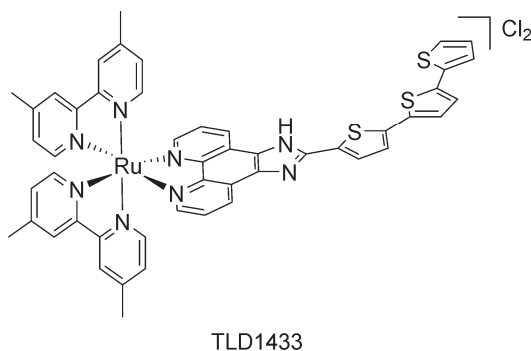


Figure 1.6. Chemical structure of TLD1433.

## 1.4 Photoreactivity of ruthenium polypyridyl complexes

Although many transition metal compounds have been explored as possible PDT photosensitizers, few have the versatile and tunable photochemistry of ruthenium(II) polypyridyl complexes. Indeed, from the  $^3\text{MLCT}$  excited state generated upon light irradiation, the system can evolve following different pathways, as shown in the Jablonski diagram depicted in Figure 1.7. As mentioned before, one of the possible pathways is the relaxation of the system to the ground state via TTA with  $^3\text{O}_2$ . In this case, the ruthenium complex can be considered as a PDT photosensitizer. A second possible pathway is the relaxation via luminescence from the  $^3\text{MLCT}$  state, with emission maxima in water generally in the 600 to 730 nm range. Luminescent

ruthenium(II) complexes form a large family of dyes for biological imaging.<sup>61-63</sup> Keyes *et al.* have reported several examples of complexes of the type  $[\text{Ru}(\text{bpy})_2(\text{L})]^{2+}$  that target the nucleus, the endoplasmic reticulum, or the mitochondria, depending on whether L is a nuclear localization signal peptide, an endoplasmic directing sequence, or a mitochondrial penetrating peptide, respectively.<sup>64-66</sup>

If the ligand field splitting of the complex is small enough, the electron in the ligand-based  $\pi^*$  state can thermally populate a metal-based  $e_g$  orbital, generating a triplet metal-centered state ( $^3\text{MC}$ ), which has dissociative character and may result in the photosubstitution of a ligand.<sup>67</sup> Smaller ligand field splitting can be achieved via distortion of the coordination sphere, for example using hindering ligands such as 6,6'-dimethyl-2,2'-bipyridine (dmbpy),<sup>68</sup> or via controlling the electronic properties of the ligands.<sup>69</sup> The photoreactivity of ruthenium(II) polypyridyl complexes was already reported by Bosnich *et al.* in 1966.<sup>70</sup> However, it was in the 1980's when Durham and Meyer pioneered the research in the field with, for example, the photoconversion of  $[\text{Ru}(\text{bpy})_2(\text{py})_2]^{2+}$  (py = pyridine) to  $[\text{Ru}(\text{bpy})_2(\text{Y})_2]^{n+}$  in dichloromethane or acetone in the presence of coordinating anions  $\text{Y}^-$  ( $\text{Y}^- = \text{F}^-, \text{Cl}^-, \text{Br}^-, \text{or } \text{SCN}^-$ ).<sup>71,72</sup> Later, Sauvage *et al.* expanded the field with the introduction of hindering ligands to achieve controlled photosubstitution, which was applied in the design of light-driven molecular machines. His work in the field merited him the Nobel Prize in Chemistry in 2016.<sup>73-76</sup>

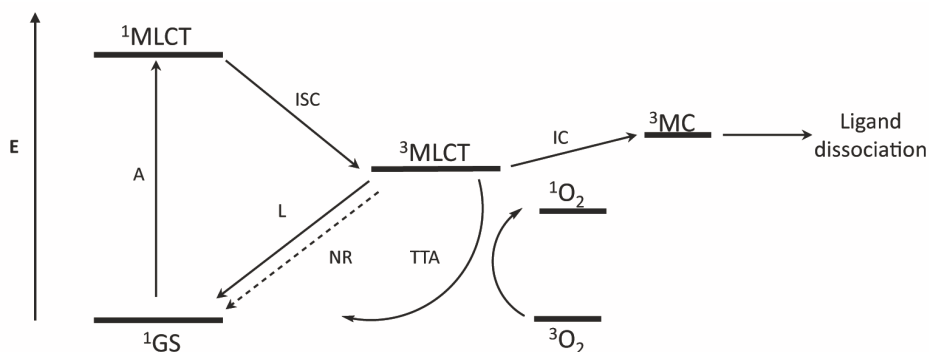
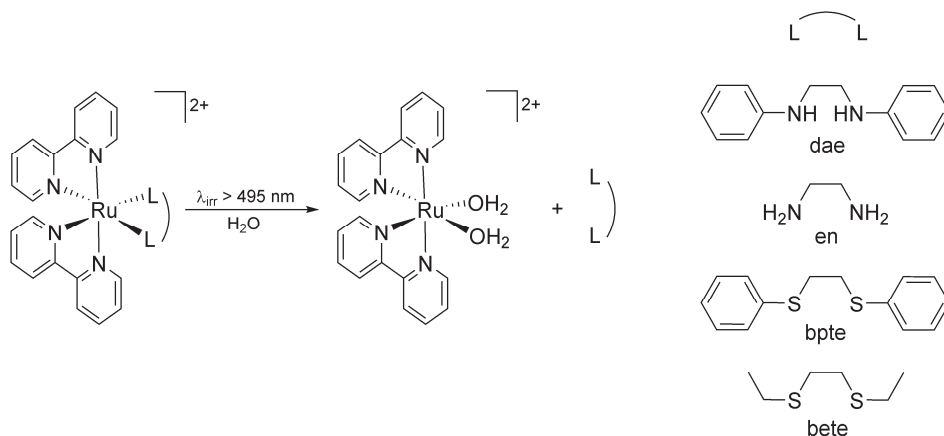


Figure 1.7. Jablonski diagram for ruthenium polypyridyl complexes. If the  $^3\text{MC}$  is too high in energy and cannot be thermally populated, then ligand dissociation does not occur. A = absorption, ISC = intersystem crossing, L = luminescence, NR = non-radiative relaxation, TTA = triplet-triplet annihilation, IC = interconversion.

More recently, Turro and co-workers compared the ability of ruthenium polypyridyl complexes to undergo photosubstitution of thioether S-ligands, namely 3,6-dithiaoctane (bete) and 1,2-bis(phenylthio)ethane (bpte), vs. amine N-ligands, namely ethylenediamine (en) and 1,2-dianilinoethane (dae), by water and  $\text{Cl}^-$  (Scheme 1.1).

According to their work, the higher ligand-exchange quantum yields of S-complexes compared to N-complexes ( $\Phi_{Cl}$  of 0.019, 0.016, 0.002, and 0.003 for bete, bpte, en, and dae complexes, respectively) are due to the greater elongation of the Ru-S bond in the triplet excited state. This elongation is a result of the transfer of electron density from the metal-based  $t_{2g}$  orbital to the bpy-based  $\pi^*$  orbital, which weakens the Ru-S bond in the excited state.<sup>77</sup> Thus, changing the nature of the ligand has an important effect on the photoreactivity. Overall, all the processes mentioned above (TTA, luminescence, and photosubstitution), as well as non-radiative relaxation, can in principle coexist in ruthenium polypyridyl complexes, and of course compete with each other.



Scheme 1.1. Complexes studied by Turro and co-workers to compare photosubstitution efficiency of S-based vs. N-based bidentate ligands.<sup>77</sup>

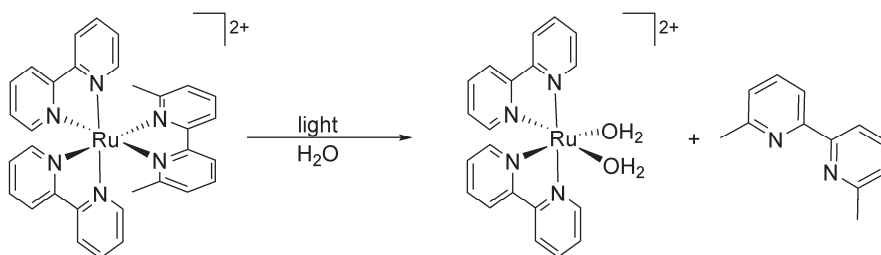
## 1.5 Photoactivated Chemotherapy (PACT)

The photosubstitution properties of ruthenium(II) complexes can be combined with the idea of timely and spatially controlled delivery of a cytotoxic species, developed in PDT, into a new type of phototherapy called photoactivated chemotherapy (PACT).<sup>78</sup> In PACT, a cytotoxic compound is “caged” by linkage to a photocleavable protecting group, creating a prodrug in which the cytotoxic compound is not able to interact with its biological target. Upon light irradiation, the photocleavable group is released to recover the biologically active compound. Although photocaging is also applied for organic molecules,<sup>79</sup> in this thesis we will focus on the ruthenium-based PACT. Ruthenium-based PACT can be applied in two ways: either a non-toxic ruthenium complex is used as a cage for a bioactive organic molecule (one of the ligands), or one of the ligands is non-toxic and used to cage a ruthenium-based cytotoxic species. In any case, coordination of the ligand to the metal complex has to be strong and stable

enough in water for the prodrug not to be activated thermally. Meanwhile, the ligand-metal bond(s) should become weak enough upon low-energy light irradiation for the ligand to be photosubstituted by water molecules, thereby releasing the two photoproducts. Examples for the photocaging of bioactive organic molecules can be found in the work of Etchenique, Turro, or more recently Renfrew, who reported many examples of such compounds.<sup>80-85</sup> Etchenique and co-workers reported the caging of nicotine (Nic), a known addictive drug, in the complex  $[\text{Ru}(\text{bpy})_2(\text{Nic})_2]^{2+}$ . Upon violet, blue, or green light irradiation this complex photosubstitutes only one of the Nic ligands, yielding free Nic and  $[\text{Ru}(\text{bpy})_2(\text{Nic})(\text{OH}_2)]^{2+}$  as side-product (Scheme 1.2).<sup>86</sup> This monosubstitution was also achieved for photocaged neurotransmitters such as tryptamine, serotonin, tyramine, and  $\gamma$ -aminobutyric acid (GABA) (shown in Scheme 1.2).<sup>83</sup> Another family of caged compounds, also developed by Etchenique *et al.*, have the formula  $[\text{Ru}(\text{bpy})_2(\text{PMe}_3)(\text{L})]$ , in which L is a biologically active amine, and  $\text{PMe}_3$  is a non-labile ligand. Compounds like glutamate and GABA have been caged using this type of complexes.<sup>86-87</sup> In our group, Lameijer and co-workers have reported the photocaging of a nicotinamide phosphoribosyl transferase (NAMPT) inhibitor STF-31 in the complex  $[\text{Ru}(\text{tpy})(\text{biq})(\text{STF-31})]^{2+}$  (biq = 2,2'-biquinoline). When tested against skin (A431 cells) and lung (A549 cells) cancer cells, a 3- to 4-fold increase in cytotoxicity was found upon red light irradiation.<sup>88</sup>



of cancer cells, while healthy cells would not be harmed by the molecule even under light irradiation.<sup>89</sup> On the other hand, McFarland *et al.* reported the cytotoxic activity of a series of complexes of the type  $[\text{Ru}(\text{dmbpy})_2(\text{IP-nT})]^{2+}$  (IP = imidazo[4,5-f][1,10]phenanthroline,  $n = 1-3$ , T = thiophenes), the strained form of TLD1433.<sup>90</sup> Upon visible light irradiation, one dmbpy is released, generating the bis-aqua  $[\text{Ru}(\text{dmbpy})(\text{IP-nT})(\text{OH}_2)_2]^{2+}$ , which is believed to be the cytotoxic species. The series of complexes showed low  $\text{EC}_{50}$  values of 1-2  $\mu\text{M}$  against HL-60 cells after visible light irradiation, with  $\text{PI}'\text{s}$  ranging from 22 to 166. However, since the  $^1\text{O}_2$  generation quantum yields ( $\Phi_A$ ) were relatively high when  $n$  was 2 or 3 ( $\Phi_A = 0.34$  and  $0.42$ , respectively), a PDT effect could not be excluded and a dual mode PACT/PDT was suggested. Finally, Turro *et al.* reported the caging of two 5-cyanouracil (5-CNU) molecules, an uracil derivative that inhibits the pyrimidine catabolism, in the complex  $[\text{Ru}(\text{bpy})_2(5\text{-CNU})_2]^{2+}$ . The bis-aqua complex is generated after photorelease of two 5-CNU via two consecutive photosubstitution reactions. The authors suggested that two biologically active species were generated, the bis-aqua ruthenium complex and the two cytotoxic 5-CNU ligands, and thus considered for this compound a dual mode of action.<sup>84</sup>



Scheme 1.3. Photoaquation of  $[\text{Ru}(\text{bpy})_2(\text{dmbpy})]^{2+}$  upon irradiation at  $\lambda > 450$  nm. Which of the photoproducts is the cytotoxic species?<sup>68</sup>

However, there is one major drawback for the application of ruthenium-based PACT in the clinic. As shown before, the photosubstitution mechanism starts via population of the  $^1\text{MLCT}$ , which is generally achieved by light in the blue region of the spectrum (440-500 nm). However, blue light does not penetrate efficiently biological tissue and it can be toxic in high doses.<sup>91</sup> In other words, it is far from the phototherapeutic window (620-850 nm). In order to overcome this issue and to obtain photosubstitution using red light, several strategies have been considered. One of the strategies is to shift the MLCT absorption band of ruthenium(II) complexes to the red part of the spectrum. Glazer and co-workers have done that by incorporating biq ligands in the complex  $[\text{Ru}(\text{phen})_2(\text{biq})]^{2+}$  (phen = 1,10-phenanthroline), thus distorting the octahedral

geometry. This complex shows some absorption at a wavelength as high as 700 nm.<sup>92</sup> On the other hand, Turro and co-workers have used negatively charged coordinating atoms such as 2-phenylpyridine (phpy<sup>-</sup>) in the cyclometalated complex [Ru(phen)(phpy)(CH<sub>3</sub>CN)<sub>2</sub>]<sub>2</sub>PF<sub>6</sub> for the same purpose.<sup>93</sup> However, cyclometalated complexes generally show limited photoreactivity. Another strategy is to “upgrade” red light locally into blue light using an upconversion drug delivery system. For example, Askes and Bonnet have developed TTA upconverting liposomes. Upon red light irradiation (630 nm) an amphiphilic [Ru(bpy)(tpy)(SRR')]<sup>2+</sup> complex, also included in the lipid bilayer of the liposome, photosubstitutes the lipophilic thioether ligand SRR' by one water molecule, thereby detaching from the membrane.<sup>94</sup> A similar approach was followed by Salassa and co-workers by using NaYF<sub>4</sub>:Yb<sup>3+</sup>/Er<sup>3+</sup> upconverting nanoparticles (UCNPs) to photoactivate *cis*-[Ru(bpy)<sub>2</sub>(py)<sub>2</sub>]Cl<sub>2</sub> in aqueous solution. Upon near infrared light irradiation (980 nm) one pyridine is substituted by one water molecule in a complex with an MLCT band in the blue region ( $\lambda_{\text{max}} = 455 \text{ nm}$ ).<sup>95</sup>

### 1.6 Aim and outline of the thesis

The goal of the research described in this thesis is the development of new PACT ruthenium(II) complexes that, upon light irradiation, substitute a non-cytotoxic bidentate chelating ligand by two solvent molecules to form a cytotoxic *cis*-ruthenium(II) photoproduct. It should be noted here that the cytotoxicity of *cis*-ruthenium(II) polypyridyl complexes remains controversial. On the one hand, Reedijk and co-workers reported the low cytotoxicity of [Ru(bpy)<sub>2</sub>Cl<sub>2</sub>], which hydrolyzes into a bis-aqua complex, while Etchenique, Renfrew, and Kodanko claim the non-toxicity of that same bis-aqua complex to cage bioactive ligands in living cells. In such applications, it is of utmost importance that the ruthenium(II) caging agent is not toxic. On the other hand, Glazer and Papish showed increased cytotoxicity with compounds producing [Ru(bpy)<sub>2</sub>(OH<sub>2</sub>)<sub>2</sub>]<sup>2+</sup> and dmbpy or dhbpy, respectively, and claimed that the phototoxicity is caused by the bis-aqua complex. Thus, some questions were unsolved when this PhD research started. In which case is a *cis*-ruthenium polypyridyl complex cytotoxic? Is it possible to distinguish the photocytotoxicity of the aquated metal complex from that of the released ligand? What is the role of the charge and lipophilicity of the prodrug on the dark cytotoxicity and light activation of the complex? And finally, is <sup>1</sup>O<sub>2</sub> generation a factor to take into account to understand the phototoxicity of these light-activated compounds?

In Chapter 2 we have first studied whether the natural amino acid L-proline (L-prol) could be used as a photolabile ligand in a series of three complexes of the type  $[\text{Ru}(\text{N},\text{N})_2(\text{L-prol-}\kappa\text{N},\kappa\text{O})]\text{PF}_6$  ( $\text{N},\text{N} = \text{bpy}$  or  $\text{dmbpy}$ ). In this series of complexes, the strain is systematically increased by adding zero, two, or four methyl substituents at the 6 and 6' position of the bpy ligand(s). In water, none of the complexes is photoreactive, whereas in  $\text{CH}_3\text{CN}$ , a less polar solvent and better coordinating molecule, the more strained complexes proved to be photoreactive. However, the photoreactivity is not selective and either L-prol or dmbpy are substituted in parallel by two  $\text{CH}_3\text{CN}$  molecules. The difficulty of selectively photosubstituting an anionic N,O chelating ligand made us investigate further sulfur-based neutral chelating ligands, some of which are known to be excellent photolabile ligands for ruthenium polypyridyl complexes.<sup>96</sup> Indeed, in Chapter 3 we show that the N,S chelating ligand 2-(methylthio)methylpyridine (mtmp) is a good photolabile ligand in  $[\text{Ru}(\text{bpy})_2(\text{mtmp-}\kappa\text{N},\kappa\text{S})]\text{Cl}_2$ , which generates *cis*- $[\text{Ru}(\text{bpy})_2(\text{OH}_2)_2]^{2+}$  upon light irradiation. Cytotoxicity assays against A549 cells show that the mtmp ligand itself is non-cytotoxic and that  $[\text{Ru}(\text{bpy})_2(\text{mtmp})]\text{Cl}_2$  is non-cytotoxic in the dark and after light irradiation. By contrast, we verified Glazer's result that  $[\text{Ru}(\text{bpy})_2(\text{dmbpy})]\text{Cl}_2$  shows an enhanced cytotoxic effect after light irradiation. However, we demonstrate dmbpy to be cytotoxic. As a consequence, due to the low lipophilicity and low cellular uptake of both ruthenium prodrugs, we attribute the photocytotoxic effect of  $[\text{Ru}(\text{bpy})_2(\text{dmbpy})]\text{Cl}_2$  to the released dmbpy ligand, rather than to the bis-aqua ruthenium complex. These results contradict the available literature, in which the photocytotoxicity is attributed, based on the cisplatin analogy, to the metal-base photoproduct  $[\text{Ru}(\text{bpy})_2(\text{OH}_2)_2]^{2+}$ .

In Chapter 4 the synthesis, photochemistry, and cytotoxicity of a series of ruthenium complexes bearing the non-cytotoxic N,S chelating ligand 3-(methylthio)propylamine (mtpa) is described. The series consists of complexes of the type  $[\text{Ru}(\text{N},\text{N})_2(\text{mtpa})]^{2+}$  ( $\text{N},\text{N} = \text{bpy}$  or  $\text{dmbpy}$ ) in which the distortion of the octahedral sphere and the lipophilicity of the complex are increased by addition of two or four methyl substituents at the 6 and 6' positions of the N,N ligand, *i.e.* by using one or two dmbpy ligands instead of bpy. We show that an intermediate level of octahedral distortion, such as that in the complex  $[\text{Ru}(\text{bpy})(\text{dmbpy})(\text{mtpa})]^{2+}$ , is necessary to obtain full photosubstitution of the N,S chelating ligand while keeping thermal stability.

In Chapter 5 we study cyclometalation as a strategy to increase the absorption wavelength of a PACT ruthenium compound. The synthesis and photochemistry of a

series of complexes of the type  $[\text{Ru}(\text{bpy})(\text{phpy})(\text{N,S})]^+$  (phpy = 2-phenylpyridine) is described, where the N,S chelating ligand is either mtpa, mtea (2-(methylthio)ethylamine), mtmp, or mtep (2-(methylthio)ethyl-2-pyridine). Mtpa and mtmp were already used in previous chapters, and by adding mtea and mtep in the series we investigate the influence of the size of the N,S chelating ring (five- or six-membered ring) and the nature of its coordinated nitrogen atom (pyridine vs. primary amine) on the stereoselectivity of the synthesis of these highly dissymmetric complexes, on their stability towards aerial oxidation, and on their photoreactivity. We show that complexes bearing ligands that form a six-membered ring (*i.e.* mtpa and mtep) are synthesized stereoselectively to obtain only one of the eight possible isomers, and that these complexes are photoreactive in  $\text{CH}_3\text{CN}$ . Furthermore, complexes bearing a pyridine-based N,S ligand (*i.e.* mtmp and mtep) are less prone to oxidize under air than amine-based complexes due to the  $\pi$ -acceptor properties of the pyridine.

Finally, the toxicity of a series of ruthenium complexes bearing a photolabile non-toxic N,S ligand is tested in human cancer cells under hypoxia (1%  $\text{O}_2$ ) to investigate the oxygen dependency of their biological effect (Chapter 6). We show that the cytotoxicity of all compounds is lower under hypoxia compared to that under normoxia (21%  $\text{O}_2$ ) probably due to the chemoresistance acquired by cancer cells under hypoxia. However, the cytotoxicity of some of the complexes is clearly enhanced upon green light irradiation, which is the first experimental demonstration of light-induced cytotoxicity under hypoxia for a metal-based PACT compound releasing a non-toxic organic ligand.

## 1.7 References

1. *World health statistics 2017: monitoring health for the SDGs, Sustainable Development Goals*, World Health Organization, Geneva, **2017**.
2. A. Gilman and F. S. Philips, *Science*, **1946**, 103, 409-436.
3. A. Gilman, *Am. J. Surg.*, **1963**, 105, 574-578.
4. B. Rosenberg, L. Vancamp, J. E. Trosko and V. H. Mansour, *Nature*, **1969**, 222, 385-386.
5. E. Wiltshaw, *Platinum Met. Rev.*, **1979**, 23, 90-98.
6. S. Dilruba and G. V. Kalayda, *Cancer Chemother. Pharmacol.*, **2016**, 77, 1103-1124.
7. M. Galanski, *Recent Pat. Anti-Cancer Drug Discovery*, **2006**, 1, 285-295.
8. D. Lebowohl and R. Canetta, *Eur. J. Cancer*, **1998**, 34, 1522-1534.
9. E. R. Jamieson and S. J. Lippard, *Chem. Rev.*, **1999**, 99, 2467-2498.
10. H. N. A. Fraval, C. J. Rawlings and J. J. Roberts, *Mutat. Res., Fundam. Mol. Mech. Mutagen.*, **1978**, 51, 121-132.
11. S. Dasari and P. B. Tchounwou, *Eur. J. Pharmacol.*, **2014**, 740, 364-378.
12. K. S. Lovejoy and S. J. Lippard, *Dalton Trans.*, **2009**, 48, 10651-10659.
13. J. Reedijk, *Chem. Rev.*, **1999**, 99, 2499-2510.
14. D. W. Shen, L. M. Pouliot, M. D. Hall and M. M. Gottesman, *Pharmacol. Rev.*, **2012**, 64, 706-721.
15. L. Amable, *Pharmacol. Res.*, **2016**, 106, 27-36.

16. L. Galluzzi, I. Vitale, J. Michels, C. Brenner, G. Szabadkai, A. Harel-Bellan, M. Castedo and G. Kroemer, *Cell Death Dis.*, **2014**, e1257.
17. T. Karasawa and P. S. Steyger, *Toxicol. Lett.*, **2015**, 237, 219-227.
18. R. J. Cersosimo, *Ann. Pharmacother.*, **1993**, 27, 438-441.
19. N. M. Martins, N. A. G. Santos, C. Curti, M. L. P. Bianchi and A. C. Santos, *J. Appl. Toxicol.*, **2008**, 28, 337-344.
20. M. A. Jakupec, M. Galanski, V. B. Arion, C. G. Hartinger and B. K. Keppler, *Dalton Trans.*, **2008**, 0, 183-194.
21. D. L. Ma, C. M. Che, F. M. Siu, M. S. Yang and K. Y. Wong, *Inorg. Chem.*, **2007**, 46, 740-749.
22. P. J. Barnard and S. J. Berners-Price, *Coord. Chem. Rev.*, **2007**, 251, 1889-1902.
23. R. Trondl, P. Heffeter, C. R. Kowol, M. A. Jakupec, W. Berger and B. K. Keppler, *Chem. Sci.*, **2014**, 5, 2925-2932.
24. E. Alessio, *Eur. J. Inorg. Chem.*, **2017**, 1549-1560.
25. B. K. Keppler and W. Rupp, *J. Cancer Res. Clin. Oncol.*, **1986**, 111, 166-168.
26. B. Keppler, W. Rupp, U. Juhl, H. Endres, R. Niebl and W. Balzer, *Inorg. Chem.*, **1987**, 26, 4366-4370.
27. F. Lentz, A. Drescher, A. Lindauer, M. Henke, R. A. Hilger, C. G. Hartinger, M. E. Scheulen, C. Dittrich, B. K. Keppler, U. Jaehde and R. Cent European Soc Anticanc Drug, *Anti-Cancer Drugs*, **2009**, 20, 97-103.
28. C. G. Hartinger, M. A. Jakupec, S. Zorbas-Seifried, M. Groessl, A. Egger, W. Berger, H. Zorbas, P. J. Dyson and B. K. Keppler, *Chem. Biodiversity*, **2008**, 5, 2140-2155.
29. S. Kapitza, M. A. Jakupec, M. Uhl, B. K. Keppler and B. Marian, *Cancer Lett.*, **2005**, 226, 115-121.
30. G. Sava, S. Pacor, G. Mestroni and E. Alessio, *Clin. Exp. Metastasis*, **1992**, 10, 273-280.
31. G. Sava, S. Zorzet, C. Turrin, F. Vita, M. Soranzo, G. Zabucchi, M. Cocchietto, A. Bergamo, S. DiGiovine, G. Pezzoni, L. Sartor and S. Garbisa, *Clin. Cancer Res.*, **2003**, 9, 1898-1905.
32. G. Sava, F. Frausin, M. Cocchietto, F. Vita, E. Podda, P. Spessotto, A. Furlani, V. Scarcia and G. Zabucchi, *Eur. J. Cancer*, **2004**, 40, 1383-1396.
33. S. Leijen, S. A. Burgers, P. Baas, D. Pluim, M. Tibben, E. van Werkhoven, E. Alessio, G. Sava, J. H. Beijnen and J. H. M. Schellens, *Invest. New Drugs*, **2015**, 33, 201-214.
34. S. Betanzos-Lara, L. Salassa, A. Habtemariam and P. J. Sadler, *Chem. Commun.*, **2009**, 6622-6624.
35. G. S. Smith and B. Therrien, *Dalton Trans.*, **2011**, 40, 10793-10800.
36. C. S. Allardyce, P. J. Dyson, D. J. Ellis and S. L. Heath, *Chem. Commun.*, **2001**, 1396-1397.
37. P. J. Dyson, *Chimia*, **2007**, 61, 698-703.
38. G. Suess-Fink, *Dalton Trans.*, **2010**, 39, 1673-1688.
39. O. Novakova, J. Kasparkova, O. Vrana, P. M. Vanvliet, J. Reedijk and V. Brabec, *Biochemistry*, **1995**, 34, 12369-12378.
40. A. H. Velders, H. Kooijman, A. L. Spek, J. G. Haasnoot, D. de Vos and J. Reedijk, *Inorg. Chem.*, **2000**, 39, 2966-2967.
41. A. C. G. Hotze, S. E. Caspers, D. de Vos, H. Kooijman, A. L. Spek, A. Flamigni, M. Bacac, G. Sava, J. G. Haasnoot and J. Reedijk, *J. Biol. Inorg. Chem.*, **2004**, 9, 354-364.
42. E. Corral, A. C. G. Hotze, H. den Dulk, A. Leczkowska, A. Rodger, M. J. Hannon and J. Reedijk, *J. Biol. Inorg. Chem.*, **2009**, 14, 439-448.
43. A. C. G. Hotze, E. P. L. van der Geer, S. E. Caspers, H. Kooijman, A. L. Spek, J. G. Haasnoot and J. Reedijk, *Inorg. Chem.*, **2004**, 43, 4935-4943.
44. M. Roveri, M. Bernasconi, J.-C. Leroux and P. Luciani, *J. Mater. Chem. B*, **2017**, 5, 4348-4364.
45. M. Hagimori, Y. Fuchigami and S. Kawakami, *Chem. Pharm. Bull.*, **2017**, 65, 618-624.
46. D. Peer, J. M. Karp, S. Hong, O. C. Farokhzad, R. Margalit and R. Langer, *Nat Nano*, **2007**, 2, 751-760.

## Chapter 1

47. M. Triesscheijn, P. Baas, J. H. M. Schellens and F. A. Stewart, *Oncologist*, **2006**, 11, 1034-1044.
48. D. E. J. G. J. Dolmans, D. Fukumura and R. K. Jain, *Nat. Rev. Cancer*, **2003**, 3, 380-387.
49. H. F. Blum, *Photodynamic action and diseases caused by light*, New York, **1941**.
50. W. L. Fowlks, *J. Invest. Dermatol.*, **1959**, 32, 233-247.
51. I. Diamond, A. McDonagh, C. Wilson, S. Granelli, S. Nielsen and R. Jaenicke, *The Lancet*, **1972**, 300, 1175-1177.
52. T. J. Dougherty, *JNCI, J. Natl. Cancer Inst.*, **1974**, 52, 1333-1336.
53. S. H. Tomson, E. A. Emmett and S. H. Fox, *Cancer Res.*, **1974**, 34, 3124-3127.
54. M. Tanaka, T. Uchibayashi, T. Obata and T. Sasaki, *Cancer Lett.*, **1995**, 90, 163-169.
55. T. Gianferrara, I. Bratsos, E. Iengo, B. Milani, A. Ostric, C. Spagnul, E. Zangrando and E. Alessio, *Dalton Trans.*, **2009**, 10742-10756.
56. L. B. Josefsen and R. W. Boyle, *Metal-Based Drugs*, **2008**, 276109.
57. C. J. Gomer and N. J. Razum, *Photochem. Photobiol.*, **1984**, 40, 435-439.
58. K. Szacilowski, W. Macyk, A. Drzewiecka-Matuszek, M. Brindell and G. Stochel, *Chem. Rev.*, **2005**, 105, 2647-2694.
59. Y. Arenas, S. Monro, G. Shi, A. Mandel, S. McFarland and L. Lilge, *Photodiagn. Photodyn. Ther.*, **2013**, 10, 615-625.
60. G. Shi, S. Monro, R. Hennigar, J. Colpitts, J. Fong, K. Kasimova, H. Yin, R. DeCoste, C. Spencer, L. Chamberlain, A. Mandel, L. Lilge and S. A. McFarland, *Coord. Chem. Rev.*, **2015**, 282-283, 127-138.
61. U. Neugebauer, Y. Pellegrin, M. Devocelle, R. J. Forster, W. Signac, N. Moran and T. E. Keyes, *Chem. Commun.*, **2008**, 5307-5309.
62. M. R. Gill, J. Garcia-Lara, S. J. Foster, C. Smythe, G. Battaglia and J. A. Thomas, *Nat Chem*, **2009**, 1, 662-667.
63. M. R. Gill and J. A. Thomas, *Chem. Soc. Rev.*, **2012**, 41, 3179-3192.
64. L. Blackmore, R. Moriarty, C. Dolan, K. Adamson, R. J. Forster, M. Devocelle and T. E. Keyes, *Chem. Commun.*, **2013**, 49, 2658-2660.
65. A. Byrne, C. S. Burke and T. E. Keyes, *Chem. Sci.*, **2016**, 7, 6551-6562.
66. A. Martin, A. Byrne, C. S. Burke, R. J. Forster and T. E. Keyes, *J. Am. Chem. Soc.*, **2014**, 136, 15300-15309.
67. L. Salassa, C. Garino, G. Salassa, R. Gobetto and C. Nervi, *J. Am. Chem. Soc.*, **2008**, 130, 9590-9597.
68. B. S. Howerton, D. K. Heidary and E. C. Glazer, *J. Am. Chem. Soc.*, **2012**, 134, 8324-8327.
69. S. Bonnet and J.-P. Collin, *Chem. Soc. Rev.*, **2008**, 37, 1207-1217.
70. B. Bosnich and F. Dwyer, *Aust. J. Chem.*, **1966**, 19, 2229-2233.
71. B. Durham, J. L. Walsh, C. L. Carter and T. J. Meyer, *Inorg. Chem.*, **1980**, 19, 860-865.
72. D. V. Pinnick and B. Durham, *Inorg. Chem.*, **1984**, 23, 1440-1445.
73. A.-C. Laemmel, J.-P. Collin and J.-P. Sauvage, *Eur. J. Inorg. Chem.*, **1999**, 383-386.
74. P. Mobian, J.-M. Kern and J.-P. Sauvage, *Angew. Chem.*, **2004**, 116, 2446-2449.
75. J.-P. Collin, D. Jouvenot, M. Koizumi and J.-P. Sauvage, *Inorg. Chem.*, **2005**, 44, 4693-4698.
76. S. Bonnet, J. P. Collin, M. Koizumi, P. Mobian and J. P. Sauvage, *Adv. Mater.*, **2006**, 18, 1239-1250.
77. R. N. Garner, L. E. Joyce and C. Turro, *Inorg. Chem.*, **2011**, 50, 4384-4391.
78. N. J. Farrer, L. Salassa and P. J. Sadler, *Dalton Trans.*, **2009**, 10690-10701.
79. G. C. R. Ellis-Davies, *Nat. Methods*, **2007**, 4, 619-628.
80. H. Chan, J. B. Ghrayche, J. Wei and A. K. Renfrew, *Eur. J. Inorg. Chem.*, **2017**, 1679-1686.
81. N. Karaoun and A. K. Renfrew, *Chem. Commun.*, **2015**, 51, 14038-14041.
82. A. K. Renfrew, *Metallomics*, **2014**, 6, 1324-1335.
83. L. Zayat, M. Salierno and R. Etchenique, *Inorg. Chem.*, **2006**, 45, 1728-1731.
84. R. N. Garner, J. C. Gallucci, K. R. Dunbar and C. Turro, *Inorg. Chem.*, **2011**, 50, 9213-9215.

85. Y. Liu, D. B. Turner, T. N. Singh, A. M. Angeles-Boza, A. Chouai, K. R. Dunbar and C. Turro, *J. Am. Chem. Soc.*, **2009**, 131, 26-27.
86. O. Filevich, M. Salierno and R. Etchenique, *J. Inorg. Biochem.*, **2010**, 104, 1248-1251.
87. V. Lopes-dos-Santos, J. Campi, O. Filevich, S. Ribeiro and R. Etchenique, *Braz. J. Med. Biol. Res.*, **2011**, 44, 688-693.
88. L. N. Lameijer, D. Ernst, S. L. Hopkins, M. S. Meijer, S. H. C. Askes, S. E. Le Dévédec and S. Bonnet, *Angew. Chem., Int. Ed.*, **2017**, 56, 11549-11553.
89. K. T. Hufziger, F. S. Thowfeik, D. J. Charboneau, I. Nieto, W. G. Dougherty, W. S. Kassel, T. J. Dudley, E. J. Merino, E. T. Papish and J. J. Paul, *J. Inorg. Biochem.*, **2014**, 130, 103-111.
90. T. Sainuddin, M. Pinto, H. Yin, M. Hetu, J. Colpitts and S. A. McFarland, *J. Inorg. Biochem.*, **2016**, 158, 45-54.
91. S. L. Hopkins, B. Siewert, S. H. C. Askes, P. Veldhuizen, R. Zwier, M. Heger and S. Bonnet, *Photochem. Photobiol. Sci.*, **2016**, 15, 644-653.
92. E. Wachter, D. K. Heidary, B. S. Howerton, S. Parkin and E. C. Glazer, *Chem. Commun.*, **2012**, 48, 9649-9651.
93. A. M. Palmer, B. Pena, R. B. Sears, O. Chen, M. El Ojaimi, R. P. Thummel, K. R. Dunbar and C. Turro, *Philos. Trans. R. Soc., A*, **2013**, 20120135.
94. S. H. C. Askes, A. Bahreman and S. Bonnet, *Angew. Chem., Int. Ed.*, **2014**, 53, 1029-1033.
95. E. Ruggiero, S. Alonso-de Castro, A. Habtemariam and L. Salassa, *Dalton Trans.*, **2016**, 45, 13012-13020.
96. R. E. Goldbach, I. Rodriguez-Garcia, J. H. van Lenthe, M. A. Siegler and S. Bonnet, *Chem. - Eur. J.*, **2011**, 17, 9924-9929.



# 2

## Influence of steric bulk and solvent on the photoreactivity of ruthenium polypyridyl complexes coordinated to L-proline

*Here, the use of the natural amino acid L-proline as a protecting ligand for ruthenium-based PACT compounds is investigated in the series of complexes  $[Ru(bpy)_2(L-prol)]PF_6$  ( $[1a]PF_6$ ,  $bpy = 2,2'$ -bipyridine,  $L-prol = L$ -proline),  $[Ru(bpy)(dmbpy)(L-prol)]PF_6$  ( $[2a]PF_6$  and  $[2b]PF_6$ ,  $dmbpy = 6,6'$ -dimethyl-2,2'-bipyridine), and  $[Ru(dmbpy)_2(L-prol)]PF_6$  ( $[3a]PF_6$ ). The synthesis of the tris-heteroleptic complex bearing the dissymmetric L-proline ligand yielded only two of the four possible regioisomers, called  $[2a]PF_6$  and  $[2b]PF_6$ . Both isomers were isolated and characterized by a combination of spectroscopies and DFT calculations. The photoreactivity of all four complexes  $[1a]PF_6$ ,  $[2a]PF_6$ ,  $[2b]PF_6$ , and  $[3a]PF_6$ , was studied in water and acetonitrile using UV-visible spectroscopy, circular dichroism spectroscopy, mass spectrometry, and  $^1H$  NMR spectroscopy. In water, upon visible light irradiation in presence of oxygen no photosubstitution took place, but the amine of complex  $[1a]PF_6$  was photooxidized to an imine. Contrary to expectations, enhancing the steric strain by addition of two ( $[2b]PF_6$ ) or four ( $[3a]PF_6$ ) methyl substituents did not lead, in phosphate buffered saline (PBS), to ligand photosubstitution. However, it prevented photooxidation, probably as a consequence of the electron-donating effect of the methyl substituents. In addition, whereas  $[2b]PF_6$  was photostable in PBS,  $[2a]PF_6$  quantitatively isomerized to  $[2b]PF_6$  upon light irradiation. In pure acetonitrile,  $[2a]PF_6$  and  $[3a]PF_6$  showed non-selective photosubstitution of both L-proline and dmbpy ligands, whereas the non-strained complex  $[1a]PF_6$  was photostable. Finally, in water-acetonitrile mixtures  $[3a]PF_6$  showed selective photosubstitution of L-proline, thus demonstrating the active role played by the solvent on the photoreactivity of this series of complexes. The role of solvent polarity, and coordination properties on the photochemical properties of polypyridyl complexes is discussed.*

This chapter was published as an Original Research paper: J. A. Cuello-Garibo, E. Pérez-Gallent, L. van der Boon, M. A. Siegler, and S. Bonnet, *Inorg. Chem.*, **2017**, 56, 4818-4828.

## 2.1 Introduction

Due to their unique photophysical and photochemical properties, ruthenium polypyridyl complexes have found many applications in supramolecular chemistry,<sup>1-6</sup> molecular imaging,<sup>7-11</sup> chemical biology,<sup>12-14</sup> and medicinal chemistry.<sup>15</sup> Notably, several groups are studying the biological activity of ruthenium-based Photoactivated Chemotherapy (PACT) prodrugs.<sup>16-20</sup> These compounds are non-toxic or poorly toxic in the dark, but they become highly cytotoxic, or more cytotoxic, upon visible light irradiation. Unlike in Photodynamic Therapy (PDT), another phototherapeutic technique where phototoxicity comes from the light-induced generation of reactive oxygen species such as singlet oxygen, in PACT light activation occurs via an oxygen-independent mechanism that often relies on ligand photosubstitution reactions.<sup>21</sup> Ligand photosubstitution in polypyridyl complexes is typically attributed to the thermal promotion of photogenerated triplet metal-to-ligand charge-transfer (<sup>3</sup>MLCT) excited states into dissociative, low-lying metal-centered triplet (<sup>3</sup>MC) excited states. In many reported examples, ruthenium PACT compounds are based on complexes of the [Ru(bpy)<sub>3</sub>]<sup>2+</sup> (bpy = 2,2'-bipyridine) family, where the photosubstituted ligand is a sterically hindering 2,2'-bipyridyl ligand such as 6,6'-dimethyl-2,2'-bipyridine (dmbpy).<sup>19, 22,23</sup> The increased cytotoxicity is generally attributed to the intracellular formation of the bis-aqua complex *cis*-[Ru(bpy)<sub>2</sub>(OH<sub>2</sub>)<sub>2</sub>]<sup>2+</sup>, which is believed to be the cytotoxic species. It should be noted, however, that upon light irradiation of [Ru(bpy)<sub>2</sub>(dmbpy)]<sup>2+</sup> the free dmbpy ligand is also generated, which biological properties and cytotoxicity have not been evaluated yet.

In order to specifically address the question of the cytotoxicity of the metal-containing fragment, we embarked into investigating whether natural amino acids such as L-proline, instead of hindering bipyridyl ligands, could be used to cage a *cis* bis-aqua ruthenium species. Amino acids are naturally present in a cell, so that the photochemical generation of one equivalent of such ligands is not expected to have any impact on cell survival. For amino acid-caged ruthenium polypyridyl complexes, any light-induced toxicity would be solely attributed to the metal fragment. In literature several examples of *cis* ruthenium(II)-diimine complexes coordinated to deprotonated L-amino acids are described that, upon light irradiation, interconvert between the  $\Lambda$ -L and the  $\Delta$ -L isomers.<sup>24-25</sup> However, to our knowledge, photosubstitution of an amino acid by solvent molecules has not been described yet. As reported for complexes with similar N,O chelating ligands,<sup>26-28</sup> the strong  $\sigma$ -donor properties of the carboxylate moiety usually increases the  $e_g$  level of the metal complex, and thereby the gap

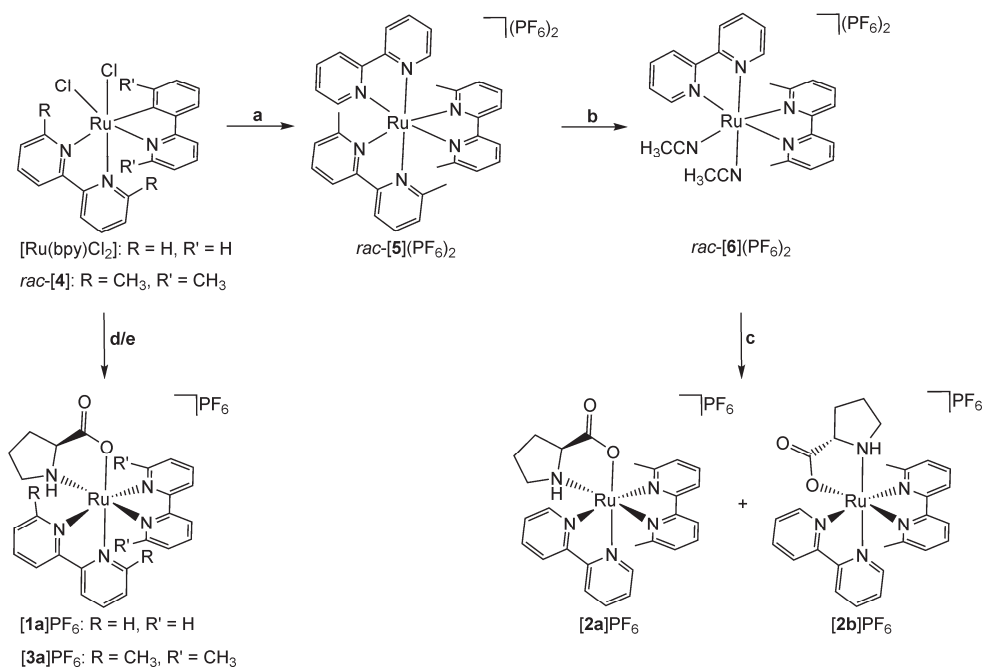
between the  $^3\text{MLCT}$  and  $^3\text{MC}$ . Such increased gap enhances the photostability of the complex by quenching photosubstitution reactions involving the  $^3\text{MC}$  states. In order to recover ligand photosubstitution properties, sterically hindering chelates such as dmbpy can be reintroduced, but if possible as spectator ligands, to see whether the  $^3\text{MC}$  states are low enough in energy to come in the vicinity of that of the photochemically generated  $^3\text{MLCT}$  states.<sup>29</sup>

Of course, octahedral complexes bearing chiral and/or dissymmetric bidentate ligands such as amino acids can lead to the formation of many different isomers.<sup>30</sup> Thus, the preparation of such complexes is *a priori* challenging, although diastereoselective coordination reactions making use of interligand repulsion and chromatographic separation techniques have been described in the past.<sup>31-33</sup> Here, we report on the synthesis of a series of L-proline-bound ruthenium complexes comprising  $\Lambda$ -[Ru(bpy)<sub>2</sub>(L-prol)]PF<sub>6</sub> (**[1a]**PF<sub>6</sub>),  $\Lambda$ -[Ru(bpy)(dmbpy)(L-prol)]PF<sub>6</sub> (**[2a]**PF<sub>6</sub> and **[2b]**PF<sub>6</sub>), and  $\Lambda$ -[Ru(dmbpy)<sub>2</sub>(L-prol)]PF<sub>6</sub> (**[3a]**PF<sub>6</sub>, see Scheme 2.1). In this series, the number of sterically hindering methyl groups increases from zero in **[1a]**PF<sub>6</sub>, to two in **[2a]**PF<sub>6</sub> and **[2b]**PF<sub>6</sub>, and four in **[3a]**PF<sub>6</sub>. The influence of the solvent on the photoreactivity of these complexes was also investigated.

## 2.2 Results and discussion

### 2.2.1 Synthesis and characterization

The four L-proline-coordinated ruthenium polypyridyl complexes were prepared as shown in Scheme 2.1. Complexes **[1a]**PF<sub>6</sub> and **[3a]**PF<sub>6</sub> were synthesized by reacting the precursor *rac*-[Ru(bpy)<sub>2</sub>Cl<sub>2</sub>] or *rac*-[Ru(dmbpy)<sub>2</sub>Cl<sub>2</sub>], respectively, with L-proline.<sup>34</sup> As reported by Meggers *et al.*, coordination of the chiral ligand L-proline to these racemic mixtures is diastereoselective and leads to the  $\Lambda$ -L diastereoisomer as the major (**[1a]**<sup>+</sup>) or sole (**[3a]**<sup>+</sup>) products.<sup>34-36</sup> The least strained complex was obtained as a 17:1 **[1a]**<sup>+</sup>:**[1b]**<sup>+</sup> mixture of diastereoisomers, where **[1b]**<sup>+</sup> is the  $\Delta$ -L isomer. This mixture can further be resolved by silica column chromatography to obtain analytically pure samples of **[1a]**PF<sub>6</sub>. On the other hand, the most strained complex, **[3a]**PF<sub>6</sub>, was directly obtained as a single  $\Lambda$ -L diastereoisomer without traces of the  $\Delta$ -L diastereoisomer **[3b]**<sup>+</sup>, as shown by the <sup>1</sup>H NMR of the crude product with a single set of 12 protons in the aromatic region.



Scheme 2.1. Synthesis of  $[\text{1a}]\text{PF}_6$ ,  $[\text{2a}]\text{PF}_6$ ,  $[\text{2b}]\text{PF}_6$ , and  $[\text{3a}]\text{PF}_6$ . a) i) *rac*-[4] (1 equiv), bpy (0.8 equiv), ethylene glycol, 3.5 h, 190 °C, pressure tube; ii)  $\text{KPF}_6$ , 79%; b)  $\text{CH}_3\text{CN}$ , 25 °C, White light Xe lamp, 59%; c) *L*-proline (2.5 equiv),  $\text{K}_2\text{CO}_3$  (1.25 equiv), ethylene glycol, 40 min, 190 °C, pressure tube; d)  $[\text{1a}]\text{PF}_6$  was synthesized according to Meggers *et al.*<sup>34</sup> e) i) *rac*-[4] (1 equiv), *L*-proline (2.2 equiv),  $\text{K}_2\text{CO}_3$  (1.1 equiv), ethylene glycol, 45 min, 190 °C, pressure tube; ii)  $\text{KPF}_6$ , 56%.

The tris-heteroleptic complexes  $[\text{2a}]\text{PF}_6$  and  $[\text{2b}]\text{PF}_6$  bear three different bidentate ligands and are less straightforward to prepare. Several methodologies to synthesize tris-heteroleptic polypyridyl ruthenium complexes are known in the literature, and most of them rely on the sequential addition of the different diimine ligands to a starting compound such as  $[\text{Ru}(\text{CO}_2)_2\text{Cl}_2]_n$ , *cis*- $[\text{Ru}(\text{DMSO})_4\text{Cl}_2]$ , or  $[\text{Ru}(\text{C}_6\text{H}_6)\text{Cl}_2]_2$ .<sup>37-42</sup> However, for the synthesis of the tris-heteroleptic complex bearing one dmbpy,  $[\text{2}]\text{PF}_6$ , we adapted a two-step synthesis introduced by von Zelewsky *et al.* using the highly strained  $[\text{Ru}(\text{bpy})(\text{biq})_2]^{2+}$  species (biq = 2,2'-biquinoline) as an intermediate which, after irradiation in  $\text{CH}_3\text{CN}$ , leads to the tris-heteroleptic precursor  $[\text{Ru}(\text{bpy})(\text{biq})(\text{CH}_3\text{CN})_2]^{2+}$ .<sup>43</sup> With this method we take advantage of the photoreactivity of strained ruthenium complexes and avoid the issues of adding a single equivalent of the first diimine ligand when other synthetic routes are used. Thus, as shown in Scheme 2.1, *rac*- $[\text{Ru}(\text{dmbpy})_2\text{Cl}_2]$  (*rac*-[4]) was first converted into *rac*- $[\text{Ru}(\text{bpy})(\text{dmbpy})_2](\text{PF}_6)_2$  (*rac*-[5] $(\text{PF}_6)_2$ ) by addition of one equivalent of bpy in ethylene glycol at 190 °C in a pressure tube. Limited ligand scrambling was observed,

resulting in a sample containing also *rac*-[Ru(dmbpy)<sub>3</sub>](PF<sub>6</sub>)<sub>2</sub> and *rac*-[Ru(bpy)<sub>2</sub>(dmbpy)](PF<sub>6</sub>)<sub>2</sub> as minor impurities (as observed by mass spectrometry, see Figure AIII.1). A solution of *rac*-[**5**](PF<sub>6</sub>)<sub>2</sub> in CH<sub>3</sub>CN was then irradiated using white light, whereby one dmbpy ligand was substituted by two solvent molecules to afford *rac*-[Ru(bpy)(dmbpy)(CH<sub>3</sub>CN)<sub>2</sub>](PF<sub>6</sub>)<sub>2</sub> (*rac*-[**6**](PF<sub>6</sub>)<sub>2</sub>). Several impurities derived from ligand scrambling and their photolysis products were present as well at that stage (Figure AIII.2), but they could be for the most part removed after L-proline coordination. In the final step, L-proline was reacted with *rac*-[**6**](PF<sub>6</sub>)<sub>2</sub> in ethylene glycol to yield the tris-heteroleptic complex [**2**]PF<sub>6</sub> in 62% yield as a mixture of isomers.

In octahedral complexes with two bpy or two dmbpy ligands and one L-proline the geometry is rather straightforward and only the two diastereoisomers  $\Lambda$ -L and  $\Delta$ -L can exist. In contrast, for heteroleptic complexes with three different bidentate ligands the geometry is more complex: besides the chirality of the octahedron ( $\Lambda$  or  $\Delta$ ) and that of the proline ligand (here only L), which generates two diastereoisomers, the two possible orientations of the N,O dissymmetric proline ligand results in two different regioisomers. In other words, for the  $\Lambda$ -L and  $\Delta$ -L isomers of [**2**]PF<sub>6</sub> either the amine group or the carboxylic acid moiety of L-proline is *trans* to dmbpy. The four possible diastereoisomers of [**2**]<sup>+</sup> are named [**2a**]<sup>+</sup>, [**2b**]<sup>+</sup>, [**2c**]<sup>+</sup>, and [**2d**]<sup>+</sup>, and their structures are shown in Figure AIII.20. According to <sup>1</sup>H NMR, the crude product [**2**]PF<sub>6</sub> was obtained, together with traces of [**3a**]PF<sub>6</sub>, as a mixture of only two diastereoisomers in a ratio close to 1:1, as shown by the two characteristic doublets at 8.58 and 9.18 ppm corresponding to the position 6' on the bpy (Figure AIII.3). After purification by alumina chromatography using CH<sub>2</sub>Cl<sub>2</sub>:CH<sub>3</sub>OH (CH<sub>3</sub>OH = 1% to 3%) as an eluent, this mixture could be efficiently resolved. The first fraction was obtained as an NMR-pure sample whereas the second fraction was isolated as a mixture of a single isomer of [**2**]PF<sub>6</sub> and [**3a**]PF<sub>6</sub> in a ratio 85:15 (Figure AIII.3). Circular dichroism spectroscopy of these two isomers in H<sub>2</sub>O showed a positive band at 300 nm for both isolated species (Figure AIII.4), which means that they both have the  $\Lambda$  octahedral configuration.<sup>44-45</sup> As a consequence, these isomers are necessarily complexes [**2a**]PF<sub>6</sub> and [**2b**]PF<sub>6</sub> (Figure AIII.20). NOESY analysis of the first fraction in D<sub>2</sub>O showed an off-diagonal correlation between the  $\alpha$  proton of the L-proline ligand and the methyl substituent on the dmbpy (Figure AIII.5), whereas no signal between those protons was found for the second fraction. Since the  $\alpha$  proton and the methyl substituent on the dmbpy are closer in complex [**2a**]PF<sub>6</sub> than in complex [**2b**]PF<sub>6</sub>, it is concluded that these complexes are

found in the first and the second fraction, respectively. Finally, single crystals suitable for X-ray structure determination were obtained for  $[\mathbf{2b}]PF_6$  by slow crystallization in water. The space group (P1) is chiral and the X-ray structure contained a single configuration of the coordination octahedron ( $\Lambda$ ). The molecular structure, shown in Figure 2.1a, shows a long N5-C26 single bond (1.510(5) Å, Table 2.1) for the L-proline ligand, and the oxygen atom of L-proline is found *trans* to the dmbpy ligand. Thus, the nature of the isomer  $[\mathbf{2b}]PF_6$  is unequivocally confirmed, and as a consequence  $[\mathbf{2a}]PF_6$  was analysed as the  $\Lambda$ -L isomer having the oxygen *trans* to the bpy ligand.

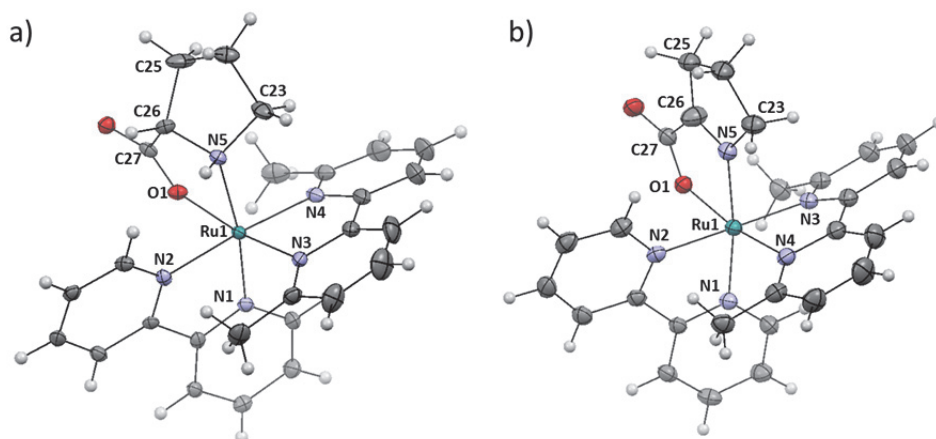


Figure 2.1. Displacement ellipsoid plot (50% probability level) of the crystal structure of a)  $[\mathbf{2b}]PF_6$  and b)  $[\mathbf{2b} - 2H]PF_6$ . Hexafluoridophosphate counteranions, lattice  $H_2O$ , and disorder have been omitted for clarity.

Table 2.1. Selected bond length (Å) and angles ( $^\circ$ ) for  $[\mathbf{2b}]PF_6$  and  $[\mathbf{2b} - 2H]PF_6$ .

	$[\mathbf{2b}]PF_6$	$[\mathbf{2b} - 2H]PF_6$
<b>Ru1-O1</b>	2.100(3)	2.111(1)
<b>Ru1-N1</b>	2.024(3)	2.047(1)
<b>Ru1-N2</b>	2.067(4)	2.066(2)
<b>Ru1-N3</b>	2.074(3)	2.074(2)
<b>Ru1-N4</b>	2.098(4)	2.067(2)
<b>Ru1-N5</b>	2.143(3)	2.046(1)
<b>N5-C26</b>	1.510(5)	1.305(3)
<b>C25-C26-N5</b>	115.5(2)	106.0(3)
<b>C23-N5-C26-C27</b>	122.1(4)	-174.4(2)

Density Functional Theory (DFT) calculations of both diastereoisomers  $\Lambda$ -L and  $\Delta$ -L of  $[1]^+$  and  $[3]^+$ , and the four possible diastereoisomers of  $[2]^+$ , were performed in water using the COSMO model to simulate solvent effects (see Experimental section). The optimized structures, their energies in water, and their dipole moments are given in Figure AIII.20 and Table AIII.3, respectively. In water, the  $\Lambda$  complexes  $[1a]^+$  and  $[3a]^+$  are 6.9 and 19.6  $\text{kJ}\cdot\text{mol}^{-1}$  more stable than their  $\Delta$  diastereoisomers  $[1b]^+$  and  $[3b]^+$ , respectively. These results confirm that the diastereoselectivity of L-proline coordination to *rac*-[Ru(bpy)<sub>2</sub>Cl<sub>2</sub>] or *rac*-[Ru(dmbpy)<sub>2</sub>Cl<sub>2</sub>] is enhanced when hindering methyl substituents are put on the bpy ligands. For the heteroleptic complex  $[2]^+$ , the isomer  $[2b]^+$  was found to be the most stable in water of all four isomers, followed by  $[2a]^+$ ,  $[2d]^+$ , and  $[2c]^+$ , at +1.9  $\text{kJ}\cdot\text{mol}^{-1}$ , +2.2  $\text{kJ}\cdot\text{mol}^{-1}$ , and +25.7  $\text{kJ}\cdot\text{mol}^{-1}$ , respectively. Although  $[2c]^+$  clearly is too high in energy to be formed under thermodynamic control, the isomers  $[2a]^+$ ,  $[2b]^+$ , and  $[2d]^+$  are too close in energy to predict any stereoselectivity based on thermodynamic arguments. The fact that  $[2d]^+$  is not observed experimentally can be interpreted as a sign that the coordination of L-proline to [Ru(bpy)(dmbpy)(CH<sub>3</sub>CN)<sub>2</sub>]<sup>2+</sup> is under kinetic control. DFT models could also be used to find signs of steric hindrance in this series of complexes. The structural distortion parameters, *i.e.* the bond angle variance ( $\sigma^2$ ) and the mean quadratic elongation ( $\lambda$ ), were calculated for complexes  $[1a]^+$ ,  $[2b]^+$ , and  $[3a]^+$  (Table AIII.4).<sup>46-48</sup> The values found, 50.5, 75.7, and 90.4 ( $\sigma^2$ ), and  $2.21\cdot 10^{-4}$ ,  $2.50\cdot 10^{-4}$ , and  $3.06\cdot 10^{-4}$  ( $\lambda$ ), respectively, confirmed that addition of two or four methyl substituents at the 6 and 6' position of the bpy ligands has a major impact in the distortion of the octahedral geometry of the ruthenium complexes. Surprisingly, this distortion has no significant effect on the Ru-O bond distances, being 2.109, 2.105, and 2.109 Å in complexes  $[1a]^+$ ,  $[2b]^+$ , and  $[3a]^+$ , respectively.

### 2.2.2 Photochemistry

The photoreactivity of  $[1a]PF_6$  was studied first. The evolution of the UV-vis spectrum of a solution of  $[1a]PF_6$  in phosphate buffer saline (PBS) was studied upon irradiation at 493 nm under air. A hypsochromic shift in the <sup>1</sup>MLCT band was observed, with a change in the absorption maximum from 495 nm to 467 nm and an isosbestic point at 486 nm (Figure 2.2a). Mass spectrometry after irradiation showed a peak at  $m/z = 526.1$  (Figure 2.3a), which is two units smaller than the starting complex (calcd  $m/z = 528.1$ ). These two units correspond to the loss of two hydrogen atoms. According to Keene *et al.*, these hydrogens are derived from the  $\alpha$ -hydrogen and the amine hydrogen

of L-proline, *i.e.* the imine complex  $[\text{Ru}(\text{bpy})_2(\text{L-prol} - 2\text{H})]\text{PF}_6$  ( $[\mathbf{7}]\text{PF}_6$ ) was formed.<sup>49</sup> A quantum yield ( $\Phi_{\text{PR}}$ ) of 0.0010 was calculated for this photoreaction in PBS (see Appendix I and Figure AI.3) and a dark control experiment at 37 °C did not show any change in the UV-vis spectrum over time (Figure AIII.6), which excludes a thermal reaction. The oxidative nature of the photoreaction was confirmed by performing the same photoreaction under Ar. No change either in the UV-vis spectra (Figure 2.2b) or in the mass spectrum (Figure 2.3c) was observed in absence of molecular oxygen. When monitoring the irradiation with NMR under Ar, a new doublet appeared at 8.91 ppm, which corresponds to the  $\Delta$ -L isomer  $[\mathbf{1b}]^+$  (Figure AIII.7).<sup>34</sup> In addition, a decrease in the band at 300 nm in the CD spectra was observed upon irradiation under the same conditions (Figure AIII.8), confirming the isomerization. Finally, addition of the antioxidant glutathione (GSH) before irradiation under air partially slowed down the photoreaction (Figure 2.2c and Figure AIII.9a). Under such conditions, mass spectrometry after 180 min of irradiation (Figure 2.3b) showed a mixture of  $[\mathbf{1}]^+$  ( $m/z = 528.1$ ) and  $[\mathbf{7}]^+$  ( $m/z = 526.1$ ), since the relative intensity of the peak at  $m/z = 528.1$  in the isotopic pattern of  $[\mathbf{7}]\text{PF}_6$  was slightly higher than expected, as shown in the calculated isotopic pattern for a given 7:3 mixture of  $[\mathbf{1}]^+:[\mathbf{7}]^+$  in Figure AIII.10.

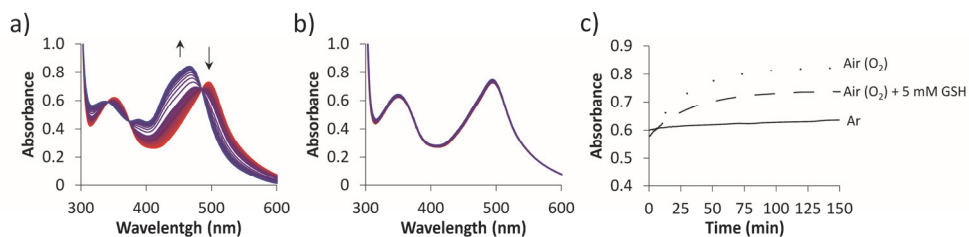


Figure 2.2. Evolution of the UV-vis spectra of a 0.078 mM solution of  $[\mathbf{1a}]\text{PF}_6$  in PBS irradiated at 298 K with a 493 nm LED at a photon flux of  $1.61 \cdot 10^{-7} \text{ mol} \cdot \text{s}^{-1}$  (a) under air and (b) under Ar. (c) Evolution of the Absorbance at 473 nm upon irradiation under air (dotted line), under air in presence of 5 mM GSH (dashed line), and under Ar (continuous line).

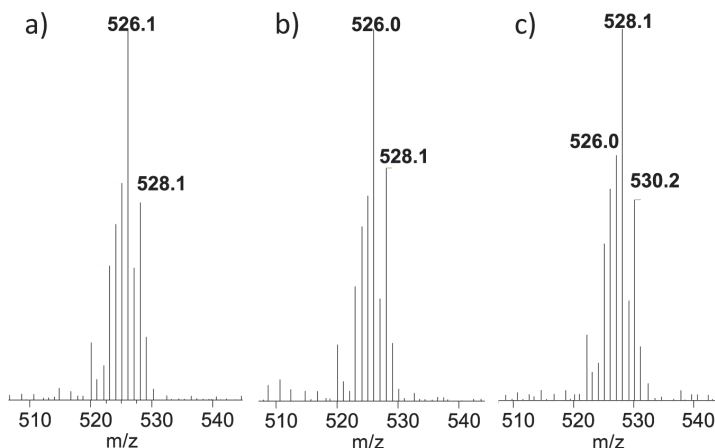
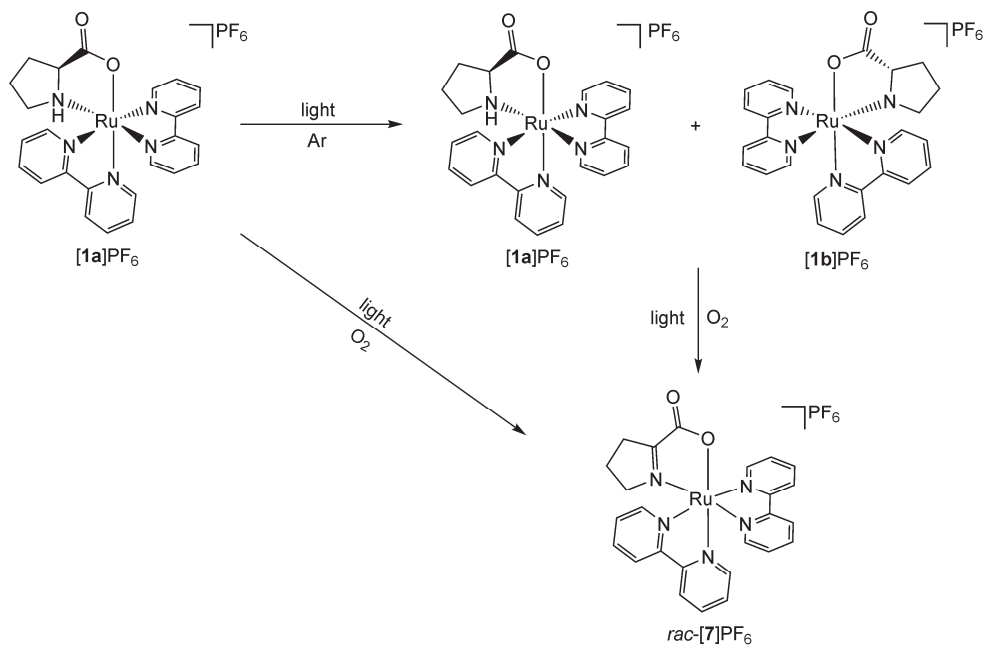


Figure 2.3. Mass spectrum of a 0.078 mM solution of **[1a]**PF<sub>6</sub> in PBS after light irradiation at 298 K with a 493 nm LED at a photon flux of  $1.61 \cdot 10^{-7} \text{ mol} \cdot \text{s}^{-1}$  (a) under air, (b) under air in presence of 5 mM GSH, and (c) under Ar. Conditions are detailed in Table AIII.1.

In order to confirm that irradiation led to photooxidation and to compare our results under light irradiation to those obtained using electrochemical oxidation by Yamaguchi *et al.*,<sup>50</sup> a spectroelectrochemistry analysis of **[1a]**PF<sub>6</sub> was performed. Chronoamperometry of a solution of **[1a]**PF<sub>6</sub> in PBS with a constant potential of +0.645 V vs. Ag/AgCl using carbon sponges as working and counter electrodes was monitored with UV-vis spectroscopy. After 2 h, the current stabilized at 0.05 mA and the oxidative reaction was considered as finished. As shown in Figure AIII.18a and Figure AIII.19 the UV-vis and the mass spectra showed the same change as upon light irradiation, *i.e.* a hypsochromic shift from 495 nm to 466 nm in the MLCT band with an isosbestic point at 486 nm, and a peak at a  $m/z = 526.1$ . Thus, as shown in Scheme 2.2, upon light irradiation of **[1a]**<sup>+</sup> under Ar partial photoisomerization from  $\Lambda$ -L to  $\Delta$ -L takes place, as has been described extensively in the literature for *cis*-ruthenium(II) diimine complexes coordinated to deprotonated amino acids.<sup>24-25</sup> However, in presence of O<sub>2</sub> the coordinated ligand L-proline is oxidized to its imine analogue **[7]**<sup>+</sup>, as described for the complex [Ru(bpy)<sub>2</sub>(2-(L-aminoethyl)(pyridine))(PF<sub>6</sub>)<sub>2</sub>] by Keene *et al.* and for [Os(bpy)<sub>2</sub>(2-aminoethanesulfinate)](PF<sub>6</sub>) by Tamura *et al.*<sup>49, 51</sup> Although the exact mechanism of photooxidation is unclear, we suggest that the amine may be oxidized by the singlet oxygen (<sup>1</sup>O<sub>2</sub>) generated in presence of light and molecular oxygen, as it has been demonstrated that <sup>1</sup>O<sub>2</sub> is a much better oxidant than the ground state <sup>3</sup>O<sub>2</sub>.<sup>52</sup> More in-depth studies would be needed to confirm this hypothesis.



Scheme 2.2. Scheme of the photoisomerization and photooxidation observed upon visible light irradiation of  $[1a]PF_6$  in PBS at 298 K with a 493 nm LED at a photon flux of  $1.61 \cdot 10^{-7} \text{ mol} \cdot \text{s}^{-1}$ .

In a second step, the reactivity of the more strained complexes  $[2a]PF_6$ ,  $[2b]PF_6$ , and  $[3a]PF_6$ , was investigated. When a solution of  $[3a]PF_6$  was irradiated in PBS at 493 nm under air no change in the UV-vis or mass spectra was observed (Figure 2.4a and Figure AIII.9). Like for  $[1a]^+$ , partial isomerization from  $\Lambda$ -L to  $\Delta$ -L occurred as shown by the decrease of the band at 300 nm in the CD spectrum (Figure AIII.11). Thus, for complex  $[3a]PF_6$  photooxidation does not occur in PBS, which represents a dramatic change compared to the photoreactivity of  $[1a]PF_6$ . Surprisingly, despite the much higher steric hindrance of the complex, irradiation did not lead to photosubstitution reactions either. On the other hand, when a solution of  $[2a]PF_6$  in deuterated PBS was irradiated with a 1000 W Xe lamp equipped with a 450 nm blue light filter and monitored with  $^1\text{H}$  NMR, a doublet at 9.1 ppm, characteristic of the 6' proton of the bpy ligand in  $[2b]PF_6$ , arose upon 15 min irradiation. Under such conditions photoconversion of  $[2a]PF_6$  to  $[2b]PF_6$  was completed after 150 min irradiation (Figure 2.4b). By contrast, no change in the  $^1\text{H}$  NMR spectrum was observed when irradiating  $[2b]PF_6$  under the same conditions (Figure 2.4c). Thus, isomer  $[2a]PF_6$ , which is a kinetic product formed by coordination of L-proline to  $[\text{Ru}(\text{bpy})(\text{dmbpy})(\text{CH}_3\text{CN})_2]^{2+}$ , isomerizes photochemically into  $[2b]PF_6$ , which is the thermodynamically most stable isomer of  $[2]^+$ . According to the UV-vis spectra evolution shown in Figure 2.4a, Figure

AIII.9b, and Figure AIII.9c, isomerization of  $[2a]^+$  to  $[2b]^+$  is not the only process occurring upon irradiation, and photooxidation takes place as well. However, this process occurs at a much lower rate than for  $[1a]^+$ .

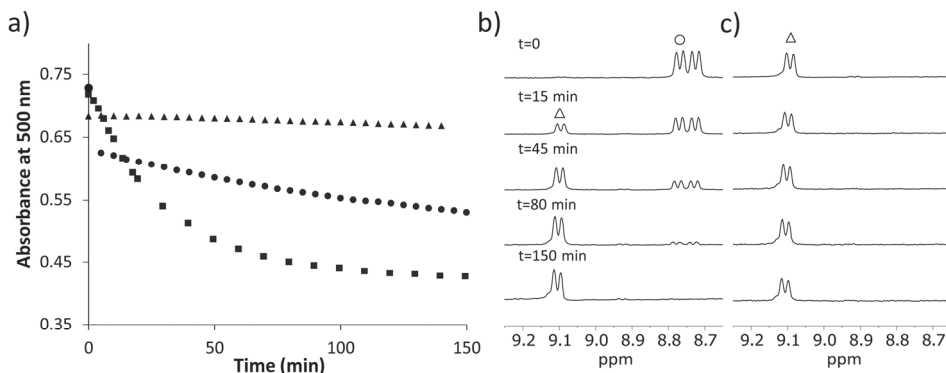


Figure 2.4. a) Evolution of the absorption at 500 nm of a solution of  $[1a]PF_6$  (0.078 mM, circles),  $[2a]PF_6$  (0.032 mM, squares), and  $[3a]PF_6$  (0.077 mM, triangles) in PBS upon irradiation under air with a 493 nm LED with a photon flux of  $1.61 \cdot 10^{-7}$ ,  $1.17 \cdot 10^{-7}$ , and  $1.48 \cdot 10^{-7} \text{ mol} \cdot \text{s}^{-1}$ , respectively. Conditions are detailed in Table AIII.1. b & c) Evolution of the  $^1H$  NMR spectra of a solution of b)  $[2a]PF_6$  (2.7 mg in 0.7 mL, circles) and c)  $[2b]PF_6$  (2.6 mg in 0.7 mL, triangles) in deuterated PBS upon light irradiation with the beam of a 1000 W Xe lamp filtered with a 450 nm blue light filter under air.

When a solution of  $[2a]PF_6$  in water was left to slowly crystallize in presence of dimmed daylight, single crystals were obtained that could be analysed by X-ray crystallography. The crystal structure (Figure 2.1b) shows a short N5-C26 bond in the L-proline ligand (1.305(3) Å, Table 2.1) characteristic of a N=C double bond. Furthermore, the torsion angle between atoms C23-N5-C25-C27 is 174.4(2) in the new structure (vs. 122.1(4) in the crystal structure of  $[2b]PF_6$ ), confirming the quasi-planar geometry of N5 and C26 in the new structure, and thus the oxidation of L-proline into an imine. In addition, the carboxylate O-donor group is found to be *trans* to dmbpy like in  $[2b]^+$ , which confirms the photochemical isomerization of  $[2a]^+$  to  $[2b]^+$  during crystallization. Thus, the obtained crystal structure corresponds to the imine complex  $[2b - 2H]^+$ . It should be noted that as this ruthenium complex crystallized in a space group that contained an inversion center (P-1), it is a racemate. Because NMR experiments showed that irradiation of  $[2b]^+$  did not lead to the  $\Delta$  isomer  $[2d]^+$ , finding both enantiomers in the crystal structure of  $[Ru(bpy)(dmbpy)(L\text{-}prol - 2H)](PF_6) \cdot H_2O$  means that the  $\Lambda$ -to- $\Delta$  racemization occurred after the photoisomerization of  $[2a]^+$  to  $[2b]^+$  and after photooxidation. According to Gomez *et al.*, the acidity of the amine of the coordinated L-proline ligand may have a crucial effect on the rate of

dehydrogenation for amino acids coordinated to polypyridyl ruthenium complexes.<sup>53</sup> The more acidic the amine, the faster the dehydrogenation takes place. In our case, the presence of more methyl substituents on the bpy ligands clearly leads to lower L-proline photooxidation rates. Since the methyl substituents are electron donating, a plausible interpretation of this observation is that more methyl substituents will thus increase the electron density on ruthenium and hence decrease the acidity of the coordinated L-proline amine. At that stage, however, it remains impossible to say whether or not the steric effects of the methyl groups contribute as well to the dramatic switch in photoreactivity observed in water between  $[2a]^+$ ,  $[2b]^+$ , and  $[3a]^+$ , and the non-strained complex  $[1a]^+$ .

At that point, the absence of any photodissociation reaction upon irradiation of all four complexes in aqueous medium may be surprising, as the X-ray structure of  $[2b]^+$  and the DFT-minimized geometries of the strained molecules  $[2a]^+$ ,  $[2b]^+$ , and  $[3a]^+$  are distorted enough to suggest the presence of low-lying  $^3MC$  states. In order to investigate further this question, irradiation was performed in  $CH_3CN$ , which is a much less polar solvent than water, as well as an excellent ligand for ruthenium(II). When a  $CH_3CN$  solution of  $[1a]PF_6$  was irradiated at 493 nm under Ar no change in the maximum absorbance of the MLCT was observed (Figure 2.5). However, when the same experiment was performed using  $[2a]PF_6$ ,  $[2b]PF_6$ , or  $[3a]PF_6$ , a clear photoreaction was observed by UV-vis spectroscopy, characterized by a hypsochromic shift of the MLCT band of all three complexes (Figure 2.5). For the heteroleptic complex  $[2a]^+$ , the maximum absorbance of the  $^1MLCT$  band shifted from 509 nm to 432 nm (Figure 2.5b), and the mass spectrum after irradiation showed peaks at  $m/z = 185.4$ , 261.9, 452.2, and 669.2 (Figure AIII.12a). These peaks correspond to the free ligand  $\{dmbpy + H\}^+$  (calcd  $m/z = 185.2$ ),  $[Ru(bpy)(dmbpy)(CH_3CN)_2]^{2+}$  (calcd  $m/z = 262.1$ ),  $[Ru(bpy)(L-Prol - 2H)(CH_3CN)_2]^+$  (calcd  $m/z = 452.1$ ), and  $\{[Ru(bpy)(dmbpy)(CH_3CN)_2]PF_6\}^+$  (calcd  $m/z = 669.1$ ), respectively. Thus, in  $CH_3CN$  both bidentate ligands L-proline and dmbpy are photosubstituted by two solvent molecules. Similar results were found when a  $CH_3CN$  solution of  $[3a]PF_6$  was irradiated at 493 nm. A shift in the absorbance maximum of the MLCT band occurred from 516 nm to 444 nm (Figure 2.5d), and the mass spectrum after irradiation showed peaks at  $m/z = 185.5$ , 276.3, 480.2, and 697.2, corresponding to the free ligand  $\{dmbpy+H\}^+$  (calcd  $m/z = 185.2$ ),  $[Ru(dmbpy)_2(CH_3CN)_2]^{2+}$  (calcd  $m/z = 276.1$ ),  $[Ru(dmbpy)(L-prol - 2H)(CH_3CN)_2]^+$  (calcd  $m/z = 480.1$ ), and  $\{[Ru(dmbpy)_2(CH_3CN)_2]PF_6\}^+$  (calcd  $m/z = 697.1$ ), respectively (Figure AIII.12b).

Thus, also for  $[3a]^+$  irradiation in  $CH_3CN$  triggers the non-selective photosubstitution of both the L-proline and the dmbpy ligands. When the reaction was performed at a lower light intensity, the photosubstitution rate was lowered and a first isosbestic point at 493 nm could be observed during the first 10 min of the reaction (see Figure AIII.14a). A mass spectrum measured at that time point showed no peaks corresponding to free dmbpy (Figure AIII.14b), suggesting that L-proline is substituted more rapidly than dmbpy. Overall, in  $CH_3CN$  the strained complexes  $[2a]^+$  and  $[3a]^+$  indeed triggered the expected photosubstitution reactions that were not observed in PBS. However, these photoreactions are not selective and lead to the substitution of both L-proline and dmbpy.

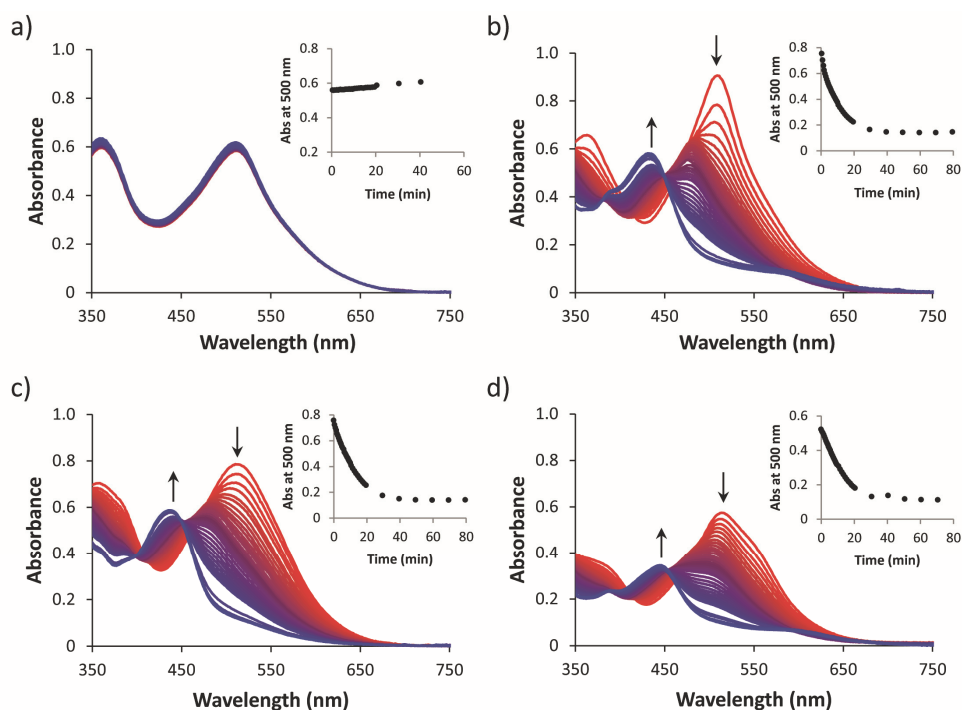


Figure 2.5. a) Evolution of the UV-vis spectra of a solution of a)  $[1a]PF_6$  (0.071 mM), b)  $[2a]PF_6$  (0.092 mM), c)  $[2b]PF_6$  (0.121 mM), and d)  $[3a]PF_6$  (0.07 mM) in  $CH_3CN$  upon irradiation under Ar with a 493 nm LED with a photon flux of  $1.10 \cdot 10^{-7}$ ,  $1.12 \cdot 10^{-7}$ ,  $1.05 \cdot 10^{-7}$ , and  $1.12 \cdot 10^{-7} \text{ mol} \cdot \text{s}^{-1}$ , respectively. Conditions are detailed in Table AIII.1.

Considering the discrepancy between the photoreactivity observed in aqueous buffer and that observed in  $CH_3CN$ , photosubstitution was also studied for  $[3a]^+$  in water mixtures containing large amounts (1 to 80 vol%) of  $CH_3CN$ , thus in pseudo first-order conditions. As shown in Figure AIII.15, in all cases photosubstitution occurred, as

demonstrated by an isosbestic point at 388 nm, two sequential isosbestic points at 457 and at 479 nm showing a two-stage reaction, and the overall shift of the maximum absorbance of the <sup>1</sup>MLCT band from 504 nm to 445 nm. Interestingly, mass spectra measured after the first stage of the reaction showed, next to the peaks at  $m/z = 275.8$  and  $697.5$  corresponding to the final photoproduct  $[\text{Ru}(\text{dmbpy})_2(\text{CH}_3\text{CN})_2]^{2+}$  (calcd  $m/z = 276.1$ ) and  $\{[\text{Ru}(\text{dmbpy})_2(\text{CH}_3\text{CN})_2]\text{PF}_6\}^+$  (calcd  $m/z = 697.1$ ), an additional peak at  $m/z = 313.3$  characteristic for an intermediate where one of the bidentate ligands is bound in a monodentate fashion and one  $\text{CH}_3\text{CN}$  is coordinated, e.g.  $\{[\text{Ru}(\text{dmbpy})_2(\eta^1\text{-L-prol})(\text{CH}_3\text{CN})] + \text{H}\}^{2+}$  (calcd  $m/z = 313.1$ , see Figure AIII.16). Mass spectrometry at the steady state neither showed this intermediate  $m/z = 313.3$  peak, nor free dmbpy ligand. Clearly, the two-step photochemical reaction observed by UV-vis corresponds to the initial substitution of one coordinating atom of L-proline by one  $\text{CH}_3\text{CN}$  ligand, followed by the selective substitution of the second coordinating atom of L-proline by a second  $\text{CH}_3\text{CN}$  ligand. The absorbance of the solution at 500 nm evolved linearly with irradiation time during the first 5 min of all experiments, showing that under such conditions the reaction rate was constant (see Figure AIII.17a and Table AIII.2). Surprisingly, the observed rate constants ( $k_{\text{obs}}$ ) for the formation of the final photoproduct  $[\text{Ru}(\text{dmbpy})_2(\text{CH}_3\text{CN})_2]^{2+}$  evolved linearly with  $\text{CH}_3\text{CN}$  concentrations in water (Figure AIII.17b), which discards a fully dissociative mechanism for such two-step ligand photosubstitution. Since an associative mechanism is unlikely due to the crowdedness of the strained complex  $[\mathbf{3a}]^+$ , we suggest that the photosubstitution may take place *via* an interchange mechanism, although further kinetic studies should be performed to differentiate between a dissociative interchange and an associative interchange mechanism.<sup>54-55</sup> Overall, an important observation is that the selectivity of the photosubstitution reaction in a 2:8  $\text{H}_2\text{O}:\text{CH}_3\text{CN}$  mixture was different from that observed in pure  $\text{CH}_3\text{CN}$ : in the former case photosubstitution was selective and only the L-proline ligand dissociated from the complex, whereas in the latter case both dmbpy and L-proline were photosubstituted.

The different photoreactivity of  $[\mathbf{2a}]^+$ ,  $[\mathbf{2b}]^+$ , and  $[\mathbf{3a}]^+$  in PBS,  $\text{CH}_3\text{CN}$ , and  $\text{H}_2\text{O}:\text{CH}_3\text{CN}$  mixtures is puzzling, but it may be rationalized by different hypotheses. First, the coordinating properties of  $\text{CH}_3\text{CN}$  molecules towards ruthenium(II) are better than that of  $\text{H}_2\text{O}$ . As the photosubstitution of L-proline or dmbpy seems to proceed *via* intermediates having  $\eta^1$ -coordinated bidentate ligands, more coordinating monodentate ligands may stabilize these intermediates, lowering overall activations barrier, and thus increasing photosubstitution rates in presence of  $\text{CH}_3\text{CN}$ . Second, the carboxylate

group of L-proline is highly polar and it has excellent hydrogen bond-accepting properties. Putative intermediates where L-proline is coordinated in  $\eta^1$ ,  $\kappa\text{N}$  fashion, may hence be stabilized in presence of water, which would enhance the rate of L-proline photosubstitution *vs.* that of dmbpy. In contrast, in  $\text{CH}_3\text{CN}$  these  $[\text{Ru}(\text{dmbpy})_2(\eta^1, \kappa\text{N-L-prol})]^+$  intermediates may be relatively destabilized, while photosubstitution of the less polar dmbpy ligands may occur *via* stabilized  $[\text{Ru}(\eta^2\text{-dmbpy})(\eta^2\text{-L-prol})(\eta^1\text{-dmbpy})(\text{CH}_3\text{CN})]^+$  intermediates. Finally, the different triplet excited states involved in photosubstitution reactions are stabilized to a different extent in polar *vs.* apolar solvents.  $^3\text{MLCT}$  states are charge-transfer states that will be stabilized by solvents with a higher polarity (water), while  $^3\text{MC}$  states are not charge-transfer excited states and will be less stabilized by high-polarity solvents. Thus, in water the  $^3\text{MLCT}$ - $^3\text{MC}$  energy gap should be larger compared to that in  $\text{CH}_3\text{CN}$ , and hence the rate of photosubstitution reactions will be lower. Low photosubstitution rates mean that slow photooxidation and photoisomerization reactions will be observed, whereas in pure  $\text{CH}_3\text{CN}$  photosubstitution outcompetes these processes. Thorough – and challenging – theoretical studies including triplet state modelling with explicit solvent molecules will be needed to evaluate the contribution of these three different effects on the solvent dependence of photosubstitution reactions.

## 2.3 Conclusions

In this work, we demonstrated that heteroleptic complexes bearing the dissymmetric N,O ligand L-proline can be prepared stereoselectively, isolated, and characterized. In complex  $[\mathbf{1a}]^+$  the absence of steric hindrance and the electron-rich oxygen ligand of L-proline prevents any photosubstitution reaction, both in chloride-containing aqueous solution and in  $\text{CH}_3\text{CN}$ . Instead, photooxidation occurs in presence of air, leading to the formation of a  $\text{N}=\text{C}$  double bond. In parallel, partial isomerization of the chiral ruthenium center from  $\Lambda$  to  $\Delta$  occurs, as reported for other amino acidato analogues.<sup>24</sup> Increasing steric hindrance as in  $[\mathbf{2a-b}]^+$  and  $[\mathbf{3a}]^+$  did not promote photosubstitution in aqueous solution (PBS), unlike demonstrated with other ruthenium complexes such as  $[\text{Ru}(\text{bpy})_2(\text{dmbpy})]^{2+}$  or  $[\text{Ru}(\text{tpy})(\text{dmbpy})(\text{L})]^{2+}$ .<sup>23, 56</sup> Under such conditions, increasing the number of methyl groups on the bpy ligands strongly slows down photooxidation of the L-proline ligand, probably because of the electron-donating effect of the methyl groups. It was necessary to add an excess of  $\text{CH}_3\text{CN}$  in water to trigger the selective photosubstitution of L-proline in  $[\mathbf{3a}]^+$ . In pure  $\text{CH}_3\text{CN}$  however, the increased strain in  $[\mathbf{2a}]^+$ ,  $[\mathbf{2b}]^+$ , and  $[\mathbf{3a}]^+$  did promote photosubstitution reactions, but two ligands were photosubstituted in a non-selective fashion, *i.e.* L-proline *and* dmbpy. The influence of

the solvent on reactivity opens interesting mechanistic questions concerning photosubstitution reactions of ruthenium polypyridyl complexes. It also increases the complexity of the speciation of light-activatable anticancer compounds in cells. Photosubstitution reactions occurring in cells are usually modelled in aqueous, dichloromethane, or acetonitrile solutions, without discussing the difference between these media. Our results clearly demonstrate that solvents of different polarities and different coordinating properties may lead to different photoreactivities, and that choosing water vs. an organic solvent to study photosubstitution is not innocent. Finally, it may be noted that cellular microenvironments such as membranes, DNA, or protein binding pockets are rather hydrophobic, and that in such microenvironments photoreactions that seem not to occur in water, may actually take place.

## 2.4 Experimental

### 2.4.1 Materials and Methods

The ligands 2,2'-bipyridine (bpy), 6,6'-dimethyl-2,2'-bipyridine (dmbpy), and L-proline (L-prol) were purchased from Sigma-Aldrich, as well as monopotassium phosphate ( $\text{KH}_2\text{PO}_4$ ), sodium chloride (NaCl), and *cis*-bis(2,2'-bipyridine)dichlororuthenium(II) hydrate (*cis*-[Ru(bpy) $_2$ Cl $_2$ ]). Lithium chloride (LiCl) and potassium hexafluoridophosphate (KPF $_6$ ) were purchased from Alfar-Aesar and potassium carbonate (K $_2$ CO $_3$ ) was obtained from Merck. All reactants and solvents were used without further purification. The synthesis of *cis*-[Ru(dmbpy) $_2$ Cl $_2$ ] and [1a]PF $_6$  were carried out according to literature procedures.<sup>34, 57</sup> Sephadex LH-20 was used for the Size Exclusion Column (SEC).

Electrospray mass spectra (ES MS) were recorded by using a Thermoquest Finnagen AQA Spectrometer and a MSQ Plus Spectrometer, and CD spectra were recorded on a Bio-Logic MOS-500 spectrometer with a Bio-Logic ALX-300 lamp. For the irradiation experiments of NMR tubes, the light of a LOT 1000 W Xenon Arc lamp was used mounted with an infrared filter and either a 400 nm long pass or a 450 nm 450FS10-50 filter from Andover Corporation. UV-vis experiments were performed on a Cary 50 Varian spectrometer. When monitoring photoreactions with UV-vis, mass spectrometry, or circular dichroism (CD), a LED light source ( $\lambda_{\text{ex}} = 493$  nm, with a Full Width at Half Maximum of 14 nm) with a photon flux between  $1.08 \cdot 10^{-7}$  and  $1.55 \cdot 10^{-7}$  mol $\cdot$ s $^{-1}$  was used. For the spectroelectrochemistry a UV-vis light source

Avantes-DH-S-BAL and an Avantes Avaspec-2048 spectrometer were used. An Autolab PGSTAT101 potentiostat was used to perform the chronoamperometry.

All  $^1\text{H}$  NMR spectra were recorded on Bruker DPX-300 or DMX-400 spectrometers. Chemical shifts are indicated in ppm relative to the residual solvent peak. For NMR experiments under Ar, NMR tubes with a PTFE stopper were used. For some NMR reactions a deuterated phosphate buffer saline (PBS) was used as a solvent. A 10 mM PBS with 110 mM NaCl was prepared by dissolving  $\text{KH}_2\text{PO}_4$  (6.5 mg, 0.047 mmol),  $\text{K}_2\text{HPO}_4$  (36.8 mg, 0.211 mmol), and NaCl (160.8 mg, 2.752 mmol) in  $\text{D}_2\text{O}$  (25 mL) to reach a final pH of 7.54 at 295 K. The pH was measured with a pH meter, taking into account that the measured pD = pH + 0.4.<sup>58</sup> For the rest of irradiations followed by UV-vis, MS, or CD, a 10 mM PBS with 110 mM NaCl was prepared by dissolving  $\text{KH}_2\text{PO}_4$  (64.3 mg, 0.472 mmol),  $\text{K}_2\text{HPO}_4$  (353.6 mg, 2.030 mmol), and NaCl (1.605 g, 27.464 mmol) in Milli-Q water (250 mL) to reach a final pH of 7.35 at 295 K.

## 2.4.2 Synthesis

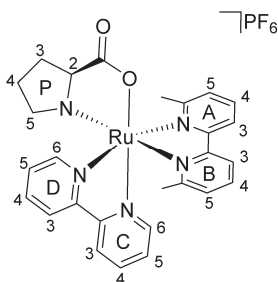
**[Ru(bpy)<sub>2</sub>(L-prol – 2H)]PF<sub>6</sub>** ([7]PF<sub>6</sub>). Synthesis of complex [7]PF<sub>6</sub> was adapted from a literature procedure.<sup>50</sup> Complex [1a]PF<sub>6</sub> (3.0 mg, 4.5 μmol) was dissolved in 50 mL PBS (pH 7.35) and transferred into one of the compartments of the two-compartment cell. Oxidation at constant potential of +0.645 V vs. Ag/AgCl reference electrode was carried out under Ar in a two-compartment cell with a nafion membrane. Carbon sponge electrodes were used as working and counter electrodes. Electrolysis was continued until the current stabilized. Then, complex [7]PF<sub>6</sub> was extracted with  $\text{CH}_2\text{Cl}_2$  (3 × 20 mL) and dried over  $\text{MgSO}_4$ . After evaporation of the solvent by reduced pressure an orange solid was obtained. (2.8 mg, 93%).  $^1\text{H}$  NMR (300 MHz,  $\text{CD}_3\text{OD}$ )  $\delta$  8.72 (d, J = 5.6 Hz, 1H), 8.66 (d, J = 8.1 Hz, 2H), 8.59 – 8.50 (m, 3H), 8.21 (dtd, J = 12.1, 7.9, 1.5 Hz, 2H), 7.97 – 7.70 (m, 5H), 7.57 (d, J = 5.8 Hz, 1H), 7.33 – 7.20 (m, 2H), 3.88 (s, 1H), 3.20 – 3.02 (m, 1H), 2.97 – 2.79 (m, 1H), 2.30 (m, 1H), 2.05 (m, 1H). ES MS m/z (calcd): 526.2 (526.1, [M – PF<sub>6</sub>]<sup>+</sup>).

**rac-[Ru(bpy)(dmbpy)<sub>2</sub>](PF<sub>6</sub>)<sub>2</sub>** (*rac*-[5](PF<sub>6</sub>)<sub>2</sub>). 2,2'-bipyridine (35 mg, 0.23 mmol, 0.8 equiv) and *rac*-[Ru(dmbpy)<sub>2</sub>Cl<sub>2</sub>] (150 mg, 0.28 mmol) were dissolved in ethylene glycol (5 mL), and the solution was deaerated by bubbling Ar for 30 min in a pressure tube. The tube was closed, put in a pre-heated oven at 190 °C for 3.5 h, and then cooled down to RT. After addition of water (10 mL) and saturated KPF<sub>6</sub> aqueous solution (0.5 mL) an orange precipitate was obtained. The suspension was filtered and the precipitate was washed with cold water and cold ethanol. After drying under air an

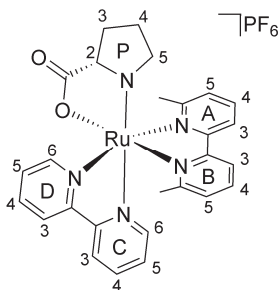
orange powder was obtained (200 mg, 79%), which shows traces of ligand scrambling.  $^1\text{H}$  NMR (300 MHz,  $\text{CD}_3\text{CN}$ )  $\delta$  8.46 (d,  $J = 8.0$  Hz, 2H), 8.29 (d,  $J = 7.8$  Hz, 2H), 8.14 (q,  $J = 8.3$  Hz, 4H), 7.91 (td,  $J = 8.0, 1.4$  Hz, 2H), 7.86 (d,  $J = 5.2$  Hz, 2H), 7.72 (t,  $J = 7.9$  Hz, 2H), 7.51 – 7.46 (m, 2H), 7.34 (ddd,  $J = 7.4, 5.9, 1.3$  Hz, 2H), 7.07 (dd,  $J = 7.8, 0.9$  Hz, 2H), 1.79 (s, 6H), 1.68 (s, 6H).  $^{13}\text{C}$  NMR (75 MHz,  $\text{CD}_3\text{CN}$ )  $\delta$  167.80, 166.08, 160.54, 159.42, 158.52, 153.31, 139.49, 138.93, 138.15, 129.04, 128.18, 127.97, 124.56, 124.20, 123.52, 26.40, 25.45. ES MS  $m/z$  (calcd): 313.5 (313.1,  $[\text{M} - 2 \times \text{PF}_6]^{2+}$ ), 771.4 (771.1,  $[\text{M} - \text{PF}_6]^+$ ).

***rac*-[Ru(bpy)(dmbpy)(CH<sub>3</sub>CN)<sub>2</sub>](PF<sub>6</sub>)<sub>2</sub>** (*rac*-[**6**](PF<sub>6</sub>)<sub>2</sub>). *rac*-[**5**](PF<sub>6</sub>)<sub>2</sub> (150 mg, 0.16 mmol) was dissolved in a preparative irradiation cell in CH<sub>3</sub>CN (110 mL). After deaerating the mixture by bubbling Ar for 20 min, the orange solution was irradiated with the beam of a 1000 W Xe lamp with both IR- and UV-cut-off filters. After 2 h irradiation, the solvent was removed under reduced pressure. The orange solid was re-dissolved in CH<sub>3</sub>OH and purified by SEC in CH<sub>3</sub>OH to remove free dmbpy ligand. After solvent evaporation an orange solid was obtained (84 mg, 59%).  $^1\text{H}$  NMR (300 MHz,  $\text{CD}_3\text{CN}$ )  $\delta$  9.39 (ddd,  $J = 5.6, 1.5, 0.7$  Hz, 1H), 8.38 (dt,  $J = 8.1, 1.1$  Hz, 1H), 8.27 (dt,  $J = 8.0, 1.0$  Hz, 2H), 8.20 (td,  $J = 7.9, 1.5$  Hz, 1H), 8.14 – 8.06 (m, 2H), 7.93 (td,  $J = 7.9, 1.5$  Hz, 1H), 7.82 – 7.66 (m, 4H), 7.52 (ddd,  $J = 5.7, 1.6, 0.8$  Hz, 1H), 7.31 (ddd,  $J = 7.4, 5.7, 1.4$  Hz, 1H), 7.12 (dd,  $J = 7.7, 1.3$  Hz, 1H), 2.47 (s, 3H), 1.84 (s, 3H).  $^{13}\text{C}$  NMR (75 MHz,  $\text{CD}_3\text{CN}$ )  $\delta$  167.33, 167.06, 159.84, 159.52, 159.39, 158.51, 155.64, 153.34, 139.36, 139.29, 138.87, 138.74, 128.30, 128.05, 127.97, 127.69, 124.64, 124.34, 122.53, 121.91, 27.23, 25.26, 4.74. ES MS  $m/z$  (calcd): 262.3 (262.1,  $[\text{M} - 2 \times \text{PF}_6]^{2+}$ ), 669.2 (669.1,  $[\text{M} - \text{PF}_6]^+$ ).

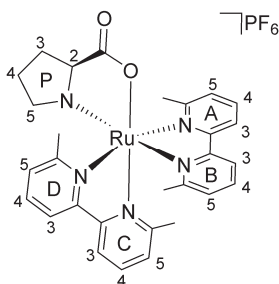
**[Ru(bpy)(dmbpy)(L-prol)]PF<sub>6</sub>** ([**2**]PF<sub>6</sub>). L-proline (25 mg, 0.22 mmol, 2.5 equiv), K<sub>2</sub>CO<sub>3</sub> (15 mg, 0.11 mmol, 1.25 equiv), and *rac*-[**6**](PF<sub>6</sub>)<sub>2</sub> (70.0 mg, 0.086 mmol) were dissolved in ethylene glycol (5 mL) and deaerated by bubbling Ar for 20 min in a pressure tube. The tube was closed and put in a pre-heated oven at 190 °C. After 40 min at 190 °C the reaction mixture was cooled down to RT, and most of the solvent was removed under high vacuum at 40 °C. Then, the dark red paste was dissolved in water (15 mL) and extracted with CH<sub>2</sub>Cl<sub>2</sub> (3 × 10 mL). The organic phases were combined and dried over MgSO<sub>4</sub>, which was filtered. The solvent was then evaporated under reduced pressure and the solid was purified by an Alumina Chromatography column using a mixture CH<sub>2</sub>Cl<sub>2</sub>:CH<sub>3</sub>OH 99:1 as eluent. Two main fractions were obtained from a long band (with an R<sub>f</sub> around 0.35), which corresponded to the diastereoisomers [**2a**]PF<sub>6</sub> and [**2b**]PF<sub>6</sub>:



[**2a**] $\text{PF}_6$  (red solid, 19 mg, 31%) was isolated as 85% pure containing traces of [**3**] $\text{PF}_6$ .  $^1\text{H}$  NMR (500 MHz,  $\text{D}_2\text{O}$ )  $\delta$  8.76 (d,  $J = 5.6$  Hz, 1H, D6), 8.73 (d,  $J = 5.7$  Hz, 1H, C6), 8.52 (d,  $J = 8.1$  Hz, 1H, D3), 8.41 (d,  $J = 8.2$  Hz, 1H, C3), 8.22 (d,  $J = 8.1$  Hz, 1H, A3), 8.14 – 8.09 (m, 2H, B3, D4), 7.96 (t,  $J = 8.0$  Hz, 1H, A4), 7.85 (t,  $J = 8.0$ , 1H, C4), 7.70 (t,  $J = 7.9$  Hz, 1H, B4), 7.67 – 7.63 (m, 1H, D5), 7.53 (d,  $J = 7.7$  Hz, 1H, A5), 7.30 (td,  $J = 6.4, 5.8, 1.2$  Hz, 1H, C5), 7.01 (d,  $J = 7.6$  Hz, 1H, B5), 2.98 (s, 3H, AMe), 2.03 (q,  $J = 10.1$  Hz, 1H, P3), 1.93 (dd,  $J = 11.2, 5.6$  Hz, 1H, P5), 1.54 (td,  $J = 13.2, 12.1, 6.5$  Hz, 1H, P3), 1.46 (dt,  $J = 13.1, 6.3$  Hz, 1H, P4), 1.20 (s, 4H), 1.14 (tt,  $J = 11.3, 5.6$  Hz, 1H, P5). ES MS  $m/z$  (calcd): 556.1 (556.1,  $[\text{M} - \text{PF}_6]^+$ ), 584.0 (584.1  $[\text{3}]^+$ )



[**2b**] $\text{PF}_6$  (red solid, 8.1 mg, 13%)  $^1\text{H}$  NMR (300 MHz,  $\text{D}_2\text{O}$ )  $\delta$  9.11 (d,  $J = 5.6$  Hz, 1H, D6), 8.53 (d,  $J = 8.2$  Hz, 1H, D3), 8.43 (d,  $J = 8.2$  Hz, 1H, C3), 8.31 (d,  $J = 8.1$  Hz, 1H, A3), 8.20 (d,  $J = 8.0$  Hz, 1H, B3), 8.10 (m, 2H, C6/D4), 8.00 (t,  $J = 7.9$  Hz, 1H, A4), 7.89 (dt,  $J = 7.8, 1.5$  Hz, 1H, C4), 7.74 – 7.66 (m, 2H, A4/D5), 7.60 (d,  $J = 7.7$  Hz, 1H, A5), 7.23 (ddd,  $J = 7.3, 5.7, 1.3$  Hz, 1H, C5), 7.08 (d,  $J = 7.6$  Hz, 1H, B5), 6.09 – 5.96 (m, 1H), 4.08 (q,  $J = 8.9$  Hz, 1H), 2.55 (s, 4H), 2.23 (td,  $J = 10.0, 5.8$  Hz, 1H), 1.62 (s, 3H), 1.55 – 1.34 (m, 2H), 1.30 – 1.16 (m, 1H). ES MS  $m/z$  (calcd): 556.1 (556.1,  $[\text{M} - \text{PF}_6]^+$ ). UV-vis  $\lambda$  in nm ( $\epsilon$  in  $\text{M}^{-1} \cdot \text{cm}^{-1}$ ): 511 (12300) in  $\text{CH}_3\text{CN}$ ; 497 (9500) in PBS.



$\Lambda$ -[Ru(dmbpy)<sub>2</sub>(L-prol)]PF<sub>6</sub> ([3a]PF<sub>6</sub>). L-proline (22 mg, 0.19 mmol, 2.2 equiv), K<sub>2</sub>CO<sub>3</sub> (13 mg, 0.094 mmol, 1.1 equiv), and *rac*-[Ru(dmbpy)<sub>2</sub>Cl<sub>2</sub>] (48 mg, 0.088 mmol) were dissolved in ethylene glycol (1 mL) and deaerated by bubbling Ar for 20 min in a pressure tube. The tube was closed and put in a pre-heated oven at 190 °C and after 45 min the mixture was cooled down to RT. After addition of water (4 mL) and saturated KPF<sub>6</sub> aqueous solution (0.5 mL) a red precipitate was obtained. The suspension was filtered and the solid was washed with cold water and cold Et<sub>2</sub>O. The red solid was purified by SEC in CH<sub>3</sub>OH, obtaining a pure red solid (36 mg, 56%). <sup>1</sup>H NMR (300 MHz, CD<sub>3</sub>OD)  $\delta$  8.45 – 8.35 (m, 3H, D3, A3, C3), 8.33 (d, *J* = 8.0 Hz, 1H, B3), 8.01 (m, 2H, A4, D4), 7.85 (td, *J* = 7.9, 1.9 Hz, 2H, B4, C4), 7.57 – 7.49 (m, 2H, D3, A5), 7.37 (dd, *J* = 7.5, 0.6 Hz, 1H, C5), 7.26 (d, *J* = 7.5 Hz, 1H, B5), 3.43 – 3.35 (m, 1H, P2), 2.88 (s, 3H, AMe), 2.48 (s, 3H, DMe), 2.14 (m, 1H, P5), 2.00 (s + m, 4H, CMe, P3), 1.66 (s + m, 4H, BMe, P3), 1.46 (m, 1H, P4), 1.34 (m, 1H, P4), 0.78 (qd, *J* = 11.4, 6.0 Hz, 1H, P5). High Resolution ES MS *m/z* (calcd): 584.15951 (584.16018, [M-PF<sub>6</sub>]<sup>+</sup>). Anal. Calcd for C<sub>29</sub>H<sub>32</sub>F<sub>6</sub>N<sub>5</sub>O<sub>2</sub>PRu: C, 47.80; H, 4.43; N, 9.61 Found: C, 47.13; H, 4.41; N, 9.45. UV-vis  $\lambda$  in nm ( $\epsilon$  in M<sup>-1</sup>.cm<sup>-1</sup>): 515 (7660) in CH<sub>3</sub>CN.

### 2.4.3 Single Crystal X-Ray crystallography

#### Complex [2b]PF<sub>6</sub>

**Crystal growth:** [2b]PF<sub>6</sub> (2.0 mg, 0.003 mmol) was dissolved in water (0.7 mL) in a GC vial. After two weeks, quality crystals suitable for X-ray structure determination were obtained.

**X-ray structure:** All reflection intensities were measured at 110(2) K using a SuperNova diffractometer (equipped with Atlas detector) with Mo K $\alpha$  radiation ( $\lambda$  = 0.71073 Å) under the program CrysAlisPro (Version 1.171.36.32 Agilent Technologies, 2013). The temperature of the data collection was controlled using the system Cryojet (manufactured by Oxford Instruments). CrysAlisPro program was used

to refine the cell dimensions and for data reduction. The structure was solved by direct methods with SHELXS-2014/7 and was refined on F2 with SHELXL-2014/7.<sup>59</sup> Analytical numeric absorption correction based on a multifaceted crystal model was applied using CrysAlisPro. The H atoms were placed at calculated positions (unless otherwise specified) using the instructions AFIX 13, AFIX 23, AFIX 43 or AFIX 137 with isotropic displacement parameters having values 1.2 or 1.5 Ueq of the attached C or N atoms. The H atoms attached to O1W and O2W were found from difference Fourier map, and their coordinates were refined freely. The DFIX restraints were used to keep the O...H and H...H distances within acceptable ranges.

**Details of the crystal structure:** The structure is partly disordered. The asymmetric unit contains two crystallographically independent Ru molecules, two PF<sub>6</sub><sup>-</sup> counterions, and two lattice water solvent molecules. Both PF<sub>6</sub><sup>-</sup> counterions are disordered over two orientations, and the occupancy factors of the major components of the disorder refine to 0.52(3) and 0.777(9). Fw = 718.60, 0.43 × 0.14 × 0.03 mm<sup>3</sup>, triclinic, *PI*, *a* = 8.5551(2), *b* = 9.6743(2), *c* = 17.6421(6),  $\alpha$  = 87.003(2)°,  $\beta$  = 76.564(2)°,  $\gamma$  = 89.5481(19)°, *V* = 1418.22(7) Å<sup>3</sup>, *Z* = 2,  $\mu$  = 0.69 mm<sup>-1</sup>, *T*<sub>min</sub>–*T*<sub>max</sub>: 0.805–0.981. 19350 reflections were measured up to a resolution of (sin  $\theta/\lambda$ )<sub>max</sub> = 0.650 Å<sup>-1</sup>. 11397 reflections were unique (*R*<sub>int</sub> = 0.026), of which 10840 were observed [*I* > 2 $\sigma$ (*I*)]. 907 parameters were refined using 489 restraints. *R*1/*wR*2 [all refl.]: 0.028/0.065. *S* = 1.03. Residual electron density found between –0.62 and 0.63 e Å<sup>-3</sup>.

### **Oxidized complex [2b – 2H]PF<sub>6</sub>**

**Crystal growth:** [2a]PF<sub>6</sub> (2.0 mg, 0.003 mmol) was dissolved in water (0.7 mL) into a GC vial and left in dimmed daylight. After six weeks, single crystals suitable for X-ray diffraction were obtained.

**X-ray structure:** All reflection intensities were measured at 110(2) K using a SuperNova diffractometer (equipped with Atlas detector) with Cu K $\alpha$  radiation ( $\lambda$  = 1.54178 Å) under the program CrysAlisPro (Version 1.171.36.32 Agilent Technologies, 2013). The same program was used to refine the cell dimensions and for data reduction. The structure was solved with the program SHELXS-2014/7 and was refined on F2 with SHELXL-2014/7.<sup>59</sup> Analytical numeric absorption correction using a multifaceted crystal model was applied using CrysAlisPro. The temperature of the data collection was controlled using the system Cryojet (manufactured by Oxford Instruments). The H atoms were placed at calculated positions (unless otherwise specified) using the instructions AFIX 23, AFIX 43 or AFIX 137 with isotropic

displacement parameters having values 1.2 or 1.5 of the attached C atoms. The D atoms attached to O1W were found from difference Fourier maps, and their coordinates were refined freely.

**Details of the crystal structure:** The structure is ordered.  $F_w = 718.59$ ,  $0.33 \times 0.15 \times 0.059 \text{ mm}^3$ , triclinic,  $P-1$ ,  $a = 8.5548(2)$ ,  $b = 11.6719(3)$ ,  $c = 14.8892(3)$ ,  $\alpha = 93.9396(17)^\circ$ ,  $\beta = 92.7616(17)^\circ$ ,  $\gamma = 105.915(2)^\circ$ ,  $V = 1422.85(6) \text{ \AA}^3$ ,  $Z = 2$ ,  $\mu = 5.71 \text{ mm}^{-1}$ ,  $T_{\text{min}}-T_{\text{max}}: 0.348-0.681$ . 18143 reflections were measured up to a resolution of  $(\sin \theta/\lambda)_{\text{max}} = 0.616 \text{ \AA}^{-1}$ . 5564 reflections were unique ( $R_{\text{int}} = 0.022$ ), of which 5371 were observed [ $I > 2\sigma(I)$ ]. 907 parameters were refined using 396 restraints.  $R1/wR2$  [all refl.]: 0.025/0.061.  $S = 1.03$ . Residual electron density found between  $-0.76$  and  $0.68 \text{ e \AA}^{-3}$ .

#### 2.4.4 Irradiation experiments monitored with $^1\text{H}$ NMR

**Irradiation of [1a](PF<sub>6</sub>):** A stock solution of [1a]PF<sub>6</sub> in deuterated PBS (1.5 mg, 5 mL, 0.045 mM) was prepared and deaerated with Ar. Then, 650  $\mu\text{L}$  were transferred, under Ar, into a NMR tube. The tube was irradiated at 310 K with a LOT Xenon 1000 W lamp equipped with IR short pass and  $>400 \text{ nm}$  long pass filters. In addition, a control experiment without white light irradiation was performed, in which no reaction was observed after 5 hours. The reactions were monitored by  $^1\text{H}$  NMR at various time intervals.

**Irradiation of [2a](PF<sub>6</sub>) and [2b](PF<sub>6</sub>):** [2a](PF<sub>6</sub>) (2.7 mg) and [2b](PF<sub>6</sub>) (2.6 mg) were weighed in two NMR tubes and dissolved in D<sub>2</sub>O (0.7 mL in each tube). The tubes were irradiated at RT with a Xenon 1000 W lamp equipped with a 450 nm blue light filter 450FS10-50 from Andover Corporation. In addition, a control experiment without white light irradiation was performed, in which no reaction was observed after 5 hours. The reactions were monitored by  $^1\text{H}$  NMR at various time intervals.

#### 2.4.5 Irradiation experiments monitored with MS, UV-vis, and CD

UV-vis spectroscopy was performed using a UV-vis spectrometer equipped with temperature control set to 298 K and a magnetic stirrer. The irradiation experiments were performed in a quartz cuvette containing 3 mL of solution. A stock solution of the desired complex was prepared using either CH<sub>3</sub>CN or PBS, which was then diluted in the cuvette to a working solution concentration. When the experiment was carried out under Ar the sample was deaerated 15 min by gentle bubbling of Ar and the

atmosphere was kept inert during the experiment by a gentle flow of Ar on top of the cuvette. A UV-vis spectrum was measured every 30 s for the first 10 min, every 1 min for the next 10 min, and eventually every 10 min until the end of the experiment. Data was analysed with Microsoft Excel. The quantum yield for the photooxidation of [1a]PF<sub>6</sub> in PBS was calculated by modelling the time evolution of the absorbance spectrum of the solution using the Glotaran software (see Appendix I and Figure AI.3).<sup>60</sup> Experimental conditions are detailed in Table AIII.1.

#### 2.4.6 Spectroelectrochemistry

A solution of [1a]PF<sub>6</sub> in PBS (0.1 mM) was transferred into one of the compartments of a two-compartment cell separated by a nafion membrane, whereas the other compartment contained only PBS. Carbone sponges with a resistance lower than 10 mΩ were used as working and counter electrodes. An Ag/AgCl electrode in the main compartment was used as a reference electrode. Once the solution was deaerated by bubbling Ar for 15 min, the UV-vis probe was submerged into the working solution. The chronoamperometry was performed at a constant potential of +0.645 V vs. Ag/AgCl reference electrode taking points every second while UV-vis spectra were recorded every 2 min. When the current of the chronoamperometry was constant the experiment was terminated.

#### 2.4.7 DFT calculations

Electronic structure calculations were performed using DFT as implemented in the ADF program (SCM). The structures of all possible isomers of [1a]<sup>+</sup>, [2b]<sup>+</sup>, and [3a]<sup>+</sup> were optimized in water using the conductor-like screening model (COSMO) to simulate the effect of solvent. The PBE0 functional and a triple zeta potential basis set (TZP) were used for all calculations.

#### 2.4.8 Supporting information available

Appendix III: <sup>1</sup>H NMR spectra, mass spectra, and circular dichroism spectra of [1a]PF<sub>6</sub>, [2a]PF<sub>6</sub>, [2b]PF<sub>6</sub>, and [3a]PF<sub>6</sub>; UV-vis, mass spectrometry, circular dichroism, and <sup>1</sup>H NMR of the irradiation of [1a]PF<sub>6</sub>, [2a]PF<sub>6</sub>, [2b]PF<sub>6</sub>, and [3a]PF<sub>6</sub>; spectro-electrochemistry of [1a]PF<sub>6</sub>; DFT calculations.

## 2.5 References

1. S. Bonnet, J. P. Collin, M. Koizumi, P. Mobian and J. P. Sauvage, *Adv. Mater.*, **2006**, 18, 1239-1250.
2. B. Champin, P. Mobian and J.-P. Sauvage, *Chem. Soc. Rev.*, **2007**, 36, 358-366.
3. J. Sauvage, J. Collin, J. Chambron, S. Guillerez, C. Coudret, V. Balzani, F. Barigelletti, L. De Cola and L. Flamigni, *Chem. Rev.*, **1994**, 94, 993-1019.
4. V. Balzani, G. Bergamini, F. Marchioni and P. Ceroni, *Coord. Chem. Rev.*, **2006**, 250, 1254-1266.
5. V. Balzani, P. Ceroni, A. Juris, M. Venturi, S. Campagna, F. Puntoriero and S. Serroni, *Coord. Chem. Rev.*, **2001**, 219, 545-572.
6. V. Balzani, A. Credi and M. Venturi, *Chem. Soc. Rev.*, **2009**, 38, 1542-1550.
7. V. Fernandez-Moreira, F. L. Thorp-Greenwood and M. P. Coogan, *Chem. Commun.*, **2010**, 46, 186-202.
8. A. Martin, A. Byrne, C. S. Burke, R. J. Forster and T. E. Keyes, *J. Am. Chem. Soc.*, **2014**, 136, 15300-15309.
9. M. R. Gill, J. Garcia-Lara, S. J. Foster, C. Smythe, G. Battaglia and J. A. Thomas, *Nat. Chem.*, **2009**, 1, 662-667.
10. M. R. Gill and J. A. Thomas, *Chem. Soc. Rev.*, **2012**, 41, 3179-3192.
11. L. Blackmore, R. Moriarty, C. Dolan, K. Adamson, R. J. Forster, M. Devocelle and T. E. Keyes, *Chem. Commun.*, **2013**, 49, 2658-2660.
12. J. Lee, D. G. Udugamasooriya, H.-S. Lim and T. Kodadek, *Nat. Chem. Biol.*, **2010**, 6, 258-260.
13. J. Y. Lee, P. Yu, X. S. Xiao and T. Kodadek, *Mol. BioSyst.*, **2008**, 4, 59-65.
14. J. Prakash and J. J. Kodanko, *Curr. Opin. Chem. Biol.*, **2013**, 17, 197-203.
15. C. Mari, V. Pierroz, S. Ferrari and G. Gasser, *Chem. Sci.*, **2015**, 6, 2660-2686.
16. K. T. Hufziger, F. S. Thowfeik, D. J. Charboneau, I. Nieto, W. G. Dougherty, W. S. Kassel, T. J. Dudley, E. J. Merino, E. T. Papish and J. J. Paul, *J. Inorg. Biochem.*, **2014**, 130, 103-111.
17. V. Lopes-dos-Santos, J. Campi, O. Filevich, S. Ribeiro and R. Etchenique, *Braz. J. Med. Biol. Res.*, **2011**, 44, 688-693.
18. J. Mosquera, M. I. Sanchez, J. L. Mascarenas and M. Eugenio Vazquez, *Chem. Commun.*, **2015**, 51, 5501-5504.
19. A. N. Hidayatullah, E. Wachter, D. K. Heidary, S. Parkin and E. C. Glazer, *Inorg. Chem.*, **2014**, 53, 10030-10032.
20. T. Respondek, R. N. Garner, M. K. Herroon, I. Podgorski, C. Turro and J. J. Kodanko, *J. Am. Chem. Soc.*, **2011**, 133, 17164-17167.
21. Y. Chen, W. Lei, G. Jiang, Y. Hou, C. Li, B. Zhang, Q. Zhou and X. Wang, *Dalton Trans.*, **2014**, 43, 15375-15384.
22. T. Sainuddin, M. Pinto, H. Yin, M. Hetu, J. Colpitts and S. A. McFarland, *J. Inorg. Biochem.*, **2016**, 158, 45-54.
23. B. S. Howerton, D. K. Heidary and E. C. Glazer, *J. Am. Chem. Soc.*, **2012**, 134, 8324-8327.
24. R. S. Vagg and P. A. Williams, *Inorg. Chim. Acta*, **1981**, 52, 69-72.
25. R. S. Vagg and P. A. Williams, *Inorg. Chim. Acta*, **1981**, 51, 61-65.
26. D. Leane and T. E. Keyes, *Inorg. Chim. Acta*, **2006**, 359, 1627-1636.
27. T. E. Keyes, J. G. Vos, J. A. Kolnaar, J. G. Haasnoot, J. Reedijk and R. Hage, *Inorg. Chim. Acta*, **1996**, 245, 237-242.
28. D. K. Heidary, B. S. Howerton and E. C. Glazer, *J. Med. Chem.*, **2014**, 57, 8936-8946.
29. Q. Sun, S. Mosquera-Vazquez, L. M. Lawson Daku, L. Guénée, H. A. Goodwin, E. Vauthey and A. Hauser, *J. Am. Chem. Soc.*, **2013**, 135, 13660-13663.
30. U. Knof and A. von Zelewsky, *Angew. Chem., Int. Ed.*, **1999**, 38, 302-322.
31. L. Gong, S. P. Mulcahy, K. Harms and E. Meggers, *J. Am. Chem. Soc.*, **2009**, 131, 9602-9603.
32. D. Heseck, Y. Inoue, S. R. L. Everitt, H. Ishida, M. Kunieda and M. G. B. Drew, *Chem. Commun.*, **1999**, 0, 403-404.

33. P. Hayoz, A. Von Zelewsky and H. Stoeckli-Evans, *J. Am. Chem. Soc.*, **1993**, 115, 5111-5114.
34. C. Fu, M. Wenzel, E. Treutlein, K. Harms and E. Meggers, *Inorg. Chem.*, **2012**, 51, 10004-10011.
35. T. J. Goodwin, P. A. Williams, F. S. Stephens and R. S. Vagg, *Inorg. Chim. Acta*, **1984**, 88, 165-181.
36. T. J. Goodwin, P. A. Williams and R. S. Vagg, *Inorg. Chim. Acta*, **1982**, 63, 133-140.
37. C. S. Burke and T. E. Keyes, *Rsc Advances*, **2016**, 6, 40869-40877.
38. D. Mulhern, S. Brooker, H. Gorls, S. Rau and J. G. Vos, *Dalton Trans.*, **2006**, 51-57.
39. D. A. Freedman, J. K. Evju, M. K. Pomije and K. R. Mann, *Inorg. Chem.*, **2001**, 40, 5711-5715.
40. M. Myahkostopov and F. N. Castellano, *Inorg. Chem.*, **2011**, 50, 9714-9727.
41. L. Spiccia, G. B. Deacon and C. M. Kepert, *Coord. Chem. Rev.*, **2004**, 248, 1329-1341.
42. P. A. Anderson, G. B. Deacon, K. H. Haarmann, F. R. Keene, T. J. Meyer, D. A. Reitsma, B. W. Skelton, G. F. Strouse and N. C. Thomas, *Inorg. Chem.*, **1995**, 34, 6145-6157.
43. A. von Zelewsky and G. Gremaud, *Helv. Chim. Acta*, **1988**, 71, 1108-1115.
44. B. Bosnich, *Inorg. Chem.*, **1968**, 7, 2379-2386.
45. B. Bosnich, *Inorg. Chem.*, **1968**, 7, 178-180.
46. K. Robinson, G. V. Gibbs and P. H. Ribbe, *Science*, **1971**, 172, 567-570.
47. M. E. Fleet, *Mineral. Mag.*, **1976**, 40, 531-533.
48. A. Dikhtiarenko, P. Villanueva-Delgado, R. Valiente, J. García and J. Gimeno, *Polymers*, **2016**, 8, 48.
49. F. R. Keene, M. J. Ridd and M. R. Snow, *J. Am. Chem. Soc.*, **1983**, 105, 7075-7081.
50. M. Yamaguchi, K. Machiguchi, T. Mori, K. Kikuchi, I. Ikemoto and T. Yamagishi, *Inorg. Chem.*, **1996**, 35, 143-148.
51. M. Tamura, K. Tsuge, A. Igashira-Kamiyama and T. Konno, *Chem. Commun.*, **2011**, 47, 12464-12466.
52. K. Krumova and G. Cosa, in *Singlet Oxygen: Applications in Biosciences and Nanosciences, Volume 1*, The Royal Society of Chemistry, **2016**, 1-21.
53. J. Gomez, G. Garcia-Herbosa, J. V. Cuevas, A. Arnaiz, A. Carbayo, A. Munoz, L. Falvello and P. E. Fanwick, *Inorg. Chem.*, **2006**, 45, 2483-2493.
54. E. Wachter and E. C. Glazer, *J. Phys. Chem. A*, **2014**, 118, 10474-10486.
55. S. Tachiyashiki and K. Mizumachi, *Coord. Chem. Rev.*, **1994**, 132, 113-120.
56. J. D. Knoll, B. A. Albani, C. B. Durr and C. Turro, *J. Phys. Chem. A*, **2014**, 118, 10603-10610.
57. J. P. Collin and J. P. Sauvage, *Inorg. Chem.*, **1986**, 25, 135-141.
58. A. Krężel and W. Bal, *J. Inorg. Biochem.*, **2004**, 98, 161-166.
59. G. M. Sheldrick, *Acta Crystallogr., Sect. C: Struct. Chem.*, **2015**, 71, 3-8.
60. J. J. Snellenburg, S. P. Laptanok, R. Seger, K. M. Mullen and I. H. M. van Stokkum, *J. Stat. Softw.*, **2012**, 49, 1-22.



# 3

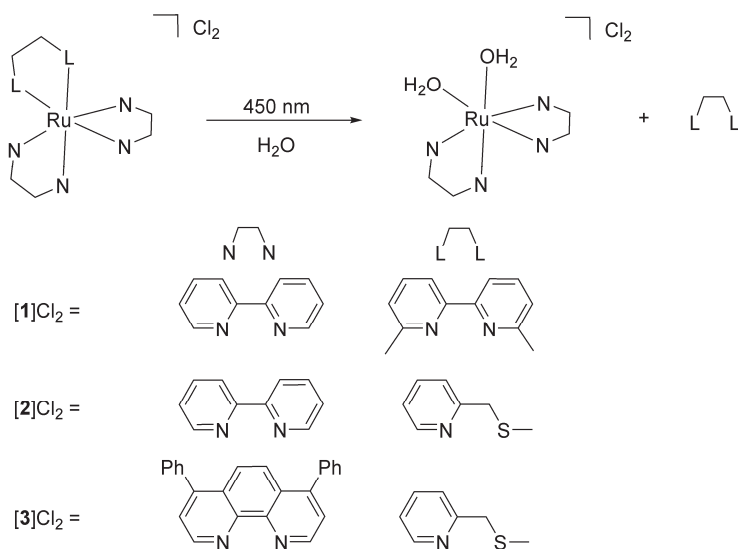
## To cage or to be caged? The cytotoxic species in ruthenium-based photoactivated chemotherapy is not always the metal

*In metal-based Photoactivated Chemotherapy (PACT), two photoproducts are generated by light-triggered photosubstitution of a metal-bound ligand: the dissociated ligand and an aquated metal complex. By analogy with cisplatin, the aquated metal complex is usually presented as the biologically active species, as it can typically bind to DNA. In this work, we show that this qualitative assumption is not necessarily valid by comparing the biological activity, logP, and cellular uptake of three ruthenium-based PACT complexes,  $[Ru(bpy)_2(dmbpy)]^{2+}$ ,  $[Ru(bpy)_2(mtmp)]^{2+}$ , and  $[Ru(Ph,phen)_2(mtmp)]^{2+}$ . For the first complex, the photoreleased dmbpy ligand is responsible for the observed phototoxicity, whereas the second complex is not phototoxic, and for the third complex it is the ruthenium bis-aqua photoproduct that is the sole cytotoxic species.*

This chapter was published as a communication: J. A. Cuello-Garibo, M. S. Meijer, S. Bonnet *Chem. Commun.*, **2017**, 53, 6768-6771.

### 3.1 Introduction

Ruthenium polypyridyl complexes are well known for their versatile and tunable photophysical and photochemical properties.<sup>1-4</sup> In recent years, they have raised much interest for application in molecular imaging and photopharmacology,<sup>5-7</sup> and in particular for Photodynamic Therapy (PDT) and Photoactivated Chemotherapy (PACT).<sup>8-9</sup> In PACT, like in PDT, a non-toxic or poorly cytotoxic prodrug becomes much more cytotoxic upon light irradiation, allowing for a time- and spatially-resolved delivery of the toxicity of the anticancer drug. Whereas in PDT the photocytotoxicity relies on the photochemical generation of reactive oxygen species (ROS) such as singlet oxygen ( $^1\text{O}_2$ ), in PACT a photochemical bond-breaking reaction occurs, which for coordination compounds is often realized *via* the photosubstitution of one of the ligands by water molecules.<sup>10-11</sup> To synthesize ruthenium-based compounds for PACT,  $[\text{Ru}(\text{bpy})_3]^{2+}$ -like complexes (bpy = 2,2'-bipyridine) must be modified in such a way that the triplet metal-centered excited states ( $^3\text{MC}$ ) comes in close proximity to the triplet metal-to-ligand charge transfer states ( $^3\text{MLCT}$ ).<sup>12-13</sup> Such modification typically entails the use of sterically hindering bidentate ligands such as 6,6'-dimethyl-2,2'-bipyridine (dmbpy) and its derivatives.<sup>14-15</sup> For example, irradiation of  $[\text{Ru}(\text{bpy})_2(\text{dmbpy})]^{2+}$  in water leads to the photosubstitution of dmbpy by two water molecules, generating the aquated species *cis*- $[\text{Ru}(\text{bpy})_2(\text{OH}_2)_2]^{2+}$  (Scheme 3.1), which was shown to bind to plasmid DNA.<sup>16</sup> When performed in presence of growing cancer cells, this photoreaction clearly leads to photocytotoxicity, which many have interpreted to be a consequence of the cytotoxicity of *cis*- $[\text{Ru}(\text{bpy})_2(\text{OH}_2)_2]^{2+}$ , by analogy to the cytotoxic aquated form of cisplatin, *cis*- $[\text{Pt}(\text{NH}_3)_2(\text{OH}_2)_2]^{2+}$ . On the other hand, ruthenium polypyridyl complexes have also been used as photocaging groups for neurotransmitters and organic enzyme inhibitors,<sup>17-21</sup> for which the absence of acute toxicity is a prerequisite. The parent compound  $[\text{Ru}(\text{bpy})_2\text{Cl}_2]$ , which thermally hydrolyzes to *cis*- $[\text{Ru}(\text{bpy})_2(\text{OH}_2)_2]^{2+}$ , was shown by Reedijk and co-workers not to be cytotoxic.<sup>22</sup>



Scheme 3.1. Chemical structures of PACT ruthenium compounds [1]Cl<sub>2</sub> – [3]Cl<sub>2</sub> and their reaction upon blue light irradiation in water.

As several groups have designed analogues of [Ru(bpy)<sub>2</sub>(dmbpy)]<sup>2+</sup> for developing new PACT compounds, we asked ourselves which photoproducts, from the two that are formed upon light irradiation, actually are cytotoxic enough to kill cancer cells: the *cis* bis-aqua ruthenium complex, or the free ligand? To address this question, we compared the known compound [Ru(bpy)<sub>2</sub>(dmbpy)]Cl<sub>2</sub> ([1]Cl<sub>2</sub>) to the photoactive compound [Ru(bpy)<sub>2</sub>(mtmp)]Cl<sub>2</sub> ([2]Cl<sub>2</sub>) containing the bidentate chelating ligand 2-(methylthio)methylpyridine (mtmp) (Scheme 3.1).<sup>7</sup> Sulfur is a soft donor atom that coordinate well to ruthenium(II) ions in the ground state, but they can be photosubstituted more efficiently than pyridines due to the relative lability of the Ru-S bond in the excited state, compared to Ru-N bonds.<sup>23</sup>

### 3.2 Results and discussion

When a solution of [2]Cl<sub>2</sub> is irradiated with blue light (445 nm), a shift of the <sup>1</sup>MLCT absorption maximum from 432 nm to 491 nm was observed, as well as two consecutive isosbestic points at 439 nm and 458 nm (Figure 3.1a). Mass spectrometry of the reaction mixture after 50 min irradiation (Figure AIV.1) showed peaks at *m/z* = 140.2, 225.0, and 448.1, which correspond to {mtmp + H}<sup>+</sup> (calcd *m/z* = 140.2), [Ru(bpy)<sub>2</sub>(OH<sub>2</sub>)<sub>2</sub>]<sup>2+</sup> (calcd *m/z* = 225.0), and [Ru(bpy)<sub>2</sub>(OH<sub>2</sub>)(OH)]<sup>+</sup> (calcd *m/z* = 448.5), respectively. Thus, light irradiation of [2]<sup>2+</sup>, like [1]<sup>2+</sup>, leads to the formation of the bis-aqua complex *cis*-[Ru(bpy)<sub>2</sub>(OH<sub>2</sub>)<sub>2</sub>]<sup>2+</sup>, but the free ligand obtained as second

photoproduct is mtmp, instead of dmbpy with  $[1]Cl_2$  (Scheme 3.1). The two sequential isosbestic points observed by UV-vis during irradiation of  $[2]Cl_2$  suggest that photosubstitution is taking place in a two-step process. The first process is very fast (it was completed within the first 30 s of irradiation) and is assumed to be the photosubstitution of one coordination bond of mtmp by a single water molecule. The second photosubstitution was much slower, as usually reported for two monodentate ligands,<sup>24</sup> and leads to the final photoproducts mtmp and  $cis-[Ru(bpy)_2(OH_2)_2]^{2+}$ . The quantum yield of this second process ( $\Phi_{PR}$ ) is 0.0030 based on Glotaran global fitting (see Appendix I and Figure AIV.3).

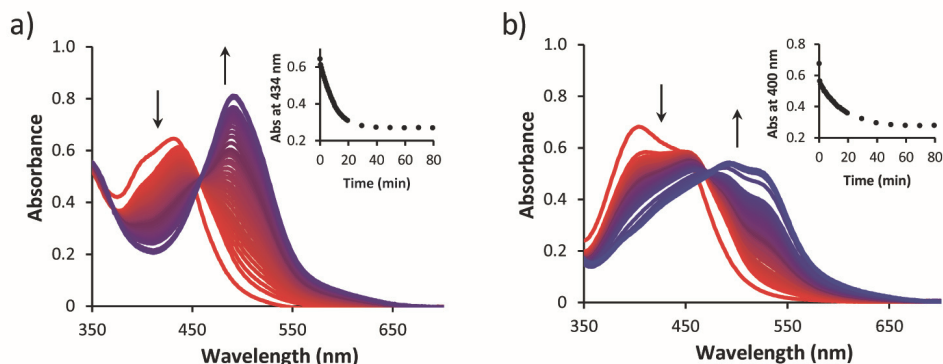


Figure 3.1. Evolution of the UV-vis absorption spectra of a solution of (a)  $[2]Cl_2$  and (b)  $[3]Cl_2$  in water upon irradiation with a 445 nm LED under  $N_2$  at 25 °C. Conditions: a) 80 min, 0.109 mM,  $1.49 \cdot 10^{-7} \text{ mol} \cdot \text{s}^{-1}$ , b) 80 min, 0.038 mM,  $1.31 \cdot 10^{-7} \text{ mol} \cdot \text{s}^{-1}$ .

The cytotoxicity of the free ligands dmbpy and mtmp was first compared in A549 lung cancer cell line. Both organic ligands are rather lipophilic, as demonstrated by octanol/water partition coefficient values ( $\log P$ ) of +3.29 and +1.63 for dmbpy and mtmp, respectively (Table 3.2). Both ligands are therefore expected to be taken up at least passively by the cells. The cell growth inhibition effective concentrations values ( $EC_{50}$ ), *i.e.* the compound concentration at which the cell viability is reduced by 50% compared to the non-treated control, were measured following a protocol adapted from Hopkins *et al.* (see Appendix II).<sup>25</sup> Clearly, dmbpy was found to be cytotoxic, with an  $EC_{50}$  value of 8.7 and 6.5  $\mu\text{M}$  in the dark and upon light irradiation, respectively (Figure 3.2 and Table 3.1), whereas no cytotoxicity was observed for mtmp up to 200  $\mu\text{M}$ . Although cellular localization of chemicals may differ whether they are simply incubated with the cells, or generated inside the cells upon light irradiation of a prodrug such as  $[1]Cl_2$ , this result suggests that the photocytotoxicity reported for  $[1]Cl_2$  may be at least partly due to the release of the dmbpy ligand.

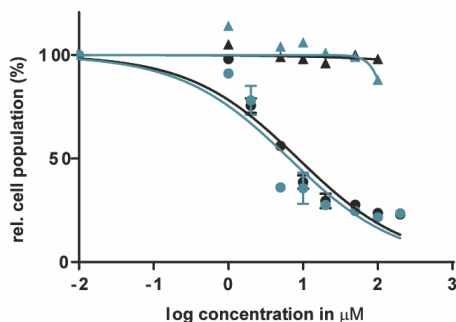


Figure 3.2. Dose-response curves for A549 cells incubated with dmbpy (circles) or mtmp (triangles) and irradiated 10 min with blue light ( $454\text{ nm}$ ,  $6.5\text{ J}\cdot\text{cm}^{-2}$ ) 6 h after treatment (blue data points), or left in the dark (black data points). Photocytotoxicity assay outline: cells seeded at  $5\cdot 10^3$  cells/well at  $t = 0\text{ h}$ , treated with dmbpy or mtmp at  $t = 24\text{ h}$ , irradiated at  $t = 30\text{ h}$ , and SRB cell-counting assay performed at  $t = 96\text{ h}$ . Incubation conditions:  $37\text{ }^\circ\text{C}$  and  $7\%\text{ CO}_2$ .

In a second step, the  $\text{EC}_{50}$  values of complexes  $[1]\text{Cl}_2$  and  $[2]\text{Cl}_2$  were measured in A549 cells, both in the dark and upon blue light irradiation, following the same protocol applied for the free ligand (Table 3.1). The selected light dose ( $6.5\text{ J}\cdot\text{cm}^{-2}$ ) guarantees that no toxic effect for the cells occurs due to the irradiation itself.<sup>25</sup> At that light dose,  $[1]\text{Cl}_2$  and  $[2]\text{Cl}_2$  are fully activated below  $40\text{ }\mu\text{M}$  (see Figure AIV.2). As shown in Figure 3.3 no significant decrease in the cell population was observed after treatment with less than  $100\text{ }\mu\text{M}$  of complexes  $[1]\text{Cl}_2$  or  $[2]\text{Cl}_2$  in the dark (Table 3.1). Thus, these species can be considered as essentially non-cytotoxic in the dark. After blue light irradiation, an  $\text{EC}_{50}$  value of  $10.9\text{ }\mu\text{M}$  was found for  $[1]\text{Cl}_2$ , corresponding to a photo index (PI), *i.e.* the ratio of the  $\text{EC}_{50}$  value obtained in a dark control and that obtained after light irradiation, of 19, which qualitatively fits the data reported by Glazer *et al.* on this compound.<sup>16</sup> However, no photocytotoxicity was observed for  $[2]\text{Cl}_2$ , in spite of the fact that this compound also results in the formation of the *cis*- $[\text{Ru}(\text{bpy})_2(\text{OH}_2)_2]^{2+}$  species upon irradiation. In order to explain these differences, the  $\log P$  value (see Experimental Section),<sup>26</sup> the cellular uptake, and the quantum yield for singlet oxygen generation were measured for both complexes (Table 3.2).  $\log P$  values of  $-1.42$  and  $-1.33$  were found for  $[1]\text{Cl}_2$  and  $[2]\text{Cl}_2$ , respectively, which means that both complexes have a similar hydrophilicity and are not prone to enter the cell by passive diffusion through the membrane. As expected from this high hydrophilicity, the cellular uptake before light activation was found to be very low:  $1.32$  and  $1.27\text{ ng Ru}/10^6$  cells for  $[1]\text{Cl}_2$  and  $[2]\text{Cl}_2$ , respectively, compared to values usually found above  $10\text{--}20\text{ ng Ru}/10^6$  cells for compounds that are well taken up.<sup>27-28</sup> Thus, the higher

cytotoxicity found for [1]Cl<sub>2</sub> after light activation cannot be attributed to a higher uptake of the complex prior to irradiation.

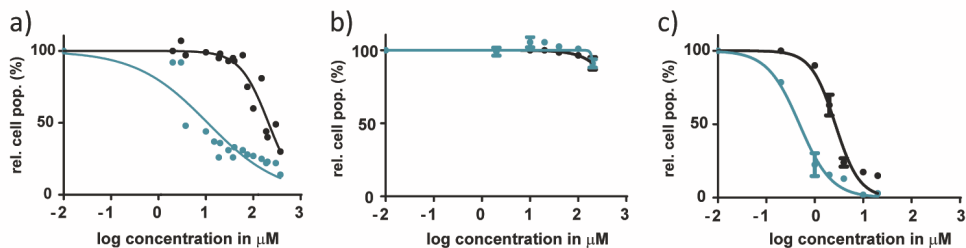


Figure 3.3. Dose-response curves for A549 cells incubated with [1]Cl<sub>2</sub> (a), [2]Cl<sub>2</sub> (b), or [3]Cl<sub>2</sub> (c) and irradiated 10 min with blue light (454 nm, 6.5 J·cm<sup>-2</sup>) 6 h after treatment (blue data points), or left in the dark (black data points). Photocytotoxicity assay outline: cells seeded at 5·10<sup>3</sup> cells/well at *t* = 0 h, treated with [1]Cl<sub>2</sub>, [2]Cl<sub>2</sub>, or [3]Cl<sub>2</sub> at *t* = 24 h, irradiated at *t* = 30 h, and SRB assay performed at *t* = 96 h. Incubation conditions: 37 °C and 7% CO<sub>2</sub>.

Table 3.1. Cancer cell growing inhibition effective concentrations (EC<sub>50</sub> values with 95% confidence interval (CI) in μM), in the dark and upon blue light irradiation (6.5 J·cm<sup>-2</sup>), for [1]Cl<sub>2</sub>, [2]Cl<sub>2</sub>, [3]Cl<sub>2</sub>, dmbpy, and mtmp on A549 cells, and photo indices (PI) defined as EC<sub>50,dark</sub>/EC<sub>50,light</sub>.

	[1]Cl <sub>2</sub>	CI (95%)	[2]Cl <sub>2</sub>	CI (95%)	[3]Cl <sub>2</sub>	CI (95%)	dmbpy	CI (95%)	mtmp	CI (95%)
EC <sub>50</sub> dark (μM)	210	-41 +51	> 150	-	2.66	-0.46 +0.56	8.56	-2.76 +4.08	> 150	-
EC <sub>50</sub> light (μM)	10.9	-4.3 +7.1	> 150	-	0.48	-0.08 +0.10	6.55	-2.54 +4.17	> 150	-
PI	19		-		6		1.3		-	

Many reported phototherapeutic ruthenium complexes are excellent PDT agents, *i.e.* they generate <sup>1</sup>O<sub>2</sub> *via* energy transfer from the <sup>3</sup>MLCT to molecular oxygen present in the cells.<sup>29-31</sup> Although it is commonly admitted that photosubstitutionally labile ruthenium complexes are poor singlet oxygen generators, experimental values of <sup>1</sup>O<sub>2</sub> generation quantum yields ( $\Phi_A$ ) are rarely reported for PACT compounds. In order to rule out that [1]Cl<sub>2</sub> and [2]Cl<sub>2</sub> may act as PDT agents,  $\Phi_A$  was experimentally determined for both complexes under blue light irradiation (450 nm), by direct detection of the 1274 nm infrared phosphorescence of <sup>1</sup>O<sub>2</sub> in CD<sub>3</sub>OD.  $\Phi_A$  values of 0.023 and <0.005 were found for [1]Cl<sub>2</sub> and [2]Cl<sub>2</sub> (Table 3.2), respectively, using [Ru(bpy)<sub>3</sub>]Cl<sub>2</sub> as reference ( $\Phi_A$  = 0.73).<sup>32</sup> Thus, since both complexes are mediocre photosensitizers for <sup>1</sup>O<sub>2</sub>, the phototoxicity of [1]Cl<sub>2</sub> cannot be due to a photodynamic effect.

To summarize, [1]Cl<sub>2</sub> and [2]Cl<sub>2</sub> have similar negative *log P* values, similarly low cellular uptake after 6 h incubation in the dark, similarly low <sup>1</sup>O<sub>2</sub> generation quantum yields, and they both form [Ru(bpy)<sub>2</sub>(OH<sub>2</sub>)<sub>2</sub>]<sup>2+</sup> upon light irradiation. Their main difference is that they photochemically release either dmbpy or mtmp, respectively. Meanwhile, we also demonstrated three points. First, light activation of [1]Cl<sub>2</sub> resulted in a 19-fold lower EC<sub>50</sub> value compared to the dark, whereas light irradiation of [2]Cl<sub>2</sub> does not influence the negligible cytotoxicity. Second, dmbpy is cytotoxic to A549 cells, whereas mtmp is not. Third, the EC<sub>50</sub> value of [1]Cl<sub>2</sub> after irradiation (10.9 μM) is close, in the same protocol, to the EC<sub>50</sub> value found for dmbpy (6.6 μM). All together, these results strongly suggest that the phototoxicity observed with complex [1]Cl<sub>2</sub> is caused by the dmbpy ligand that is photoreleased and taken up after extracellular activation, rather than by the *cis*-[Ru(bpy)<sub>2</sub>(OH<sub>2</sub>)<sub>2</sub>]<sup>2+</sup> species. In other words, [Ru(bpy)<sub>2</sub>(OH<sub>2</sub>)<sub>2</sub>]<sup>2+</sup> is a photocaging group for the cytotoxic dmbpy ligand, rather than the reverse.

Table 3.2. Partition coefficient (*log P* values), singlet oxygen generation quantum yields ( $\Phi_A$ ), and cellular uptake of [1]Cl<sub>2</sub>, [2]Cl<sub>2</sub>, [3]Cl<sub>2</sub>, dmbpy, and mtmp.

	[1]Cl <sub>2</sub>	[2]Cl <sub>2</sub>	[3]Cl <sub>2</sub>	dmbpy	mtmp
<i>log P</i>	-1.42	-1.33	0.29	3.29 <sup>a</sup>	1.63 <sup>a</sup>
$\Phi_A$	0.023	<0.005	0.020	-	-
Cellular uptake (ng Ru/10 <sup>6</sup> cells)	1.32 ± 0.06	1.27 ± 0.10	-	-	-

<sup>a</sup> *Log P* estimation model from ChemDraw Professional (v16.0, CambridgeSoft).

These surprising results do not discredit, in our eyes, the concept of ruthenium-based PACT. The problem of compounds such as [1]Cl<sub>2</sub> or [2]Cl<sub>2</sub> is only that their ruthenium-based photoproduct, *cis*-[Ru(bpy)<sub>2</sub>(OH<sub>2</sub>)<sub>2</sub>]<sup>2+</sup>, is not lipophilic enough to cross membranes and cause significant damage inside the cells. To demonstrate this idea, we synthesized a much more lipophilic version of compound [2]Cl<sub>2</sub>, *i.e.* [Ru(Ph<sub>2</sub>phen)<sub>2</sub>(mtmp)]Cl<sub>2</sub> ([3]Cl<sub>2</sub>, Ph<sub>2</sub>phen = 4,7-Diphenyl-1,10-phenanthroline, see Scheme 3.1), by reacting [Ru(Ph<sub>2</sub>phen)<sub>2</sub>Cl<sub>2</sub>] with mtmp in ethylene glycol at 115 °C. [3]Cl<sub>2</sub> has a much higher *log P* value of 0.28, as expected from the more lipophilic Ph<sub>2</sub>phen spectator ligands. The photoreactivity of [3]Cl<sub>2</sub> in water under blue light irradiation (445 nm) is similar to that of [2]Cl<sub>2</sub>: a shift of the <sup>1</sup>MLCT absorption maximum from 404 nm to 492 nm and two sequential isosbestic points at 447 nm and 472 nm, were observed (Figure 3.1b). Mass spectrometry of the reaction mixture after 80 min irradiation (Figure AIV.1b) also showed photosubstitution of the non-toxic mtmp ligand, with peaks at *m/z* = 140.2, 412.3, and 424.5, corresponding to {mtmp +

$H\}^+$ ,  $[Ru(Ph_2phen)_2(CH_3CN)(OH_2)]^{2+}$  (calcd  $m/z = 412.6$ ), and  $[Ru(Ph_2phen)_2(CH_3CN)_2]^{2+}$  (calcd  $m/z = 424.1$ ), respectively. The last two species are formed in the mass spectrometer and indicate the photochemical formation of the bis-aqua photoproduct  $[Ru(Ph_2phen)_2(OH_2)_2]^{2+}$ . The photosubstitution reaction has a quantum yield ( $\Phi_{PR}$ ) of 0.0010, slightly lower than that for  $[2]Cl_2$  (Figure AIV.4), and the  $^1O_2$  generation quantum yield was found to be similar to that for  $[1]Cl_2$  (*i.e.*  $\Phi_d = 0.020$ , see Table 3.2). Thus,  $[3]Cl_2$  is a poor PDT sensitizer but potentially a good PACT compound. Like  $[2]Cl_2$ , it photosubstitutes the non-toxic mtmp ligand to deliver  $[Ru(Ph_2phen)_2(OH_2)_2]^{2+}$ , a lipophilic analogue of  $[Ru(bpy)_2(OH_2)_2]^{2+}$ . In A549 cells,  $[3]Cl_2$  showed a higher cytotoxicity in the dark ( $EC_{50} = 2.66 \mu M$ ), as expected from its higher lipophilicity. The  $EC_{50}$  value decreased 6-fold down to  $0.48 \mu M$  under a blue light dose of  $6.5 J \cdot cm^{-2}$  (Table 3.1). Such increased cytotoxicity can, this time, only be attributed to the photochemical generation of  $[Ru(Ph_2phen)_2(OH_2)_2]^{2+}$ , as the second photoproduct mtmp is non-toxic. Compound  $[3]Cl_2$  is thus a true metal-based PACT compound in which the toxicity of the ruthenium-based aqua species is “caged” by coordination of the mtmp ligand.

### 3.3 Conclusions

In conclusion, our results demonstrate that determining which photoproduct is the cytotoxic species is not straightforward, as factors such as ligand toxicity, lipophilicity of the prodrug, cellular uptake and localization, and/or  $^1O_2$  generation, may all influence the phototoxicity of a given compound. Although we demonstrated here that the phototoxicity of  $[1]Cl_2$  is not caused by the ruthenium-based photoproduct but caused by the released dmbpy ligand, compound  $[3]Cl_2$  demonstrates that PACT compounds in which the ruthenium photoproduct bears the toxic load can be made, only if the lipophilicity of the compound is high enough to enter the cell.

## 3.4 Experimental

### 3.4.1 Synthesis

The ligands 6,6'-dimethyl-2,2'-bipyridine (dmbpy) and 4,7-diphenyl-1,10-phenanthroline (Ph<sub>2</sub>phen) were purchased from Sigma-Aldrich, as well as *cis*-bis(2,2'-bipyridine)dichlororuthenium(II) hydrate (*[cis-Ru(bpy)<sub>2</sub>Cl<sub>2</sub>]*). Lithium chloride (LiCl) was purchased from Alfa-Aesar. All reactants and solvents were used without further purification. The synthesis of *cis*- $[Ru(Ph_2phen)_2Cl_2]$ ,  $[1]Cl_2$ ,  $[2]Cl_2$  and the ligand 2-(methylthio)methylpyridine was carried out according to literature procedures.<sup>16, 33-34</sup>

Electrospray mass spectra (ES MS) were recorded by using a MSQ Plus Spectrometer. High resolution mass spectra were recorded by direct injection (2  $\mu\text{L}$  of 2  $\mu\text{M}$  solution in water/acetonitrile, 50/50, v/v and 0.1% formic acid) in a mass spectrometer (Thermo Finnigan LTQ Orbitrap) equipped with an electrospray (250  $^{\circ}\text{C}$ ) with resolution  $R = 60,000$  at  $m/z$  400 (mass range  $m/z = 150 - 2000$ ) and dioctylphtalate ( $m/z = 391.28428$ ) as a lock mass. The high resolution mass spectrometer was calibrated prior to measurements with a calibration mixture (Thermo Finnigan). UV-vis experiments were performed on a Cary Varian spectrometer. All  $^1\text{H}$  NMR spectra were recorded on a Bruker DMX-400 spectrometer. Chemical shifts are indicated in ppm relative to the residual solvent peak.

**[Ru(Ph<sub>2</sub>phen)<sub>2</sub>(mtmp)]Cl<sub>2</sub> ([3]Cl<sub>2</sub>).** *cis*-[Ru(Ph<sub>2</sub>phen)<sub>2</sub>Cl<sub>2</sub>] (50 mg, 0.060 mmol) was dissolved in ethylene glycol (4 mL), after which mtmp (26 mg, 0.19 mmol) and Et<sub>3</sub>N (28  $\mu\text{L}$ , 0.20 mmol) were added. The reaction mixture was placed under N<sub>2</sub> atmosphere, deaerated, and heated at 115  $^{\circ}\text{C}$  for 2 h. The crude was purified by column chromatography on deactivated alumina using CH<sub>2</sub>Cl<sub>2</sub> as an eluent. The orange fraction was collected and the solvent was removed by rotatory evaporation. Traces of ethylene glycol were removed by co-evaporation with toluene (30 mg, 50%).  $^1\text{H}$  NMR (400 MHz, CD<sub>3</sub>OD)  $\delta$  9.93 (d,  $J = 5.4$  Hz, 1H), 8.80 (d,  $J = 5.4$  Hz, 1H), 8.38 – 8.32 (m, 2H), 8.30 – 8.22 (m, 2H), 8.16 (d,  $J = 5.5$  Hz, 1H), 8.13 (d,  $J = 5.1$  Hz, 3H), 7.93 – 7.88 (m, 2H), 7.86 – 7.81 (m, 2H), 7.80 – 7.75 (m, 2H), 7.75 – 7.64 (m, 7H), 7.63 – 7.53 (m, 12H), 7.20 – 7.13 (m, 1H), 5.08 (d,  $J = 16.7$  Hz, 1H), 4.61 (d,  $J = 16.5$  Hz, 1H), 1.55 (s, 3H).  $^{13}\text{C}$  NMR (101 MHz, CD<sub>3</sub>OD)  $\delta$  154.09, 153.78, 153.50, 153.32, 152.31, 151.74, 151.59, 151.52, 150.91, 150.37, 150.11, 149.69, 149.23, 139.16, 137.07, 137.04, 136.93, 136.85, 131.21-130.24 (20C, 4 phenyl groups), 130.60, 128.17, 127.84, 127.74, 127.65, 127.57, 127.36, 127.32, 127.14, 126.43, 126.00, 16.88. High Resolution MS  $m/z$  (calcd): 452.60837 (452.60576, [3]<sup>2+</sup>), 940.17804 (940.18092, [3 + Cl]<sup>+</sup>). Anal. Calcd for C<sub>55</sub>H<sub>41</sub>Cl<sub>2</sub>N<sub>5</sub>RuS·8.5 H<sub>2</sub>O: C, 58.51; H, 5.18; N, 6.20 Found: C, 59.56; H, 5.16; N, 5.95. UV-vis  $\lambda$  in nm ( $\epsilon$  in M<sup>-1</sup>·cm<sup>-1</sup>): 405 (17300) in water.

### 3.4.2 Irradiation experiments monitored with MS and UV-vis

UV-vis spectroscopy was performed using a Cary Varian spectrometer equipped with a temperature control set to 298 K and a magnetic stirrer. For the irradiation a LED light source was used ( $\lambda_{\text{ex}} = 445$  nm, with a Full Width at Half Maximum of 22 nm) with a photon flux of  $1.49 \cdot 10^{-7}$  or  $1.31 \cdot 10^{-7}$  mol·s<sup>-1</sup> (for [2]Cl<sub>2</sub> and [3]Cl<sub>2</sub>, respectively). Experiments were performed in a quartz cuvette containing 3 mL of solution. A stock

solution of the desired complex was prepared using demineralized water, which was then diluted in the cuvette to the desired working concentration. When the experiment was carried out under N<sub>2</sub> the sample was deaerated for 15 min by gentle bubbling of N<sub>2</sub> and the atmosphere was kept inert during the experiment by a gentle flow of N<sub>2</sub> on top of the cuvette. A UV-vis spectrum was measured every 30 s for the first 10 min, every 1 min for the next 10 min, and eventually every 10 min until the end of the experiment. Data was analysed with Microsoft Excel. The quantum yields of the photoreactions ( $\Phi_{PR}$ ) were calculated by modelling the time evolution of the absorbance spectrum of the solution using the Glotaran software (see Appendix I, Figure AIV.3, and Figure AIV.4). Experimental conditions are detailed in Table 3.3.

Table 3.3. Conditions of the photoreactions monitored with UV-vis spectroscopy and Mass spectrometry.

Complex	Stock solution			Working solution (mM)	Photon flux 450 nm LED (mol·s <sup>-1</sup> )
	w (mg)	V (mL)	M (mM)		
[2]Cl <sub>2</sub>	1.0	10	0.164	0.109	1.49·10 <sup>-7</sup>
[3]Cl <sub>2</sub>	1.1	10	0.113	0.038	1.31·10 <sup>-7</sup>

### 3.4.3 Blue light irradiation in the cell irradiation setup

In order to assess which light dose should be used for the photocytotoxicity assay, the photochemical reactivity of [1]Cl<sub>2</sub> and [2]Cl<sub>2</sub> was tested in 96-well plates, *i.e.* in the conditions of the cell experiments, but without cells and using UV-vis spectroscopy to measure to which extent the compounds are activated at different light doses. Two solutions of each compound (40 μM and 200 μM) were prepared in OptiMEM complete (see Appendix II) and distributed in a 96-well plate (200 μL per well). The plate was irradiated with blue light (454 nm) at different irradiation times (0, 2, 5, 8, 10 min) using the blue LED source described in details in Hopkins *et al.*<sup>6</sup> At 40 μM and below both complexes received enough light at 10 min irradiation (dose 6.5 J·cm<sup>-2</sup>) to be fully activated. At 200 μM, complex [2]Cl<sub>2</sub> was only partly activated (Figure AIV.2). Higher light doses would be necessary to fully activate the highest concentrations used for [2]Cl<sub>2</sub>, but they would also be inherently cytotoxic to A549 cells, as described in Hopkins *et al.*<sup>6</sup> Thus, 10 min irradiation, for a dose of 6.5 J·cm<sup>-2</sup>, was chosen for all photocytotoxicity experiments.

### 3.4.4 Partition coefficient ( $\log P$ )

The partition coefficient determination was adapted from Wang *et al.*<sup>26</sup> Stock solutions of [1]Cl<sub>2</sub>, [2]Cl<sub>2</sub>, and [3]Cl<sub>2</sub> were prepared in octanol-saturated water (1 mM). Aliquots of the stock solutions (0.2 mL) were transferred per triplicate to 15 mL centrifuge tubes and diluted up to 1 mL with octanol-saturated water to give 0.2 mM solutions. Then, 1 mL of water-saturated octanol was added and the mixtures were shaken in a IKA Vibrax shaker for 1 h at 2200 rpm. The mixtures were centrifuged (4300 rpm, 10 min, RT). Aliquots of the water layer (0.2 mL) were diluted with MilliQ water (2.4 mL) and 65% HNO<sub>3</sub> (0.4 mL) per duplicate, to give a final solution at 5% HNO<sub>3</sub>. The ruthenium content of these samples was determined by ICP-OES using a Vista-MPX CCD Simultaneous ICP-OES. The partition coefficient values can be found in Table 3.2 and were determined by using Equation 3.1,

$$\log P_{oct} = \log \frac{[Ru]_{total} - [Ru]_{aq}}{[Ru]_{aq}}$$

Equation 3.1

where [Ru]<sub>total</sub> is the concentration of ruthenium in the control sample (where no water-saturated octanol was added) and [Ru]<sub>aq</sub> is the concentration of ruthenium in the aqueous layer as a mean of the six replicates.

### 3.4.5 Cell culture and EC<sub>50</sub> (photo)cytotoxicity assay

Following the protocol described in Appendix II, 24 h after seeding A549 cells aliquots (100 μL) of six different concentrations (2 – 200 μM for all the compounds, except for [3]Cl<sub>2</sub> where 0.1 – 20 μM were used) of freshly prepared stock solutions of [1]Cl<sub>2</sub>, [2]Cl<sub>2</sub>, [3]Cl<sub>2</sub>, dmbpy, or mtmp in OptiMEM were added to the wells in triplicate. Plates were incubated in the dark for an additional 6 h. After this period, half of the plates were irradiated for 10 min with blue light ( $\lambda = 454 \pm 11$  nm, power density =  $10.5 \pm 0.7$  mW cm<sup>-2</sup>, irradiation time = 10 min, light dose =  $6.5$  J·cm<sup>-2</sup>) and the other half were kept in the dark. After irradiation all the plates were incubated for an additional 66 h (making a total assay of 96 h).

### 3.4.6 Cellular uptake

Cell uptake studies for complexes [1]Cl<sub>2</sub> and [2]Cl<sub>2</sub> were conducted on A549 cells.  $8 \cdot 10^5$  cells were seeded at  $t = 0$  h in OptiMEM complete (3 mL) in 6 cm diameter

dishes. At  $t = 24$  h cells were treated with solutions of  $[1]Cl_2$  and  $[2]Cl_2$  to give a final concentration of 20 and 80  $\mu M$ , respectively, in a total volume of 6 mL. After 6 h of drug incubation at 37 °C, the medium was aspirated and the cells were washed twice with 4 mL PBS. Then, the cells were trypsinized (1 mL), suspended with OptiMEM (3 mL), and centrifuged (1200 rpm, 4 min). After aspiration of the supernatant, the cells were resuspended in PBS (1mL) and counted. After a second centrifugation, the supernatant was discarded and the pellets were resuspended in MilliQ water (154  $\mu L$ ) and 65%  $HNO_3$  (up to 2 mL) for overnight digestion. Then, 1 mL of the solution was diluted with MilliQ water to obtain a final concentration of 5%  $HNO_3$ . For ICP-MS measurements, the system was optimized with a ruthenium-platinum solution. The calibration range was from 0 to 25  $\mu g/L$ , and obtained detection limit for all isotopes was 0.01  $\mu g/L$ . Silver and indium were used for internal standard, to correct for sample dependent matrix effects. No reference sample was available, therefore, several samples were spiked with a known concentration. The recoveries of the spiked concentrations were all within a 10% deviation. The data from two independent biological replications was used to obtain the uptake values shown in Table 3.2.

### 3.5 References

1. V. Balzani, G. Bergamini, F. Marchioni and P. Ceroni, *Coord. Chem. Rev.*, **2006**, 250, 1254-1266.
2. S. Campagna, F. Puntoriero, F. Nastasi, G. Bergamini and V. Balzani, *Spin Crossover In Transition Metal Compounds III*, Springer-Verlag Berlin Heidelberg, **2007**.
3. E. Baranoff, J. Collin, J. Furusho, Y. Furusho, A. Laemmel and J. Sauvage, *Inorg. Chem.*, **2002**, 41, 1215-1222.
4. E. Baranoff, J.-P. Collin, Y. Furusho, A.-C. Laemmel and J.-P. Sauvage, *Chem. Commun.*, **2000**, 1935-1936.
5. V. Fernandez-Moreira, F. L. Thorp-Greenwood and M. P. Coogan, *Chem. Commun.*, **2010**, 46, 186-202.
6. A. Martin, A. Byrne, C. S. Burke, R. J. Forster and T. E. Keyes, *J. Am. Chem. Soc.*, **2014**, 136, 15300-15309.
7. M. R. Gill, J. Garcia-Lara, S. J. Foster, C. Smythe, G. Battaglia and J. A. Thomas, *Nat Chem*, **2009**, 1, 662-667.
8. C. Mari, V. Pierroz, S. Ferrari and G. Gasser, *Chem. Sci.*, **2015**, 6, 2660-2686.
9. M. Frascioni, Z. Liu, J. Lei, Y. Wu, E. Strelakova, D. Malin, M. W. Ambrogio, X. Chen, Y. Y. Botros, V. L. Cryns, J.-P. Sauvage and J. F. Stoddart, *J. Am. Chem. Soc.*, **2013**, 135, 11603-11613.
10. R. N. Garner, J. C. Gallucci, K. R. Dunbar and C. Turro, *Inorg. Chem.*, **2011**, 50, 9213-9215.
11. B. A. Albani, B. Peña, N. A. Leed, N. A. B. G. de Paula, C. Pavani, M. S. Baptista, K. R. Dunbar and C. Turro, *J. Am. Chem. Soc.*, **2014**, 136, 17095-17101.
12. A.-C. Laemmel, J.-P. Collin and J.-P. Sauvage, *Eur. J. Inorg. Chem.*, **1999**, 383-386.
13. L. Salassa, C. Garino, G. Salassa, R. Gobetto and C. Nervi, *J. Am. Chem. Soc.*, **2008**, 130, 9590-9597.
14. T. Sainuddin, M. Pinto, H. Yin, M. Hetu, J. Colpitts and S. A. McFarland, *J. Inorg. Biochem.*, **2016**, 158, 45-54.

15. K. T. Hufziger, F. S. Thowfeik, D. J. Charboneau, I. Nieto, W. G. Dougherty, W. S. Kassel, T. J. Dudley, E. J. Merino, E. T. Papish and J. J. Paul, *J. Inorg. Biochem.*, **2014**, 130, 103-111.
16. B. S. Howerton, D. K. Heidary and E. C. Glazer, *J. Am. Chem. Soc.*, **2012**, 134, 8324-8327.
17. O. Filevich, M. Salierno and R. Etchenique, *J. Inorg. Biochem.*, **2010**, 104, 1248-1251.
18. L. Zayat, O. Filevich, L. M. Baraldo and R. Etchenique, *Philos. Trans. R. Soc., A*, **2013**, 371.
19. N. Karaoun and A. K. Renfrew, *Chem. Commun.*, **2015**, 51, 14038-14041.
20. T. Respondek, R. Sharma, M. K. Herroon, R. N. Garner, J. D. Knoll, E. Cueny, C. Turro, I. Podgorski and J. J. Kodanko, *ChemMedChem*, **2014**, 9, 1306-1315.
21. N. A. Smith, P. Zhang, S. E. Greenough, M. D. Horbury, G. J. Clarkson, D. McFeely, A. Habtemariam, L. Salassa, V. G. Stavros, C. G. Dowson and P. J. Sadler, *Chem. Sci.*, **2017**, 8, 395-404.
22. O. Novakova, J. Kasparkova, O. Vrana, P. M. Vanvliet, J. Reedijk and V. Brabec, *Biochemistry*, **1995**, 34, 12369-12378.
23. R. N. Garner, L. E. Joyce and C. Turro, *Inorg. Chem.*, **2011**, 50, 4384-4391.
24. D. V. Pinnick and B. Durham, *Inorg. Chem.*, **1984**, 23, 1440-1445.
25. S. L. Hopkins, B. Siewert, S. H. C. Askes, P. Veldhuizen, R. Zwier, M. Heger and S. Bonnet, *Photochem. Photobiol. Sci.*, **2016**, 15, 644-653.
26. F. Wang, J. Xu, A. Habtemariam, J. Bella and P. J. Sadler, *J. Am. Chem. Soc.*, **2005**, 127, 17734-17743.
27. V. H. S. van Rixel, B. Siewert, S. L. Hopkins, S. H. C. Askes, A. Busemann, M. A. Siegler and S. Bonnet, *Chem. Sci.*, **2016**, 7, 4922-4929.
28. Y. Fu, C. Sanchez-Cano, R. Soni, I. Romero-Canelon, J. M. Hearn, Z. Liu, M. Wills and P. J. Sadler, *Dalton Trans.*, **2016**, 45, 8367-8378.
29. C. Mari, V. Pierroz, R. Rubbiani, M. Patra, J. Hess, B. Spingler, L. Oehninger, J. Schur, I. Ott, L. Salassa, S. Ferrari and G. Gasser, *Chem. - Eur. J.*, **2014**, 20, 14421-14436.
30. A. Frei, R. Rubbiani, S. Tubafard, O. Blacque, P. Anstaett, A. Felgentrager, T. Maisch, L. Spiccia and G. Gasser, *J. Med. Chem.*, **2014**, 57, 7280-7292.
31. G. Shi, S. Monro, R. Hennigar, J. Colpitts, J. Fong, K. Kasimova, H. Yin, R. DeCoste, C. Spencer, L. Chamberlain, A. Mandel, L. Lilge and S. A. McFarland, *Coord. Chem. Rev.*, **2015**, 282-283, 127-138.
32. D. Garcia-Fresnadillo, Y. Georgiadou, G. Orellana, A. M. Braun and E. Oliveros, *Helv. Chim. Acta*, **1996**, 79, 1222-1238.
33. J. H. Wallenstein, J. Sundberg, C. J. McKenzie and M. Abrahamsson, *Eur. J. Inorg. Chem.*, **2016**, 897-906.
34. E. Reisner, T. C. Abikoff and S. J. Lippard, *Inorg. Chem.*, **2007**, 46, 10229-10240.



# 4

## Ruthenium-based PACT compounds based on an N,S protecting ligand: a delicate balance between photoactivation and thermal stability

*We have shown that sterically hindering bipyridyl molecules such as dmbpy cannot be used as protecting ligands in ruthenium PACT complexes on account of their cytotoxicity. Thus, new non-toxic ligands that provide efficient and selective photosubstitution are investigated. In this chapter, we report on the synthesis, stereochemical characterization, and cytotoxicity of the series of complexes  $[Ru(N,N)_2(mtpa)](PF_6)_2$  where N,N is a bipyridyl ligand and mtpa is 3-(methylthio)propylamine, a non-toxic bidentate N,S ligand. The number of sterically hindering methyl groups increases from zero in  $[Ru(bpy)_2(mtpa)](PF_6)_2$  (**[1]**(PF<sub>6</sub>)<sub>2</sub>, bpy = 2,2'-bipyridine) to two in  $[Ru(bpy)(dmbpy)(mtpa)](PF_6)_2$  (**[2]**(PF<sub>6</sub>)<sub>2</sub>, dmbpy = 6,6'-dimethyl-2,2'-bipyridine), and up to four in  $[Ru(dmbpy)_2(mtpa)](PF_6)_2$  (**[3]**(PF<sub>6</sub>)<sub>2</sub>). The identification of the isomer(s) effectively obtained in solution, including the configuration of the prochiral sulfur, required a combination of crystallography, NOESY spectroscopy, and DFT calculations. The number of methyl groups has a crucial effect on the photochemistry and cytotoxicity of these complexes: while the non-strained complex **[1]**<sup>2+</sup> is not capable of fully releasing mtpa and thus is not photocytotoxic against lung cancer cells (A549), the more strained complex **[2]**<sup>2+</sup> shows efficient mtpa photosubstitution upon blue light irradiation, leading to photocytotoxicity. However, if the complex is too strained (**[3]**(PF<sub>6</sub>)<sub>2</sub>), it also activates thermally in the dark, losing the photoactivation.*

This chapter has been accepted for publication as a full paper: J. A. Cuello-Garibo, C. James, M. A. Siegler, S. Bonnet, *Chem*<sup>2</sup>, **2017**, *in press*.

## 4.1 Introduction

In the last decade, Photoactivated Chemotherapy (PACT) using ruthenium-based complexes has caught attention because it has the potential to control the cytotoxicity of anticancer drugs in space and time. Whereas in Photodynamic Therapy (PDT) cytotoxicity is obtained by the photochemical generation of reactive oxygen species (ROS) such as singlet oxygen,<sup>1-3</sup> in metal-based PACT a new cytotoxic drug is formed *in situ* via photosubstitution of at least one of the ligands of the original prodrug.<sup>4-5</sup> In many reported examples, ruthenium PACT agents are based on complexes of the  $[\text{Ru}(\text{bpy})_2(\text{dmbpy})]^{2+}$  family, where bpy is 2,2'-bipyridine and dmbpy is the sterically hindering ligand 6,6'-dimethyl-2,2'-bipyridine that increases the distortion of the coordination octahedron.<sup>6-7</sup> In such strained complexes, the triplet metal-centered excited state ( $^3\text{MC}$ ) of the complex is lowered and can thus be thermally populated from the photochemically generated triplet metal-to-ligand charge-transfer state ( $^3\text{MLCT}$ ), leading to photosubstitution of dmbpy by two solvent molecules. The increased cytotoxicity of the compound after light irradiation was generally attributed to the formation of the bis-aqua complex  $\text{cis-}[\text{Ru}(\text{bpy})_2(\text{OH}_2)_2]^{2+}$ , which was initially proposed to be the cytotoxic species. However, we demonstrated in Chapter 3 that the second photoproduct obtained upon irradiation of  $[\text{Ru}(\text{bpy})_2(\text{dmbpy})]^{2+}$  in water, *i.e.* the free dmbpy ligand, is the actual cytotoxic species.<sup>8</sup> These findings resulted in the formulation of two questions: first, can we design a light-activated ruthenium complex in which the ruthenium bis-aqua photoproduct is the cytotoxic species? And secondly, if sterically hindering bipyridyl chelates such as dmbpy cannot be used on account of its cytotoxicity, which kind of non-toxic ligands are available, and how can we fine-tune the metal complex to obtain efficient and selective photosubstitution?

In Chapter 2 we have described the use of L-proline as a possible replacement for dmbpy in a series of ruthenium polypyridyl complexes with different steric hindrance.<sup>9</sup> We concluded that, although L-proline was not photosubstituted in water in any case, it could be photosubstituted in more apolar solvents such as  $\text{CH}_3\text{CN}$  if the strain was high enough. This result suggested that photoactivation of such compounds may happen within cancer cells in an apolar environment such as the cell membrane. However, later (*unreported*) high-throughput screening of these complexes against A549 lung cancer cells did not show any cytotoxicity, neither in the dark nor upon light irradiation. Thus, we decided to move from the anionic N,O chelating ligand L-proline to neutral N,S chelating ligands. Our group actively investigates the use of thioether ligands for the caging of aquated ruthenium complexes.<sup>10</sup> Thioethers are excellent ligands for

ruthenium(II) due to their softness, which often leads to thermally stable complexes. In addition, many ruthenium complexes coordinated to thioethers show selective photosubstitution of the thioether ligand by solvent molecule(s) upon visible light irradiation.<sup>11-12</sup> For example, we have shown in Chapter 3 that complexes  $[\text{Ru}(\text{bpy})_2(\text{mtmp})]\text{Cl}_2$  and  $[\text{Ru}(\text{Ph}_2\text{phen})_2(\text{mtmp})]\text{Cl}_2$  (where  $\text{Ph}_2\text{phen}$  = 4,7-diphenyl-1,10-phenanthroline and  $\text{mtmp}$  = 2-(methylthio)methylpyridine) can efficiently photosubstitute the non-toxic N,S chelating ligand  $\text{mtmp}$  by two solvent molecules in water. When A549 cells were treated with the two complexes and irradiated with light, only the more lipophilic complex  $[\text{Ru}(\text{Ph}_2\text{phen})_2(\text{mtmp})]\text{Cl}_2$  showed a strong cytotoxicity characterized by an  $\text{EC}_{50}$  value in the submicromolar range, as  $[\text{Ru}(\text{bpy})_2(\text{mtmp})]\text{Cl}_2$  could not enter the cells.  $[\text{Ru}(\text{Ph}_2\text{phen})_2(\text{mtmp})]\text{Cl}_2$  was, unfortunately, also very toxic in the dark ( $\text{EC}_{50} \sim 2.7 \mu\text{M}$ ), probably due to its high lipophilicity. Thus, a different strategy to fine-tune the lipophilicity of these compounds is now introduced, which consists in varying the number of methyl substituents in the spectator  $\text{bpy}$  ligands. In this work, we report on the synthesis and stereochemical characterization of the series of complexes  $[\text{Ru}(\text{bpy})_2(\text{mtpa})](\text{PF}_6)_2$  (**[1]** $(\text{PF}_6)_2$ ),  $[\text{Ru}(\text{bpy})(\text{dmbpy})(\text{mtpa})](\text{PF}_6)_2$  (**[2a]** $(\text{PF}_6)_2$  and **[2b]** $(\text{PF}_6)_2$ ), and  $[\text{Ru}(\text{dmbpy})_2(\text{mtpa})](\text{PF}_6)_2$  (**[3]** $(\text{PF}_6)_2$ ), where  $\text{mtpa}$  is 3-(methylthio)propylamine, a dissymmetric bidentate ligand derived from methionine by decarboxylation (Figure 4.1). The number of sterically hindering methyl groups increases from zero in **[1]** $(\text{PF}_6)_2$  to two in **[2a]** $(\text{PF}_6)_2$  and **[2b]** $(\text{PF}_6)_2$ , and up to four in **[3]** $(\text{PF}_6)_2$ . Next to increasing steric hindrance, more methyl groups also increase the lipophilicity of the complex, and hence its ability to cross membranes in the cells. The effect of the number of methyl groups on the photochemistry and cytotoxicity of these complexes is discussed.

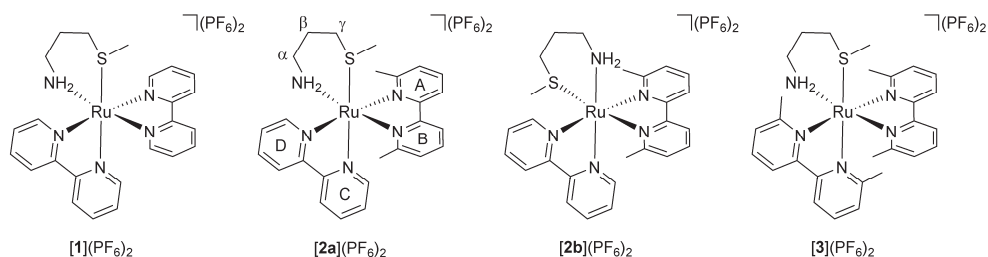


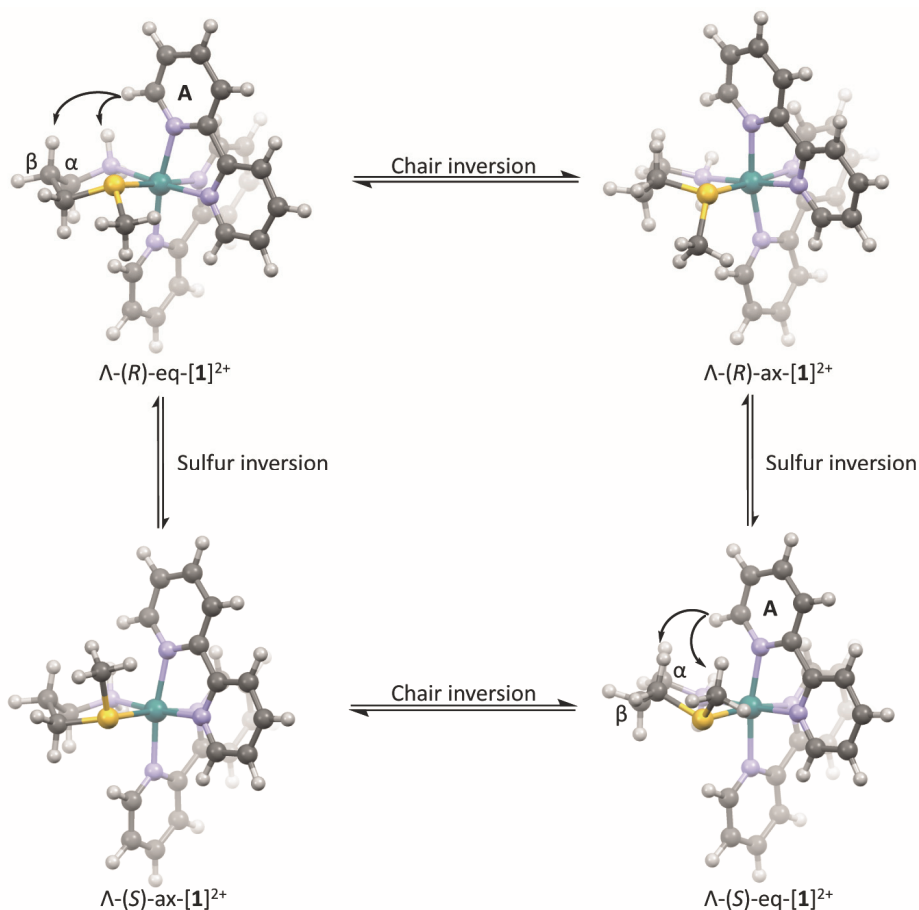
Figure 4.1. Structures of the complexes **[1]** $(\text{PF}_6)_2$ , **[2a]** $(\text{PF}_6)_2$ , **[2b]** $(\text{PF}_6)_2$ , and **[3]** $(\text{PF}_6)_2$ . The configuration of the sulfur center is not specified. For clarity only the  $\Delta$  isomers are shown, but all samples were obtained as racemic  $\Delta/\Delta$  mixtures.

## 4.2 Results

### 4.2.1 Synthesis

A series of three ruthenium complexes with zero, two, or four methyl groups on the bpy ligands was synthesized (Figure 4.1). Complexes  $[1](PF_6)_2$  and  $[3](PF_6)_2$  were obtained in a similar manner by reacting their precursors  $[Ru(bpy)_2Cl_2]$  and  $[Ru(dmbpy)_2Cl_2]$  with the mtpa ligand, to afford racemic mixtures in both cases. Besides the chirality of the octahedron ( $\Delta$  or  $\Lambda$ ), two other sources of isomerism are present (Scheme 4.1): the configuration ( $S$  or  $R$ ) of the sulfur atom, and the chair inversion of the six-membered ring resulting from the coordination of the N,S chelating ligand to the ruthenium center, which transforms an axial thioether methyl group ( $ax$ ) into an equatorial one ( $eq$ ) and *vice versa*. This isomerism leads to a total of four possible isomers, *i.e.*  $\Lambda$ -( $R$ )- $eq$ - $[Ru]^{2+}$ ,  $\Lambda$ -( $R$ )- $ax$ - $[Ru]^{2+}$ ,  $\Lambda$ -( $S$ )- $eq$ - $[Ru]^{2+}$ , and  $\Lambda$ -( $S$ )- $ax$ - $[Ru]^{2+}$  (where  $[Ru]^{2+}$  is either  $[1]^{2+}$ ,  $[2a]^{2+}$ ,  $[2b]^{2+}$ , or  $[3]^{2+}$ ), together with their enantiomers  $\Delta$ -( $S$ )- $eq$ - $[Ru]^{2+}$ ,  $\Delta$ -( $S$ )- $ax$ - $[Ru]^{2+}$ ,  $\Delta$ -( $R$ )- $eq$ - $[Ru]^{2+}$ , and  $\Delta$ -( $R$ )- $ax$ - $[Ru]^{2+}$ , respectively. As shown in Scheme 4.1, inversion of the chair does not change the configuration ( $S$  or  $R$ ) of the chiral sulfur center but the conformation of the chair, thus changing the position of the methyl substituent from equatorial ( $eq$ ) to axial ( $ax$ ) or *vice versa*. According to the signals of  $^1H$  NMR, complexes  $[1](PF_6)_2$  and  $[3](PF_6)_2$  were obtained as a mixture of two diastereoisomers, with ratios of 1:0.05 and 1:0.12, respectively. The temperature-dependent  $^1H$  NMR spectrum of  $[1](PF_6)_2$  in  $CD_3OD$  did not show any significant difference at 193 K, 293 K, and 333 K, refuting the hypothesis that inversion of the sulfur from  $R$  to  $S$  or *vice versa* may be fast at room temperature, and confirming that two stable diastereoisomers have been obtained for  $[1]^{2+}$  and by extension for  $[3]^{2+}$ . On the other hand, a previously reported synthetic route was used to synthesize  $[2](PF_6)_2$ ,<sup>9</sup> which consisted first in preparing *cis*- $[Ru(bpy)(dmbpy)(CH_3CN)_2](PF_6)_2$  ( $[4](PF_6)_2$ ) by visible light irradiation of the precursor  $[Ru(bpy)(dmbpy)_2](PF_6)_2$  ( $[5](PF_6)_2$ ) in  $CH_3CN$ , and then reacting  $[4](PF_6)_2$  with mtpa in water. The  $^1H$  NMR spectrum of the crude product of  $[2](PF_6)_2$  showed two doublets at 9.55 and 9.17 ppm, characteristic for the hydrogen in position 6 or 6' on the bpy, in a ratio of 1:0.55. Mass spectrometry showed peaks at  $m/z = 273.2$ , 287.4, and 692.0, which correspond to  $[Ru(bpy)(dmbpy)(mtpa)]^{2+}$  (calcd  $m/z = 273.6$ ),  $[Ru(dmbpy)_2(mtpa)]^{2+}$  (calcd  $m/z = 287.6$ ), and  $\{[Ru(bpy)(dmbpy)(mtpa)](PF_6)\}^+$  (calcd  $m/z = 692.1$ ), respectively, indicating the occurrence of ligand scrambling. Since the two doublets in the 9–10 ppm range cannot belong to  $[Ru(dmbpy)_2(mtpa)]^{2+}$ , the two main species present in the mixture share the same mass peaks, *i.e.* they are two of

the expected isomers of  $[2]^{2+}$ . Resolution of both isomers by alumina column chromatography using a mixture of  $\text{CH}_2\text{Cl}_2/\text{CH}_3\text{OH}$  (99:1) as eluent did produce a main fraction containing both isomers in a ratio 1:0.07 according to  $^1\text{H}$  NMR.



Scheme 4.1. Isomers of  $[1]^{2+}$  as a result of the inversion of either the chirality of the sulfur atom (*R* or *S*) or the conformation of the chair. Isomers  $\Lambda\text{-(R)-eq-[1]}^{2+}$  and  $\Lambda\text{-(S)-eq-[1]}^{2+}$  show distances between  $N_{\text{eq}}$  and  $A_6$  of 3.398 and 2.585 Å, respectively, and distances between the  $\alpha_{\text{ax}}$  and  $A_6$  of 4.638 and 1.983 Å, respectively.

The tris-heteroleptic complex  $[2](\text{PF}_6)_2$  bears three different bidentate ligands, thus the two different orientations of mtpa lead to two different regioisomers: either (OC-6-43)- $[\text{Ru}(\text{bpy})(\text{dmbpy})(\text{mtpa})]^{2+}$ , in which the thioether sulfur donor is *trans* to the bpy, or (OC-6-34)- $[\text{Ru}(\text{bpy})(\text{dmbpy})(\text{mtpa})]^{2+}$ , in which the thioether ligand is *trans* to the dmbpy ligand. For simplicity, these two regioisomers are called  $[2\mathbf{a}](\text{PF}_6)_2$  and  $[2\mathbf{b}](\text{PF}_6)_2$ , respectively (Figure 4.1). Like for  $[1](\text{PF}_6)_2$  and  $[3](\text{PF}_6)_2$ , each of the regioisomers of  $[2](\text{PF}_6)_2$  has four possible isomers, which leads to a total of eight

possible  $\Lambda$  diastereoisomers and their corresponding eight  $\Delta$  enantiomers. NOESY analysis in  $D_2O$  showed an off-diagonal correlation between a proton of the amine and the methyl substituent on the dmbpy for the major isomer, which means that in this isomer the amine must be *trans* to dmbpy. Thus, the major isomer in this fraction was  $[2a]^{2+}$ , while the minor isomer remains unassigned. However, after storage for two weeks as a powder in the freezer ( $-20\text{ }^\circ\text{C}$ ), this purified sample had isomerized back into a 1:0.4 mixture of isomers, which showed that isomerization was occurring even under such conditions, and thus that the two isomers cannot be kept in separate flasks. Below,  $[2](PF_6)_2$  is used as a mixture of these two regioisomers.

#### 4.2.2 Characterization by DFT and NOESY studies

In order to understand the stereoselectivity of sulfur coordination in solution, Density Functional Theory (DFT) calculations of complexes  $[1]^{2+}$ ,  $[2a]^{2+}$ ,  $[2b]^{2+}$ , and  $[3]^{2+}$  were performed in water using the COSMO model for simulating solvent effects (see Experimental Section). In each case only the  $\Lambda$  enantiomer having the six-membered ring in a chair conformation was modelled. The sulfur atom was either in *R* or *S* configuration, with the methyl group either in equatorial or in axial position by inversion of the chair, following Scheme 4.1 and resulting in a total of four possible isomers per complex. The optimized structures and their energies in water are given in Scheme 4.1, Figure AV.11, Figure AV.12, and Table 4.1, respectively. Complex  $\Lambda$ -(*S*)-*eq*- $[1]^{2+}$  is the lowest in energy, followed by  $\Lambda$ -(*S*)-*ax*- $[1]^{2+}$  at  $+5.4\text{ kJ}\cdot\text{mol}^{-1}$ , obtained by inversion of the chair. NOESY analysis of  $[1](PF_6)_2$  in  $D_2O$  showed an off-diagonal correlation between the A6 proton on bpy and the  $N_{eq}$  proton of mtpa, and a correlation between A6 and the  $\alpha_{ax}$  proton (Figure AV.1). In the calculated structure of  $\Lambda$ -(*R*)-*eq*- $[1]^{2+}$  the distances between those atoms are 3.398 and 4.638 Å, respectively, whereas in  $\Lambda$ -(*S*)-*eq*- $[1]^{2+}$  the distances are much shorter, *i.e.* 2.585 and 1.983 Å, respectively (Figure 4.2). Thus, altogether the DFT and NMR studies suggest that  $[1]^{2+}$  in solution is a racemic mixture containing  $\Lambda$ -(*S*)-*eq*- $[1]^{2+}$  and  $\Delta$ -(*R*)-*eq*- $[1]^{2+}$ , which are also the most thermodynamically stable pair of enantiomers.

Table 4.1. Absolute and relative energies in water (COSMO) of the isomers of  $[1]^{2+}$ ,  $[2a]^{2+}$ ,  $[2b]^{2+}$ , and  $[3]^{2+}$  optimized by DFT/PBE0/TZP.

Isomer	Absolute energy in water (Hartree)	Relative energy $\Delta E$ in water ( $\text{kJ}\cdot\text{mol}^{-1}$ )
$\Lambda\text{-(R)-eq-[1]}^{2+}$	-16.23684667	6.4
$\Lambda\text{-(R)-ax-[1]}^{2+}$	-16.23341885	15.4
$\Lambda\text{-(S)-eq-[1]}^{2+}$	-16.23930307	0.0
$\Lambda\text{-(S)-ax-[1]}^{2+}$	-16.23723835	5.4
$\Lambda\text{-(R)-eq-[2a]}^{2+}$	-17.67935607	0.0
$\Lambda\text{-(R)-ax-[2a]}^{2+}$	-17.67277958	17.3
$\Lambda\text{-(S)-eq-[2a]}^{2+}$	-17.67921051	0.4
$\Lambda\text{-(S)-ax-[2a]}^{2+}$	-17.67779925	4.1
$\Lambda\text{-(R)-eq-[2b]}^{2+}$	-17.67166128	20.2
$\Lambda\text{-(R)-ax-[2b]}^{2+}$	-17.66922670	26.6
$\Lambda\text{-(S)-eq-[2b]}^{2+}$	-17.67649787	7.5
$\Lambda\text{-(S)-ax-[2b]}^{2+}$	-17.67485691	11.8
$\Lambda\text{-(R)-eq-[3]}^{2+}$	-19.12274771	8.4
$\Lambda\text{-(R)-ax-[3]}^{2+}$	-19.11917987	17.7
$\Lambda\text{-(S)-eq-[3]}^{2+}$	-19.11171121	37.3
$\Lambda\text{-(S)-ax-[3]}^{2+}$	-19.12592873	0.0

For the tris-heteroleptic complex  $[2]^{2+}$ , isomer  $\Lambda\text{-(R)-eq-[2a]}^{2+}$  appeared to be the most stable in water according to DFT, followed by the other isomers of  $[2a]^{2+}$ . The isomers of  $[2b]^{2+}$  were found at higher energies, ranging from +7.5 to +26.6  $\text{kJ}\cdot\text{mol}^{-1}$ . Furthermore, NOESY analysis in  $\text{CD}_3\text{OD}$  shows an off-diagonal correlation between the D6 proton on the bpy of the major isomer with both MeS- and the  $\gamma$  proton of mtpa (Figure AV.2). In the calculated structure of  $\Lambda\text{-(R)-eq-[2a]}^{2+}$  the distances between those atoms are short (2.083 and 2.147 Å, respectively, see Figure 4.2), whereas in  $\Lambda\text{-(S)-eq-[2a]}^{2+}$  the distances are larger, being 4.198 and 3.918 Å, respectively. Thus, NMR data agree with DFT that the major and most stable isomer is  $\Lambda\text{-(R)-eq-[2a]}^{2+}$ . Meanwhile, DFT calculations suggest that the minor isomer would correspond to  $\Lambda\text{-(S)-eq-[2a]}^{2+}$  if the formation of  $[2]^{2+}$  would be under thermodynamic control. Unfortunately, it was impossible to isolate the minor isomer and to confirm this hypothesis. Finally, for the most strained complex of the series, isomer  $\Lambda\text{-(S)-ax-[3]}^{2+}$  was the most stable according to DFT, followed by  $\Lambda\text{-(R)-eq-[3]}^{2+}$ ,  $\Lambda\text{-(R)-ax-[3]}^{2+}$ , and  $\Lambda\text{-(S)-eq-[3]}^{2+}$  at +8.4, +17.7, and +37.3  $\text{kJ}\cdot\text{mol}^{-1}$ , respectively. NOESY analysis in

CD<sub>3</sub>OD showed an off-diagonal correlation between the methyl substituent DMe and the proton  $\gamma_{ax}$ , and another correlation between the methyl substituent AMe and the methyl of the thioether group, with a relative intensity of the signals of 65% and 35%, respectively (Figure AV.3). According to the calculated structures, the distances between those hydrogens are 3.439 and 3.102 Å in  $\Lambda$ -(S)-eq-[3]<sup>2+</sup>, 2.133 and 6.246 Å in  $\Lambda$ -(R)-eq-[3]<sup>2+</sup>, and 2.127 and 2.995 Å in  $\Lambda$ -(S)-ax-[3]<sup>2+</sup>, respectively (Figure 4.2). Thus, isomer  $\Lambda$ -(S)-ax-[3]<sup>2+</sup>, observed in the crystal structure, fits best the obtained NOESY data in solution. Overall, irrespective of the steric hindrance the major isomer in solution in this series of complexes is the most stable one according to DFT calculations.

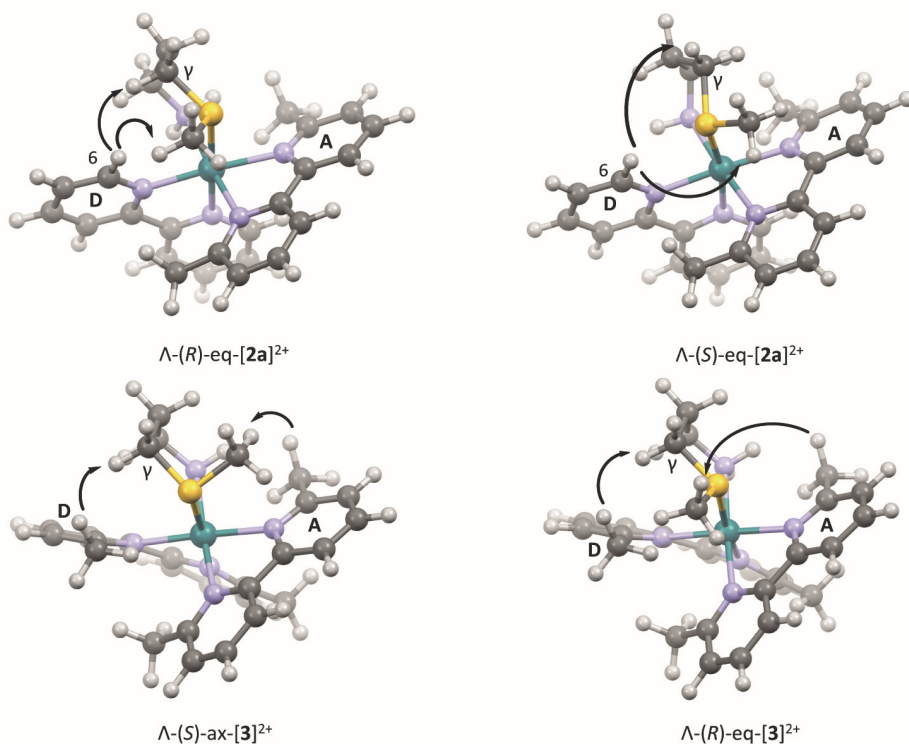


Figure 4.2. Structures of selected isomers of [2]<sup>2+</sup> and [3]<sup>2+</sup> optimized by DFT in water (COSMO). Isomers  $\Lambda$ -(R)-eq-[2a]<sup>2+</sup> and  $\Lambda$ -(S)-eq-[2a]<sup>2+</sup> show distances between  $\gamma_{ax}$  and D6 of 2.147 and 3.918 Å, respectively, and distances between the methyl thioether group and D6 of 2.083 and 4.198 Å, respectively. Isomers  $\Lambda$ -(S)-ax-[3]<sup>2+</sup> and  $\Lambda$ -(R)-eq-[3]<sup>2+</sup> show distances between  $\gamma_{ax}$  and DMe of 2.127 and 2.133 Å, respectively, and distances between the methyl thioether group and AMe of 2.995 and 6.246 Å, respectively

To quantify steric hindrance in this series of complexes, the structural distortion parameter,<sup>13</sup> i.e. the bond angle variance ( $\sigma^2$ ), was calculated from the DFT models for

all the isomers with the methyl group in equatorial position as well as for  $\Lambda$ -(*S*)-*ax*-[**3**]<sup>2+</sup> (Table AV.1). In a simple assumption, more strained molecules should have a more distorted coordination octahedron, thus a higher  $\sigma^2$  value. However, the change in the configuration of the sulfur atom appears to have a great impact on  $\sigma^2$ . All the isomers with *R* configuration were found to have a higher  $\sigma^2$  value than their corresponding *S* isomer (e.g.  $\sigma^2$  is 62.4 and 45.0 for  $\Lambda$ -(*R*)-*eq*-[**1**]<sup>2+</sup> and  $\Lambda$ -(*S*)-*eq*-[**1**]<sup>2+</sup>, respectively). The  $\sigma^2$  value for the tris-heteroleptic *R* complex  $\Lambda$ -(*R*)-*eq*-[**2a**]<sup>+</sup> is even higher than that of the, in principle, more strained *S* complex  $\Lambda$ -(*S*)-*eq*-[**3**]<sup>+</sup> (81.8 vs 76.3). Thus, the orientation of specific bulky moieties such as MeS- has a greater effect on the distortion of the octahedron than the overall number of methyl groups. Furthermore, a direct relation between  $\sigma^2$  and their DFT-calculated energies in water was found only for the non-strained complex [1]<sup>2+</sup>. Indeed, for this complex the least distorted isomer  $\Lambda$ -(*S*)-[1]<sup>2+</sup> was found to have the lowest energy. For complex [2]<sup>2+</sup> the most distorted isomer ( $\Lambda$ -(*R*)-*eq*-[2a]<sup>2+</sup>) has the lowest energy in water, whereas for complex [3]<sup>2+</sup> isomers  $\Lambda$ -(*S*)-*ax*-[3]<sup>2+</sup> and  $\Lambda$ -(*S*)-*eq*-[3]<sup>2+</sup>, having similar  $\sigma^2$  values (76.0 and 76.3, respectively), showed the greatest difference in energy (37.3 kJ·mol<sup>-1</sup>). Since a correlation between octahedral distortion and stability could not be drawn, the interligand repulsion between the methyl substituents and mtpa was also considered. We found that all the isomers that have the H<sub>ax</sub> in positions 3 and 5 of the six-membered chair facing directly the methyl substituent in the 6 position of the dmbpy ligand, are always higher in energy. As shown in Figure 4.3, for complex  $\Lambda$ -(*S*)-*eq*-[3]<sup>2+</sup>, which is the least stable of the isomers of [3]<sup>2+</sup> in water, the distances between H<sub>ax</sub> in positions 3 and 5 and their spatially closest methyl substituents are only 2.097 and 1.860 Å, respectively. Overall, two factors influence the stability of these complexes and the stereoselectivity of the coordination of mtpa: the octahedral distortion and the interligand repulsion. In the case of the non-strained complex [1]<sup>2+</sup> only the octahedral distortion plays a role, whereas when hindering methyl substituents are introduced in the complex, interligand repulsion becomes the driving force for the stereoselectivity of the reaction.

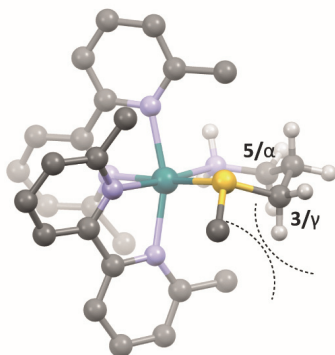


Figure 4.3. Schematic drawing of isomer  $\Lambda$ -(*S*)-*eq*-[**3**]<sup>2+</sup> showing the steric effect between the methyl substituent on *dmbpy* facing directly the  $H_{ax}$  in positions 3 and 5 of the six-membered ring in a chair conformation.

### 4.2.3 X-Ray crystallography

Single crystals suitable for X-Ray structure determination were obtained for complexes [**1**](PF<sub>6</sub>)<sub>2</sub>, [**2a**](PF<sub>6</sub>)<sub>2</sub>, and [**3**](PF<sub>6</sub>)<sub>2</sub> by slow vapor diffusion of the solvent of a methanol solution of the complex into toluene, ethyl acetate, and di-*tert*-butyl ether, respectively. For complex [**1**](PF<sub>6</sub>)<sub>2</sub> the structure contains two enantiomers  $\Lambda$ -(*S*) and  $\Delta$ -(*R*) of [Ru(*bpy*)<sub>2</sub>(*mtpa*-κN,κS)](PF<sub>6</sub>)<sub>2</sub>·CH<sub>3</sub>OH. The molecular structure, shown in Figure 4.4a, shows a methyl group in equatorial position, obtaining  $\Lambda$ -(*S*)-*eq*-[**1**](PF<sub>6</sub>)<sub>2</sub>, the same isomer suggested by NMR and DFT data in solution. Although [**2**](PF<sub>6</sub>)<sub>2</sub> was crystallized using a mixture of two regioisomers, the crystal structure contains a racemate of a single isomer of [**2a**](PF<sub>6</sub>)<sub>2</sub> in the orthorhombic space group *Pbca*, containing both configurations  $\Lambda$ -(*R*) and  $\Delta$ -(*S*). The molecular structure shown in Figure 4.4b shows a longer Ru-S bond (2.3668(7) Å) compared to that in  $\Lambda$ -(*S*)-*eq*-[**1**]<sup>2+</sup> (2.3314(7) Å, Table 4.2) and the *mtpa* amine is located *trans* to the *dmbpy* ligand, confirming the NMR assignment in solution. The methyl group is found to be in equatorial position, thus the crystallized isomer is  $\Lambda$ -(*R*)-*eq*-[**2a**](PF<sub>6</sub>)<sub>2</sub>, the same isomer suggested by NMR and DFT data in solution. Finally, [**3**](PF<sub>6</sub>)<sub>2</sub> crystallized in a triclinic *P-1* space group having an inversion point, and contains the racemate  $\Lambda$ -(*S*) and  $\Delta$ -(*R*) [**3**](PF<sub>6</sub>)<sub>2</sub>. The structure shown in Figure 4.4c shows the longest Ru-S bond (2.3845(8) Å) of the series. Thus, more methyl groups in the complex lead to longer Ru-S bonds but do not affect Ru-N bonds distances. The methyl group of the thioether is in axial position, resulting in the isomer  $\Lambda$ -(*S*)-*ax*-[**3**](PF<sub>6</sub>)<sub>2</sub>, the same isomer suggested by NMR and DFT data in solution. Interestingly, whereas for complex [**1**](PF<sub>6</sub>)<sub>2</sub> and [**3**](PF<sub>6</sub>)<sub>2</sub> the obtained structures have the configuration  $\Lambda$ -(*S*) and  $\Delta$ -(*R*),

in  $[2\mathbf{a}](\text{PF}_6)_2$  they are  $\Lambda$ -(*R*) and  $\Delta$ -(*S*). In every case, the six-membered ring resulting from the coordination of mtpa to the ruthenium center is in a chair conformation, as modelled in the DFT calculations. Furthermore, comparing the structures of  $\Lambda$ -(*S*)- $[1](\text{PF}_6)_2$  and  $\Lambda$ -(*R*)- $[2](\text{PF}_6)_2$  a flip in the chair conformation accompanied the change in the configuration of the sulfur atom from (*S*) to (*R*), probably in order to keep the methyl group in the equatorial position.

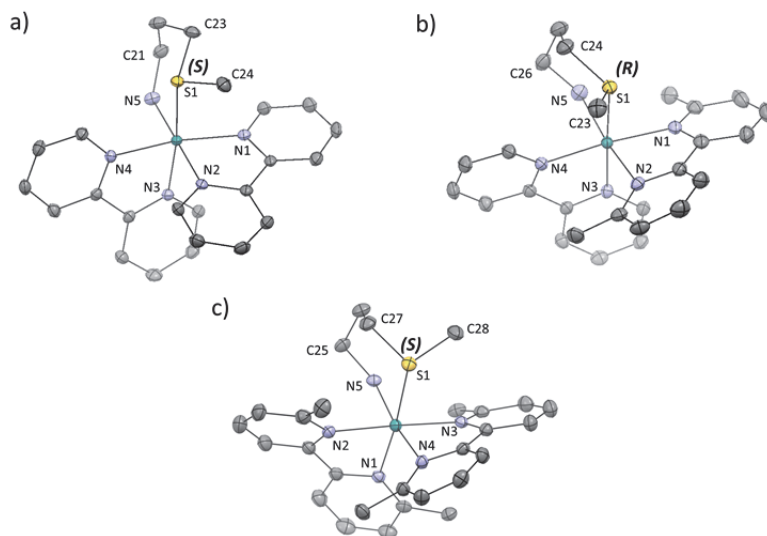


Figure 4.4. Displacement ellipsoid plot (50% probability level) of the cationic complex in the crystal structure of the  $\Lambda$  enantiomer of a)  $\Lambda$ -(*S*)-eq- $[1](\text{PF}_6)_2$ , b)  $\Lambda$ -(*R*)-eq- $[2\mathbf{a}](\text{PF}_6)_2$ , and c)  $\Lambda$ -(*S*)-ax- $[3](\text{PF}_6)_2$ . Hexafluoridophosphate counteranions, hydrogen atoms, lattice  $\text{CH}_3\text{OH}$  (in the case of  $[1](\text{PF}_6)_2$ ), and disorder have been omitted for clarity.

Table 4.2. Selected bond lengths ( $\text{\AA}$ ) and angles ( $^\circ$ ) for  $\Lambda$ -(*S*)-eq- $[1](\text{PF}_6)_2$ ,  $\Lambda$ -(*R*)-eq- $[2\mathbf{a}](\text{PF}_6)_2$ , and  $\Lambda$ -(*S*)-ax- $[3](\text{PF}_6)_2$ .

	$\Lambda$ -( <i>S</i> )-eq- $[1](\text{PF}_6)_2$	$\Lambda$ -( <i>R</i> )-eq- $[2\mathbf{a}](\text{PF}_6)_2$	$\Lambda$ -( <i>S</i> )-ax- $[3](\text{PF}_6)_2$
<b>Ru1-S1</b>	2.3314(7)	2.3668(7)	2.3845(8)
<b>Ru1-N1</b>	2.079(2)	2.117(2)	2.102(2)
<b>Ru1-N2</b>	2.066(2)	2.112(2)	2.113(2)
<b>Ru1-N3</b>	2.079(2)	2.064(2)	2.087(2)
<b>Ru1-N4</b>	2.083(2)	2.081(2)	2.087(2)
<b>Ru1-N5</b>	2.149(2)	2.167(2)	2.164(2)
<b>S1-C23-C21-N5</b>	-12.8(2)	-	-
<b>S1-C24-C26-N5</b>	-	-8.1(2)	-
<b>S1-C25-C27-N5</b>	-	-	-4.7(2)

#### 4.2.4 Photochemistry and thermal stability

The photoreactivity and thermal stability of all the complexes was studied in water and monitored with a variety of techniques including  $^1\text{H}$  NMR, UV-vis spectroscopy, and mass spectrometry. Complex  $[\mathbf{1}](\text{PF}_6)_2$ , when irradiated with blue light (445 nm), showed a bathochromic shift in the  $^1\text{MLCT}$  band with a change in the maximum absorption from 450 nm to 486 nm, and clear isosbestic points at 325 nm, 390 nm, and 460 nm, indicating a one-step process (Figure 4.5a). After 6 min at  $\sim 3 \cdot 10^{-8} \text{ mol} \cdot \text{s}^{-1}$  photon flux the photoreaction had reached the steady state. Mass spectrometry performed at that point showed major peaks at  $m/z = 260.0$ ,  $269.0$ , and  $536.2$ , corresponding to  $[\text{Ru}(\text{bpy})_2(\text{mtpa})]^{2+}$  (calcd  $m/z = 259.6$ ),  $[\text{Ru}(\text{bpy})_2(\text{mtpa})(\text{OH}_2)]^{2+}$  (calcd  $m/z = 268.6$ ), and  $[\text{Ru}(\text{bpy})_2(\text{mtpa})(\text{OH})]^+$  (calcd  $m/z = 536.1$ ), respectively, but no peaks corresponding to the bis photosubstituted species  $[\text{Ru}(\text{bpy})_2(\text{OH}_2)_2]^{2+}$  (calcd  $m/z = 225.03$ , Figure AV.6). Thus, only one coordination position was substituted by a water molecule and it appeared impossible to reach full conversion, since peaks belonging to the starting compound  $[\mathbf{1}](\text{PF}_6)_2$  were still present at the steady state. As shown in Figure 4.6b, when the same photoreaction was monitored with NMR in  $\text{D}_2\text{O}$ , doublets at 9.79 and 9.24 ppm, characteristic of hydrogens in positions 6 and 6' of bpy in  $[\mathbf{1}](\text{PF}_6)_2$ , decreased in intensity after 40 min, whereas new doublets at 9.23 and 9.21 ppm arose for the photoproduct, reaching the steady state with a ratio of 3.4:1 between the photoproduct and the starting complex. Furthermore, the singlet peak of the methyl thioether shifted downfield from 1.20 to 1.92 ppm, which is characteristic for a free methyl thioether. Thus, as shown in Scheme 4.2, the sulfur moiety was photosubstituted, but the amine ligand stayed bound, *i.e.* the photoproduct is  $[\text{Ru}(\text{bpy})_2(\text{mtpa}-\kappa\text{N})(\text{OH}_2)]^{2+}$ . Furthermore, when the photoproduct was kept in the dark at room temperature, the reverse reaction took place very slowly, with the doublets at 9.23 and 9.21 ppm, characteristic of  $[\mathbf{1}](\text{PF}_6)_2$ , increasing again after 30 days (Figure 4.6b). The reversibility of the ring opening photoreaction was also studied using UV-vis spectroscopy by irradiating  $[\mathbf{1}](\text{PF}_6)_2$  four times during 5 min, each time followed by  $\sim 2$  h of equilibration in the dark at  $37^\circ\text{C}$  (to increase the rate of back coordination). As shown in Figure 4.6a, the ring opening is clearly reversible. Photosubstitution of only one monodentate amine or pyridine ligand L in ruthenium  $[\text{Ru}(\text{bpy})_2(\text{L})_2]^{2+}$  complexes is classical in literature,<sup>14-15</sup> as well as hemilability followed by either fast rechelation (also called recaptation) or full dissociation of the bidentate ligand.<sup>16-18</sup> However, hemilability followed by such a slow rechelation is rare. Here, it appears to be a consequence of the difference in binding properties between the thioether and amine donor atoms. Thus, complex  $[\mathbf{1}]^{2+}$  shows a light-

controlled Ru-S bond breaking and thermal recovery, *i.e.* it behaves like a photoswitch (Scheme 4.2).

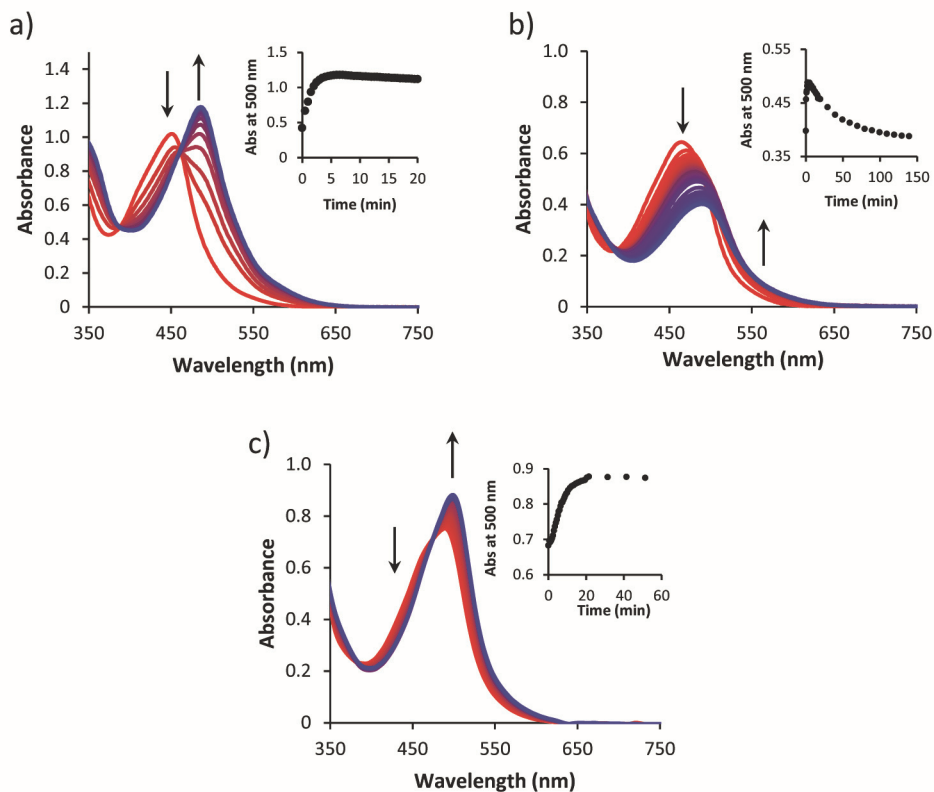


Figure 4.5. Evolution of the UV-vis spectra of water solutions of (a)  $[1](PF_6)_2$  (0.145 mM), (b)  $[2](PF_6)_2$  (0.101 mM), and (c)  $[3]Cl_2$  (0.123 mM) upon irradiation with a 445 nm LED ( $2.9 \pm 0.1 \cdot 10^{-8} \text{ mol} \cdot \text{s}^{-1}$ ) under  $N_2$  at 25 °C. Insets: evolution of the absorbance at 500 nm vs. time.

The photoreactivity of the most strained complex  $[3]^{2+}$  was studied in water for comparison. First,  $[3](PF_6)_2$  was converted to the chloride salt  $[3]Cl_2$  to increase water solubility. When a solution of  $[3]Cl_2$  in water was irradiated with a 445 nm LED a change in the MLCT band of the UV-vis spectra was observed, with a small bathochromic shift of the maximum absorption to 500 nm (Figure 4.5c). The steady state was reached after 20 min irradiation at the same photon flux as above ( $\sim 3 \cdot 10^{-8} \text{ mol} \cdot \text{s}^{-1}$ ). A mass spectrum of the irradiated sample showed no peaks that would correspond to the starting complex (Figure AV.8). When a solution of  $[3]Cl_2$  was kept in the dark and monitored with UV-vis, a qualitatively similar but less pronounced change in the spectra was observed. When  $[3]Cl_2$  was dissolved in  $D_2O$  to monitor the photoreaction with  $^1H$  NMR, two sets of peaks were present already at  $t = 0$  h, with a doublet at 7.22 ppm (integrating for two H, characteristic of the

hydrogen at position 3 in the dmbpy), and two doublets at 7.30 and 7.35 ppm (integrating for one H each), indicating the presence of two species in a ratio of 1:0.5 (Figure AV.5a). When this mixture was kept in the dark at room temperature for 72 h, almost no change was observed. However, when the solution was irradiated with a Xe lamp mounted with a 450 nm bandpass filter, the doublets at 7.30 and 7.35 ppm disappeared after 3 h, whereas the intensity of the doublet at 7.22 ppm increased (Figure AV.5b). This peak belongs to the solvated complex  $[\text{Ru}(\text{dmbpy})_2(\text{OH}_2)_2]^{2+}$ . Thus,  $[\mathbf{3}](\text{PF}_6)_2$  in water is not stable in the dark. The mtpa ligand is substituted by two water molecules, to reach an equilibrium between  $[\mathbf{3}]^{2+}$  and  $[\text{Ru}(\text{dmbpy})_2(\text{OH}_2)_2]^{2+}$  (Scheme 4.2). This equilibrium can be displaced by light irradiation, as has been reported for other types of strained ruthenium complexes.<sup>11, 19</sup>

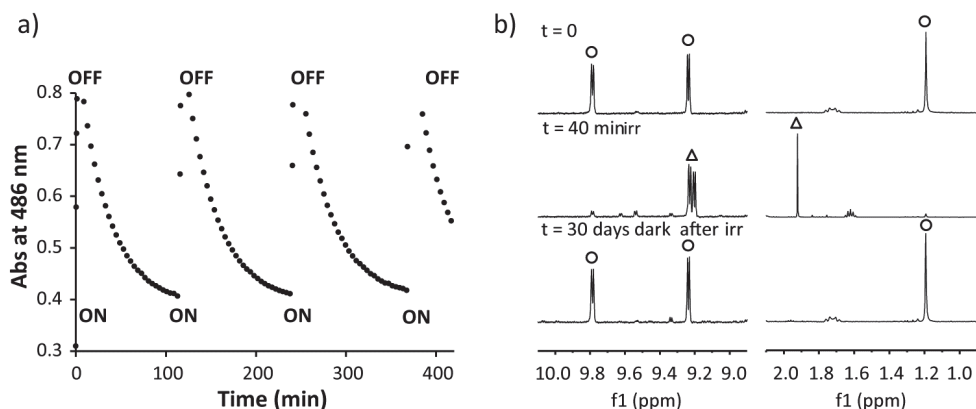
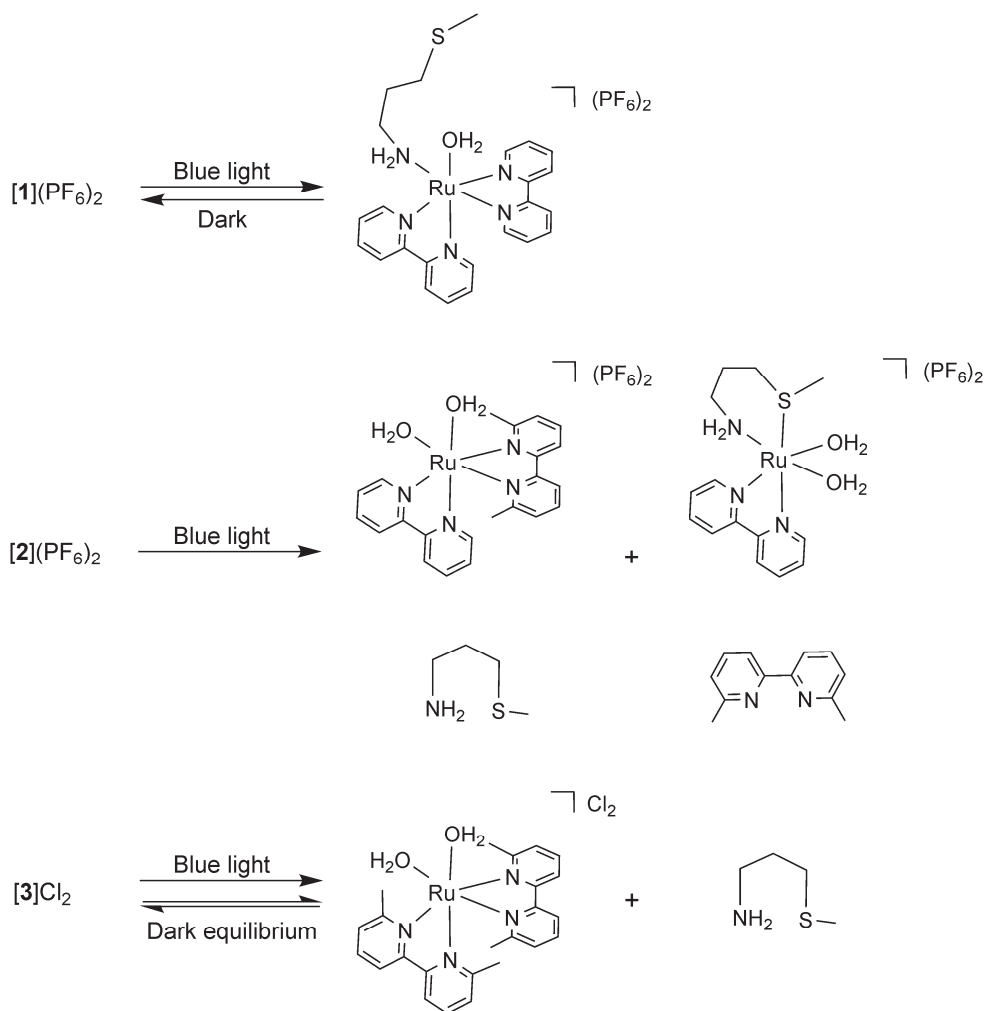


Figure 4.6. a) Evolution of the absorbance at 486 nm vs. time of a solution of  $[\mathbf{1}](\text{PF}_6)_2$  in water (0.099 mM) upon switching ON and OFF several times a source of blue light ( $\lambda_e = 445 \text{ nm}$ ,  $2.9 \cdot 10^{-8} \text{ mol} \cdot \text{s}^{-1}$ ) at 310 K under  $\text{N}_2$ . b) Evolution of the  $^1\text{H}$  NMR spectra (regions 10 – 9 ppm and 2 – 1 ppm) of a solution of  $[\mathbf{1}](\text{PF}_6)_2$  in  $\text{D}_2\text{O}$  (3.04 mM) irradiated with a Xe lamp for 40 min (ON) and then left in the dark for 30 days (OFF) at room temperature. The doublets at 9.79 and 9.24 ppm (circles) correspond to the  $\text{H}_6$  protons on the bpy for complex  $[\mathbf{1}]^{2+}$  and the arising doublets at 9.23 and 9.21 ppm (triangle) correspond to the  $\text{H}_6$  proton on the bpy for the monodentate-bound mtpa ligand in  $[\text{Ru}(\text{bpy})_2(\text{mtpa}-\kappa\text{N})(\text{OH}_2)_2]^{2+}$ . The singlet at 1.20 ppm (circles) corresponds to the methyl thioether group, and the arising singlet at 1.92 ppm (triangle) corresponds to the decoordinates thioether.

Finally, the photoreactivity of the moderately strained complex  $[\mathbf{2}](\text{PF}_6)_2$  was investigated by irradiating a solution of  $[\mathbf{2}](\text{PF}_6)_2$  in water with a 445 nm LED. UV-vis spectra showed a bathochromic shift of the absorption maximum from 464 nm to 492 nm, without any clear isosbestic point in the MLCT region (Figure 4.5b). Mass spectra after completion of the photoreaction showed peaks at  $m/z = 261.9$  and  $222.5$ , corresponding to  $[\text{Ru}(\text{bpy})(\text{dmbpy})(\text{CH}_3\text{CN})_2]^{2+}$  (calcd  $m/z = 262.1$ ) and  $[\text{Ru}(\text{bpy})(\text{mtpa})(\text{CH}_3\text{CN})_2]^{2+}$  (calcd  $m/z = 222.5$ , Figure AV.7), respectively, which means that both dmbpy and mtpa ligands are photosubstituted in two parallel

photoreactions. The CH<sub>3</sub>CN molecules come from the eluent used for the mass spectrometry as irradiation was performed in water. To confirm that photosubstitution of both mtpa and dmbpy occurred, white light irradiation of a solution of [2](PF<sub>6</sub>)<sub>2</sub> in D<sub>2</sub>O was monitored by <sup>1</sup>H NMR. As shown in Figure AV.4, after 60 min the doublet of the starting complex at 9.57 ppm completely vanished, while three new doublets appeared in the 9.00 – 10.00 ppm range, at 9.72, 9.38, and 9.21 ppm in a 1:1:0.5 ratio. This result indicates that [2](PF<sub>6</sub>)<sub>2</sub> was fully converted into two new species, as the doublets at 9.72 and 9.38 ppm belong to the same species. In addition to these two new species, the signals of free dmbpy (7.86, 7.74, and 7.37 ppm) and free mtpa (singlet at 2.10 ppm) were also found, thus confirming the competing photosubstitution of both dmbpy and mtpa. Although parallel photosubstitution of two distinct ligands has not been described very often, it has been observed recently in our group in a similar complex, [Ru(bpy)(dmbpy)(L-proline)]PF<sub>6</sub> (Chapter 2).<sup>9</sup> These results highlight that methylated ligands are not always the ones that are photosubstituted, and that the selectivity of photosubstitution reactions is the result of a delicate interplay between the energies and shapes of the excited state hypersurfaces that is difficult to predict.



Scheme 4.2. Photoreaction and thermal equilibria in aqueous solutions of [1](PF<sub>6</sub>)<sub>2</sub>, [2](PF<sub>6</sub>)<sub>2</sub>, and [3]Cl<sub>2</sub>.

#### 4.2.5 Cytotoxicity assays

The cytotoxicity of compounds [1](PF<sub>6</sub>)<sub>2</sub>, [2](PF<sub>6</sub>)<sub>2</sub>, [3](PF<sub>6</sub>)<sub>2</sub>, and of the ligand mtpa was tested against lung cancer cells (A549) following a protocol detailed by Hopkins *et al.*<sup>20</sup> In short, cells were seeded and incubated for 6 h and then treated per triplicate with six different concentrations of the ligand or complexes in two identical plates. After 24 h incubation with the compounds, one of the plates was irradiated with blue light (454 nm), using a light dose of 6.3 J·cm<sup>-2</sup>, whereas the other plate was kept in the dark. Both plates were further incubated for another 48 h without refreshing the media, and a sulforhodamine assay was performed at t = 96 h. By comparing the cell viability

of treated *vs.* non-treated wells the effective concentrations ( $EC_{50}$ ), *i.e.* the compound concentration needed to decrease the cell survival to 50% compared to non-treated control, was determined for each compound. Before performing cytotoxicity assays, we first verified that a light dose of  $6.3 \text{ J}\cdot\text{cm}^{-2}$  was *i)* enough to activate all three ruthenium compounds at the highest concentration used in the assays ( $86 \mu\text{M}$  solution) and under exactly the same conditions (Figure AV.9), and *ii)* non-toxic to A549 cells.<sup>20</sup> The  $EC_{50}$  values in the dark and upon light irradiation are given in Table 4.3.

The free ligand mtpa showed no significant cytotoxicity below  $100 \mu\text{M}$  (Figure AV.10), thus any biological activity of the complexes should be attributed to the metal-containing photoproduct (see Chapter 3). As shown in Figure 4.7a, no significant decrease in the cell population was observed after treatment with complex [1]( $\text{PF}_6$ )<sub>2</sub> both in the dark and after blue light irradiation. On the other hand, complex [3]( $\text{PF}_6$ )<sub>2</sub> showed similar cell viability curves and  $EC_{50}$  values in the dark and upon light activation, *i.e.*  $51.8$  and  $43.4 \mu\text{M}$ , respectively, corresponding to a negligible photo index (PI), *i.e.* the ratio of the  $EC_{50}$  value obtained in a dark control and that after light irradiation, of 1.2. Most importantly, use of compound [2]( $\text{PF}_6$ )<sub>2</sub> resulted in a decrease of the  $EC_{50}$  value from  $110 \mu\text{M}$  in the dark to  $13.8 \mu\text{M}$  after light activation, corresponding to a PI of 8.

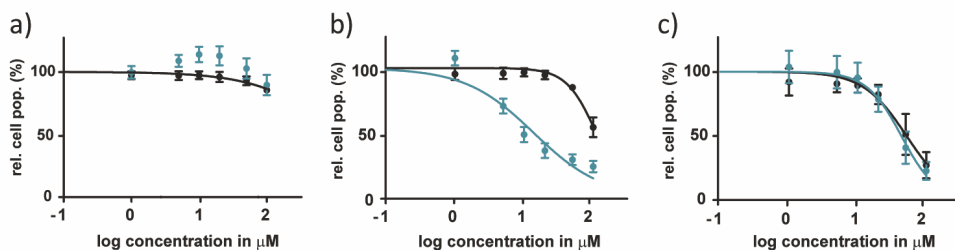


Figure 4.7. Dose-response curves for A549 cells in presence of a) [1]( $\text{PF}_6$ )<sub>2</sub>, b) [2]( $\text{PF}_6$ )<sub>2</sub>, or c) [3]( $\text{PF}_6$ )<sub>2</sub> irradiated with blue light ( $454 \text{ nm}$ ,  $6.35 \text{ J}\cdot\text{cm}^{-2}$ ) 6 h after treatment (blue data points) or left in the dark (black data points). Phototoxicity assay outline: cells seeded at  $5\cdot 10^3$  cells/well at  $t = 0 \text{ h}$ , treated with [1]( $\text{PF}_6$ )<sub>2</sub>, [2]( $\text{PF}_6$ )<sub>2</sub>, or [3]( $\text{PF}_6$ )<sub>2</sub> at  $t = 24 \text{ h}$ , irradiated at  $t = 30 \text{ h}$ , and SRB cell-counting assay performed at  $t = 96 \text{ h}$ . Incubation conditions:  $37 \text{ }^\circ\text{C}$  and  $7.0\% \text{ CO}_2$ .

Table 4.3. (Photo)cytotoxicity ( $EC_{50}$  with confidence interval (CI) (95%) in  $\mu\text{M}$ ) of [1](PF<sub>6</sub>)<sub>2</sub>, [2](PF<sub>6</sub>)<sub>2</sub>, [3](PF<sub>6</sub>)<sub>2</sub>, and mtpa on A549 cells, and photo indices (PI) defined as  $EC_{50}$  dark/ $EC_{50}$  light.

	[1](PF <sub>6</sub> ) <sub>2</sub>	CI (95%)	[2](PF <sub>6</sub> ) <sub>2</sub>	CI (95%)	[3](PF <sub>6</sub> ) <sub>2</sub>	CI (95%)	mtpa	CI (95%)
<b>EC<sub>50</sub> dark</b> ( $\mu\text{M}$ )	>150	-	110	+15	51.8	+12.2	>150	-
		-		-13		-9.9		-
<b>EC<sub>50</sub> light</b> ( $\mu\text{M}$ )	>150	-	13.8	+4.6	43.5	+9.2	>150	-
		-		-3.4		-7.6		-
<b>PI</b>	-		8.0		1.2		-	

### 4.3 Discussion

While many polypyridyl ruthenium complexes bearing a thioether-based ligand have been reported, to our knowledge only few publications pay attention to the stereoselectivity of the binding of the sulfur atom. For example, Sauvage *et al.* reported on the synthesis of [Ru(phen)<sub>2</sub>(Ph-S-(CH<sub>2</sub>)<sub>n</sub>-S-Ph)](PF<sub>6</sub>)<sub>2</sub> (where phen = 1,10-phenanthroline, Ph = phenyl, and n = 2 or 3), for which the single diastereoisomer  $\Lambda$ -R,R/ $\Delta$ -S,S is formed and suggested that the reason of this stereoselectivity was the  $\pi$ - $\pi$  interactions between the phenyl group and the phen ligand, which stabilize the structure.<sup>21</sup> A deeper study from Connick *et al.* suggested that this configuration was also favored by the reduced steric repulsion between the phenyl groups and the H <sub>$\alpha$</sub>  atoms of the polypyridyl ligands compared to the other possible configurations.<sup>22</sup> Thus, interligand interactions are crucial in determining the configuration of the sulfur. However, Tresoldi *et al.* consider the isomers of [Ru(bpy)<sub>2</sub>(2-mpps)]<sup>2+</sup> (2-mpps = 2-methylpyridyl pyridyl sulfide) resulting from the inversion of the chiral coordinated sulfur as invertomers.<sup>23</sup> According to this group, fast inversion occurs at room temperature, making the distinction of the invertomers by <sup>1</sup>H NMR impossible since only a single set of broad peaks is visible, while in some cases the inversion becomes slower at lower temperatures and the NMR peaks split.<sup>23-24</sup> This second option can be discarded for [1](PF<sub>6</sub>)<sub>2</sub>, as no significant change in the NMR peaks was observed between 193 K and 333 K.

Overall, our data suggest that activation of the mtpa-based complexes via thermal- or light-induced substitution of one of the bidentate ligands by two water molecules is the key factor leading to cytotoxicity. According to spectroscopic studies [1](PF<sub>6</sub>)<sub>2</sub> is indeed not fully “activated” upon light irradiation, as only the thioether part of the mtpa

ligand is substituted by one water molecule, without formation of the bis-aqua complex. This result, together with the probable low cellular uptake of complexes of that kind,<sup>8</sup> may explain the absence of cytotoxicity after light activation. On the other hand, **[3]**(PF<sub>6</sub>)<sub>2</sub> shows similar cytotoxicity in the dark and upon light irradiation because formation of the bis-aqua complex by substitution of mtpa occurs already in the dark. In other terms, it is too strained to be thermally stable, which prevents light activation by photosubstitution to be efficient. However, a greater difference in EC<sub>50</sub> values between dark and irradiated conditions may be expected because the thermal equilibrium between **[3]**(PF<sub>6</sub>)<sub>2</sub> and the bis-aqua complex is shifted towards the bis-aqua complex by light. Considering the dynamics of speciation in a cell, the different modes by which the drug may be taken up, and the different localization of the prodrug and of the activated drug, it is difficult to claim that equilibrium shifts observed in a simple water solution can replicate in a cell and explain minute cytotoxicity differences between dark and irradiated conditions. However, it is clear that the compound with intermediate steric hindrance and intermediate lipophilicity, *i.e.* **[2]**(PF<sub>6</sub>)<sub>2</sub>, shows at the same time a significant PI, a high thermal stability compared to **[3]**(PF<sub>6</sub>)<sub>2</sub>, and a better photoreactivity compared to **[1]**(PF<sub>6</sub>)<sub>2</sub>. This complex seems thus to be the optimal trade-off between stability and photoreactivity in this family of complexes.

#### 4.4 Conclusions

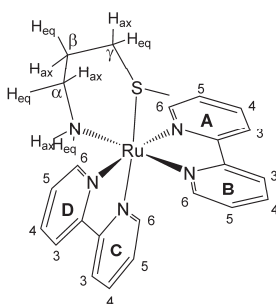
In this work, we have successfully synthesized a series of complexes bearing the non-toxic thioether mtpa ligand as caging ligand for the bis-aqua species. However, mtpa is a prochiral and dissymmetric ligand, which potentially generates many isomers once coordinated to a ruthenium center. The characterization of the isomer(s) effectively obtained in solution required a combination of crystallography, NOESY spectroscopy, and DFT calculations. In addition, while the non-strained complex **[1]**<sup>2+</sup> is not capable of fully releasing mtpa, the more strained complexes **[2]**<sup>2+</sup> and **[3]**<sup>2+</sup>, like dmbpy-based analogues, show efficient mtpa photosubstitution upon blue light irradiation, which in the mildly strained compound **[2]**(PF<sub>6</sub>)<sub>2</sub> leads to effective light activation in cancer cells. However, when fine-tuning steric hindrance and introducing two different “spectator” bipyridyl ligands, we have lost the selectivity of the photosubstitution reaction in **[2]**(PF<sub>6</sub>)<sub>2</sub>, as both dmbpy and mtpa are substituted by water molecules. Thus, we cannot attribute the enhanced photocytotoxicity of **[2]**(PF<sub>6</sub>)<sub>2</sub> solely to the photochemically generated *cis*-[Ru(bpy)(dmbpy)(OH<sub>2</sub>)<sub>2</sub>]<sup>2+</sup> species, because dmbpy is also toxic (see Chapter 3), and because *cis*-[Ru(bpy)(mtpa)(OH<sub>2</sub>)<sub>2</sub>]<sup>2+</sup> is photoreleased as well, the biological properties of which are unknown. Overall, adding methyl groups

in hindering position on the bipyridine ligands does allow for fine-tuning the lipophilicity and photoreactivity of light-activated ruthenium anticancer complexes, but achieving selective substitution of a non-toxic ligand to study the biological properties of a single metal-based photoproduct remains a chemical challenge.

## 4.5 Experimental

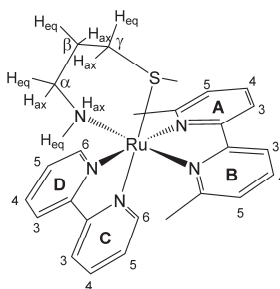
### 4.5.1 Synthesis

**General:** The ligands 2,2'-bipyridine (bpy), 6,6'-dimethyl-2,2'-bipyridine (dmbpy), and 3-(methylthio)propylamine (mtpa) were purchased from Sigma-Aldrich, as well as *cis*-bis(2,2'-bipyridine)dichlororuthenium(II) hydrate (*cis*-[Ru(bpy)<sub>2</sub>Cl<sub>2</sub>]). Silver nitrate (AgNO<sub>3</sub>) and potassium hexafluoridophosphate (KPF<sub>6</sub>) were purchased from Alfa-Aesar. Triethylamine (Et<sub>3</sub>N) was purchased from Merck. All reactants and solvents were used without further purification. The syntheses of *cis*-[Ru(dmbpy)<sub>2</sub>Cl<sub>2</sub>], *rac*-[Ru(bpy)(dmbpy)<sub>2</sub>](PF<sub>6</sub>)<sub>2</sub> (**[5]**(PF<sub>6</sub>)<sub>2</sub>), and *rac*-[Ru(bpy)(dmbpy)(CH<sub>3</sub>CN)<sub>2</sub>](PF<sub>6</sub>)<sub>2</sub> (**[4]**(PF<sub>6</sub>)<sub>2</sub>) were carried out according to literature procedures.<sup>9, 25</sup> Sephadex LH-20 was used for the Size Exclusion Column (SEC) chromatography. Electrospray mass spectra (ES MS) were recorded by using a Thermoquest Finnagen AQA Spectrometer and a MSQ Plus Spectrometer. All <sup>1</sup>H NMR spectra were recorded on a Bruker DPX-300 or DMX-400 spectrometers. Chemical shifts are indicated in ppm relative to the residual solvent peak.



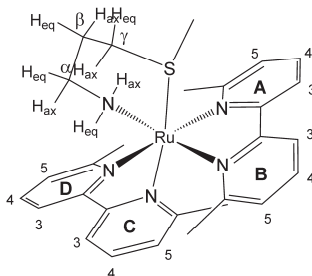
**[Ru(bpy)<sub>2</sub>(mtpa)](PF<sub>6</sub>)<sub>2</sub> (**[1]**(PF<sub>6</sub>)<sub>2</sub>). *cis*-[Ru(bpy)<sub>2</sub>Cl<sub>2</sub>] (49 mg, 0.10 mmol) and AgNO<sub>3</sub> (37 mg, 0.21 mmol) were added to deaerated water (10 mL) and stirred at 90 °C for 30 min. After the solution was filtered to remove the grey solid formed (AgCl), Et<sub>3</sub>N (17 μL, 0.12 mmol) and mtpa (14 μL, 0.12 mmol) were added to the filtrate, which was stirred at 90 °C for 1 h under Ar. Then, after addition of saturated KPF<sub>6</sub> aqueous solution an orange precipitate was obtained. After filtration, the product was purified by SEC chromatography using CH<sub>3</sub>OH as eluent. The main orange fraction**

was collected and, after solvent evaporation, an orange solid was obtained. Yield: 40 mg (50%). Two isomers in a ratio 1:0.05.  $^1\text{H}$  NMR of the major isomer ( $\Delta$ -(*S*),  $\Delta$ -(*R*))-**[1]**(PF<sub>6</sub>)<sub>2</sub> (400 MHz, D<sub>2</sub>O)  $\delta$  9.79 (d, *J* = 5.7 Hz, 1H, D6), 9.23 (d, *J* = 5.3 Hz, 1H, A6), 8.54 (m, 2H, A3 + D3), 8.41 (d, *J* = 8.2 Hz, 1H, C3), 8.35 (d, *J* = 8.2 Hz, 1H, B3), 8.25 (t, *J* = 8.0 Hz, 1H, A4), 8.20 (td, *J* = 7.9, 1.5 Hz, 1H, D4), 7.93 (td, *J* = 7.9, 1.6 Hz, 1H, C4), 7.89 – 7.80 (m, 3H, A5 + B4 + D5), 7.65 (d, *J* = 5.5 Hz, 1H, B6), 7.56 (d, *J* = 5.6 Hz, 1H, C6), 7.25 (ddd, *J* = 7.2, 5.6, 1.4 Hz, 1H, C5), 7.14 (ddd, *J* = 7.2, 5.6, 1.4 Hz, 1H, B5), 3.92 (d, *J* = 12.1 Hz, 1H, N<sub>eq</sub>), 3.17 – 2.92 (m, 3H,  $\gamma_{\text{eq}}$  + N<sub>ax</sub> +  $\alpha_{\text{ax}}$ ), 2.86 – 2.76 (m, 1H,  $\alpha_{\text{eq}}$ ), 2.53 (t, *J* = 11.7 Hz, 1H,  $\gamma_{\text{ax}}$ ), 2.28 – 2.15 (m, 1H,  $\beta_{\text{eq}}$ ), 1.79 – 1.66 (m, 1H,  $\beta_{\text{ax}}$ ), 1.19 (s, 3H, MeS-). High Resolution ES MS *m/z* (calcd): 259.55127 (259.55098, [**1**]<sup>2+</sup>), 664.06787 (664.0667, [**1** + PF<sub>6</sub>]<sup>+</sup>). Anal. Calcd for C<sub>29</sub>H<sub>32</sub>F<sub>6</sub>N<sub>5</sub>O<sub>2</sub>PRu: C, 35.65; H, 3.37; N, 8.66 Found: C, 35.67; H, 3.34; N, 8.64



**[Ru(bpy)(dmbpy)(mtpa)](PF<sub>6</sub>)<sub>2</sub>** (**[2]**(PF<sub>6</sub>)<sub>2</sub>). **[4]**(PF<sub>6</sub>)<sub>2</sub> (50 mg, 0.061 mmol), mtpa (13  $\mu\text{L}$ , 0.12 mmol), and Et<sub>3</sub>N (45  $\mu\text{L}$ , 0.32 mmol) were dissolved in deaerated water (5 mL) and refluxed under Ar for 2 h, after which the solvent was removed under reduced pressure by rotary evaporation at 40 °C. The crude reaction mixture was purified by an alumina chromatography column using a CH<sub>2</sub>Cl<sub>2</sub>/CH<sub>3</sub>OH mixture in a gradient 0 – 1% of CH<sub>3</sub>OH as eluent. The yellow (*R<sub>f</sub>* = 0.65) and orange (*R<sub>f</sub>* = 0.6) fractions were collected and the solvent was removed under reduced pressure by rotary evaporation at 40 °C. Yield: 32 mg (62%). Two isomers in a ratio 1:0.09.  $^1\text{H}$  NMR of the the major isomer ( $\Delta$ -(*R*),  $\Delta$ -(*S*))-**[2a]**(PF<sub>6</sub>)<sub>2</sub>  $^1\text{H}$  NMR (400 MHz, CD<sub>3</sub>OD)  $\delta$  9.55 (d, *J* = 5.4 Hz, 1H, D6), 8.71 (d, *J* = 7.8 Hz, 1H, D3), 8.65 (d, *J* = 8.1 Hz, 1H, C3), 8.45 (d, *J* = 7.8 Hz, 1H, A3), 8.29 (d, *J* = 7.9 Hz, 1H, B3), 8.25 (td, *J* = 7.9, 1.4 Hz, 1H, D4), 8.21 (d, *J* = 5.2 Hz, 1H, C6), 8.17 – 8.10 (m, 2H, A4 + C4), 7.86 – 7.80 (m, 2H, D5 + B4), 7.76 (dd, *J* = 7.8, 1.3 Hz, 1H, A5), 7.50 (ddd, *J* = 7.3, 5.7, 1.3 Hz, 1H, C5), 7.21 (dd, *J* = 7.8, 1.2 Hz, 1H, B5), 3.87 – 3.76 (m, 1H, N<sub>ax</sub>), 3.14 – 3.01 (m, 2H, N<sub>eq</sub> +  $\gamma_{\text{ax}}$ ), 2.92 (s, 3H, AMe), 2.67 – 2.57 (m, 1H,  $\alpha$ ), 2.53 – 2.43 (m, 1H,  $\gamma_{\text{eq}}$ ), 2.17 – 2.07 (m, 1H,  $\alpha$ ), 2.06 – 1.97 (m, 1H,  $\beta$ ), 1.96 – 1.87 (m, 1H,  $\beta$ ), 1.62 (s, 3H, BMe), 1.58 (s, 3H, MeS-).  $^{13}\text{C}$

NMR (101 MHz, CD<sub>3</sub>OD)  $\delta$  167.54, 167.01, 161.41, 161.35, 160.57, 159.71, 156.75, 155.03, 139.57, 139.28, 139.17, 138.75, 128.90, 128.39, 128.25, 127.87, 126.08, 125.46, 122.68, 122.46, 42.32, 35.25, 27.17, 26.48, 24.69, 17.74. High Resolution ES MS  $m/z$  (calcd): 273.56708 (273.56663, [2]<sup>2+</sup>), 692.09851 (692.09800, [2 + PF<sub>6</sub>]<sup>+</sup>). Anal. Calcd for C<sub>29</sub>H<sub>32</sub>F<sub>6</sub>N<sub>5</sub>O<sub>2</sub>PRu: C, 37.33; H, 3.73; N, 8.37 Found: C, 37.41; H, 3.87; N, 8.31



**[Ru(dmbpy)<sub>2</sub>(mtpa)](PF<sub>6</sub>)<sub>2</sub> ([3](PF<sub>6</sub>)<sub>2</sub>). *cis*-[Ru(dmbpy)<sub>2</sub>Cl<sub>2</sub>] (50 mg, 0.093 mmol) was dissolved in deaerated water (3 mL) and heated under Ar at 60 °C for 5 min, after which mtpa (17  $\mu$ L, 0.16 mmol) and Et<sub>3</sub>N (20  $\mu$ L, 0.14 mmol) were added to the reaction mixture and stirred at 60 °C for 45 min. Then, after addition of saturated KPF<sub>6</sub> aqueous solution (1 mL), a reddish precipitate was obtained. The suspension was filtered and washed with cold water (5 mL) and diethyl ether. Yield: 40 mg (50%). Two isomers in a ratio 1:0.12. <sup>1</sup>H NMR of the major isomer ( $\Lambda$ -(*S*),  $\Delta$ -(*R*))-ax-[3](PF<sub>6</sub>)<sub>2</sub> (400 MHz, CD<sub>3</sub>OD)  $\delta$  8.53 (d,  $J$  = 7.9 Hz, 1H, D3), 8.50 (d,  $J$  = 8.2 Hz, 1H, C3), 8.44 (m, 2H, A3 + B3), 8.12 (td,  $J$  = 7.9, 3.4 Hz, 1H, D4 + A4), 8.06 (t,  $J$  = 7.9 Hz, 1H, C4), 7.97 (t,  $J$  = 7.9 Hz, 1H, B4), 7.68 (td,  $J$  = 7.5, 1.3 Hz, 2H, A5 + D5), 7.45 (d,  $J$  = 7.8 Hz, 1H, C5), 7.41 (d,  $J$  = 7.8 Hz, 1H, B5), 3.26 – 3.18 (m, 1H), 2.83 (s, 3H, DMe), 2.75 – 2.68 (m, 1H,  $\gamma_{eq}$ ), 2.67 (s, 3H, AMe), 2.50 (d,  $J$  = 12.6 Hz, 1H), 2.44 – 2.33 (m, 1H,  $\gamma_{ax}$ ), 1.94 (s, 3H, BMe), 1.86 (s, 3H, CMe), 1.79 – 1.68 (m, 1H), 1.20 (s, 3H, MeS-), 0.33 (d,  $J$  = 12.0 Hz, 1H). <sup>13</sup>C NMR (101 MHz, acetone-d<sub>6</sub>)  $\delta$  168.21, 167.82, 167.35, 167.27, 161.13, 160.95, 160.34, 160.14, 139.16, 139.03, 138.91, 138.28, 128.15, 127.45, 127.32, 126.93, 124.33, 123.34, 123.04, 122.43, 41.93, 34.74, 26.39, 25.35, 24.60, 24.39, 23.38, 15.62. High Resolution ES MS  $m/z$  (calcd): 287.58243 (287.58228, [3]<sup>2+</sup>), 720.12781 (720.12930, [3 + PF<sub>6</sub>]<sup>+</sup>). Anal. Calcd for C<sub>29</sub>H<sub>32</sub>F<sub>6</sub>N<sub>5</sub>O<sub>2</sub>PRu: C, 38.89; H, 4.08; N, 8.10 Found: C, 38.02; H, 4.18; N, 7.64**

## 4.5.2 Photochemistry

**General:** For the irradiation experiments of NMR tubes, the light of a LOT 1000 W Xenon Arc lamp mounted with infrared and 400 nm long pass filters was used. When specified, a 450 nm 450FS10-50 from Andover Corporation filter was used. For NMR experiments under N<sub>2</sub>, NMR tubes with PTFE stopper were used. UV-vis experiments were performed on a Cary 50 Varian spectrometer. When monitoring photoreactions by UV-vis and mass spectrometry, a LED light source ( $\lambda_{\text{ex}} = 445 \text{ nm}$ , with a Full Width at Half Maximum of 14 nm, Part. No H2A1-H450, Roithner LaserTechnik, Vienna, Austria) with a light intensity between  $2.79 \cdot 10^{-8}$  and  $2.98 \cdot 10^{-8} \text{ mol} \cdot \text{s}^{-1}$  was used.

**Experiments monitored with <sup>1</sup>H NMR:** A stock solution in deuterated water of either [1](PF<sub>6</sub>)<sub>2</sub>, [2](PF<sub>6</sub>)<sub>2</sub>, or [3]Cl<sub>2</sub> was prepared and deaerated under N<sub>2</sub> (see Table 4.4 for the details). Then, 600  $\mu\text{L}$  of the stock solution were transferred, under N<sub>2</sub>, into a NMR tube. The tube was irradiated at room temperature with a LOT Xenon 1000 W lamp equipped with IR short pass and >400 nm long pass filters. In addition, a control experiment without white light irradiation was performed. The reactions were monitored with <sup>1</sup>H NMR at various time intervals.

Table 4.4. Conditions of the photoreactions of [1](PF<sub>6</sub>)<sub>2</sub>, [2](PF<sub>6</sub>)<sub>2</sub>, and [3]Cl<sub>2</sub> in D<sub>2</sub>O monitored with <sup>1</sup>H NMR.

Complex	w (mg)	V ( $\mu\text{L}$ )	Mw (g/mol)	Concentration (mM)
[1](PF <sub>6</sub> ) <sub>2</sub>	1.6	660	808.57	3.0
[2](PF <sub>6</sub> ) <sub>2</sub>	1.0	600	836.63	2.0
[3]Cl <sub>2</sub> <sup>a</sup>	1.0	600	645.65	2.6

<sup>a</sup> Complex [3](PF<sub>6</sub>)<sub>2</sub> was converted to [3]Cl<sub>2</sub> for solubility reasons by addition of Bu<sub>4</sub>NCl in acetone, followed by filtration and washing with cold acetone and diethyl ether.

**Irradiation experiments monitored with UV-vis and MS:** UV-vis spectroscopy was performed using a UV-vis spectrometer equipped with temperature control set to 25 or 37 °C and a magnetic stirrer. The irradiation experiments were performed in a quartz cuvette containing 3 mL of solution. A stock solution of the desired complex was prepared using demineralized water, which was then diluted in the cuvette to a working solution concentration. When the experiment was carried out under N<sub>2</sub> the sample was deaerated 15 min by gentle bubbling of N<sub>2</sub> and the atmosphere was kept inert during the experiment by a gentle flow of N<sub>2</sub> on top of the cuvette. A UV-vis spectrum was measured every 30 s for the first 10 min, every 1 min for the next 10 min, and eventually every 10 min until the end of the experiment. Data was analysed with Microsoft Excel. Experimental conditions are detailed in Table 4.5.

Table 4.5. Conditions of the photoreactions of [1](PF<sub>6</sub>)<sub>2</sub>, [2](PF<sub>6</sub>)<sub>2</sub>, and [3]Cl<sub>2</sub> in demineralized water monitored with MS and UV-vis.

Complex	Stock solution			Working solution (mM)	Photon flux 445 nm LED (mol·s <sup>-1</sup> )	Temperature (°C)
	w (mg)	V (mL)	M <sub>w</sub> (g/mol)			
[1](PF <sub>6</sub> ) <sub>2</sub>	2.4	10	808.57	0.297	2.95·10 <sup>-8</sup>	25
[2](PF <sub>6</sub> ) <sub>2</sub>	0.6	5	836.63	0.151	2.91·10 <sup>-8</sup>	37
[3]Cl <sub>2</sub> <sup>a</sup>	1.6	10	645.65	0.245	2.92·10 <sup>-8</sup>	25
					2.79·10 <sup>-8</sup>	25

<sup>a</sup> Complex [3](PF<sub>6</sub>)<sub>2</sub> was converted to [3]Cl<sub>2</sub> for solubility reasons by addition of Bu<sub>4</sub>NCl in acetone, followed by filtration and washing with cold acetone and diethyl ether.

**Blue light irradiation in the cell irradiation setup:** The photochemical reactivity of [1](PF<sub>6</sub>)<sub>2</sub>, [2](PF<sub>6</sub>)<sub>2</sub>, and [3](PF<sub>6</sub>)<sub>2</sub> in 96-well plates was measured using UV-vis spectroscopy. Solutions of each compound were prepared in OptiMEM complete (86 μM), transferred into a 96-well plate, and irradiated with blue light (454 nm) at different irradiation times using the blue LED source described in details in Hopkins *et al.* to mimic the conditions used in the photocytotoxicity assay.<sup>20</sup> Figure AV.9 shows that the three complexes are fully activated at 86 μM after 10 min irradiation. Thus, 10 min was chosen as the blue light irradiation time in the photocytotoxicity assay, which corresponded to a light dose of 6.3 J.cm<sup>-2</sup>.

### 4.5.3 Single Crystal X-Ray crystallography

**General:** All reflection intensities were measured at 110(2) K using a SuperNova diffractometer (equipped with Atlas detector) with Cu Kα radiation (λ = 1.54178 Å) or Mo Kα radiation (λ = 0.71073 Å) under the program CrysAlisPro (Version 1.171.36.32 Agilent Technologies, 2013). The same program was used to refine the cell dimensions and for data reduction. The structure was solved with the program SHELXS-2013 and was refined on F<sup>2</sup> with SHELXL-2013.<sup>26</sup> Analytical numeric absorption correction based on a multifaceted crystal model was applied using CrysAlisPro. The temperature of the data collection was controlled using the system Cryojet (manufactured by Oxford Instruments). The H atoms were placed at calculated positions (unless otherwise specified) using the instructions AFIX 23, AFIX 43, AFIX 137 or AFIX 147 with isotropic displacement parameters having values 1.2 U<sub>eq</sub> of the attached C or O atoms.

#### Complex [1](PF<sub>6</sub>)<sub>2</sub>·CH<sub>3</sub>OH

**Crystal growing:** [1](PF<sub>6</sub>)<sub>2</sub> (1.0 mg) was dissolved in CH<sub>3</sub>OH (1 mL, 1.2 mM) in a GC vial, which was placed in a larger vial that contained toluene (3 mL) as a counter

solvent. The large vial was stoppered. After a few days, quality crystals suitable for X-ray structure determination were obtained by vapour diffusion.

**Crystal structure determination:** The H atoms attached to N5 were found from difference Fourier maps, and their coordinates and isotropic temperature factors were refined freely.

**Details of the crystal structure:** The structure is mostly ordered. The lattice CH<sub>3</sub>OH solvent molecule is disordered over two orientations and the occupancy factor of the major component of the disorder refines to 0.70(2). Fw = 840.62, red block, 0.38 × 0.28 × 0.25 mm<sup>3</sup>, monoclinic, C2/c (no. 15), *a* = 12.5589(2), *b* = 14.0651(2), *c* = 36.3739(7), β = 98.5152(18)°, *V* = 6354.34(19) Å<sup>3</sup>, *Z* = 8, *D*<sub>x</sub> = 1.757 g cm<sup>-3</sup>, μ = 6.502 mm<sup>-1</sup>, *T*<sub>min</sub>–*T*<sub>max</sub>: 0.224–0.383. 20578 Reflections were measured up to a resolution of (sin θ/λ)<sub>max</sub> = 0.62 Å<sup>-1</sup>. 6232 Reflections were unique (*R*<sub>int</sub> = 0.0175), of which 6168 were observed [*I* > 2σ(*I*)]. 449 Parameters were refined using 37 restraints. *R*1/*wR*2 [*I* > 2σ(*I*)]: 0.0335/0.0811. *R*1/*wR*2 [all refl.]: 0.0339/0.0814. *S* = 1.147. Residual electron density found between –0.68 and 0.84 e Å<sup>-3</sup>.

### Complex [2a](PF<sub>6</sub>)<sub>2</sub>

**Crystal growing:** [2](PF<sub>6</sub>)<sub>2</sub> (1.0 mg) was dissolved in CH<sub>3</sub>OH (1 mL, 1.2 mM) in a GC vial, which was placed in a larger vial that contained ethyl acetate (3 mL) as a counter solvent. The large vial was stoppered. After few days, quality crystals suitable for X-ray structure determination were obtained by vapour diffusion.

**Crystal structure determination:** The H atoms attached to N5 were found from difference Fourier map, and their coordinates and isotropic temperature factors were refined freely. The structure is partly disordered.

**Details of the crystal structure:** One of the two PF<sub>6</sub><sup>-</sup> counter ions is disordered over 3 orientations. The occupancy factors of the three different orientation can be retrieved in the .cif file. Fw = 836.63, 0.24 × 0.21 × 0.07 mm<sup>3</sup>, orthorhombic, Pbc<sub>a</sub>, *a* = 9.17330(14), *b* = 18.2183(3), *c* = 36.9112(5), *V* = 6168.67(16) Å<sup>3</sup>, *Z* = 8, μ = 6.67 mm<sup>-1</sup>, *T*<sub>min</sub>–*T*<sub>max</sub>: 0.331–0.673. 36039 Reflections were measured up to a resolution of (sin θ/λ)<sub>max</sub> = 0.616 Å<sup>-1</sup>. 6052 Reflections were unique (*R*<sub>int</sub> = 0.039), of which 5360 were observed [*I* > 2σ(*I*)]. 552 Parameters were refined using 619 restraints. *R*[*F*<sup>2</sup> > 2σ(*F*<sup>2</sup>)]: 0.028. *wR*(*F*<sup>2</sup>): 0.067. *S* = 1.04. Residual electron density found between –0.58 and 0.56 e Å<sup>-3</sup>.

### Complex [3](PF<sub>6</sub>)<sub>2</sub>

**Crystal growing:** [3](PF<sub>6</sub>)<sub>2</sub> (1.0 mg) was dissolved in CH<sub>3</sub>OH (1 mL, 1.2 mM) in a GC vial, which was placed in a larger vial that contained di-*tert*-butyl ether (3 mL) as a counter solvent. The large vial was stoppered. After few days, quality crystals suitable for X-ray structure determination were obtained by vapour diffusion.

**Crystal structure determination:** The structure is partly disordered.

**Details of the crystal structure:** One of the two PF<sub>6</sub><sup>-</sup> counterions is found to be disordered over three orientations, and the occupancy factors of the three components refine to 0.732(3), 0.180(3) and 0.088(3). Fw = 864.68, 0.21 × 0.16 × 0.05 mm<sup>3</sup>, triclinic, P-1, *a* = 10.6739(3), *b* = 11.7852(3), *c* = 14.2773(4), *V* = 1662.91(8) Å<sup>3</sup>, *Z* = 2,  $\mu = 0.73 \text{ mm}^{-1}$ , *T*<sub>min</sub>–*T*<sub>max</sub>: 0.661–1.000. 25022 Reflections were measured up to a resolution of  $(\sin \theta/\lambda)_{\text{max}} = 0.650 \text{ \AA}^{-1}$ . 7639 Reflections were unique (*R*<sub>int</sub> = 0.038), of which 6580 were observed [*I* > 2σ(*I*)]. 564 Parameters were refined using 253 restraints. *R* [*F*<sup>2</sup> > 2σ(*F*<sup>2</sup>)]: 0.035. *wR* (*F*<sup>2</sup>): 0.078. *S* = 1.03. Residual electron density found between –0.52 and 1.14 e Å<sup>-3</sup>.

#### 4.5.4 DFT calculations

Electronic structure calculations were performed using DFT as implemented in the ADF program (SCM). The structures of all possible isomers of [1]<sup>2+</sup>, [2a]<sup>2+</sup>, [2b]<sup>2+</sup>, and [3]<sup>2+</sup> were optimized in water using the conductor-like screening model (COSMO) to simulate the effect of solvent. The PBE0 [31] functional and a triple zeta potential basis set (TZP) were used for all calculations.

#### 4.5.5 Cell culture and EC50 (photo)cytotoxicity assay

Following the protocol described in Appendix II, A549 cells were seeded at *t* = 0 h, and 24 h after aliquots (100 μL) of six different concentrations (1 – 100 μM for all the compounds) of freshly prepared stock solutions of [1](PF<sub>6</sub>)<sub>2</sub>, [2](PF<sub>6</sub>)<sub>2</sub>, [3](PF<sub>6</sub>)<sub>2</sub>, or mtpa in OptiMEM were added. Plates were incubated in the dark for an additional 6 h. After this period, half of the plates were irradiated for 10 min with blue light ( $\lambda = 454 \pm 11 \text{ nm}$ , power density =  $10.5 \pm 0.7 \text{ mW cm}^{-2}$ , irradiation time = 10 min, light dose =  $6.5 \text{ J cm}^{-2}$ ) and the other half were kept in the dark. After irradiation, all the plates were incubated for an additional 66 h (making a total assay of 96 h).

## 4.6 References

1. G. Shi, S. Monro, R. Hennigar, J. Colpitts, J. Fong, K. Kasimova, H. Yin, R. DeCoste, C. Spencer, L. Chamberlain, A. Mandel, L. Lilge and S. A. McFarland, *Coord. Chem. Rev.*, **2015**, 282–283, 127-138.
2. H. Huang, B. Yu, P. Zhang, J. Huang, Y. Chen, G. Gasser, L. Ji and H. Chao, *Angew. Chem., Int. Ed.*, **2015**, 54, 14049-14052.
3. V. Pierroz, R. Rubbiani, C. Gentili, M. Patra, C. Mari, G. Gasser and S. Ferrari, *Chem. Sci.*, **2016**, 7, 6115-6124.
4. E. Wachter, D. K. Heidary, B. S. Howerton, S. Parkin and E. C. Glazer, *Chem. Commun.*, **2012**, 48, 9649-9651.
5. R. N. Garner, J. C. Gallucci, K. R. Dunbar and C. Turro, *Inorg. Chem.*, **2011**, 50, 9213-9215.
6. B. S. Howerton, D. K. Heidary and E. C. Glazer, *J. Am. Chem. Soc.*, **2012**, 134, 8324-8327.
7. T. Sainuddin, M. Pinto, H. Yin, M. Hetu, J. Colpitts and S. A. McFarland, *J. Inorg. Biochem.*, **2016**, 158, 45-54.
8. J. A. Cuello-Garibo, M. S. Meijer and S. Bonnet, *Chem. Commun.*, **2017**, 53, 6768-6771.
9. J.-A. Cuello-Garibo, E. Pérez-Gallent, L. van der Boon, M. A. Siegler and S. Bonnet, *Inorg. Chem.*, **2017**, 56, 4818-4828.
10. R. E. Goldbach, I. Rodriguez-Garcia, J. H. van Lenthe, M. A. Siegler and S. Bonnet, *Chem. - Eur. J.*, **2011**, 17, 9924-9929.
11. A. Bahreman, B. Limburg, M. A. Siegler, E. Bouwman and S. Bonnet, *Inorg. Chem.*, **2013**, 52, 9456-9469.
12. R. N. Garner, L. E. Joyce and C. Turro, *Inorg. Chem.*, **2011**, 50, 4384-4391.
13. M. E. Fleet, *Mineral. Mag.*, **1976**, 40, 531-533.
14. V. H. S. van Rixel, B. Siewert, S. L. Hopkins, S. H. C. Askes, A. Busemann, M. A. Siegler and S. Bonnet, *Chem. Sci.*, **2016**.
15. O. Filevich, M. Salierno and R. Etchenique, *J. Inorg. Biochem.*, **2010**, 104, 1248-1251.
16. R. Arakawa, S. Tachiyashiki and T. Matsuo, *Anal. Chem.*, **1995**, 67, 4133-4138.
17. L. Zayat, O. Filevich, L. M. Baraldo and R. Etchenique, *Philos. Trans. R. Soc., A*, **2013**, 371.
18. S. Tachiyashiki and K. Mizumachi, *Coord. Chem. Rev.*, **1994**, 132, 113-120.
19. A. Bahreman, B. Limburg, M. A. Siegler, R. Koning, A. J. Koster and S. Bonnet, *Chem. - Eur. J.*, **2012**, 18, 10271-10280.
20. S. L. Hopkins, B. Siewert, S. H. C. Askes, P. Veldhuizen, R. Zwier, M. Heger and S. Bonnet, *Photochem. Photobiol. Sci.*, **2016**, 15, 644-653.
21. J. P. Collin, D. Jouvenot, M. Koizumi and J. P. Sauvage, *Inorg. Chim. Acta*, **2007**, 360, 923-930.
22. N. A. F. Al-Rawashdeh, S. Chatterjee, J. A. Krause and W. B. Connick, *Inorg. Chem.*, **2014**, 53, 294-307.
23. G. Tresoldi, L. Baradello, S. Lanza and P. Cardiano, *Eur. J. Inorg. Chem.*, **2005**, 2005, 2423-2435.
24. G. Tresoldi, S. Lo Schiavo, S. Lanza and P. Cardiano, *Eur. J. Inorg. Chem.*, **2002**, 2002, 181-191.
25. J. P. Collin and J. P. Sauvage, *Inorg. Chem.*, **1986**, 25, 135-141.
26. G. M. Sheldrick, *Acta Crystallogr., Sect. A: Found. Adv.*, **2008**, 64, 112-122.



# 5

## Tuning the stereoselectivity, photoreactivity, and redox potential of cycloruthenated complexes by small changes in the N,S ligand

*Cycloruthenated complexes may have more potential as anti-cancer agents than their non-cyclometalated analogues due to favorable charge, lipophilicity, and electrochemical properties. Their general red shift in the absorption spectrum makes them promising complexes for Photoactivated Chemotherapy (PACT). However, cycloruthenated complexes usually do not substitute a ligand upon light irradiation. In this chapter, we report the synthesis and photochemistry of four cyclometalated ruthenium complexes having the formula  $[Ru(bpy)(phpy)(L)]PF_6$  ( $bpy = 2,2'$ -bipyridine and  $phpy = 2$ -phenylpyridine) in which  $L$  is either 3-(methylthio)propylamine ( $mtpa$ ,  $[2]PF_6$ ), 2-(methylthio)ethylamine ( $mtea$ ,  $[3]PF_6$ ), 2-(methylthio)ethyl-2-pyridine ( $mtep$ ,  $[4]PF_6$ ), or 2-(methylthio)methylpyridine ( $mtmp$ ,  $[5]PF_6$ ). We show that the stereoselectivity of the synthesis, the photoreactivity, and the electrochemical properties depend critically on the size of the N,S chelating ring and the nature of the nitrogen ligand – primary amine vs. pyridine.*

This chapter is to be submitted as a full paper: J. A. Cuello-Garibo, C. James, S. L. Hopkins, M. A. Siegler, S. Bonnet, *in preparation*.

## 5.1 Introduction

Cyclometalated complexes are complexes containing a metallacycle in which at least one of the donor atoms in the first coordination sphere is either an  $sp^2$  or an  $sp^3$  carbon. In the last two decades cycloruthenated complexes have been intensively studied for Grätzel-type dye-sensitized solar cells (DSSCs) and for anticancer therapy.<sup>1-3</sup> In the latter, they show, in general, higher cytotoxicity *in vitro* compared to their non-cyclometalated analogues.<sup>3-4</sup> This higher cytotoxicity may be due to the higher lipophilicity of the complexes, which allows a higher cellular uptake, and a lower  $Ru^{III/II}$  redox potential, which causes interactions with proteins such as oxido-reductase enzymes.<sup>5</sup> These advantages, together with their ability to generate reactive oxygen species (ROS) upon light irradiation, make them good candidates for Photodynamic Therapy (PDT).<sup>6</sup> Furthermore, the destabilization of the  $t_{2g}$  orbitals of the ruthenium(II) center due to the strong  $\pi$ -donor character of the metal-bound carbon atom in, for example, the chelate 2-phenylpyridine (phpy<sup>-</sup>), shifts the metal-to-ligand charge transfer (<sup>1</sup>MLCT) absorption band to lower energies compared to non-cyclometalated analogues.<sup>2</sup> This property is particularly relevant in the phototherapy field, in which photoactive complexes should absorb light, if possible, in the phototherapeutic window (700 – 1000 nm) which penetrates deep enough in biological tissues. However, in the field of Photoactivated Chemotherapy (PACT), an oxygen-independent therapy that relies on the activation of a prodrug by exchange of one or more of the ligands upon light irradiation, the impact of cycloruthenated complexes in the literature is still scarce due to their often limited photoreactivity. Destabilization of the  $e_g$  orbitals of the ruthenium(II) center compared to non-cyclometalated analogues increases the gap between the  $\pi^*$  orbital of the ligand and the  $e_g$  orbital and thus makes the thermal population of the <sup>3</sup>MC excited state from the <sup>3</sup>MLCT more difficult,<sup>7-8</sup> which is at the basis of ligand photosubstitution reactions in octahedral  $d^6$  metal complexes.<sup>9-11</sup> In non-cyclometalated complexes a common strategy to enhance photoreactivity is to lower the energy of the <sup>3</sup>MC by using hindering polypyridyl ligands and increasing the octahedral distortion.<sup>12-13</sup> However, this strategy proved not to be useful in the case of  $[Ru(biq)_2(phpy)]PF_6$  (biq = 2,2'-biquinoline), as this complex is neither photoreactive in  $CH_3CN$  nor in water upon green light irradiation.<sup>14</sup> To date, only a few cyclometalated ruthenium compounds have been reported that release one of the ligands upon light irradiation. One of the first examples of a light-activatable cyclometalated ruthenium complex, discovered by Pfeffer *et al.*<sup>3</sup> and later studied more in detail by Turro *et al.*, is  $[Ru(phen)(phpy)(CH_3CN)_2]PF_6$  (phen = 1,10-phenanthroline, [**1a**] $PF_6$ ), which photosubstitutes one  $CH_3CN$  by a  $Cl^-$  in  $CH_2Cl_2$  in

the presence of 2 mM of TBACl. When OVCAR-5 cells were treated with this complex, EC<sub>50</sub> values of 1 μM and 70 nM were found in the dark and upon light irradiation, respectively, with a photo index (PI) of 14.<sup>15</sup>

In Chapter 3 we demonstrated that upon light irradiation polypyridyl complexes such as [Ru(bpy)<sub>2</sub>(mtmp)]<sup>2+</sup> (bpy = 2,2'-bipyridine; mtmp = 2-(methylthio)methylpyridine) or [Ru(Ph<sub>2</sub>phen)<sub>2</sub>(mtmp)]<sup>2+</sup> (Ph<sub>2</sub>phen = 4,7-diphenyl-1,10-phenanthroline) will substitute the non-cytotoxic N,S ligand mtmp by two water molecules. While complexes bearing two bpy ligands generally did not show any cytotoxicity against lung cancer cells (A549 cells) due to their high hydrophilicity and low cellular uptake, complexes with two Ph<sub>2</sub>phen ligands showed low EC<sub>50</sub> values after irradiation, but were already toxic in the dark (EC<sub>50</sub> = 2.7 μM), probably due to their high lipophilicity.<sup>16</sup> These results led us to wonder whether it would be possible to synthesize a photoactivatable cyclometalated complex that, upon light irradiation, photosubstitutes a bidentate N,S chelate such as mtmp. In this chapter, we report the synthesis and properties of four cyclometalated complexes having the formula [Ru(bpy)(phpy)(L)]PF<sub>6</sub>, in which L is either 3-(methylthio)propylamine (mtpa, [2]PF<sub>6</sub>), 2-(methylthio)ethylamine (mtea, [3]PF<sub>6</sub>), 2-(methylthio)ethyl-2-pyridine (mtep, [4]PF<sub>6</sub>), or mtmp ([5]PF<sub>6</sub>). In particular, the stereoselectivity of the synthesis and the photoreactivity were found to depend critically on both the size of the the N,S chelate ring and the nature of the nitrogen ligand – primary amine vs. pyridine.

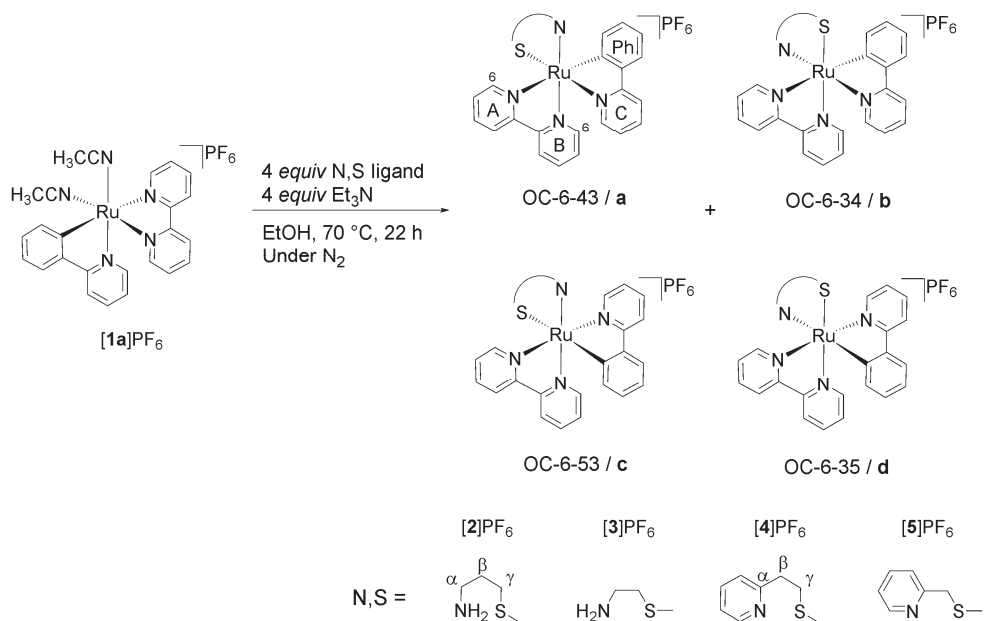
## 5.2 Results

### 5.2.1 Stereoselectivity of the synthesis

The four cycloruthenated complexes [2]PF<sub>6</sub> – [5]PF<sub>6</sub> were prepared as shown in Scheme 5.1, following the synthetic route established by the group of Michel Pfeiffer.<sup>17-18</sup> The dimer [(η<sup>6</sup>-C<sub>6</sub>H<sub>6</sub>)RuCl(μ-Cl)]<sub>2</sub> was heated in CH<sub>3</sub>CN at 45 °C together with NaOH, KPF<sub>6</sub>, and Hphpy to yield the cycloruthenated complex [Ru(phpy)(CH<sub>3</sub>CN)<sub>4</sub>]PF<sub>6</sub>. After purification by column chromatography on alumina using CH<sub>2</sub>Cl<sub>2</sub> as eluent, the complex was further reacted with 0.8 equiv of bpy in CH<sub>2</sub>Cl<sub>2</sub> at room temperature for 20 h to obtain *cis*-[Ru(bpy)(phpy)(CH<sub>3</sub>CN)<sub>2</sub>]PF<sub>6</sub> ([1a]PF<sub>6</sub>), with the carbon donor atom *trans* to bpy. Achieving the controlled coordination of only one equivalent of bpy is not straightforward, as formation of [Ru(bpy)<sub>2</sub>(phpy)]PF<sub>6</sub> easily occurs in this reaction. To avoid formation of this product, only 0.8 equiv of bpy was added to the reaction mixture. As shown by Ryabov *et al.* only the isomer having the σ-bound C atom *trans* to bpy ([1a]PF<sub>6</sub>) was obtained.<sup>19</sup>

Coordination of the third ligand (*i.e.* mtpa, mtea, mtep, or mtmp) was performed under identical conditions, which consisted in heating the precursor [**1a**]PF<sub>6</sub> at 70 °C in EtOH in presence of *ca.* 4 equiv of the N,S ligand and 4 equiv of Et<sub>3</sub>N (to ensure coordination of the amine of the N,S ligand) for 22 h under Ar. After crystallization by vapour diffusion of diethyl ether into the crude mixture, yields between 44% and 58% were obtained for complexes [**2**]PF<sub>6</sub>, [**3**]PF<sub>6</sub>, [**4**]PF<sub>6</sub>, and [**5**]PF<sub>6</sub>. Interestingly, synthesis of complexes [**2**]PF<sub>6</sub> and [**3**]PF<sub>6</sub> was attempted several times since in many occasions a dark green solid was obtained, which is believed to be an oxidized ruthenium(III) species. This did not happen when synthesizing complexes [**4**]PF<sub>6</sub> and [**5**]PF<sub>6</sub>, which already indicates the strong influence of the nature of the nitrogen ligand of the N,S chelate on the properties of the cyclometalated complexes.

Octahedral complexes bearing three different bidentate ligands, two of which are dissymmetric, potentially have many isomers. The carbon donor atom can be either *trans* or *cis* to the nitrogen donor atoms of the bpy ligand, and in each of these cases the nitrogen of the N,S ligand can be *trans* to either the bpy or to the phpy<sup>-</sup> ligand, leading to up to four coordination isomers, each of which exists as an enantiomeric pair  $\Lambda/\Delta$  (Scheme 5.1). Following the IUPAC configuration index convention, these four coordination isomers are named (OC-6-43)-[Ru(bpy)(phpy)(N,S)]PF<sub>6</sub>, (OC-6-34)-[Ru(bpy)(phpy)(N,S)]PF<sub>6</sub>, (OC-6-53)-[Ru(bpy)(phpy)(N,S)]PF<sub>6</sub>, and (OC-6-35)-[Ru(bpy)(phpy)(N,S)]PF<sub>6</sub>, but for an easier reading in this chapter we will name them isomers **a**, **b**, **c**, and **d**, respectively (Scheme 5.1). Next to the different configurations of the coordination sphere created by the dissymmetry of the ligands, the coordinating sulfur atom is a prochiral center that, after coordination to ruthenium, can adopt either an *R* or an *S* configuration. Thus, for each of the four  $\Lambda$  coordination isomers a pair of diastereoisomers  $\Lambda$ -*R* and  $\Lambda$ -*S* may exist, obtaining a total of eight possible  $\Lambda$ -isomers for [**3**]<sup>+</sup> and [**5**]<sup>+</sup>. Finally, in the case of complexes [**2**]<sup>+</sup> and [**4**]<sup>+</sup>, the N,S chelate creates a six-membered ring that can switch between two chair conformations where the methyl group of the thioether is either in equatorial (*eq*) or in axial (*ax*) position depending on the conformation of the chair (see Scheme 4.1 and Chapter 4). These configurations are not identical, and there are hence 16 possible  $\Lambda$ -isomers for these two complexes.



Scheme 5.1. Synthesis of  $\text{[2]PF}_6$ ,  $\text{[3]PF}_6$ ,  $\text{[4]PF}_6$ , and  $\text{[5]PF}_6$  and the four possible regioisomers. For clarity only the  $\Lambda$  isomers are shown, but all samples were obtained as racemic  $\Delta/\Lambda$  mixtures.

In spite of the high number of possible isomers for these molecules,  $\text{[2]PF}_6$  and  $\text{[4]PF}_6$  were obtained as single  $\Lambda/\Delta$  enantiomeric pair of isomers according to the  $^1\text{H}$  NMR spectra in acetone- $d_6$ . Characteristic doublets for H in the 6 position on the bpy were found to be at 9.82 and 9.44 ppm for  $\text{[2]PF}_6$  and  $\text{[4]PF}_6$ , respectively, as shown in Figure 5.1a and Figure 5.1c. Single sets of peaks in the aromatic region corresponding to 16 and 20 H were found, respectively. Mass spectrometry of  $\text{[2]PF}_6$  and  $\text{[4]PF}_6$  showed peaks at 517.1 and 565.5, respectively, corresponding to  $\text{[2]}^+$  (calcd  $m/z$  = 517.1) and  $\text{[4]}^+$  (calcd  $m/z$  = 565.1). On the other hand, as shown in Figure 5.1b, the  $^1\text{H}$  NMR spectrum of  $\text{[3]PF}_6$  in acetone- $d_6$  showed two doublets at 9.02 and 9.11 ppm in an integration ratio of 1:0.8. Mass spectrometry showed a single peak at  $m/z$  = 503.5 corresponding to  $\text{[3]}^+$  (calcd  $m/z$  = 503.1), which means that the two sets of NMR peaks belong to two different isomers. A similar situation was observed for complex  $\text{[5]PF}_6$ , with three doublets in the  $^1\text{H}$  NMR spectrum at 9.16, 9.39, and 9.49 ppm in a ratio of 0.3:1:0.2 (Figure 5.1d). Mass spectrometry also showed a single peak at  $m/z$  = 552.1 corresponding to  $\text{[5]}^+$  (calcd  $m/z$  = 551.1), indicating the formation of three isomers out of the eight possible. Overall, despite the apparent complexity of this synthesis, the right number of carbon atoms (*i.e.* three) between the N and the S atoms of the N,S chelate allows to prepare the tris-heteroleptic cyclometalated complexes

[2]PF<sub>6</sub> and [4]PF<sub>6</sub> stereoselectively, *i.e.* as a single pair of  $\Lambda/\Delta$  enantiomers, while a shorter chain (two carbon atoms) leads to mixtures of isomers in [3]PF<sub>6</sub> and [5]PF<sub>6</sub>.

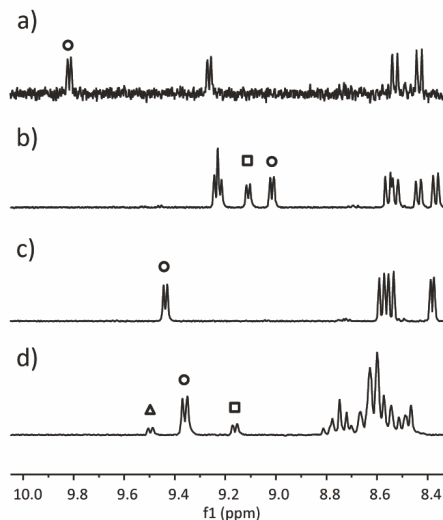


Figure 5.1. <sup>1</sup>H NMR of solutions of [2]PF<sub>6</sub> (a), [3]PF<sub>6</sub> (b), [4]PF<sub>6</sub> (c), and [5]PF<sub>6</sub> (d) in acetone-*d*<sub>6</sub>. Peaks corresponding to the H at position 6 on the bpy of the major isomer are marked with a circle, and the peaks corresponding to the H at position 6 on the bpy of the second and third isomers (if any) are marked with a square and triangle, respectively.

### 5.2.2 Structural characterization (DFT, NOESY, and X-Ray)

The identification of the configuration of these complexes is challenging, and only [2]PF<sub>6</sub> and [4]PF<sub>6</sub> were studied further, since they were obtained as single isomers. First, Density Functional Theory (DFT) minimization of the isomers of both complexes was performed in water using the COSMO model to simulate solvent effects (see Experimental Section). In each case only the  $\Lambda$  enantiomers with the six-membered chelate ring in a chair conformation were modelled. The sulfur atom was placed either in the *R* or *S* configuration. To reduce the amount of structures to be optimized, only the isomers with the methyl group in an equatorial position were calculated (see Chapter 4). The optimized structures and their energies in water are given in Figure AVI.5, Figure AVI.6, and in Table 5.1, respectively. For [2]<sup>+</sup>, the isomer  $\Lambda$ -(*S*)-*eq*-[2d]<sup>+</sup> was found to be the most stable, with the other isomers at energies ranging from +2.6 to +10.0 kJ·mol<sup>-1</sup> (Table 5.1). Although the energy differences are relatively small, it is clear that the thermodynamically most stable isomer is  $\Lambda$ -(*S*)-*eq*-[2d]<sup>+</sup>, which has the  $\sigma$ -bound C atom *trans* to the amine of mtpa. For complex [4]<sup>+</sup>, isomer  $\Lambda$ -(*S*)-*eq*-[4d]<sup>+</sup> was also found to be the most stable in water, followed by the other *S*

isomers at energies ranging from +8.8 to 10.6 kJ·mol<sup>-1</sup>, and then the *R* isomers at energies ranging from +10.9 to +21.2 kJ·mol<sup>-1</sup> (Table 5.1). In this case, the energy differences between the most and least stable isomers are significantly larger than for [2]<sup>+</sup>, which highlights the different geometric requirements of the sp<sup>2</sup> carbon and nitrogen atoms in [4]<sup>+</sup> vs. that of the sp<sup>3</sup> atoms in [2]<sup>+</sup>. Notably, the six-membered ring involving the mtep ligand was found to be in a *pseudo-chair* conformation in the minimized structures, due to the different orbital hybridization of the N and C atoms of the pyridine ring. For example, in  $\Lambda$ -(*S*)-*eq*-[4d]<sup>+</sup> the angle C<sub>β</sub>-C<sub>α</sub>-N is 120.17°, whereas in  $\Lambda$ -(*S*)-*eq*-[2d]<sup>+</sup> it is 113.54°. Another potential reason for the increased stabilization of isomer **d** of [4]<sup>+</sup> is that the electron-rich carbon ligand is *trans* to the π-accepting pyridine ligand of mtep, while in [2d]<sup>+</sup> the *trans* primary amine cannot accept the excess electron density. Overall, all the isomers of both complexes with the sulfur in *R* configuration and the methyl group in equatorial position show very short distances between that methyl group and the closest proton at position 6 on bpy or phpy<sup>-</sup> (~ 2.1 Å, Table 5.1), whereas with the *S* configuration that distance is much longer (~ 3.5 Å, Table 5.1). In the latter configuration, the methyl group sits above the middle of either the bpy or the phpy<sup>-</sup> ligands (called ancillary ligands), lowering steric repulsions and thus explaining the general preference for an *S* configuration of the sulfur atom. Although the structures having the methyl group in axial position were not minimized, a similar trend is expected. As explained in Chapter 4 (Scheme 4.1), the inversion of the *pseudo-chair* does not change the configuration of the sulfur atom but it changes the position of the methyl group from equatorial to axial and *vice versa*. This inversion does not affect the position of the methyl group with respect to the ancillary ligands and their corresponding steric effects.

Table 5.1. Absolute and relative energies in water (COSMO) of the isomers of [2]<sup>+</sup> and [4]<sup>+</sup> optimized by DFT/PBE0/TZP, and distances (Å) between H of the N,S ligand and the spatially closest H<sub>6</sub> of the ancillary ligands.

	Absolute energy in water (Hartree)	Relative energy ΔE in water (kJ.mol <sup>-1</sup> )	SCH <sub>3</sub> ...H <sub>6</sub>	H <sub>γ</sub> ...H <sub>6</sub>	H <sub>β</sub> ...H <sub>6</sub>
Λ-(R)-eq-[2a] <sup>+</sup>	-16.34735195	10.0	2.0901	2.0916	3.2482
Λ-(R)-eq-[2b] <sup>+</sup>	-16.34749222	9.6	2.2032	2.1088	3.3374
Λ-(R)-eq-[2c] <sup>+</sup>	-16.34868079	6.5	2.1478	2.2332	3.0378
Λ-(R)-eq-[2d] <sup>+</sup>	-16.34791025	8.5	2.1245	2.0899	3.1498
Λ-(S)-eq-[2a] <sup>+</sup>	-16.34864080	6.6	3.6948	2.9525	3.2417
Λ-(S)-eq-[2b] <sup>+</sup>	-16.34956230	4.2	3.7037	2.0800	3.1900
Λ-(S)-eq-[2c] <sup>+</sup>	-16.35015479	2.6	3.8634	3.0299	3.1182
Λ-(S)-eq-[2d] <sup>+</sup>	-16.35015479	0.0	3.8355	2.8732	3.1084
Λ-(R)-eq-[4a] <sup>+</sup>	-17.90977751	21.2	2.0115	2.335	2.4537
Λ-(R)-eq-[4b] <sup>+</sup>	-17.91011750	20.3	2.026	2.6181	2.3643
Λ-(R)-eq-[4c] <sup>+</sup>	-17.91162229	16.3	2.0457	2.6024	2.3409
Λ-(R)-eq-[4d] <sup>+</sup>	-17.91370630	10.9	2.0361	2.2468	2.4817
Λ-(S)-eq-[4a] <sup>+</sup>	-17.91402838	10.0	3.282	3.3278	2.2499
Λ-(S)-eq-[4b] <sup>+</sup>	-17.91448159	8.8	3.5303	3.0197	2.3136
Λ-(S)-eq-[4c] <sup>+</sup>	-17.91378390	10.6	3.4180	3.1008	2.2527
Λ-(S)-eq-[4d] <sup>+</sup>	-17.91783987	0.0	3.4844	2.909	2.3536

In order to see whether this theoretical result is confirmed by experiments, <sup>1</sup>H NMR studies in acetone-d<sub>6</sub> were performed to assign the structure of the species in solution. Unfortunately, the instability and easy degradation of compound [2]PF<sub>6</sub> made the acquisition of a high-quality NOESY spectrum impossible, making the detection of the main off-diagonal signals challenging. However, COSY, HSQC, and NOESY spectroscopy of [4]PF<sub>6</sub> in acetone-d<sub>6</sub> at room temperature allowed for the assignment of the peaks corresponding to the three ligands. The NOESY spectrum showed equivalent off-diagonal signals between A6 of bpy and H<sub>γ</sub> of mtep and between H<sub>β</sub> and A6 of bpy and C6 of phpy<sup>-</sup> (Figure 5.2a). The DFT modelled structures showed that signals between A6 and H<sub>β</sub> and H<sub>γ</sub> of mtep are unlikely in the same complex due to the great difference of both distances in every modelled isomer (Figure 5.2b). NOESY studies at 193 K were performed to detect inversion of the coordinated sulfur atom. At such temperature, the off-diagonal signal between A6 and H<sub>γ</sub> is much weaker than that

between C6 and H<sub>β</sub>, and the off-diagonal signal between A6 and H<sub>β</sub> is not present (Figure 5.2c). All the DFT modelled structures with the sulfur atom in *R* configuration were discarded since, together with those signals, a stronger signal between the thioether methyl group and A6 should be observed due to the short distance between those atoms (~2 Å) (Figure 5.2 and Table 5.1). Among the other isomers, the one that fits best with the reported off-diagonal signals is  $\Lambda$ -(*S*)-*eq*-[4c]<sup>+</sup> (with sulfur *trans* to the  $\sigma$ -bound C), with distances between A6 and H<sub>γ</sub> and between C6 and H<sub>β</sub> of 3.101 and 2.253 Å, respectively. Isomer  $\Lambda$ -(*S*)-*ax*-[4d]<sup>+</sup> would also fit with the reported off-diagonal signals, although not modelled with DFT. Single crystals suitable for X-Ray structure determination were obtained for complexes [4]PF<sub>6</sub> by slow vapor diffusion of diethyl ether into a solution of the complex in acetone. The crystal structure is a racemate of a single isomer of [Ru(bpy)(phpy)(mtep-κN,κS)]PF<sub>6</sub> in an orthorhombic P<sub>2</sub>12<sub>1</sub>1 space group, containing both configurations  $\Lambda$ -(*S*) and  $\Delta$ -(*R*) with the pyridine of the N,S ligand *trans* to the  $\sigma$ -bound C donor atom and the methyl group in a *pseudo*-axial position. Thus, the obtained structure corresponds to the isomer  $\Lambda$ -(*S*)-*ax*-[4d]PF<sub>6</sub>, confirming the geometry predicted by NOESY studies in solution. The structure, shown in Figure 5.3, shows a longer Ru-S bond (2.3331(8) Å) compared to the Ru-N bonds of the ancillary ligands (between 2.049(2) and 2.085(2) Å), as expected from the higher ionic radius of sulfur compared to nitrogen. The Ru-N bond (2.239(3) Å) *trans* to the Ru-C bond (2.027(3) Å) is also significantly longer than the other Ru-N bonds, which fits with the expected *trans* influence of the electron-rich carbon donor atom.

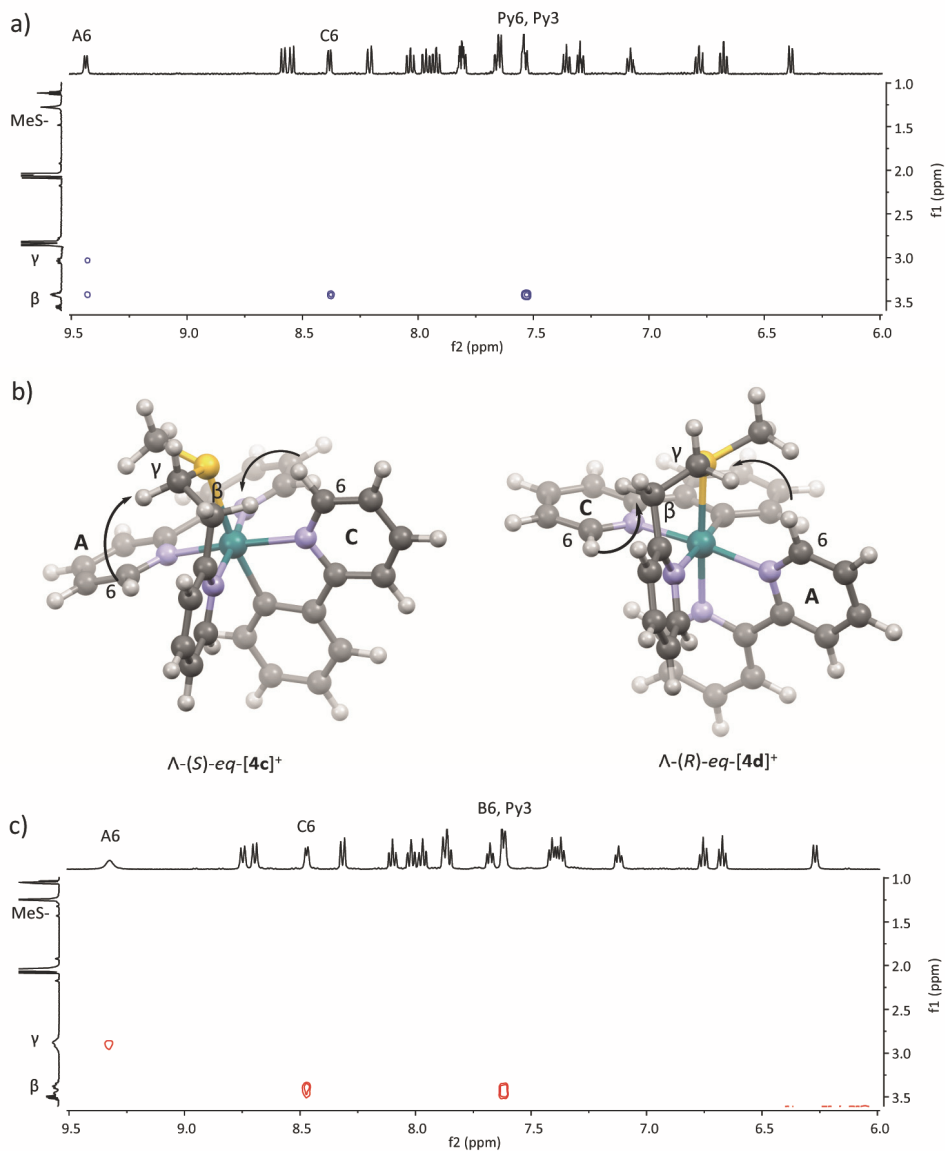


Figure 5.2. NOESY spectra of acetone- $d_6$  solution of  $[4]PF_6$  at 293 K (a) showing off-diagonal signals between  $H_\beta$  and C6,  $H_\beta$  and A6, and  $H_\gamma$  and A6. At 193 K (c), the off-diagonal signal between  $H_\beta$  and A6 is not visible. b) Isomers  $\Lambda$ -(S)-eq-[4c]<sup>+</sup> and  $\Lambda$ -(R)-eq-[4d]<sup>+</sup> modelled by DFT show the short distances between  $H_\beta$  and C6 (2.2527 and 2.4817 Å, respectively) and  $H_\gamma$  and A6 (3.1008 and 2.2468 Å, respectively), thus these isomers would fit with the NOESY signals. However, in  $\Lambda$ -(R)-eq-[4d]<sup>+</sup> an interaction between  $CH_3S$ - and A6 should be also visible due to the short distance (2.0361 Å).

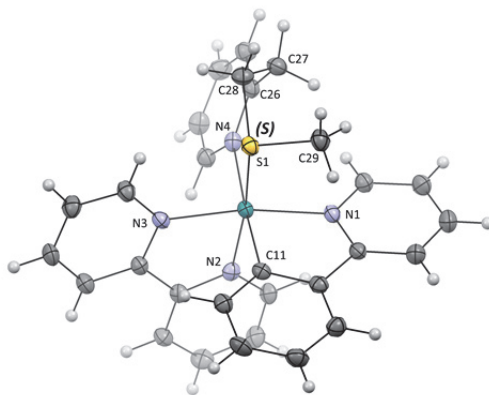


Figure 5.3. Displacement ellipsoid plot (50% probability level) of the  $\Delta$  enantiomer of the cationic complex in the crystal structure of the pair  $\Delta$ -(S)/ $\Delta$ -(R)-ax-[4d]PF<sub>6</sub>. The hexafluoridophosphate counteranion has been omitted for clarity.

Table 5.2. Selected bond length (Å) and angles (°) for  $\Delta$ -(S)/ $\Delta$ -(R)-ax-[4d]PF<sub>6</sub>.

$\Delta$ -(S)-ax-[4d]PF <sub>6</sub>	
<b>Ru1-S1</b>	2.3310(8)
<b>Ru1-N1</b>	2.085(2)
<b>Ru1-N2</b>	2.060(2)
<b>Ru1-N3</b>	2.049(2)
<b>Ru1-N4</b>	2.239(3)
<b>Ru1-C11</b>	2.027(3)
<b>S1-C28-C26-N4</b>	26.4(2)

### 5.2.3 Electronic spectroscopy and electrochemistry

The UV-vis absorption spectra in CH<sub>3</sub>CN of compounds [2]PF<sub>6</sub> – [5]PF<sub>6</sub> are provided in Figure 5.4 and their absorption maxima ( $\lambda_{\text{max}}$ ) and molar extinction coefficients ( $\epsilon$ ) are listed in Table 5.3. It must be noted that for complexes [3]PF<sub>6</sub> and [5]PF<sub>6</sub>, mixtures of two or three isomers were used. A common feature in all the absorption spectra is the presence of two main bands in the MLCT region: one with a  $\lambda_{\text{max}}$  around 390 nm and a broader band between 450 and 650 nm with a lower molar absorption coefficient, with the tail of the band reaching the 700 nm region. According to Bomben *et al.* the first band corresponds to a <sup>1</sup>MLCT transition involving the coordinated carbon atom of the phpy<sup>-</sup> ligand, whereas the broad band at a lower energy corresponds to a Ru→bpy transition.<sup>2</sup> This broad MLCT band compared to the non-cyclometalated analogues is a result of the lower symmetry of the cyclometalated compound.<sup>2</sup> The lower-energy MLCT band has a  $\lambda_{\text{max}}$  of 530 and 540 nm for primary amine-based complexes [2]PF<sub>6</sub>

and [3]PF<sub>6</sub>, respectively, whereas pyridine-based complexes [4]PF<sub>6</sub> and [5]PF<sub>6</sub> show a blue-shifted band with  $\lambda_{\text{max}}$  at 526 and 501 nm, respectively. Furthermore, the latter two compounds show bands with a shoulder, which could be ascribed to an overlapping Ru→py transition. For complex [2]PF<sub>6</sub> a band with  $\lambda_{\text{max}}$  at 725 nm is also visible, however, this band may be the result of oxidation of the complex. The degradation of [2]PF<sub>6</sub> may also explain the much lower molar absorption coefficient of the Ru→phpy<sup>-</sup> band of complex [2]PF<sub>6</sub> (6900 M<sup>-1</sup>·cm<sup>-1</sup>) compared to the other three complexes (around 10000 M<sup>-1</sup>·cm<sup>-1</sup>).

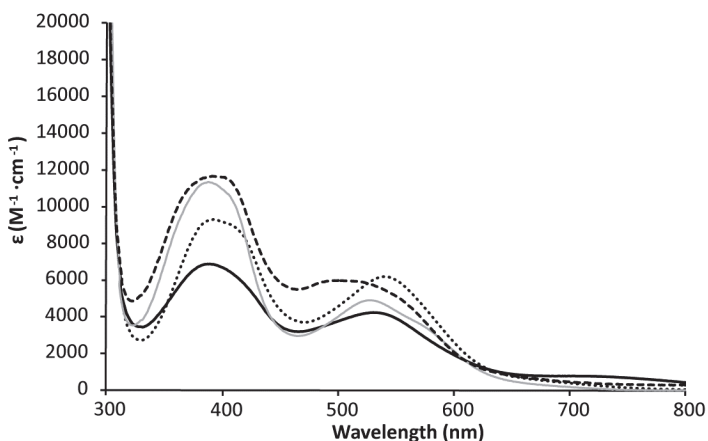


Figure 5.4. Electronic absorption spectra of solutions in CH<sub>3</sub>CN of [2]PF<sub>6</sub> (black continuous), [3]PF<sub>6</sub> (dots), [4]PF<sub>6</sub> (grey continuous), and [5]PF<sub>6</sub> (dashes).

The electrochemical properties of complexes [2]PF<sub>6</sub> – [5]PF<sub>6</sub> were investigated using cyclic voltammetry in CH<sub>3</sub>CN in order to gain more insight on the redox stability of these complexes (Figure AVI.1). For complexes [2]PF<sub>6</sub> and [3]PF<sub>6</sub> the reversible oxidation wave corresponding to the Ru<sup>III</sup>/Ru<sup>II</sup> couple is observed at a potential  $E_{1/2}$  of -0.03 and 0.00 V vs. Fc<sup>+0</sup>, respectively, whereas complexes [4]PF<sub>6</sub> and [5]PF<sub>6</sub> show a reversible peak at a significantly higher potential  $E_{1/2}$  of +0.16 V vs. Fc<sup>+0</sup> (Table 5.3), highlighting the  $\pi$ -acceptor properties of the pyridine-based N,S chelating ligand, which stabilizes the HOMO of complexes [4]PF<sub>6</sub> and [5]PF<sub>6</sub> compared to that of [2]PF<sub>6</sub> and [3]PF<sub>6</sub>. In practice, the oxidation of the former compounds is more difficult, which makes them stable in air, while compounds [2]PF<sub>6</sub> and [3]PF<sub>6</sub> are easily oxidized during their synthesis. Small changes of the N,S ligand can thus have significant consequences on the applicability of a cyclometalated complex.

Table 5.3. Wavelength of MLCT transition ( $\lambda_{\text{abs}}/\text{nm}$ ) and molar absorptivity ( $\epsilon/\text{M}^{-1}\cdot\text{cm}^{-1}$ ) of [2]PF<sub>6</sub>, [3]PF<sub>6</sub>, [4]PF<sub>6</sub>, and [5]PF<sub>6</sub> in CH<sub>3</sub>CN. Redox potentials of [2]PF<sub>6</sub>, [3]PF<sub>6</sub>, [4]PF<sub>6</sub>, and [5]PF<sub>6</sub> as measured by cyclic voltammetry.<sup>a</sup>

Complex	$\lambda_{\text{abs}}/\text{nm}$ ( $\epsilon/\text{M}^{-1}\cdot\text{cm}^{-1}$ )	$E_{1/2}(\text{Ru}^{\text{III/II}})/\text{V}^{\text{a}}$	$\Delta E_{\text{p}}/\text{V}^{\text{a}}$
[Ru(bpy)(phpy)(mtpa)]PF <sub>6</sub> [2]PF <sub>6</sub>	530 (4300), 389 (6900)	-0.03	0.060
[Ru(bpy)(phpy)(mtea)]PF <sub>6</sub> [3]PF <sub>6</sub> <sup>b</sup>	540 (6200), 392 (9300)	0.00	0.071
[Ru(bpy)(phpy)(mtep)]PF <sub>6</sub> [4]PF <sub>6</sub>	526 (4900), 388 (11400)	+0.16	0.060
[Ru(bpy)(phpy)(mtmp)]PF <sub>6</sub> [5]PF <sub>6</sub> <sup>c</sup>	501 (6000), 395 (11700)	+0.16	0.090

<sup>a</sup> Measurement conditions: 1 mM of the complexes in 0.1 M Bu<sub>4</sub>NPF<sub>6</sub>/CH<sub>3</sub>CN, scanning rate 100 mV·s<sup>-1</sup>. The potentials are referenced to Fc<sup>+1/0</sup>; <sup>b</sup>A mixture of two isomers in a ratio 1:0.8 was used; <sup>c</sup>A mixture of three isomers in a ratio 0.3:1:0.2 was used.

## 5.2.4 Thermal stability and photochemistry

The thermal stability in the dark of all four complex was studied in CH<sub>3</sub>CN using UV-vis spectroscopy. Under air, solutions in CH<sub>3</sub>CN of complexes [2]PF<sub>6</sub>, [3]PF<sub>6</sub>, [4]PF<sub>6</sub>, and [5]PF<sub>6</sub> did not show any significant changes in the UV-vis spectra over time, except for a general increase in the absorbance due to evaporation of the solvent (Figure AVI.3a-d). Thus, in CH<sub>3</sub>CN in the dark no oxidation nor thermal substitution of the N,S ligand by solvent molecules occurred.

The photoreactivity of the complexes was studied in CH<sub>3</sub>CN and monitored with UV-vis spectroscopy, mass spectrometry, and NMR spectroscopy. When a solution of [3]PF<sub>6</sub> in CH<sub>3</sub>CN was irradiated with a green (521 nm) LED at a photon flux of  $\sim 6 \cdot 10^{-8}$  mol·s<sup>-1</sup> under Ar, the UV-vis spectra did not show any change of the absorption bands. Only a general increase of the absorbance was observed due to the slow evaporation of the solvent (Figure 5.5b). Thus, [3]PF<sub>6</sub> is not photoreactive in CH<sub>3</sub>CN. However, when a solution of [2]PF<sub>6</sub> in CH<sub>3</sub>CN was irradiated under the same conditions, the UV-vis spectra showed a small shift of the  $\lambda_{\text{max}}$  of both MLCT bands from 534 nm and 388 nm to 518 nm and 378 nm, respectively, with isosbestic points at 421 nm and 552 nm (Figure 5.5a). Although the photoreaction did not reach a steady state, mass spectrometry after 3 h of irradiation showed a peak at  $m/z = 494.1$ , corresponding to [Ru(bpy)(phpy)(CH<sub>3</sub>CN)<sub>2</sub>]<sup>+</sup> (calcd  $m/z = 494.1$ ), proving that photosubstitution of mtpa by two solvent molecules occurred. Furthermore, irradiation of an acetonitrile solution of [4]PF<sub>6</sub> under the same conditions showed a similar hypsochromic shift of the maximum absorption of both MLCT bands from 526 nm and 388 nm to 516 nm and 376 nm, respectively, reaching a steady state after 6 h (Figure 5.5c). Mass spectrometry at that point showed the peak of the bis-acetonitrile photoproduct at  $m/z = 494.1$ , thus photosubstitution of mtep by two solvent molecules

occurred as well. Since complex  $[4]PF_6$  is the only air-stable complex of the series that was obtained as a pure single isomer, the quantum yield of the photoreaction could be determined. Using Glotaran global fitting, the quantum yield for the photosubstitution of mtep ( $\Phi_{PR}$ ) was calculated to be 0.00035 (see Appendix I and Figure AVI.2), which is ten times lower than the  $\Phi_{PR}$  for the irradiation of  $[Ru(bpy)_2(mtmp)]Cl_2$  in water (0.0030, see Chapter 3). Finally, irradiation of a solution of  $[5]PF_6$  showed a very slow change in the UV-vis spectra over time with a shift of the MLCT bands to the blue with isosbestic points at 474 nm and 546 nm (Figure 5.5d). Although the photoreaction did not reach a steady state, mass spectrometry after 15 h irradiation also showed a peak at  $m/z = 494.1$ . Thus, complexes  $[2]PF_6$ ,  $[4]PF_6$ , and  $[5]PF_6$  proved to be photoreactive and lead to the same photoproduct, *i.e.*  $[Ru(bpy)(phpy)(CH_3CN)_2]^+$ , although the rate of the photoreaction of  $[5]PF_6$  was much lower than that of the two other complexes.

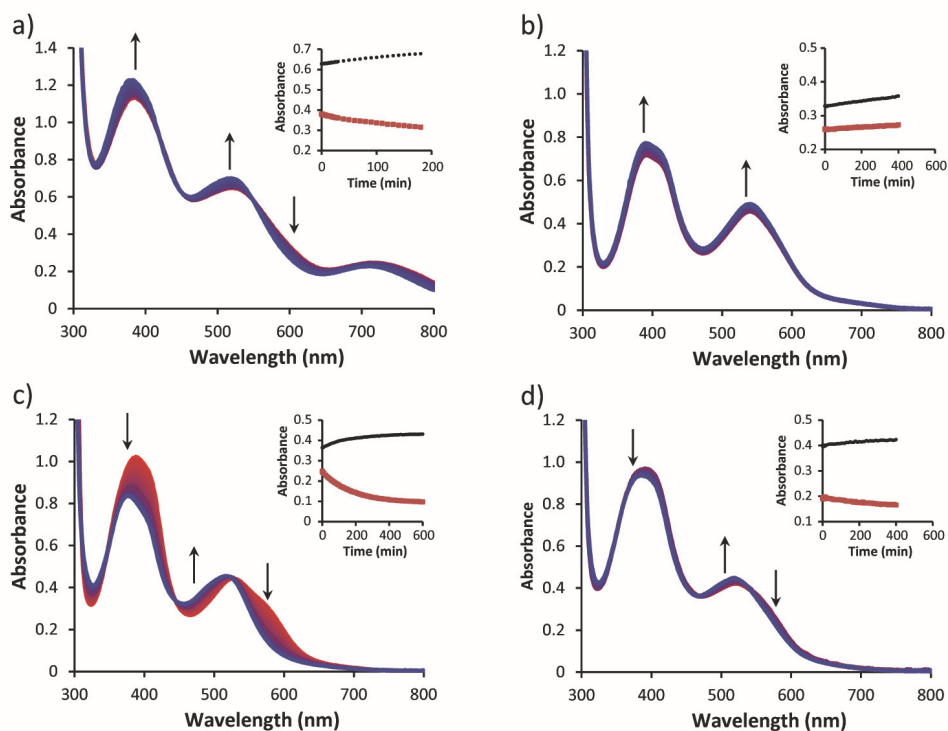
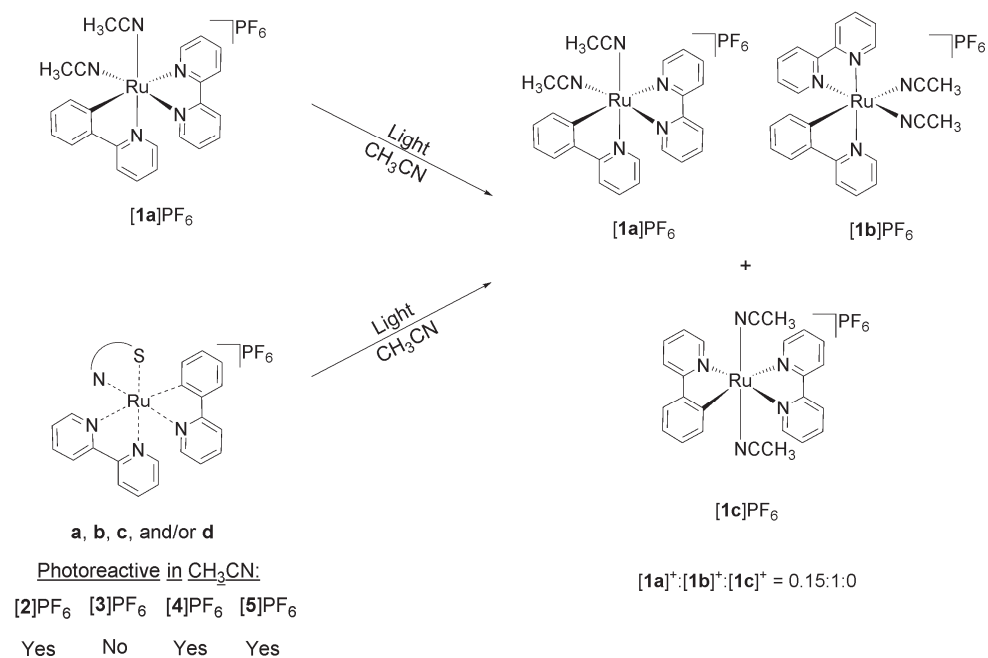


Figure 5.5. Evolution of the UV-vis spectra of  $CH_3CN$  solutions of a)  $[2]PF_6$  (0.151 mM), b)  $[3]PF_6$  (0.093 mM), c)  $[4]PF_6$  (0.094 mM), and d)  $[5]PF_6$  (0.101 mM) upon irradiation with a 521 nm LED (photon fluxes of  $8.62 \cdot 10^{-8}$ ,  $6.09 \cdot 10^{-8}$ ,  $6.80 \cdot 10^{-8}$ , and  $6.17 \cdot 10^{-8} \text{ mol} \cdot \text{s}^{-1}$ , respectively) under  $N_2$ . Inset: black dots represent the absorbance at 500 nm vs. time, and red squares represent the absorbance at 590 nm vs. time.

In order to determine which isomer of the photoproduct was obtained, the photoreactivity of complexes  $[2]PF_6$  and  $[4]PF_6$  was studied with  $^1H$  NMR in  $CD_3CN$  by irradiation with a 1000 W Xe lamp fitted with a long pass 400 nm and an IR filter. As shown in Figure 5.6b, after 6 h irradiation of a solution of  $[2]PF_6$ , the doublets at 8.95 and 9.67 ppm disappeared, whereas new doublets at 9.37, 9.26, and 9.14 ppm arose in a ratio 0.13:1:1. The same species were obtained after 1.5 h irradiation of complex  $[4]^+$  under the same conditions (Figure 5.6c). However, only the doublet at 9.37 ppm corresponds to  $[Ru(bpy)(phpy)(CH_3CN)_2]^+$  with the coordinated carbon *trans* to bpy ( $[1a]^+$ ),<sup>19</sup> which is obtained as the minor compound in the steady state. Thus, to which isomer do the other two doublets correspond? Thermal and photochemical isomerization of  $[1a]^+$  into the isomer with the coordinated carbon atom *trans* to  $CH_3CN$  ( $[1b]^+$ ) was already reported by Pfeffer *et al.* (Scheme 5.2).<sup>18</sup> However, the reported  $^1H$  NMR shifts did not fit with our NMR data. In order to study which photoproduct was obtained, a solution of  $[1a]PF_6$  in  $CD_3CN$  was irradiated under the same conditions as complexes  $[2]PF_6$  and  $[4]PF_6$ . As shown in Figure 5.6a, after 5 h the doublet at 9.37 ppm had decreased in intensity and two new doublets arose at 9.26 and 9.14 ppm reaching a steady state between both isomers with a ratio 0.16:1, thus showing that the same photoproducts were obtained in this experiment as upon irradiation of  $[2]PF_6$  and  $[4]PF_6$ . However, due to the exchange of coordinated  $CH_3CN$  by  $CD_3CN$ , the peaks belonging to the coordinated  $CH_3CN$  molecules were not visible in  $^1H$  NMR, making the assignment of the stereochemistry of these photoproducts impossible. Thus, the photoreaction was performed in  $CH_3CN$ , the solvent was removed by rotary evaporation at 20 °C, and the crude product was redissolved in  $CDCl_3$  to analyze it by  $^1H$  NMR. The spectrum showed a doublet at 9.48 ppm integrating for one H and two singlets at 2.31 and 2.27 ppm integrating for three protons each, which were assigned to the coordinated  $CH_3CN$  molecules (Figure AVI.4). The isomer with both  $CH_3CN$  molecules *trans* to each other and the polypyridyl ligands in the equatorial plane ( $[1c]PF_6$ ) was discarded as a possible photoproduct since both  $CH_3CN$  molecules would be equivalent, thus resulting in one singlet integrating for 6 protons. This control experiment only leaves one possible isomer as a photoproduct for the irradiation of  $[1a]PF_6$ ,  $[2]PF_6$ , and  $[4]PF_6$ , *i.e.* the *cis* isomer  $[1b]PF_6$  (Scheme 5.2).



Scheme 5.2. Summary of the products obtained upon irradiation of  $\text{CH}_3\text{CN}$  solutions of complexes  $[\mathbf{1a}]\text{PF}_6$ ,  $[\mathbf{2}]\text{PF}_6$ ,  $[\mathbf{3}]\text{PF}_6$ ,  $[\mathbf{4}]\text{PF}_6$ , and  $[\mathbf{5}]\text{PF}_6$  performed either with a 521 nm LED with a photon flux of  $\sim 7 \cdot 10^{-8} \text{ mol} \cdot \text{s}^{-1}$  (0.1 mM) and monitored with UV-vis spectroscopy, or with a Xe lamp (2 mM) and monitored with  $^1\text{H}$  NMR. According to  $^1\text{H}$  NMR a mixture of isomers  $[\mathbf{1a}]^+ : [\mathbf{1b}]^+$  in a ratio of  $\sim 0.15 : 1$  was always obtained, with no presence of the trans isomer  $[\mathbf{1c}]^+$ . For clarity, only the  $\Delta$  isomers are shown, but all samples were obtained as racemic  $\Delta/\Lambda$  mixtures.

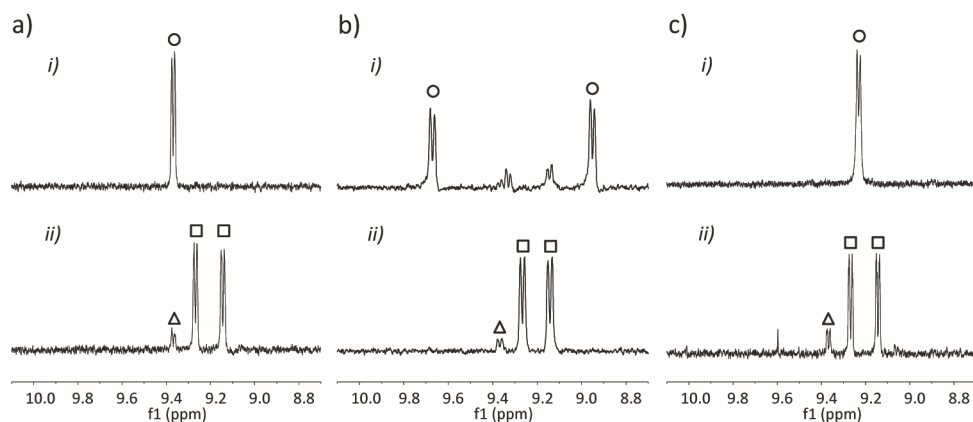


Figure 5.6. Evolution of the  $^1\text{H}$  NMR spectra (region 10.0 – 8.8 ppm) of a solution in  $\text{CD}_3\text{CN}$  of a)  $[\mathbf{1a}]\text{PF}_6$  (2.61 mM), b)  $[\mathbf{2}]\text{PF}_6$  (4.47 mM), and c)  $[\mathbf{4}]\text{PF}_6$  (1.84 mM) irradiated with a 1000 W Xe lamp fitted with a 400 nm long pass filter and an IR filter. i) At  $t = 0$ , ii) at  $t = 5$  h (a),  $t = 6$  h (b), and  $t = 1.5$  h (c). Circles: starting product, squares:  $[\mathbf{1b}]^+$ , triangles:  $[\mathbf{1a}]^+$ .

### 5.3 Discussion

In the literature it is generally accepted that in complexes of the type  $[\text{Ru}(\text{bpy})(\text{phpy})(\text{N},\text{N})]^+$ , synthesized from  $[\text{Ru}(\text{bpy})(\text{phpy})(\text{CH}_3\text{CN})_2]^+$ , the third bidentate N,N ligand coordinates to ruthenium by simply substituting the  $\text{CH}_3\text{CN}$  molecules without isomerization, *i.e.* *cis* to the carbon donor atom of  $\text{phpy}^-$ .<sup>20</sup> However, Pfeffer *et al.* recently showed that this structural assignment might not be correct.<sup>18</sup>  $\text{CH}_3\text{CN}$  is a very good ligand for ruthenium(II) and in order to turn it into a good leaving group the complex must first isomerize (either thermally or photochemically) so that one  $\text{CH}_3\text{CN}$  becomes *trans* to the carbon ligand, which is a very reactive position due to the *trans* effect of the C donor atom.<sup>18</sup> This mechanism seems to occur also for the coordination of the N,S ligands, as the obtained isomer in  $[\mathbf{4}]^+$  has the N atom of the last incoming ligand *trans* to the carbon atom of  $\text{phpy}^-$ , as proven by NOESY studies and the X-Ray structure. Furthermore, although all the complexes are stable in  $\text{CH}_3\text{CN}$  solution under air, we observed during the synthesis that complexes bearing a primary amine-based N,S ligand oxidized easier than compounds with a pyridine-based N,S ligand. Indeed, cyclic voltammetry of the four complexes showed a lower oxidation potential for  $[\mathbf{2}]\text{PF}_6$  and  $[\mathbf{3}]\text{PF}_6$  than for  $[\mathbf{4}]\text{PF}_6$  and  $[\mathbf{5}]\text{PF}_6$ . We suggest that the *trans* influence of the  $\sigma$ -bound C atom plays an important role in the oxidation. The  $\pi$ -accepting nature of the pyridine of the N,S ligand in  $[\mathbf{4}]\text{PF}_6$  and  $[\mathbf{5}]\text{PF}_6$  stabilizes the HOMO by accepting electron-density of the C donor atom in *trans* position, whereas primary amine-based ligands do not allow this, making the complexes more prone to oxidation. The higher energy of the MLCT band, *i.e.* the higher gap between the HOMO and the LUMO, of  $[\mathbf{4}]\text{PF}_6$  and  $[\mathbf{5}]\text{PF}_6$  compared to  $[\mathbf{2}]\text{PF}_6$  and  $[\mathbf{3}]\text{PF}_6$  is another sign of the stabilization of the HOMO for the pyridine-based complexes.

With regard to the photoreactivity, as explained in the Introduction, cycloruthenated complexes generally are not photoreactive, and the ones that are photoreactive are those which photosubstitute only one monodentate ligand. However, we found that six-membered rings like those found in  $[\mathbf{2}]^+$  and  $[\mathbf{4}]^+$  lower the ligand field splitting of the complexes and thus the energy of the  $^3\text{MC}$  levels well enough to recover photoreactivity in  $\text{CH}_3\text{CN}$ , without the necessity of adding hindering ligands. By contrast, N,S complexes with five-membered rings, such as  $[\mathbf{3}]^+$  and  $[\mathbf{5}]^+$ , were found to be either not photoreactive at all ( $[\mathbf{3}]^+$ ) or with only very low photoconversion rates ( $[\mathbf{5}]^+$ ). We suggest that these low photosubstitution rates are due to fast rechelation (also called recaptation) of the five-membered ring, like it occurs in the case of

$[\text{Ru}(\text{bpy})_3]^{2+}$  or  $[\text{Ru}(\text{bpy})_2(\text{glutamate-}\kappa\text{N},\kappa\text{O})]^{2+}$ .<sup>21-22</sup> Furthermore, whereas the NMR shifts of  $[\mathbf{1a}]^+$  correspond to those reported by Pfeffer *et al.* in 2005,<sup>19</sup> the NMR shifts of  $[\mathbf{1b}]^+$ , *i.e.* the isomer obtained after irradiation of  $[\mathbf{1a}]^+$ , do not correspond to those reported by Pfeffer *et al.* in 2013.<sup>18</sup> Nevertheless, as shown in the Results section, the identity of  $[\mathbf{1b}]^+$  is unequivocally assigned.

## 5.4 Conclusions

In this work, we have discovered that the ring size resulting from the coordination of an N,S ligand to ruthenium has a critical influence on the number of isomers obtained during the synthesis of  $[\mathbf{2}]^+ - [\mathbf{5}]^+$ , as well as on their photoreactivity. Under the same conditions tris-heteroleptic complexes bearing a six-membered ring ( $[\mathbf{2}]\text{PF}_6$  and  $[\mathbf{4}]\text{PF}_6$ ), in spite of their apparent configurational complexity, were obtained stereoselectively as a single couple of enantiomers  $\Lambda/\Delta$ , which in the case of  $[\mathbf{4}]\text{PF}_6$  could be assigned to  $\Lambda$ -(S)/ $\Delta$ -(R)-*ax*- $[\mathbf{4d}]\text{PF}_6$ . However, the complexes with five-membered N,S chelate rings were obtained as mixtures of isomers that could not be separated. This result opens new possibilities for the stereoselective synthesis of tris-heteroleptic ruthenium complexes bearing chiral and dissymmetric ligands. Complexes with a six-membered N,S chelate ring showed selective substitution of the N,S ligand in  $\text{CH}_3\text{CN}$  upon green light irradiation, since rechelation is apparently slow. Finally, cyclometallated complexes are electron rich, but their sensitivity to oxidation can be fine-tuned by using  $\pi$ -accepting pyridyl-containing bidentate ligands *trans* to the carbon donor atom, stabilizing the high electron density brought by cyclometalation. Thus, going away from polypyridyl ligands can be highly beneficial, both on the synthetic point of view and on the point of view of the photoreactivity, provided that the stereochemical complexity brought by the dissymmetric metallacycling ligands can be controlled by choosing the appropriate size of the ring resulting of the coordination of the N,S ligand. Overall, the novel complex  $[\mathbf{4}]\text{PF}_6$  fulfills all criteria to become a promising PACT agent: it can be synthesized in a stereoselectively manner, it is stable under  $\text{O}_2$ , and it photosubstitutes efficiently the non-toxic N,S ligand by two  $\text{CH}_3\text{CN}$  molecules. Biological studies are currently ongoing to assess the actual biological activity of this compound.

## 5.5 Experimental

### 5.5.1 Synthesis

**General:** The ligands 2-(methylthio)ethylamine (mtea), and 3-(methylthio)-propylamine (mtpa) were purchased from Sigma-Aldrich, as well as bis-[(benzene)dichlororuthenium] ( $[\eta^6\text{-}(\text{C}_6\text{H}_6)\text{RuCl}_2]_2$ ) and sodium hydroxide (NaOH). 2-Phenylpyridine (phpy), 2,2'-bipyridine (bpy), and potassium hexafluoridophosphate ( $\text{KPF}_6$ ) were purchased from Alfa-Aesar. All reactants and solvents were used without further purification. The synthesis of  $[\text{Ru}(\text{phpy})(\text{CH}_3\text{CN})_4]\text{PF}_6$ ,  $[\text{Ru}(\text{bpy})(\text{phpy})(\text{CH}_3\text{CN})_2]\text{PF}_6$  (**[1a]** $\text{PF}_6$ ), 2-(methylthio)methylpyridine (mtmp), and 2-(methylthio)ethyl-2-pyridine (mtep) were carried out according to literature procedures.<sup>17, 19, 23</sup>

Electrospray mass spectra (ES MS) were recorded by using a MSQ Plus Spectrometer. UV-vis spectra were recorded on a Cary Varian spectrometer. All  $^1\text{H}$  NMR spectra were recorded on a Bruker DPX-300 or DMX-400 spectrometers. Chemical shifts are indicated in ppm relative to the residual solvent peak.

**Synthesis of complexes [2] $\text{PF}_6$ , [3] $\text{PF}_6$ , [4] $\text{PF}_6$ , and [5] $\text{PF}_6$ .** General procedure: In a two-neck flask, a solution of **[1a]** $\text{PF}_6$  (1 equiv), N,S ligand (4 equiv), and  $\text{Et}_3\text{N}$  (4 equiv) were dissolved in deaerated EtOH (2 to 5 mL) and heated in an oil bath at 70 °C for 22 h under  $\text{N}_2$ . Then, a schlenk flask containing diethyl ether was attached to the flask containing the reaction mixture in order to obtain a crystalline dark precipitate by slow vapour diffusion. The solid was filtered, washed with diethyl ether, and stored at -20 °C.

**$[\text{Ru}(\text{bpy})(\text{phpy})(\text{mtpa})]\text{PF}_6$  (**[2]** $\text{PF}_6$ ).** According to the general procedure, a solution of **[1]** $\text{PF}_6$  (40 mg, 0.063 mmol), mtpa (28  $\mu\text{L}$ , 0.25 mmol), and  $\text{Et}_3\text{N}$  (40 mg, 0.29 mmol) in EtOH (5 mL) was heated at 70 °C for 22 h under  $\text{N}_2$ . After 6 days of slow vapour diffusion of diethyl ether into the EtOH solution, a crystalline dark precipitate was obtained (23 mg, 52%).  $^1\text{H}$  NMR (300 MHz, acetone- $d_6$ )  $\delta$  = 9.81 (dt,  $J$  = 5.8, 1.1 Hz, 1H), 9.26 (ddd,  $J$  = 5.7, 1.6, 0.8 Hz, 1H), 8.52 (dt,  $J$  = 8.2, 1.2 Hz, 1H), 8.43 (dt,  $J$  = 8.1, 1.1 Hz, 1H), 8.16 (dt,  $J$  = 8.1, 1.1 Hz, 1H), 8.07 – 8.02 (m, 1H), 7.97 (ddd,  $J$  = 8.2, 7.3, 1.6 Hz, 1H), 7.81 (ddd,  $J$  = 8.2, 7.5, 1.5 Hz, 1H), 7.74 (ddd,  $J$  = 8.8, 7.5, 1.4 Hz, 2H), 7.67 (dd,  $J$  = 5.7, 0.8 Hz, 1H), 7.46 (ddd,  $J$  = 7.2, 5.7, 1.4 Hz, 1H), 7.24 (ddd,  $J$  = 7.3, 5.7, 1.4 Hz, 1H), 6.73 – 6.66 (m, 1H), 6.59 (td,  $J$  = 7.3, 1.4 Hz, 1H), 6.40 (dd,  $J$  = 7.4, 1.2 Hz, 1H), 1.15 (s, 3H). High Resolution ES MS  $m/z$  (calcd):

517.09851 (517.09944, [2]<sup>+</sup>). UV-vis  $\lambda$  in nm ( $\epsilon$  in  $M^{-1}.cm^{-1}$ ): 530 (4300), 389 (6900) in  $CH_3CN$ .

**[Ru(bpy)(phpy)(mtea)]PF<sub>6</sub> ([3]PF<sub>6</sub>)**. According to the general procedure, a solution of [1]PF<sub>6</sub> (15 mg, 0.024 mmol), mtea (8.5  $\mu$ L, 0.095 mmol), and Et<sub>3</sub>N (7.0  $\mu$ L, 0.095 mmol) in EtOH (2 mL) was heated at 70 °C for 22 h under N<sub>2</sub>. After 5 days of slow vapour diffusion of diethyl ether into the EtOH solution, a crystalline dark precipitate was obtained (9.0 mg, 58%). Two isomers A/B in a ratio 1:0.8 were obtained. <sup>1</sup>H NMR (400 MHz, acetone-d<sub>6</sub>)  $\delta$  9.26 – 9.19 (m, 1H<sub>A</sub> + 1H<sub>B</sub>), 9.11 (d,  $J$  = 5.1 Hz, 1H<sub>B</sub>), 9.02 (d,  $J$  = 5.8 Hz, 1H<sub>A</sub>), 8.56 (d,  $J$  = 8.0 Hz, 1H<sub>A</sub>), 8.53 (d,  $J$  = 8.0 Hz, 1H<sub>B</sub>), 8.44 (dt,  $J$  = 6.5, 1.0 Hz, 1H<sub>B</sub>), 8.37 (dt,  $J$  = 8.0, 1.2 Hz, 1H<sub>A</sub>), 8.16 (d,  $J$  = 8.1 Hz, 1H<sub>B</sub>), 8.14 – 8.07 (m, 2H<sub>A</sub>), 8.05 – 8.00 (m, 1H<sub>B</sub>), 7.97 (ddd,  $J$  = 8.2, 7.3, 1.5 Hz, 1H<sub>B</sub>), 7.91 – 7.85 (m, 2H<sub>A</sub>), 7.83 (d,  $J$  = 5.8 Hz, 1H<sub>B</sub>), 7.82 – 7.73 (m, 2H<sub>A</sub> + 2H<sub>B</sub>), 7.71 – 7.64 (m, 1H<sub>A</sub> + 1H<sub>B</sub>), 7.43 (ddd,  $J$  = 7.2, 5.7, 1.4 Hz, 1H<sub>B</sub>), 7.38 (ddd,  $J$  = 7.3, 5.7, 1.5 Hz, 1H<sub>A</sub>), 7.22 (ddd,  $J$  = 7.3, 5.7, 1.4 Hz, 1H<sub>B</sub>), 7.11 (ddd,  $J$  = 7.3, 5.8, 1.4 Hz, 1H<sub>A</sub>), 6.77 (ddd,  $J$  = 7.7, 7.1, 1.4 Hz, 1H<sub>A</sub>), 6.74 – 6.67 (m, 1H<sub>A</sub> + 1H<sub>B</sub>), 6.64 (td,  $J$  = 7.3, 1.4 Hz, 1H<sub>B</sub>), 6.52 – 6.47 (m, 1H<sub>A</sub> + 1H<sub>B</sub>), 4.24 (d,  $J$  = 11.4 Hz, 1H), 4.12 (d,  $J$  = 12.1 Hz, 1H), 3.50 – 3.35 (m, 1H), 3.20 – 3.00 (m, 4H), 2.97 – 2.86 (m, 3H), 2.76 – 2.65 (m, 1H), 1.67 (s, 3H), 1.27 (s, 3H). High Resolution ES MS  $m/z$  (calcd): 503.08379 (503.08585, [3]<sup>+</sup>). UV-vis  $\lambda$  in nm ( $\epsilon$  in  $M^{-1}.cm^{-1}$ ): 540 (6200), 392 (9300) in  $CH_3CN$ .

**[Ru(bpy)(phpy)(mtep)]PF<sub>6</sub> ([4]PF<sub>6</sub>)**. According to the general procedure, a solution of [1]PF<sub>6</sub> (30 mg, 0.046 mmol), mtep (27 mg, 0.18 mmol), and Et<sub>3</sub>N (26  $\mu$ L, 0.19 mmol) in EtOH (5 mL) was heated at 70 °C for 22 h under N<sub>2</sub>. After 4 days of slow vapour diffusion of diethyl ether into the EtOH solution, a crystalline dark precipitate was obtained (14 mg, 44%). A pure single isomer was obtained. <sup>1</sup>H NMR (400 MHz, acetone-d<sub>6</sub>)  $\delta$  9.44 (d,  $J$  = 5.8 Hz, 1H, A6), 8.58 (dt,  $J$  = 7.9 Hz, 1H, A3), 8.54 (dt,  $J$  = 8.1, 1.1 Hz, 1H, B3), 8.38 (ddd,  $J$  = 5.7, 1.6, 0.8 Hz, 1H, C6), 8.21 (dt,  $J$  = 8.4, 1.2 Hz, 1H, C3), 8.06 – 8.00 (m, 1H, A4), 7.99 – 7.94 (m, 1H, C4), 7.94 – 7.88 (m, 1H, B4), 7.84 – 7.78 (m, 2H, Py5 + Ph3), 7.68 – 7.63 (m, 2H, A5 + B6), 7.56 – 7.51 (m, 2H, Py3 + Py6), 7.36 (ddd,  $J$  = 7.4, 5.7, 1.4 Hz, 1H, B5), 7.30 (ddd,  $J$  = 7.3, 5.7, 1.4 Hz, 1H, C5), 7.08 (ddd,  $J$  = 7.3, 5.7, 1.4 Hz, 1H, Py4), 6.78 (ddd,  $J$  = 7.7, 7.2, 1.3 Hz, 1H, Ph4), 6.68 (td,  $J$  = 7.3, 1.4 Hz, 1H, Ph 5), 6.42 – 6.36 (m, 1H, Ph6), 3.46 – 3.41 (m, 2H,  $\beta$ ), 3.09 – 2.99 (m, 2H,  $\gamma$ ), 1.28 (s, 3H, CH<sub>3</sub>S-). <sup>13</sup>C NMR (101 MHz, acetone-d<sub>6</sub>)  $\delta$  152.98, 152.33, 152.06, 150.15, 138.38, 137.17, 137.08, 135.80, 134.97, 128.95, 128.19, 127.52, 127.19, 124.72, 124.59, 124.43, 124.06, 123.46, 121.61,

120.16, 34.95, 32.00, 15.20. High Resolution ES MS  $m/z$  (calcd): 565.10083 (565.09944, [4]<sup>+</sup>). Anal. Calcd for C<sub>29</sub>H<sub>27</sub>F<sub>6</sub>N<sub>4</sub>PRuS: C, 49.08; H, 3.84; N, 7.90 Found: C, 48.84; H, 3.99; N, 7.65. UV-vis  $\lambda$  in nm ( $\epsilon$  in M<sup>-1</sup>.cm<sup>-1</sup>): 526 (4900), 388 (11300) in CH<sub>3</sub>CN.

**[Ru(bpy)(phpy)(mtmp)]PF<sub>6</sub>** ([5]PF<sub>6</sub>). According to the general procedure, a solution of [1]PF<sub>6</sub> (20 mg, 0.031 mmol), mtmp (17 mg, 0.12 mmol), and Et<sub>3</sub>N (20  $\mu$ L, 0.14 mmol) in EtOH (5 mL) was heated at 70 °C for 22 h under N<sub>2</sub>. After 5 days of slow vapour diffusion of diethyl ether into the EtOH solution, a crystalline dark precipitate was obtained (9.7 mg, 45%). <sup>1</sup>H NMR of 3 isomers labelled as A, B, and C (300 MHz, acetone-d<sub>6</sub>)  $\delta$  = 9.50 (d,  $J$  = 5.6 Hz, 1H<sub>A</sub>), 9.36 (dd,  $J$  = 5.5, 1.2 Hz, 1H<sub>B</sub>), 9.16 (d,  $J$  = 5.8 Hz, 1H<sub>B</sub>), 8.83 – 8.74 (m, 1H<sub>A</sub> + 1H<sub>C</sub>), 8.62 (dt,  $J$  = 7.4, 1.8 Hz, 2H<sub>B</sub>), 8.53 – 8.46 (m, 1H<sub>A</sub> + 1H<sub>C</sub>), 8.31 (d,  $J$  = 6.9 Hz, 1H<sub>C</sub>), 8.24 – 8.19 (m, 1H<sub>A</sub> + 1H<sub>B</sub> + 1H<sub>C</sub>), 8.17 – 8.09 (m, 1H<sub>C</sub>), 8.07 – 8.00 (m, 1H<sub>B</sub>), 8.02 – 7.93 (m, 1H<sub>A</sub> + 1H<sub>B</sub> + 1H<sub>C</sub>), 7.87 – 7.79 (m, 5H), 7.74 – 7.67 (m, 1H<sub>A</sub> + 1H<sub>C</sub>), 7.61 (ddd,  $J$  = 7.3, 5.8, 1.4 Hz, 1H<sub>B</sub>), 7.49 (d,  $J$  = 5.5 Hz, 1H<sub>B</sub>), 7.39 (ddd,  $J$  = 7.3, 5.7, 1.4 Hz, 1H<sub>B</sub>), 7.29 – 7.25 (m, 1H<sub>A</sub> + 1H<sub>C</sub>), 7.22 (t,  $J$  = 8.0 Hz, 1H<sub>B</sub>), 7.08 – 7.02 (m, 1H<sub>A</sub> + 1H<sub>C</sub>), 6.99 (d,  $J$  = 9.0 Hz, 1H<sub>A</sub>), 6.91 – 6.84 (m, 1H<sub>C</sub>), 6.83 – 6.76 (m, 1H<sub>B</sub>), 6.68 (td,  $J$  = 7.3, 1.4 Hz, 1H<sub>B</sub>), 6.48 (dd,  $J$  = 7.4, 1.3 Hz, 1H<sub>B</sub>), 6.42 (d,  $J$  = 6.8 Hz, 1H<sub>A</sub>). ES MS  $m/z$  (calcd): 551.1 (551.1, [5]<sup>+</sup>). UV-vis  $\lambda$  in nm ( $\epsilon$  in M<sup>-1</sup>.cm<sup>-1</sup>): 501 (6000), 395 (11700) in CH<sub>3</sub>CN.

### 5.5.2 Cyclic voltammetry

Electrochemical measurements were performed at room temperature under argon using an Autolab PGstat10 potentiostat controlled by NOVA software. A three-electrode cell system was used with a glassy carbon working electrode, a platinum counter electrode and an Ag/AgCl reference electrode. All electrochemistry measurements were done in CH<sub>3</sub>CN solution with tetrabutylammonium hexafluoridophosphate as the supporting electrolyte.

### 5.5.3 Photochemistry

**General:** For the irradiation experiments of NMR tubes, the light of a LOT 1000 W Xenon Arc lamp mounted with 400 nm long pass and IR filters was used. For NMR experiments under N<sub>2</sub>, NMR tubes with PTFE stopper were used. UV-vis experiments were performed on a Cary 50 Varian spectrometer. When following photoreactions by UV-vis and mass spectrometry, a LED light source ( $\lambda_{\text{ex}}$  = 521 nm, with a Full Width at

Half Maximum of 33 nm) with a photon flux between  $6.09$  and  $8.62 \cdot 10^{-8} \text{ mol} \cdot \text{s}^{-1}$  was used.

**Experiments monitored with  $^1\text{H}$  NMR:** A stock solution in  $\text{CD}_3\text{CN}$  of either  $[\mathbf{1a}]\text{PF}_6$  (2.61 mM),  $[\mathbf{2}]\text{PF}_6$  (4.47 mM) or  $[\mathbf{4}]\text{PF}_6$  (1.84 mM) was prepared and deaerated under  $\text{N}_2$ . Then, 660  $\mu\text{L}$  were transferred, under  $\text{N}_2$ , into a NMR tube. The tube was irradiated at room temperature with a LOT Xenon 1000 W lamp equipped with IR short pass and 400 nm long pass filters. In addition, a control experiment without white light irradiation was performed. The reactions were monitored with  $^1\text{H}$  NMR at various time intervals.

**Experiments monitored with UV-vis and MS:** UV-vis spectroscopy was performed using a UV-vis spectrometer equipped with temperature control set to 298 K and a magnetic stirrer. The irradiation experiments were performed in a quartz cuvette containing 3 mL of solution. A stock solution of the desired complex was prepared using  $\text{CH}_3\text{CN}$ , which was then diluted in the cuvette to a working solution concentration. When the experiment was carried out under  $\text{N}_2$  the sample was deaerated 15 min by gentle bubbling of  $\text{N}_2$  and the atmosphere was kept inert during the experiment by a gentle flow of  $\text{N}_2$  on top of the cuvette. A UV-vis spectrum was measured every 30 s for the first 10 min, every 1 min for the next 10 min, and eventually every 10 min until the end of the experiment. Data was analysed with Microsoft Excel. Experimental conditions are detailed in Table 5.4.

Table 5.4. Conditions of the photoreactions monitored with MS and UV-vis.

Complex	Stock solution			Working sol. (mM)	Photon flux ( $\text{mol} \cdot \text{s}^{-1}$ )
	w (mg)	V (mL)	M (mM)		
$[\mathbf{2}]\text{PF}_6$	1.0	10	0.151	0.151	$8.62 \cdot 10^{-8}$
$[\mathbf{3}]\text{PF}_6$	0.9	10	0.139	0.093	$6.09 \cdot 10^{-8}$
$[\mathbf{4}]\text{PF}_6$	1.0	10	0.141	0.094	$6.80 \cdot 10^{-8}$
$[\mathbf{5}]\text{PF}_6$	1.4	10	0.201	0.101	$6.17 \cdot 10^{-8}$

### 5.5.4 Single Crystal X-Ray crystallography

**General:** All reflection intensities were measured at 110(2) K using a SuperNova diffractometer (equipped with Atlas detector) with  $\text{Cu } K\alpha$  radiation ( $\lambda = 1.54178 \text{ \AA}$ ) under the program CrysAlisPro (Version CrysAlisPro 1.171.39.29c, Rigaku OD, 2017). The same program was used to refine the cell dimensions and for data reduction. The structure was solved with the program SHELXS-2014/7 and was

refined on  $F^2$  with SHELXL-2014/7.<sup>24</sup> Analytical numeric absorption correction based on a multifaceted crystal model was applied using CrysAlisPro. The temperature of the data collection was controlled using the system Cryojet (manufactured by Oxford Instruments). The H atoms were placed at calculated positions (unless otherwise specified) using the instructions AFIX 23, AFIX 43, or AFIX 137 with isotropic displacement parameters having values 1.2  $U_{eq}$  of the attached C atoms.

**Crystal growing:** [4]PF<sub>6</sub> (1.0 mg) was dissolved in acetone (1 mL, 1.2 mM) and transferred (300  $\mu$ L) into a GC vial, which was placed in a larger vial that contained diethyl ether (3 mL) as a counter solvent. The large vial was stoppered. After a few days quality crystals suitable for X-ray structure determination were obtained by vapor diffusion.

**Details of the crystal structure:** The structure is ordered.  $0.26 \times 0.07 \times 0.02$  mm<sup>3</sup>, orthorhombic, *Pbca*,  $a = 10.95531(15)$ ,  $b = 15.6391(3)$ ,  $c = 32.2937(4)$ ,  $V = 5532.92(15)$  Å<sup>3</sup>,  $Z = 8$ ,  $\mu = 6.46$  mm<sup>-1</sup>,  $T_{min}$ - $T_{max}$ : 0.254-0.886. 28523 reflections were measured up to a resolution of  $(\sin \theta/\lambda)_{max} = 0.617$  Å<sup>-1</sup>. 5427 reflections were unique ( $R_{int} = 0.044$ ), of which 4742 were observed [ $I > 2\sigma(I)$ ]. 380 parameters were refined using 37 restraints.  $R1/wR2$  [ $I > 2\sigma(I)$ ]: 0.035/0.083.  $S = 1.09$ . Residual electron density found between -0.61 and 0.77 e Å<sup>-3</sup>.

### 5.5.5 Density Functional Theory calculations

Electronic structure calculations were performed using DFT, as implemented in the ADF program (SCM). The structures of all possible isomers of [2]<sup>+</sup> and [4]<sup>+</sup> were optimized in water using COSMO to simulate the effect of the solvent. The PBE0 functional and a triple- $\zeta$  potential basis set (TZP) were used for all calculations.

## 5.6 References

1. S. H. Wadman, J. M. Kroon, K. Bakker, M. Lutz, A. L. Spek, G. P. M. van Klink and G. van Koten, *Chem. Commun.*, **2007**, 1907-1909.
2. P. G. Bomben, K. C. D. Robson, P. A. Sedach and C. P. Berlinguette, *Inorg. Chem.*, **2009**, 48, 9631-9643.
3. L. Leyva, C. Sirlin, L. Rubio, C. Franco, R. Le Lagadec, J. Spencer, P. Bischoff, C. Gaiddon, J.-P. Loeffler and M. Pfeffer, *Eur. J. Inorg. Chem.*, **2007**, 3055-3066.
4. H. Huang, P. Zhang, H. Chen, L. Ji and H. Chao, *Chem. - Eur. J.*, **2015**, 21, 715-725.
5. L. Fetzner, B. Boff, M. Ali, M. Xiangjun, J.-P. Collin, C. Sirlin, C. Gaiddon and M. Pfeffer, *Dalton Trans.*, **2011**, 40, 8869-8878.
6. B. Pena, A. David, C. Pavani, M. S. Baptista, J.-P. Pellois, C. Turro and K. R. Dunbar, *Organometallics*, **2014**, 33, 1100-1103.
7. C. Kreitner and K. Heinze, *Dalton Trans.*, **2016**, 45, 13631-13647.
8. J.-P. Collin, M. Beley, J.-P. Sauvage and F. Barigelletti, *Inorg. Chim. Acta*, **1991**, 186, 91-93.

## Chapter 5

9. D. V. Pinnick and B. Durham, *Inorg. Chem.*, **1984**, 23, 1440-1445.
10. L. Salassa, C. Garino, G. Salassa, R. Gobetto and C. Nervi, *J. Am. Chem. Soc.*, **2008**, 130, 9590-9597.
11. P. S. Wagenknecht and P. C. Ford, *Coord. Chem. Rev.*, **2011**, 255, 591-616.
12. J.-P. Collin, D. Jouvenot, M. Koizumi and J.-P. Sauvage, *Inorg. Chem.*, **2005**, 44, 4693-4698.
13. P. Mobian, J.-M. Kern and J.-P. Sauvage, *Angew. Chem.*, **2004**, 116, 2446-2449.
14. B. A. Albani, B. Pena, K. R. Dunbar and C. Turro, *Photochem. Photobiol. Sci.*, **2014**, 13, 272-280.
15. A. M. Palmer, B. Pena, R. B. Sears, O. Chen, M. El Ojaimi, R. P. Thummel, K. R. Dunbar and C. Turro, *Philos. Trans. R. Soc., A*, **2013**, 20120135.
16. J. A. Cuello-Garibo, M. S. Meijer and S. Bonnet, *Chem. Commun.*, **2017**, 53, 6768-6771.
17. S. Fernandez, M. Pfeffer, V. Ritleng and C. Sirlin, *Organometallics*, **1999**, 18, 2390-2394.
18. B. Boff, M. Ali, L. Alexandrova, N. Á. Espinosa-Jalapa, R. O. Saavedra-Díaz, R. Le Lagadec and M. Pfeffer, *Organometallics*, **2013**, 32, 5092-5097.
19. A. D. Ryabov, R. Le Lagadec, H. Estevez, R. A. Toscano, S. Hernandez, L. Alexandrova, V. S. Kurova, A. Fischer, C. Sirlin and M. Pfeffer, *Inorg. Chem.*, **2005**, 44, 1626-1634.
20. B. Peña, N. A. Leed, K. R. Dunbar and C. Turro, *J. Phys. Chem. C*, **2012**, 116, 22186-22195.
21. R. Arakawa, S. Tachiyashiki and T. Matsuo, *Anal. Chem.*, **1995**, 67, 4133-4138.
22. L. Zayat, O. Filevich, L. M. Baraldo and R. Etchenique, *Philos. Trans. R. Soc., A*, **2013**, 371.
23. E. Reisner, T. C. Abikoff and S. J. Lippard, *Inorg. Chem.*, **2007**, 46, 10229-10240.
24. G. M. Sheldrick, *Acta Crystallogr., Sect. A: Found. Adv.*, **2008**, 64, 112-122.

# 6

## PACT or PDT: are ruthenium(II) complexes photosubstituting a non-toxic ligand also phototoxic under hypoxic conditions?

*The cytotoxicity of a series of ruthenium complexes with a photolabile non-toxic N,S ligand is tested in human cancer cells under hypoxia (1% O<sub>2</sub>) to investigate the oxygen-dependency of their activity. All compounds show lower cytotoxicity under hypoxia (1% O<sub>2</sub>) compared to that under normoxia (21% O<sub>2</sub>), probably due to the chemoresistance acquired by cancer cells at 1% O<sub>2</sub>. The cytotoxicity of some PACT compounds was clearly enhanced after green light irradiation, which is the first experimental demonstration of light-induced cytotoxicity under hypoxia for a metal-based PACT compound releasing a non-toxic organic ligand.*

This chapter is to be submitted as a full paper: J. A. Cuello-Garibo, S. Bronkhorst, Y. Batsuin, V. H. S. van Rixel, C. Schmidt, I. Ott, M. A. Siegler, and S. Bonnet, *in preparation*.

## 6.1 Introduction

Ruthenium-based Photoactivated Chemotherapy (PACT) is a new, oxygen-independent phototherapy modality against cancer that relies on the breakage of a bond to generate a species that is more cytotoxic than the prodrug. Many examples of PACT agents have been reported in literature and the observed *in vitro* cytotoxicity is usually attributed, by analogy with cisplatin, to the photogenerated aqua complex after photosubstitution of a bidentate ligand.<sup>1-3</sup> However, two major questions are often not addressed in the literature. First, what is the actual cytotoxic species after a photoreaction that has generated two photoproducts: the aquated metal complex or the released organic ligand?<sup>4</sup> Secondly, can the observed cytotoxic effect be ascribed to the generation of even small amounts of singlet oxygen ( $^1\text{O}_2$ )? In Chapter 3 and Chapter 4, we have addressed the first question using new ruthenium polypyridyl complexes bearing non-cytotoxic N,S ligands that, upon light irradiation, are substituted by two water molecules. Furthermore, quantum yields for  $^1\text{O}_2$  generation ( $\Phi_A$ ) have systematically been measured for all ruthenium(II) complexes, usually leading to  $\Phi_A$  values lower than 0.05, while ruthenium complexes used as PDT agents have  $\Phi_A$  values typically above 0.50.<sup>5-6</sup> In this chapter, we address the second question, and try to understand whether  $\Phi_A$  values as low as 0.05 can play a role in the observed phototoxicity of “PACT-like” ruthenium compounds.

Due to the oxygen-independent character of PACT, a true PACT-agent should work also in absence of oxygen in the irradiated tissues. On the contrary, in PDT the photocytotoxicity of a photosensitizer is usually impaired under hypoxia.<sup>7</sup> Hypoxia occurs in tumors due to the poorly vascularized nature of many primary tumors, coupled to the low diffusion of oxygen in non-vascularized tissues. However, biologically speaking hypoxia does not only point to the absence of dioxygen in the irradiated tissues. The lack of dioxygen has indeed a great impact on cancerous or non-cancerous cells, as it changes many aspects of their biology.<sup>8</sup> For example, the upregulation of hypoxia-inducible factors (HIFs) has consequences on the cell metabolism, invasion properties, cell death modes, or membrane integrity, among others.<sup>9-11</sup> Furthermore, tumour radiotherapy has a lower efficiency in hypoxic tissues, where the radiosensitizing properties of molecular oxygen are missing.<sup>12</sup> A recent report from Lameijer *et al.*<sup>13</sup> demonstrated for the first time that ruthenium-based PACT compounds remained as efficient under hypoxia (1%  $\text{O}_2$ ) as under normoxia (21%  $\text{O}_2$ ): the photo index (PI) of  $[\text{Ru}(\text{tpy})(\text{biq})(\text{STF-31})]\text{Cl}_2$  (tpy = 2,2',6',2"-terpyridine and biq = 2,2'-biquinoline), in which the ligand STF-31 is an organic

inhibitor of nicotinamide phosphoribosyl transferase (NAMPT), was comparable when irradiation was performed in hypoxic or normoxic conditions.<sup>13</sup> In this report, the photocytotoxicity was primarily due to NAMPT inhibition by the organic STF-31 ligand generated upon light irradiation. To our knowledge, there is no experimental report of PACT under hypoxia where the photocytotoxicity is due to the photogenerated metal-based fragment.

In this chapter, we investigate the oxygen dependency of the cytotoxicity of a series of structurally related ruthenium(II) PACT complexes of which the ligand that is photosubstituted, 2-(methylthio)methylpyridine (mtmp), is non-toxic. The series of complexes, shown in Figure 6.1 comprises  $[\text{Ru}(\text{Ph}_2\text{phen})_2(\text{mtmp})]\text{Cl}_2$  ( $\text{Ph}_2\text{phen}$  = 4,7-diphenyl-1,10-phenanthroline, **[1]** $\text{Cl}_2$ ),  $[\text{Ru}(\text{bpy})(\text{Ph}_2\text{phen})(\text{mtmp})](\text{PF}_6)_2$  ( $\text{bpy}$  = 2,2'-bipyridine, **[2]** $(\text{PF}_6)_2$ ),  $[\text{Ru}(\text{dmbpy})_2(\text{mtmp})]\text{Cl}_2$  ( $\text{dmbpy}$  = 6,6'-dimethyl-2,2'-bipyridine, **[3]** $\text{Cl}_2$ ), and  $[\text{Ru}(\text{bpy})(\text{phpy})(\text{mtep})]\text{PF}_6$  ( $\text{phpy}^-$  = 2-phenylpyridine,  $\text{mtep}$  = 2-(methylthio)ethyl-2-pyridine, **[4]** $\text{PF}_6$ ). The synthesis and photochemistry of the new complexes **[2]** $(\text{PF}_6)_2$  and **[3]** $\text{Cl}_2$  is described, while **[1]** $\text{Cl}_2$  and **[4]** $\text{PF}_6$  were already reported in Chapter 3 and Chapter 5, respectively. In Chapter 3 we showed that mtmp is non-toxic below 150  $\mu\text{M}$ , and that irradiation of **[1]**<sup>2+</sup> leads to the photosubstitution of mtmp by two water molecules. Such photoreactivity translated in lung cancer cells (A549 cell line) into a low effective concentration ( $\text{EC}_{50}$ ), *i.e.* the compound concentration (in  $\mu\text{M}$ ) that reduces cell viability by 50% compared to untreated cells, of 0.48  $\mu\text{M}$  upon light irradiation but a photo index (PI) of only 6, which was attributed to the high lipophilicity of the complex, leading to high uptake and high dark toxicity. The tris-heteroleptic complex **[2]**<sup>2+</sup> is designed to solve this issue: with only one  $\text{Ph}_2\text{phen}$  ligand the lipophilicity and dark cytotoxicity of this complex is expected to decrease, while the photosubstitution typical for PACT should be retained. On the other hand, in Chapter 4 we demonstrated that  $[\text{Ru}(\text{dmbpy})_2(\text{mtpa})]^{2+}$  ( $\text{mtpa}$  = 3-(methylthio)propylamine) had an  $\text{EC}_{50}$  value of 44  $\mu\text{M}$  against A549 cells after light irradiation, and that the complex was lipophilic enough to cross the cell membrane. However, it was not thermally stable, so that similar  $\text{EC}_{50}$  values were obtained in the dark. By replacing the primary amine by a pyridine in the N,S ligand, we designed **[3]**<sup>2+</sup> so that it may have an enhanced thermal stability and thus a higher PI. All complexes **[1]**<sup>2+</sup> – **[4]**<sup>2+</sup> should thus show similar photosubstitution behaviour; their cytotoxicity was tested against A549 cells and prostate cancer cells (PC3pro4 cell line) under hypoxia, and compared to normoxic conditions. The activity of these PACT compounds was compared to that of Rose Bengal, a commercially available PDT type II photosensitizer, and to that of the ruthenium-based photosensitizer

$[\text{Ru}(\text{Ph}_2\text{phen})_2(\text{bpy})]\text{Cl}_2$  (**[5]Cl<sub>2</sub>**), a structurally similar photosensitizer incapable of ligand substitution. A structure-function relationship is discussed.

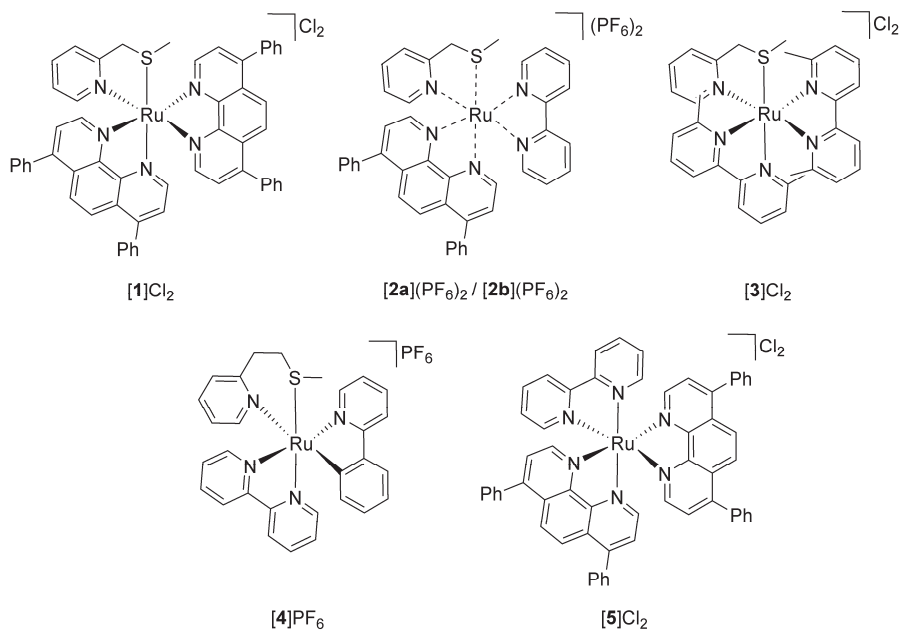


Figure 6.1. Schematic structures of the complexes **[1]Cl<sub>2</sub>**, **[2](PF<sub>6</sub>)<sub>2</sub>**, **[3]Cl<sub>2</sub>**, **[4]PF<sub>6</sub>**, and **[5]Cl<sub>2</sub>** described in this Chapter. For complex **[2](PF<sub>6</sub>)<sub>2</sub>** the configuration is not specified, and the notation **[2]<sup>2+</sup>** represents two undefined isomers **[2a]<sup>2+</sup>** and **[2b]<sup>2+</sup>**, where the sulfur atom can be either *trans* to *bpy* or to *Ph<sub>2</sub>phen* (see Appendix VII). For clarity, only the *A* enantiomer of the complexes is represented, but all compounds were synthesized and used as racemates.

## 6.2 Results

### 6.2.1 Synthesis

The synthesis of complexes **[1]Cl<sub>2</sub>**, **[4]PF<sub>6</sub>**, and **[5]Cl<sub>2</sub>** was performed as described in Chapter 3, Chapter 5, and in literature.<sup>14</sup> The synthesis of **[2](PF<sub>6</sub>)<sub>2</sub>** was adapted from a method developed by Keyes *et al.* for the synthesis of tris-heteroleptic bidentate ruthenium complexes  $[\text{Ru}(\text{L}_1)(\text{L}_2)(\text{L}_3)]^{n+}$ .<sup>15</sup> The novelty of this method, in which the three different bidentate ligands *L*<sub>1</sub>, *L*<sub>2</sub>, and *L*<sub>3</sub> are coordinated sequentially, relies on the coordination of an oxalate ligand (*ox*<sup>2-</sup>) during the coordination of the second bidentate ligand *L*<sub>2</sub> in order to prevent the formation of  $[\text{Ru}(\text{L}_1)(\text{L}_2)_2]^{n+}$ , in which two identical ligands *L*<sub>2</sub> coordinate to the metal. Here, the order of addition of the ligands was first *Ph<sub>2</sub>phen*, then *mtmp*, and finally *bpy*. Details of the synthesis can be found in Appendix VII. After the addition of *bpy*, due to the dissymmetry of *mtmp* and the tris-heteroleptic nature of the complex, two configurational isomers are expected: one

having the sulfur donor atom *trans* to bpy and another having the sulfur donor atom *trans* to Ph<sub>2</sub>phen. Thus, two isomers were obtained according to <sup>1</sup>H NMR and were separated by column chromatography: isomer [**2a**](PF<sub>6</sub>)<sub>2</sub>, which was contaminated with [Ru(Ph<sub>2</sub>phen)(bpy)<sub>2</sub>](PF<sub>6</sub>)<sub>2</sub>, and isomer [**2b**](PF<sub>6</sub>)<sub>2</sub>, which was NMR pure but obtained in a low yield (<2%). As shown in Figure AVII.1 and explained in Appendix II, the exact configuration of the two isomers could not be established. In photochemical and biological experiments, a mixture of both isomers [**2b**]<sup>2+</sup>: [**2a**]<sup>2+</sup> in a ratio 1:0.23, further indicated as [**2**](PF<sub>6</sub>)<sub>2</sub>, was used.

Compound [**3**]Cl<sub>2</sub> was obtained by reacting [Ru(dmbpy)<sub>2</sub>Cl<sub>2</sub>] with mtmp in ethylene glycol at 100 °C for 15 min. The complex was isolated by precipitation of the hexafluoridophosphate salt ([**3**](PF<sub>6</sub>)<sub>2</sub>), and then reconverted into the chloride salt by precipitation of [**3**]Cl<sub>2</sub> in acetone after addition of Bu<sub>4</sub>NCl. Single crystals suitable for X-ray structure determination were obtained for [**3**]Cl<sub>2</sub> by slow vapour diffusion of diisopropyl ether into a solution of the compound in methanol. The structure crystallizes in the centrosymmetric space group P-1 and the crystal lattice contains both enantiomeric configurations Λ-(*S*) and Δ-(*R*) of the complex [Ru(dmbpy)<sub>2</sub>(mtmp-κN,κS)]Cl<sub>2</sub>·CH<sub>3</sub>OH·H<sub>2</sub>O. The molecular structure, shown in Figure 6.2, shows that the configuration adopted by the chiral sulfur atom lowers the steric clash between the methyl group of the thioether and that of the dmbpy ligand. Furthermore, the structure shows a longer Ru-S bond (2.3709(4) Å, see Table AVII.1) and Ru-N bonds (between 2.0928(12) and 2.1362(12) Å), than those observed in the crystal structure of the non-strained analogue [Ru(3,3'-dmbpy)<sub>2</sub>(mtmp)]<sup>2+</sup> (3,3'-dmbpy = 3,3'-dimethyl-2,2'-bipyridine) reported by Wallenstein *et al.* (Ru-S = 2.3262(9) Å and Ru-N between 2.062(2) and 2.095(2) Å).<sup>16</sup>

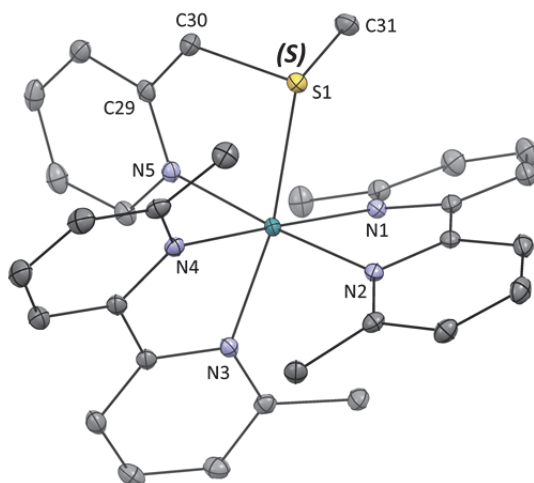


Figure 6.2. Displacement ellipsoid plot (50% probability level) of the *A* enantiomer of the cationic complex in the crystal structure of the pair *A*-(*S*)/*A*-(*R*)-[Ru(dmbpy)<sub>2</sub>(mtmp- $\kappa$ N, $\kappa$ S)]Cl<sub>2</sub>·CH<sub>3</sub>OH·H<sub>2</sub>O. The hydrogen atoms, chloride counteranions, lattice methanol and water molecules have been omitted for clarity. Selected bond distances and angles are reported in Table AVII.1.

## 6.2.2 Photoactivation and singlet oxygen generation

The photoreactivity of complexes [1]Cl<sub>2</sub> and [4]PF<sub>6</sub> has been described in Chapter 3 and Chapter 5, respectively. [1]Cl<sub>2</sub> shows photosubstitution of mtmp by two solvent molecules in water with a quantum yield of 0.0030. [4]PF<sub>6</sub> is only soluble in CH<sub>3</sub>CN in which it shows selective photosubstitution of mtmp by two CH<sub>3</sub>CN molecules with a quantum yield of 0.00035. The photoreactivity of [2](PF<sub>6</sub>)<sub>2</sub> was studied in CH<sub>3</sub>CN due to its low solubility in water, and monitored with UV-vis spectroscopy. The spectrum of a solution of [2](PF<sub>6</sub>)<sub>2</sub> irradiated for 20 min with green light (521 nm) showed an increase of the intensity of the MLCT band between 400 – 430 nm, and a decrease in the valley at 344 nm with isosbestic points at 363 nm and 440 nm (Figure 6.3a). After 15 min, when the reaction reached the steady state, mass spectrometry showed peaks at *m/z* = 140.3 and 336.3, corresponding to the free ligand {mtmp + H}<sup>+</sup> (calcd *m/z* = 140.1) and [Ru(bpy)(Ph<sub>2</sub>hen)(CH<sub>3</sub>CN)<sub>2</sub>]<sup>2+</sup> (calcd *m/z* = 336.1), respectively. Thus, upon light irradiation in CH<sub>3</sub>CN, mtmp is substituted selectively with a quantum yield of 0.111 (see Appendix I and Figure AVII.3).

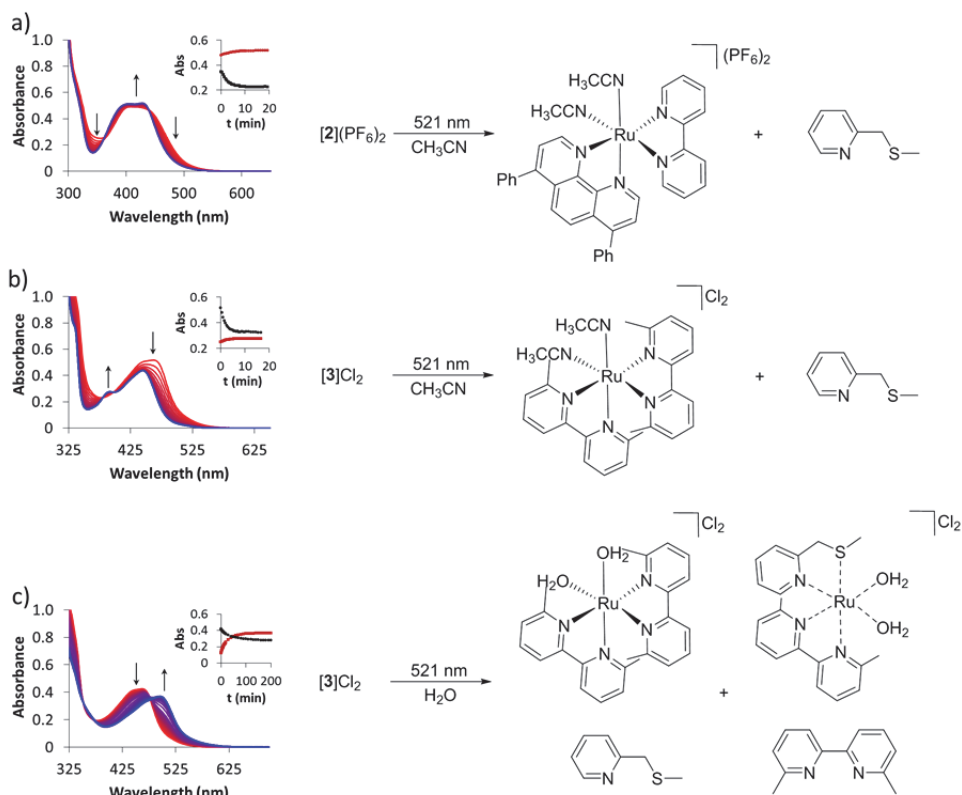


Figure 6.3. Evolution of the UV-vis spectra of solutions of a)  $[2](PF_6)_2$  in  $CH_3CN$  (0.036 mM), b)  $[3]Cl_2$  in  $CH_3CN$  (0.088 mM), and c)  $[3]Cl_2$  in water (0.073 mM) upon irradiation with a 521 nm green LED (photon fluxes were  $6.21 \cdot 10^{-8}$ ,  $6.25 \cdot 10^{-8}$ , and  $2.39 \cdot 10^{-8} \text{ mol} \cdot \text{s}^{-1}$ , respectively) under  $N_2$ . Inset: black dots represent the absorbance at 460 nm (a), 460 nm (b), and 450 nm (c) vs. time, and red squares represent the absorbance at 430 nm (a), 390 nm (b), and 500 nm (c) vs. time.

For  $[3]Cl_2$ , irradiation with green light in  $CH_3CN$  resulted in a shift of the MLCT band of the UV-vis spectra from an absorption maxima of 462 nm to 444 nm and isosbestic points at 382 nm and 395 nm (Figure 6.3b). The steady state was reached after 10 min, and mass spectrometry at that point showed a single peak at  $m/z = 275.9$  corresponding to  $[Ru(dmbpy)_2(CH_3CN)_2]^{2+}$  (calcd  $m/z = 276.1$ ). Thus, like in complex  $[2](PF_6)_2$ , upon light irradiation in  $CH_3CN$  mtmp is substituted selectively with a very high quantum yield of 0.348 (see Appendix I and Figure AVII.4). However, when the irradiation was performed in water, no clear isosbestic points were visible, which indicated the occurrence of either sequential or parallel photosubstitution reactions (Figure 6.3c). Indeed, mass spectrometry after 2.5 h irradiation showed peaks at  $m/z = 140.3$ , 185.5, 253.8, and 276.2 corresponding to  $\{mtmp + H\}^+$  (calcd  $m/z = 140.1$ ),  $\{dmbpy + H\}^+$  (calcd  $m/z = 185.1$ ),  $[Ru(dmbpy)(mtmp)(CH_3CN)_2]^{2+}$  (calcd  $m/z =$

253.6), and  $[\text{Ru}(\text{dmbpy})_2(\text{CH}_3\text{CN})_2]^{2+}$  (calcd  $m/z = 276.1$ ), respectively. The  $\text{CH}_3\text{CN}$  molecules come from the eluent used for the mass spectrometry as irradiation was performed in water. Thus, in water photosubstitution of mtmp and dmbpy occur in parallel, generating four photoproducts, *i.e.* mtmp, dmbpy,  $[\text{Ru}(\text{dmbpy})_2(\text{OH}_2)_2]^{2+}$  and  $[\text{Ru}(\text{dmbpy})(\text{mtmp})(\text{OH}_2)_2]^{2+}$ . Non-selective photosubstitution was already observed for  $[\text{Ru}(\text{bpy})(\text{dmbpy})(\text{mtpa})]^{2+}$  (Chapter 4), however, the dependence of selectivity on the solvent was not established yet.

In order to have a complete overview of the photoreactivity of these ruthenium complexes, the  $\Phi_A$  was experimentally determined.  $^1\text{O}_2$  is a highly reactive oxygen species (ROS) and it is the most common cytotoxic photoproduct in PDT type II.<sup>17-19</sup>  $\Phi_A$  was determined under blue light irradiation (450 nm) by direct detection of the 1274 nm infrared phosphorescence of  $^1\text{O}_2$  in  $\text{CD}_3\text{OD}$  using  $[\text{Ru}(\text{bpy})_3]\text{Cl}_2$  as reference ( $\Phi_A = 0.73$ ).<sup>20</sup> The  $\Phi_A$  value for the PDT agent **[5]** $\text{Cl}_2$  is surprisingly high ( $\Phi_A = 0.95$ ), whereas for the PACT complexes **[1]** $\text{Cl}_2$  and **[3]** $\text{Cl}_2$  low values of 0.020 and 0.027 were found, respectively (Table 6.1). For **[2]** $(\text{PF}_6)_2$  a significantly higher  $\Phi_A$  value of 0.069 was found, which is unexpected due to the structural similarity with **[1]** $\text{Cl}_2$  or  $[\text{Ru}(\text{bpy})_2(\text{mtmp})]\text{Cl}_2$  ( $\Phi_A = 0.023$ , see Chapter 3). Finally, the cyclometalated compound **[4]** $\text{PF}_6$  showed a  $\Phi_A$  value of 0.19, which is in accordance with its low photosubstitution quantum yield.

Table 6.1. Singlet oxygen generation quantum yields ( $\Phi_A$ ) of **[1]** $\text{Cl}_2$ , **[2]** $(\text{PF}_6)_2$ , **[3]** $\text{Cl}_2$ , **[4]** $\text{PF}_6$ , **[5]** $\text{Cl}_2$ , and Rose Bengal determined under blue light excitation (450 nm) by direct detection of the 1274 nm infrared phosphorescence of  $^1\text{O}_2$  in  $\text{CD}_3\text{OD}$  using  $[\text{Ru}(\text{bpy})_3]\text{Cl}_2$  as reference ( $\Phi_A = 0.73$ ).

	<b>[1]</b> $\text{Cl}_2$	<b>[2]</b> $(\text{PF}_6)_2$	<b>[3]</b> $\text{Cl}_2$	<b>[4]</b> $\text{PF}_6$	<b>[5]</b> $\text{Cl}_2$	Rose Bengal
$\Phi_A$	0.020	0.069	0.027	0.19	0.95	0.79 <sup>a</sup>

<sup>a</sup>Value taken from Tanielian *et al.*<sup>21</sup>

### 6.2.3 Cytotoxicity assays and cell uptake

The cytotoxicity of the five complexes and Rose Bengal was first tested under normoxia against two different cancer cell lines (A549 and PC3pro4 cells) following a protocol reported by Hopkins *et al.*<sup>22</sup> and described in the Experimental Section. A549 is a human lung cancer cell line and PC3pro4 is a cancer cell line derived from a bone metastasis obtained after injection of PC3 human prostate cancer cells into nude mice.<sup>23</sup> For each compound the effective concentrations ( $\text{EC}_{50}$ ), *i.e.* the compound concentration (in  $\mu\text{M}$ ) that reduces cell viability by 50% compared to untreated cells, are listed in Table 6.3. Photo indices (PI) were calculated as the ratio of  $\text{EC}_{50}$  obtained in the dark, divided by the values obtained after light irradiation.

Under normoxic conditions, Rose Bengal showed PI's higher than 40 and 400 for A549 and PC3pro4 cells, respectively, confirming its excellent photodynamic properties when there is no lack of dioxygen (21% O<sub>2</sub>). For the photosensitizer [5]Cl<sub>2</sub>, the higher cytotoxicity in the dark lowered the PI compared to Rose Bengal, with values of 13 and 29 for A549 and PC3pro4, respectively. On the other hand, for compounds [1]Cl<sub>2</sub>, [2](PF<sub>6</sub>)<sub>2</sub>, and [3]Cl<sub>2</sub> EC<sub>50</sub> values in the dark of 3.4, 59, and >500 μM, respectively, were found for A549 cells. After green light irradiation, the EC<sub>50</sub> values decreased to 0.62, 6.5, and 71 μM with PI's of 5.5, 9, and >7, respectively. Thus, the less lipophilic the complex is, the higher EC<sub>50</sub> values were found both in the dark and after light activation. A similar trend was observed with PC3pro4 cells. For PACT compounds cytotoxicity is indeed closely related to cellular uptake and subcellular localization, which are in turn closely related to the lipophilicity of the prodrug.<sup>24</sup> Typically, the presence of more phenyl groups results in an increase of lipophilicity,<sup>25</sup> whereas the effect of methyl groups is less pronounced. Thus, [2](PF<sub>6</sub>)<sub>2</sub> showed similar uptake (Table 6.2) as [1]Cl<sub>2</sub>, while cells were treated with solutions of very different concentration, *i.e.* 65 and 3.4 μM, respectively. Thus, due to the lower lipophilicity of [2](PF<sub>6</sub>)<sub>2</sub>, a much higher concentration was necessary to obtain the same cellular uptake and biological activity as for [1]Cl<sub>2</sub>. [3]Cl<sub>2</sub> was less efficiently taken up since a high concentration (160 μM) still resulted in a lower intracellular ruthenium concentration. This compound appeared to be the least toxic, both in the dark and after light activation.

Table 6.2. Cellular uptake of [1]Cl<sub>2</sub>, [2](PF<sub>6</sub>)<sub>2</sub>, [3]Cl<sub>2</sub>, [4]PF<sub>6</sub>, and [5]Cl<sub>2</sub> in A549 cells upon treatment near the dark EC<sub>50</sub> value.

	[1]Cl <sub>2</sub>	[2](PF <sub>6</sub> ) <sub>2</sub>	[3]Cl <sub>2</sub>	[4]PF <sub>6</sub>	[5]Cl <sub>2</sub>
<b>Treatment concentration (μM)</b>	3.4	65	160	0.08	3.8
<b>Cellular uptake (nmol Ru/mg of cell protein)</b>	2.11 ± 0.12	2.12 ± 0.33	0.78 ± 0.03	0.90 ± 0.03	2.05 ± 1.35

Finally, the EC<sub>50</sub> values for the cyclometalated compound [4]PF<sub>6</sub> were found to be 0.086 and 0.18 μM in the dark for A549 and PC3pro4 cells respectively, and 0.075 and 0.070 μM after green light irradiation, leading to negligible PI's of 1.1 and 2.6 for A549 and PC3pro4 cells, respectively. A comparable intracellular concentration (0.90 nmol Ru per mg of cell proteins) to that of [3]Cl<sub>2</sub> was obtained when treating with a 2000-fold lower dose of the cyclometalated complex [4]PF<sub>6</sub> (0.08 μM), which highlights the dramatic effect of the lower charge (+1) of this complex on the lipophilicity and passive uptake of the complex, compared to the rest of the series. In general, this series of ruthenium complexes showed a lower cytotoxicity in the dark

against PC3pro4 cells than against A549 cells, whereas the light-activated EC<sub>50</sub> values were in the same range for both cell lines. This results in a greater PI in PC3pro4 cells compared to A549 cells.

Table 6.3. Cytotoxicity expressed as effective concentrations (EC<sub>50</sub> with 95% confidence intervals, in  $\mu\text{M}$ ) of [1]Cl<sub>2</sub>, [2](PF<sub>6</sub>)<sub>2</sub>, [3]Cl<sub>2</sub>, [4]PF<sub>6</sub>, [5]Cl<sub>2</sub>, and Rose Bengal in lung (A549) and prostate (PC3pro4) cancer cell lines, under normoxia and hypoxia, in the dark and upon green light irradiation (520 nm).

Cell line	Light dose (J.cm <sup>-2</sup> )	[1]Cl <sub>2</sub>	[2](PF <sub>6</sub> ) <sub>2</sub>	[3]Cl <sub>2</sub>	[4]PF <sub>6</sub>	[5]Cl <sub>2</sub>	Rose Bengal					
A549 21% O <sub>2</sub>	0	3.4	+0.97 -0.76	+17 -13	>500	-	0.086	+0.029 -0.022	3.4	+0.39 -0.35	>50	-
	18.8	0.62	+0.14 -0.11	+2.4 -1.8	71	+25 -18	0.075	+0.027 -0.022	0.26	+0.11 -0.08	1.2	+0.39 -0.30
	PI	5.5		9.1	>7		1.1		13		>40	
	0	4.7	+0.32 -0.30	+83 -52	>500	-	0.18	+0.028 -0.024	5.1	+1.6 -1.2	29	+2.3 -2.1
PC3pro4 21% O <sub>2</sub>	18.8	0.79	+0.028 -0.027	+0.65 -0.54	33	+2.9 -2.6	0.070	+0.016 -0.013	0.22	+0.025 -0.022	0.067	+0.60 -0.066
	PI	6.0		45	>15		2.6		23		>400	
	0	8.1	1.4 -1.2	>100	-	>500	-	0.51	+0.27 -0.18	14	+1.3 -1.2	25
PC3pro4 1% O <sub>2</sub>	18.8	5.4	+0.79 -0.69	+28 -21	312	+121 -87	0.66	+0.41 -0.25	8.4	+2.0 -1.6	9.9	+3.0 -2.3
	PI	1.5		>1.3	>1.6		-		1.7		2.5	

To investigate the possible relation between <sup>1</sup>O<sub>2</sub> generation and the observed cytotoxicity, the cytotoxicity of the six compounds was tested under hypoxic conditions, in which <sup>1</sup>O<sub>2</sub> generation is seriously impaired. As shown in Figure AVII.3, cell cultures of both A549 and PC3pro4 were viable under hypoxia, showing slower growth curves compared to normoxia. Considering the higher PI observed for PC3pro4 than for A549, only PC3pro4 cells were used in the cytotoxicity assays under hypoxia. The protocol was similar to the one used for normoxia, except that dioxygen concentrations were kept at 1% during cell culturing and light irradiation, as described recently by Lameijer *et al.*<sup>13</sup> Under such conditions, Rose Bengal showed similar cytotoxicity in the dark but a much lower cytotoxicity after green light irradiation (EC<sub>50</sub> = 9.9  $\mu\text{M}$ , Table 6.3) compared to normoxia, resulting in a PI of only 2.5. The

ruthenium-based photosensitizer [5]Cl<sub>2</sub> also showed a decreased PI of 1.7, as well as a general increase of the EC<sub>50</sub> values both in the dark and after light irradiation. Overall, working at 1% O<sub>2</sub> decreased substantially the photo index of PDT photosensitizers, as reported previously.<sup>7</sup> For compounds [1]Cl<sub>2</sub>, [2](PF<sub>6</sub>)<sub>2</sub>, and [3]Cl<sub>2</sub> EC<sub>50</sub> values of 8.1, >100, and >500 μM were found in the dark, and of 5.4, 78, and 312 μM after green light irradiation, corresponding to PI's of 1.5, >1.3, and >1.6, respectively. Although after light activation EC<sub>50</sub> values were still rather high, the cell viability curves (Figure 6.4) showed a clearly enhanced cytotoxicity upon light irradiation. The extremely low cytotoxicity of [2](PF<sub>6</sub>)<sub>2</sub> and [3]Cl<sub>2</sub> in the dark (>100 and >500 μM, respectively), did not allow for an accurate calculation of the PI.

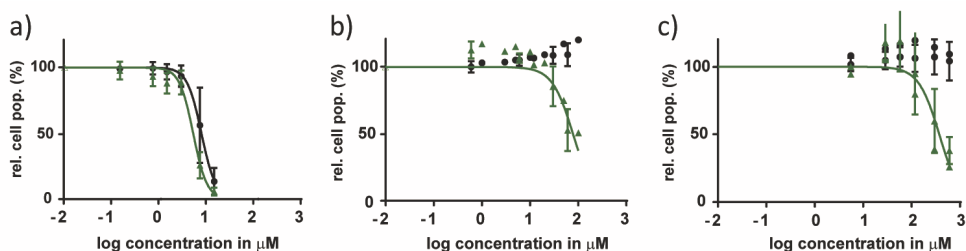


Figure 6.4. Dose-response curves for PC3pro4 cells under hypoxia treated with [1]Cl<sub>2</sub>, [2](PF<sub>6</sub>)<sub>2</sub>, or [3]Cl<sub>2</sub> and irradiated with green light (520 nm, 18.8 J·cm<sup>-2</sup>) 24 h after treatment (green data points) or left in the dark (black data points).

### 6.3 Discussion

A first analysis of the data suggests a cell dependency of the cytotoxicity of all the complexes in the series. Indeed, higher PI's were found for PC3pro4 cells than for A549 cells under normoxia. However, a more careful analysis of the data is necessary by calculating the p-value, *i.e.* the statistical significance of the differences in EC<sub>50</sub> values. When comparing the cytotoxicity of complexes [1]Cl<sub>2</sub>, [2](PF<sub>6</sub>)<sub>2</sub>, and [3]Cl<sub>2</sub> against PC3pro4 and A549 cell p-values ranging from 0.0328 to 0.585 were obtained, both in the dark and after light irradiation. These values are at or beyond the limit of statistical significance (p<0.05). Thus, a cell-selectivity of the series of complexes towards PC3pro4 under normoxia cannot be stated.

On the other hand, a lower cytotoxicity was observed under hypoxia, which is usually attributed to the acquired chemoresistance of cancer cells under such conditions.<sup>8</sup> Indeed, PC3pro4 cells were passaged twice under hypoxia before performing the phototoxicity assay, which selected *in situ* the most resistant cells capable of surviving under harsher conditions. Nevertheless, another factor has to be considered *in vitro*:

varying the concentration of O<sub>2</sub> modifies cell confluence. As shown in the growth curves (Appendix VII and Figure AVII.5), at the time of treatment and irradiation of the cells (<48 h after seeding) the cell confluence of PC3pro4 cells under normoxia and hypoxia were similar. However, during the following 48 h the cell growth under normoxia was much faster than that under hypoxia, resulting in a much lower cell density in the latter. This difference in cell density might have a great impact on the observed cytotoxicity.<sup>26</sup>

As suggested by Lameijer *et al.*, validating a compound as either a PACT or a PDT agent requires comparing the PI's, not the EC<sub>50</sub> values.<sup>13</sup> On the one hand, the PI of 2.6 observed under normoxia for [4]PF<sub>6</sub> in PC3pro4 cells seems encouraging, while the extraordinary high cytotoxicity found in the dark agrees with previous reports on cyclometalated complexes.<sup>27</sup> However, the negligible PI observed under hypoxia is strongly indicative of a photodynamic effect under normoxia, which is confirmed by the relatively high  $\Phi_A$  value (0.19) found for this complex. In other words, although photosubstitution is possible with [4]<sup>+</sup> its phototoxicity seem here to be a consequence of ROS and most probably singlet oxygen generation. A similar observation was made for [1]Cl<sub>2</sub>, the PI of which dropped from 6.0 to 1.5 when decreasing the O<sub>2</sub> concentration from 21% to 1%. For that complex, however, the very low  $\Phi_A$  value (0.020) cannot explain the light-induced cell death. Here we suggest a PDT type I, or a dual PDT-PACT mode of action, to explain the PI observed under normoxia. Finally, for complexes [2](PF<sub>6</sub>)<sub>2</sub> and [3]Cl<sub>2</sub> accurate PI values could not be determined due to the extremely low cytotoxicity found in the dark under hypoxia. However, the cytotoxicity is clearly enhanced after light irradiation (Figure 6.4). Even if the EC<sub>50</sub> values remain rather high after light irradiation one should not discard these two compounds, but instead the biological relevance of our 2D cell monolayer protocol should first be evaluated by using alternative models of hypoxic cancer, such as 3D tumor spheroids.

## 6.4 Conclusions

In conclusion, we have shown the dependency of the cell uptake and (photo)cytotoxicity on the lipophilicity in a series of ruthenium(II) complexes bearing a non-toxic photolabile ligand. Furthermore, we have shown that the cytotoxicity of all the compounds is lower under hypoxia compared to that under normoxia probably due to the acquired chemoresistance of hypoxic cells. However, upon green light irradiation, the cytotoxicity of the PACT complex [2](PF<sub>6</sub>)<sub>2</sub> was clearly enhanced, which is the first experimental demonstration of light-induced cytotoxicity under

hypoxia for a metal-based PACT compound releasing a non-toxic organic ligand. Since PDT type II would be unlikely due to both the low oxygen concentration and the low  $\Phi_A$  of PACT compounds, we are close here to prove that the cytotoxicity of PACT complexes based on N,S photolabile ligands is indeed oxygen-independent. However, more work on cell death mechanism and the mode of action of these compounds should be performed, if possible in hypoxic 3D tumor spheroids, to conclude on the medicinal potential of this series of compounds.

## 6.5 Experimental

### 6.5.1 Synthesis

**General:** The ligands 2,2'-bipyridine (bpy), 6,6'-dimethyl-2,2'-bipyridine (dmbpy), and 4,7-diphenyl-1,10-phenanthroline (Ph<sub>2</sub>phen) were purchased from Sigma-Aldrich. Potassium hexafluoridophosphate (KPF<sub>6</sub>) was purchased from Alfa-Aesar. All reactants and solvents were used without further purification. The synthesis of *cis*-[Ru(dmbpy)<sub>2</sub>Cl<sub>2</sub>], [Ru(Ph<sub>2</sub>phen)<sub>2</sub>(bpy)]Cl<sub>2</sub> ([**5**]Cl<sub>2</sub>), and 2-(methylthio)methylpyridine (mtmp) was carried out according to literature procedures.<sup>14, 28-29</sup> The synthesis of [**1**]Cl<sub>2</sub> and [**4**]PF<sub>6</sub> is described in Chapter 3 and Chapter 5, respectively. Electrospray mass spectra (ES MS) were recorded by using a MSQ Plus Spectrometer. All <sup>1</sup>H NMR spectra were recorded on a Bruker DPX-300 or DMX-400 spectrometers. Chemical shifts are indicated in ppm relative to the residual solvent peak.

**[Ru(Ph<sub>2</sub>phen)(DMSO)<sub>2</sub>Cl<sub>2</sub>] [**7**]:** *cis*-[Ru(DMSO)<sub>4</sub>Cl<sub>2</sub>] (500 mg, 1.0 mmol) and 4,7-diphenyl-1,10-phenanthroline (340 mg, 1.0 mmol) were heated at reflux in ethanol (35 mL) for 2 h. The reaction was then cooled to room temperature and the solvent volume reduced to *ca.* 10 mL *in vacuo*. The precipitate that formed upon cooling was filtered, washed with minimal cold ethanol and copious amounts of hexane/diethyl ether, and dried under vacuum. Yield: light-brown solid, 350 mg (0.52 mmol, 51%). <sup>1</sup>H NMR (400 MHz, CDCl<sub>3</sub>)  $\delta$  10.19 (dd, *J* = 5.5, 0.9 Hz, 1H), 10.00 (dd, *J* = 5.6, 0.9 Hz, 1H), 8.07 – 7.99 (m, 2H), 7.89 (dd, *J* = 5.5, 0.9 Hz, 1H), 7.72 (dd, *J* = 5.6, 0.9 Hz, 1H), 7.63 – 7.51 (m, 10H), 3.67 (s, 3H), 3.62 (s, 3H), 3.27 (s, 3H), 2.70 (s, 3H). <sup>13</sup>C NMR (101 MHz, CDCl<sub>3</sub>)  $\delta$  155.72, 152.34, 149.95, 148.98, 135.93, 135.79, 129.81, 129.68, 129.13, 128.73, 128.27, 125.49, 125.36, 125.30, 125.23, 47.15, 46.52, 45.49, 44.37.

**[Ru(Ph<sub>2</sub>phen)(ox)(mtmp)] [**8**]:** [**7**] (300 mg, 0.45 mmol) and sodium oxalate (85 mg, 0.65 mmol) were heated at reflux in water (15 mL) for 1 h. The reaction was then cooled to room temperature and added to a hot (~60 °C) solution of 2-

(methylthio)methylpyridine (63 mg, 0.45 mmol) in ethylene glycol (15 mL). The resulting mixture was heated at reflux for 3 h, cooled to room temperature, and added dropwise to 50 mL of stirring water. After 30 min, the precipitate was filtered through a 1  $\mu\text{m}$  membrane. The solids were washed with copious amounts of water and minimal acetone before drying thoroughly under vacuum. The mixture of isomers was separated by silica column ( $R_f = 0.3$ ) in  $\text{CH}_2\text{Cl}_2/\text{CH}_3\text{OH}$  (2 – 20%  $\text{CH}_3\text{OH}$ ). Only one isomer was isolated. Yield: dark red powder, 140 mg (0.21 mmol, 71%).  $^1\text{H}$  NMR (400 MHz,  $\text{CDCl}_3$ )  $\delta$  9.63 (dd,  $J = 5.6, 0.9$  Hz, 1H), 9.34 (dd,  $J = 5.4, 0.9$  Hz, 1H), 8.08 (qd,  $J = 9.4, 0.9$  Hz, 2H), 7.81 (d,  $J = 5.3$  Hz, 1H), 7.66 – 7.46 (m, 11H), 7.44 – 7.35 (m, 2H), 6.84 – 6.78 (m, 1H), 6.59 (td,  $J = 6.1, 2.4$  Hz, 1H), 4.70 (d,  $J = 13.4$  Hz, 1H), 4.61 (d,  $J = 13.5$  Hz, 1H), 2.45 (s, 3H).  $^{13}\text{C}$  NMR (101 MHz,  $\text{CDCl}_3$ )  $\delta$  168.86, 167.83, 163.08, 153.42, 152.04, 151.05, 149.48, 148.15, 145.53, 136.37, 136.29, 134.29, 129.96, 129.78, 129.53, 129.35, 129.21, 129.17, 129.03, 128.39, 125.91, 125.48, 124.44, 123.14, 122.34, 45.79, 16.12. Anal. Calcd for  $\text{C}_{33}\text{H}_{25}\text{N}_3\text{O}_4\text{RuS} \cdot 3\text{H}_2\text{O}$ : C, 55.45; H, 4.37; N, 5.88 Found: C, 56.08; H, 4.56; N, 5.46.

**[Ru(bpy)(Ph<sub>2</sub>phen)(mtmp)](PF<sub>6</sub>)<sub>2</sub> [2](PF<sub>6</sub>)<sub>2</sub>: [8]** (140 mg, 0.21 mmol) was suspended in  $\text{CH}_3\text{CN}$  (3 mL) and then perchloric acid 1 M (3 mL) was added. After refluxing for 1 h, a red-brown solution containing the ruthenium-solvate was obtained and, after cooling, it was poured in stirring water (15 mL). The orange solid that precipitated was filtered and dried to yield  $[\text{Ru}(\text{Ph}_2\text{phen})(\text{mtmp})(\text{CH}_3\text{CN})_2](\text{ClO}_4)_2$ . The intermediate was dissolved in an ethylene glycol solution (15 mL) containing the bpy ligand (33 mg, 0.21 mmol) and heated at 100 °C for 6 h. The deep red mixture was cooled to room temperature and poured in stirring aqueous  $\text{KPF}_6$  solution to precipitate the crude complex as the hexafluoridophosphate salt. Configurational isomers were resolved by column chromatography on silica  $\text{CH}_2\text{Cl}_2/\text{CH}_3\text{OH}$  95:5. Three fractions were obtained from a long orange band ( $R_f \sim 0.5$ ), from which only the last fraction contained a pure isomer (3.2 mg, 2%, Isomer B, **[2b]**(PF<sub>6</sub>)<sub>2</sub>). A mixture of isomers A/B in a ration 0.23:1 has been used (60 mg, 28%).  $^1\text{H}$  NMR (400 MHz,  $\text{CD}_3\text{CN}$ )  $\delta$  9.63 (d,  $J = 5.5$  Hz, 1H<sub>B</sub>), 9.39 (d,  $J = 5.7$  Hz, 1H<sub>A</sub>), 8.61 (d,  $J = 8.2$  Hz, 1H<sub>B</sub>), 8.58 – 8.51 (m, 2H<sub>A</sub>), 8.43 (d,  $J = 8.1$  Hz, 1H<sub>B</sub>), 8.31 (dd,  $J = 8.0, 1.5$  Hz, 1H<sub>B</sub>), 8.29 – 8.23 (m, 1H<sub>B</sub> + 1H<sub>A</sub>), 8.22 – 8.14 (m, 2H<sub>B</sub> + 2H<sub>A</sub>), 8.14 – 8.03 (m, 3H<sub>A</sub>), 8.02 (d,  $J = 5.5$  Hz, 1H<sub>B</sub>), 7.99 (d,  $J = 5.5$  Hz, 1H<sub>B</sub>), 7.93 (ddd,  $J = 7.8, 6.5, 1.5$  Hz, 1H<sub>B</sub>), 7.86 (td,  $J = 7.8, 1.6$  Hz, 1H<sub>A</sub>), 7.81 – 7.51 (m, 15H<sub>B</sub> + 15H<sub>A</sub>), 7.48 (dd,  $J = 5.9, 1.5$  Hz, 1H<sub>A</sub>), 7.32 (ddd,  $J = 7.1, 5.6, 1.3$  Hz, 1H<sub>A</sub>), 7.24 (d,  $J = 5.5$  Hz, 1H<sub>B</sub>), 7.17 (td,  $J = 7.2, 5.6, 1.4$  Hz, 1H<sub>B</sub> + 1H<sub>A</sub>), 6.98 (ddd,  $J = 7.7, 5.8, 1.6$  Hz, 1H<sub>B</sub>), 4.82 (d,  $J = 16.5$  Hz, 1H<sub>B</sub>), 4.74 (d,  $J = 16.7$  Hz, 1H<sub>A</sub>), 4.28 (dd,  $J = 16.6, 4.8$  Hz, 1H<sub>B</sub> + 1H<sub>A</sub>), 1.59 (s, 3H<sub>B</sub>), 1.32 (s, 3H<sub>A</sub>).  $^{13}\text{C}$  NMR (101

MHz, CD<sub>3</sub>CN)  $\delta$  162.96, 162.63, 158.56, 157.73, 153.51, 153.33, 153.09, 152.90, 151.98, 150.77, 150.61, 150.05, 149.66, 148.72, 139.46, 138.67, 138.55, 136.62, 136.53, 130.79, 130.70, 130.13, 130.06, 129.20, 127.78, 127.26, 127.19, 127.12, 126.92, 125.86, 125.59, 125.55, 124.93, 45.36, 17.04. High Resolution ES MS *m/z* (calcd): 364.57519 (364.57446, [2]<sup>2+</sup>), 874.11407 (874.11365, [2 + PF<sub>6</sub>]<sup>+</sup>). Anal. Calcd for C<sub>41</sub>H<sub>33</sub>F<sub>12</sub>N<sub>5</sub>P<sub>2</sub>RuS: C, 48.34; H, 3.26; N, 6.87 Found: C, 48.21; H, 3.41; N, 6.82.

**[Ru(dmbpy)<sub>2</sub>(mtmp)]Cl<sub>2</sub> [3]Cl<sub>2</sub>**: [Ru(dmbpy)<sub>2</sub>Cl<sub>2</sub>] (750 mg, 1.4 mmol), Et<sub>3</sub>N (200  $\mu$ L, 1.4 mmol), and mtmp (190 mg, 1.4 mmol) were dissolved in deaerated ethylene glycol (10 mL) and heated under N<sub>2</sub> at 100 °C for 15 min. After the reaction mixture was cooled to room temperature, water (20 mL) was added and the mixture was washed with CH<sub>2</sub>Cl<sub>2</sub> (3  $\times$  20 mL). A saturated aqueous KPF<sub>6</sub> solution was added to the water layer and the complex was extracted with CH<sub>2</sub>Cl<sub>2</sub> (3  $\times$  20 mL). After reducing the volume of CH<sub>2</sub>Cl<sub>2</sub> (5 mL), a saturated acetone Bu<sub>4</sub>NCl solution (15 mL) was added to the CH<sub>2</sub>Cl<sub>2</sub> mixture and put in an ice bath for 15 min. A red precipitate was afforded, which was filtered and washed with acetone and diethyl ether. Yield: 750 mg (60%). <sup>1</sup>H NMR (300 MHz, D<sub>2</sub>O)  $\delta$  8.35 – 8.26 (m, 2H), 8.24 (d, *J* = 8.1 Hz, 1H), 8.07 (t, *J* = 7.9 Hz, 1H), 8.03 – 7.96 (m, 2H), 7.93 (t, *J* = 7.9 Hz, 1H), 7.74 – 7.61 (m, 2H), 7.55 (d, *J* = 7.7 Hz, 1H), 7.45 (t, *J* = 7.9 Hz, 2H), 7.39 – 7.32 (m, 2H), 7.28 (d, *J* = 7.8 Hz, 1H), 7.10 (t, *J* = 6.7 Hz, 1H), 4.11 (d, *J* = 17.8 Hz, 1H), 3.96 (d, *J* = 17.8 Hz, 1H), 2.77 (s, 3H), 2.23 (s, 3H), 2.04 (s, 3H), 1.76 (s, 3H), 0.97 (s, 3H). <sup>13</sup>C NMR (75 MHz, D<sub>2</sub>O)  $\delta$  167.00, 166.55, 166.28, 166.14, 162.14, 159.57, 159.41, 159.37, 159.19, 154.98, 138.44, 138.37, 137.84, 137.54, 137.48, 127.62, 127.24, 127.16, 125.83, 123.89, 123.53, 122.31, 122.10, 121.13, 120.76, 44.93, 26.63, 24.95, 23.79, 23.46, 16.15. High Resolution ES MS *m/z* (calcd): 304.57488 (304.57446, [3]<sup>2+</sup>).

## 6.5.2 Single Crystal X-Ray crystallography

**General:** All reflection intensities were measured at 110(2) K using a SuperNova diffractometer (equipped with Atlas detector) with Mo *K* $\alpha$  radiation ( $\lambda$  = 0.71073 Å) under the program CrysAlisPro (Version CrysAlisPro 1.171.39.29c, Rigaku OD, 2017). The same program was used to refine the cell dimensions and for data reduction. The structure was solved with the program SHELXS-2014/7 and was refined on *F*<sup>2</sup> with SHELXL-2014/7.<sup>30</sup> Numerical absorption correction based on gaussian integration over a multifaceted crystal model was applied using CrysAlisPro. The temperature of the data collection was controlled using the system Cryojet (manufactured by Oxford Instruments). The H atoms were placed at calculated positions (unless otherwise specified) using the instructions AFIX 23, AFIX 43, AFIX

137 or AFIX 147 with isotropic displacement parameters having values 1.2 or 1.5  $U_{eq}$  of the attached C or O atoms. The H atoms attached to O1W (lattice water molecule) were found from difference Fourier maps, and their coordinates were refined freely.

**Crystal growing:**  $[3]Cl_2$  (1.0 mg) was dissolved in methanol (1 mL, 1.5 mM) and transferred (650  $\mu$ L) into a GC vial, which was placed in a larger vial that contained diisopropyl ether (2700  $\mu$ L) as a counter solvent. The large vial was stoppered. After a few days quality crystals suitable for X-ray structure determination were obtained by vapor diffusion.

**Details of the crystal structure:** The structure is ordered except for a small amount of very disordered (probably partially occupied or even a mixture of) lattice molecules in the crystal lattice. Their contribution has been removed from the final refinement using the SQUEEZE procedure in Platon.<sup>31</sup>  $0.54 \times 0.41 \times 0.11 \text{ mm}^3$ , triclinic,  $P-1$ ,  $a = 10.4877(3)$ ,  $b = 12.1635(3)$ ,  $c = 14.3238(3) \text{ \AA}$ ,  $\alpha = 104.346(2)$ ,  $\beta = 98.3169(19)$ ,  $\gamma = 99.403(2)^\circ$ ,  $V = 1713.41(8) \text{ \AA}^3$ ,  $Z = 2$ ,  $\mu = 0.71 \text{ mm}^{-1}$ ,  $T_{min}-T_{max}$ : 0.250-1.000. 27712 reflections were measured up to a resolution of  $(\sin \theta/\lambda)_{max} = 0.650 \text{ \AA}^{-1}$ . 7878 reflections were unique ( $R_{int} = 0.023$ ), of which 7423 were observed [ $I > 2\sigma(I)$ ]. 401 parameters were refined using 3 restraints.  $R1/wR2$  [ $I > 2\sigma(I)$ ]: 0.02180/0.0515.  $R1/wR2$  [*all reflections*]: 0.0238/0.0527.  $S = 1.046$ . Residual electron density found between  $-0.65$  and  $0.52 \text{ e \AA}^{-3}$ .

### 6.5.3 Photochemistry

When monitoring photoreactions with UV-vis spectroscopy and mass spectrometry, a Cary 50 Varian spectrometer equipped with temperature control set to 298 K and a LED light source ( $\lambda_{ex} = 521 \text{ nm}$ , with a Full Width at Half Maximum of 33 nm) with a photon flux between  $2.39$  and  $6.25 \cdot 10^{-8} \text{ mol} \cdot \text{s}^{-1}$  was used. The irradiation experiments were performed in a quartz cuvette containing 3 mL of solution. A stock solution of the desired complex was prepared using either  $H_2O$  or  $CH_3CN$ , which was then diluted in the cuvette to a working solution concentration. The sample was deaerated 15 min by gentle bubbling of  $N_2$  and the atmosphere was kept inert during the experiment by a gentle flow of  $N_2$  on top of the cuvette. A UV-vis spectrum was measured every 30 s for the first 10 min, every 1 min for the next 10 min, and eventually every 10 min until the end of the experiment. Data was analysed with Microsoft Excel. Experimental conditions are detailed in Table 6.4.

Table 6.4. Conditions of the photoreactions monitored with MS and UV-vis.

Complex	Solvent	Stock solution			Working sol. (mM)	Photon flux (mol·s <sup>-1</sup> )
		w (mg)	V (mL)	M (mM)		
[2](PF <sub>6</sub> ) <sub>2</sub>	CH <sub>3</sub> CN	1.1	10	0.108	0.036	6.21·10 <sup>-8</sup>
[3]Cl <sub>2</sub>	CH <sub>3</sub> CN	0.9	10	0.132	0.088	6.25·10 <sup>-8</sup>
[3]Cl <sub>2</sub>	H <sub>2</sub> O	1.0	10	0.147	0.073	2.39·10 <sup>-8</sup>

#### 6.5.4 Cell culture and EC<sub>50</sub> (photo)cytotoxicity assay

The PC3pro4 cell line was provided by Prof. Dr. Ewa Snaar-Jagalska. Following the protocol described in Appendix II, 24 h after seeding A549 (5,000 and 6,000 cells/well under normoxic and hypoxic conditions, respectively) or PC3pro4 cells (4,000 cells/well under both normoxic and hypoxic conditions), aliquots (100 μL) of six different concentrations of freshly prepared stock solutions of [1]Cl<sub>2</sub>, [2](PF<sub>6</sub>)<sub>2</sub>, [3]Cl<sub>2</sub>, [4]PF<sub>6</sub>, [5]Cl<sub>2</sub>, or Rose Bengal in OptiMEM were added. Plates were incubated in the dark for an additional 24 h. After this period, half of the plates were irradiated with green light ( $\lambda_e = 520$  nm, light dose = 18.8 J·cm<sup>-2</sup>) and the other half were kept in the dark. After irradiation, all the plates were incubated for an additional 48 h before fixation and cell quantification using an SRB assay. As shown in Figure AVII.2, after 15 min irradiation (18.8 J·cm<sup>-2</sup> using the normoxic setup) all the complexes seem fully photoactivated, except for complex [4]PF<sub>6</sub> and [5]Cl<sub>2</sub>. The first has indeed a very low photosubstitution quantum yield (Chapter 5) and it should be irradiated for too long to achieve full activation. The latter, like its analogue [Ru(bpy)<sub>3</sub>]Cl<sub>2</sub>, does not photosubstitute any of the ligands but deactivates by phosphorescence emission.

The protocol followed under hypoxic conditions has been described previously by Lameijer *et al.*<sup>13</sup> In short, cells were passaged at least twice under hypoxia (1% O<sub>2</sub>), before performing the (photo)cytotoxicity assay. The light irradiation was performed using a small incubator with a glass cover in order to irradiate while keeping the atmosphere at 1% O<sub>2</sub>. Due to the glass cover the power intensity of the LED array is lower than that in the irradiation set up for normoxic conditions.<sup>13</sup> Thus, 27.5 min of green light irradiation in the hypoxic setup corresponded to the same light dose as 15 min irradiation in the normoxic setup (18.8 J·cm<sup>-2</sup>).

#### 6.5.5 Cellular uptake

Cell uptake studies for complexes [1]Cl<sub>2</sub>, [2](PF<sub>6</sub>)<sub>2</sub>, [3]Cl<sub>2</sub>, [4]PF<sub>6</sub>, and [5]Cl<sub>2</sub> were conducted on A549 lung cancer cells. 1.6·10<sup>6</sup> cells were seeded in OptiMEM complete

(10 mL) in 75 cm<sup>2</sup> T-flasks at t = 0 h. At t = 24 h the media was aspirated and cells were treated with solutions of [1]Cl<sub>2</sub>, [2](PF<sub>6</sub>)<sub>2</sub>, [3]Cl<sub>2</sub>, [4]PF<sub>6</sub>, or [5]Cl<sub>2</sub> to give a final concentration at the EC<sub>50</sub> in the dark (3.4, 65, 160, 0.08, and 3.8 μM, respectively) in a total volume of 10 mL. After 24 h of drug incubation at 37 °C and 21% O<sub>2</sub>, the medium was aspirated and the cells were washed twice with PBS (5 mL). Then, the cells were trypsinized (2 mL), suspended with OptiMEM (8 mL), and centrifuged (1200 rpm, 4 min). After aspiration of the supernatant, the cells were resuspended in PBS (1 mL) and counted. After a second centrifugation, the supernatant was discarded. For metal and protein quantification, the pellets were resuspended in demineralized water (250 μL) and lysed for 30 min by ultrasonication. The protein content of lysates was determined by the Bradford method, and the ruthenium content was determined by Atomic Absorption Spectroscopy.

A contraAA 700 high-resolution continuum-source atomic absorption spectrometer (Analytik Jena AG) was used. Pure samples of the respective complex was used as standard and calibration was done in a matrix-matched manner (meaning all samples and standards were adjusted to the same cellular protein concentration of 1.0 mg/mL by dilution with distilled water if necessary). Triton-X 100 (1%, 10 μL), as well as nitric acid (13%, 10 μL), were added to each standard sample (100 μL). Samples were injected (25 μL) into coated standard graphite tubes (Analytik Jena AG) and thermally processed as previously described by Schatzschneider *et al.*<sup>32</sup> Drying steps were adjusted and the atomization temperature set to 2400 °C. Ruthenium was quantified at a wavelength of 349.90 nm. The mean integrated absorbance of double injections were used throughout the measurements. The data from two independent biological replications was used to obtain the uptake values shown in Table 6.2.

## 6.6 References

1. T. Sainuddin, M. Pinto, H. Yin, M. Hetu, J. Colpitts and S. A. McFarland, *J. Inorg. Biochem.*, **2016**, 158, 45-54.
2. K. T. Hufziger, F. S. Thowfeik, D. J. Charboneau, I. Nieto, W. G. Dougherty, W. S. Kassel, T. J. Dudley, E. J. Merino, E. T. Papish and J. J. Paul, *J. Inorg. Biochem.*, **2014**, 130, 103-111.
3. B. S. Howerton, D. K. Heidary and E. C. Glazer, *J. Am. Chem. Soc.*, **2012**, 134, 8324-8327.
4. J. A. Cuello-Garibo, M. S. Meijer and S. Bonnet, *Chem. Commun.*, **2017**, 53, 6768-6771.
5. Q.-X. Zhou, W.-H. Lei, J.-R. Chen, C. Li, Y.-J. Hou, X.-S. Wang and B.-W. Zhang, *Chem. - Eur. J.*, **2010**, 16, 3157-3165.
6. H. Huang, B. Yu, P. Zhang, J. Huang, Y. Chen, G. Gasser, L. Ji and H. Chao, *Angew. Chem.*, **2015**, 127, 14255-14258.
7. J. Fong, K. Kasimova, Y. Arenas, P. Kaspler, S. Lazic, A. Mandel and L. Lilje, *Photochem. Photobiol. Sci.*, **2015**, 14, 2014-2023.
8. W. R. Wilson and M. P. Hay, *Nat. Rev. Cancer*, **2011**, 11, 393-410.
9. N. M. Mazure, *Nature*, **2006**, 441, 437.

10. B. Keith and M. C. Simon, *Cell*, **2007**, 129, 465-472.
11. A. M. Weljie and F. R. Jirik, *Int. J. Biochem. Cell Biol.*, **2011**, 43, 981-989.
12. S. Rockwell, I. T. Dobrucki, E. Y. Kim, S. T. Marrison and V. T. Vu, *Curr. Mol. Med.*, **2009**, 9, 442-458.
13. L. N. Lameijer, D. Ernst, S. L. Hopkins, M. S. Meijer, S. H. C. Askes, S. E. Le Dévédec and S. Bonnet, *Angew. Chem., Int. Ed.*, **2017**, 56, 11549-11553.
14. O. Mazuryk, K. Magiera, B. Rys, F. Suzenet, C. Kieda and M. Brindell, *JBIC, J. Biol. Inorg. Chem.*, **2014**, 19, 1305-1316.
15. C. S. Burke and T. E. Keyes, *Rsc Advances*, **2016**, 6, 40869-40877.
16. J. H. Wallenstein, J. Sundberg, C. J. McKenzie and M. Abrahamsson, *Eur. J. Inorg. Chem.*, **2016**, 897-906.
17. C. Mari, V. Pierroz, R. Rubbiani, M. Patra, J. Hess, B. Spingler, L. Oehninger, J. Schur, I. Ott, L. Salassa, S. Ferrari and G. Gasser, *Chem. - Eur. J.*, **2014**, 20, 14421-14436.
18. A. Frei, R. Rubbiani, S. Tubafard, O. Blacque, P. Anstaett, A. Felgentrager, T. Maisch, L. Spiccia and G. Gasser, *J. Med. Chem.*, **2014**, 57, 7280-7292.
19. G. Shi, S. Monro, R. Hennigar, J. Colpitts, J. Fong, K. Kasimova, H. Yin, R. DeCoste, C. Spencer, L. Chamberlain, A. Mandel, L. Lilge and S. A. McFarland, *Coord. Chem. Rev.*, **2015**, 282-283, 127-138.
20. D. Garcia-Fresnadillo, Y. Georgiadou, G. Orellana, A. M. Braun and E. Oliveros, *Helv. Chim. Acta*, **1996**, 79, 1222-1238.
21. C. Tanielian and C. Wolff, *J. Phys. Chem.*, **1995**, 99, 9825-9830.
22. S. L. Hopkins, B. Siewert, S. H. C. Askes, P. Veldhuizen, R. Zwier, M. Heger and S. Bonnet, *Photochem. Photobiol. Sci.*, **2016**, 15, 644-653.
23. C. A. Pettaway, S. Pathak, G. Greene, E. Ramirez, M. R. Wilson, J. J. Killion and I. J. Fidler, *Clin. Cancer Res.*, **1996**, 2, 1627-1636.
24. R. W. Horobin, J. C. Stockert and F. Rashid-Doubell, *Histochem. Cell Biol.*, **2006**, 126, 165-175.
25. C. A. Puckett and J. K. Barton, *J. Am. Chem. Soc.*, **2007**, 129, 46-47.
26. T. L. Riss and R. A. Moravec, *Assay Drug Dev. Technol.*, **2004**, 2, 51-62.
27. L. Fetzter, B. Boff, M. Ali, M. Xiangjun, J.-P. Collin, C. Sirlin, C. Gaidon and M. Pfeffer, *Dalton Trans.*, **2011**, 40, 8869-8878.
28. J. P. Collin and J. P. Sauvage, *Inorg. Chem.*, **1986**, 25, 135-141.
29. E. Reisner, T. C. Abikoff and S. J. Lippard, *Inorg. Chem.*, **2007**, 46, 10229-10240.
30. G. M. Sheldrick, *Acta Crystallogr., Sect. A: Found. Adv.*, **2008**, 64, 112-122.
31. A. L. Spek, *Acta Crystallogr., Sect. D: Biol. Crystallogr.*, **2009**, 65, 148-155.
32. U. Schatzschneider, J. Niesel, I. Ott, R. Gust, H. Alborzinia and S. Wölfel, *ChemMedChem*, **2008**, 3, 1104-1109.



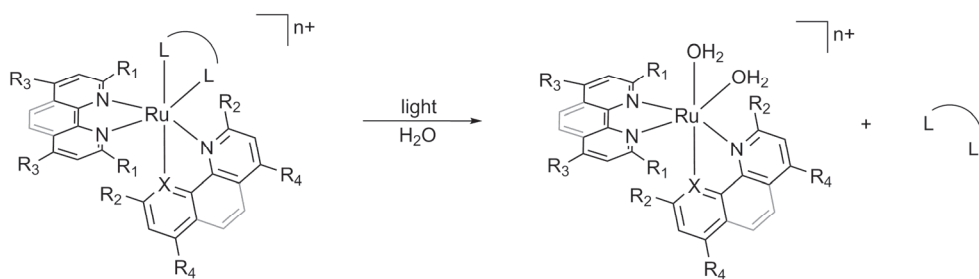
# 7

## Summary, conclusions, and outlook

*The main goal of the research described in this thesis was the development of new photoactivated chemotherapy (PACT) ruthenium(II) complexes bearing a non-toxic photolabile ligand. We first investigated whether non-toxic ligands such as L-proline, 2-(methylthio)methylpyridine (mtmp), or 3-(methylthio)propylamine (mtpa), once coordinated to ruthenium(II) complexes, could be photosubstituted upon visible light irradiation. The lipophilicity, and in some cases the strain of the ruthenium(II) complexes, were systematically varied and the effects of such variations on the cytotoxicity of the complexes in the dark and under light irradiation were studied. In the second part, the best ligand candidates (i.e. mtmp and mtpa) were coordinated to cyclometalated ruthenium complexes of the type  $[Ru(bpy)(phpy)(S,N)]PF_6$  ( $bpy = 2,2'$ -bipyridine and  $phpy = 2$ -phenylpyridine), to shift the absorption of the complex to the red region of the spectrum. The photosubstitution properties of these cyclometalated complexes were investigated in detail. The most promising ruthenium complexes were tested in cancer cell monolayers under hypoxic conditions (1%  $O_2$ ) to investigate their mode of action and distinguish between PACT and PDT.*

## 7.1 Summary

The main goal of the research described in this thesis was the development of new photoactivated chemotherapy (PACT) ruthenium(II) complexes bearing a non-toxic photolabile ligand. The suitability of the natural amino acid L-proline as protecting ligand in a series of complexes of the type  $[\text{Ru}(\text{N},\text{N})_2(\text{L-prolinate})]\text{PF}_6$  is reported in Chapter 2. The number of sterically hindering methyl groups increased from zero in  $[\text{Ru}(\text{bpy})_2(\text{L-prolinate})]\text{PF}_6$  (bpy = 2,2'-bipyridine, **[1]** $\text{PF}_6$ ) to two in  $[\text{Ru}(\text{bpy})(\text{dmbpy})(\text{L-prolinate})]\text{PF}_6$  (dmbpy = 6,6'-dimethyl-2,2'-bipyridine, **[2]** $\text{PF}_6$ ), and up to four in  $[\text{Ru}(\text{dmbpy})_2(\text{L-prolinate})]\text{PF}_6$  (**[3]** $\text{PF}_6$ ). The photoreactivity of this type of complexes was found to be solvent dependent: while in water no substitution was observed upon light irradiation for any complex of the series, in  $\text{CH}_3\text{CN}$  the strained complexes **[2]** $\text{PF}_6$  and **[3]** $\text{PF}_6$  photosubstituted either L-proline or dmbpy in parallel. Interestingly, in water **[1]** $\text{PF}_6$  loses two hydrogens upon light irradiation in presence of aerial  $\text{O}_2$ , photooxidizing to the imino complex  $[\text{Ru}(\text{bpy})_2(\text{L-prolinate} - 2\text{H})]\text{PF}_6$ . The addition of electron-donating methyl groups in **[2]** $\text{PF}_6$  and **[3]** $\text{PF}_6$  decreases the acidity of the amine, preventing its oxidation to imine. Thus, due to the stability of the ruthenium-prolinate complexes in water and non-selective photosubstitution in  $\text{CH}_3\text{CN}$ , the negatively charged L-prolinate was discarded as protecting ligand, and by extension any natural amino acid with N,O coordination.



*Scheme 7.1. Photosubstitution of a bidentate ligand upon light irradiation in water in a given ruthenium(II) polypyridyl complex. In the research described in this thesis we have tuned the strain and lipophilicity of the complexes by changing the functional groups in  $R_1$ ,  $R_2$ ,  $R_3$ ,  $R_4$ .  $X = \text{N}$  or  $\text{C}$ .*

Glazer *et al.* reported the photocytotoxicity of  $[\text{Ru}(\text{bpy})_2(\text{dmbpy})]\text{Cl}_2$  against lung cancer cells (A549 cells), which was attributed, by analogy with cisplatin, to the photogenerated compound  $\text{cis}-[\text{Ru}(\text{bpy})_2(\text{OH}_2)_2]^{2+}$ .<sup>1</sup> However, in Chapter 3 we show that dmbpy, which is also released, is cytotoxic by itself. Therefore, is  $[\text{Ru}(\text{bpy})_2(\text{OH}_2)_2]^{2+}$  cytotoxic? Can any PDT effect be discarded? In order to investigate the role of  $[\text{Ru}(\text{bpy})_2(\text{OH}_2)_2]^{2+}$  we compared the photocytotoxicity of

[Ru(bpy)<sub>2</sub>(dmbpy)]Cl<sub>2</sub> with that of [Ru(bpy)<sub>2</sub>(mtmp)]Cl<sub>2</sub> (mtmp = 2-(methylthio)methylpyridine), which has a neutral sulfur-based ligand. Both complexes are comparable: they generate [Ru(bpy)<sub>2</sub>(OH<sub>2</sub>)<sub>2</sub>]<sup>2+</sup> upon light irradiation, they have low singlet oxygen generation quantum yields, and they have similar lipophilicity and low cellular uptake. The difference is that the released mtmp is not cytotoxic by itself. When treating lung cancer cells (A549 cell line) with [Ru(bpy)<sub>2</sub>(mtmp)]Cl<sub>2</sub>, no cytotoxic effect was observed either in the dark or upon light irradiation, thus we concluded that the photogenerated [Ru(bpy)<sub>2</sub>(OH<sub>2</sub>)<sub>2</sub>]<sup>2+</sup> is not cytotoxic, and that the cytotoxicity observed after irradiation of [Ru(bpy)<sub>2</sub>(dmbpy)]Cl<sub>2</sub> is caused by the released dmbpy. However, the more lipophilic [Ru(Ph<sub>2</sub>phen)<sub>2</sub>(mtmp)]Cl<sub>2</sub> (Ph<sub>2</sub>phen = 4,7-Diphenyl-1,10-phenanthroline) shows enhanced cytotoxicity upon light irradiation. Thus, a ruthenium center can be cytotoxic, but the complex needs to be lipophilic enough to be taken up.

Knowing the suitability of N,S molecules as protecting ligands and the importance of a certain grade of lipophilicity to achieve cytotoxicity, a new series of complexes bearing the N,S ligand 3-(methylthio)propylamine (mtpa) was synthesized as described in Chapter 4. In this series the strain and the lipophilicity was increased by addition of methyl groups in positions 6 and 6' of bpy, as reported in Chapter 2 for L-prolinate complexes. The number of methyl groups has a crucial effect on the photochemistry and cytotoxicity of these complexes. While the non-strained complex [Ru(bpy)<sub>2</sub>(mtpa)](PF<sub>6</sub>)<sub>2</sub> does not fully photosubstitute mtpa and thus is not photocytotoxic against A549 cells, the more strained complex [Ru(bpy)(dmbpy)(mtpa)](PF<sub>6</sub>)<sub>2</sub> shows efficient mtpa photosubstitution upon blue light irradiation, leading to photocytotoxicity. However, if the complex is too strained, as in [Ru(dmbpy)<sub>2</sub>(mtpa)](PF<sub>6</sub>)<sub>2</sub>, it also activates thermally in the dark, losing the photoactivation feature. The characterization of these complexes was not an easy task. Besides the chirality of the octahedron ( $\Delta$  or  $\Lambda$ ), two other sources of isomerism are present: the configuration (*S* or *R*) of the sulfur atom, and the chair inversion of the six-membered ring resulting from the coordination of the N,S chelating ligand to the ruthenium center. The latter transforms an axial thioether methyl group (*ax*) into an equatorial one (*eq*) and *vice versa*, making a total of four possible isomers for [Ru(bpy)<sub>2</sub>(mtpa)](PF<sub>6</sub>)<sub>2</sub> and [Ru(dmbpy)<sub>2</sub>(mtpa)](PF<sub>6</sub>)<sub>2</sub>, and eight for [Ru(bpy)(dmbpy)(mtpa)](PF<sub>6</sub>)<sub>2</sub>, due to the thioether sulfur being *trans* either to bpy or to dmbpy. Despite the complexity of the stereochemical identification of these complexes, they were all fully characterized by a combination of 2D NMR spectroscopy and DFT calculations. The interligand interactions between the hydrogen

atoms in axial position of the mtpa chair conformation and the substituents in the position 6 of the bpy appeared to be the main driving force in the stereoselectivity of the synthesis.

As N,S ligands seemed superior to N,O ligands due to their selective photosubstitution, they were chosen for the synthesis of photoactivatable ruthenium-based cyclometalated complexes of the type  $[\text{Ru}(\text{bpy})(\text{phpy})(\text{N,S})]\text{PF}_6$  ( $\text{phpy}^- = 2\text{-phenylpyridine}$ , Chapter 5). The effect of the size of the chelate ring involving the N,S ligand and the ruthenium center (five- vs. six-membered ring) and of the nature of the nitrogen donor atom (primary amine vs. pyridine) was systematically investigated. Coordination of 2-(methylthio)ethyl-2-pyridine (mtep) or mtpa to the ruthenium(II) center, which results in a six-membered ring with chair conformation, leads to one isomer out of the 16 possible. However, when the N,S ligand leads to a five-membered chelate ring (2-(methylthio)ethylamine (mtea) or mtmp), two or three isomers were obtained, which were difficult to isolate. Thus, the size of the N,S chelating ligands can be chosen to tune the stereoselectivity of the reaction. Furthermore, complexes with N,S ligands leading to a six-membered chelate ring showed faster photosubstitution in  $\text{CH}_3\text{CN}$  than their five-membered chelate ring analogues. Probably rechelation is faster in the latter, lowering the overall photosubstitution rates. Finally, if the nitrogen of the N,S ligand is a pyridine, the complex was found to be less sensitive to oxidation than if it was a primary amine. We ascribe this effect to the location of the  $\pi$ -accepting pyridyl ligand *trans* to the carbon donor atom, which stabilizes the high electron density on the ruthenium center brought by cyclometalation. The complex  $[\text{Ru}(\text{bpy})(\text{phpy})(\text{mtep})]\text{PF}_6$ , which bears a pyridyl-based N,S ligand forming a six-membered chelate ring, fulfills all criteria to become a promising PACT agent: it can be synthesized in a stereoselectively manner, it is stable under  $\text{O}_2$  in the dark, and it photosubstitutes efficiently the non-toxic N,S ligand upon irradiation with green light.

In the last chapter, we questioned whether or not the ruthenium compounds described in this thesis are true PACT agents. In other words: can their low singlet oxygen production quantum yields ( $\Phi_{\Delta}$ ) explain the observed cytotoxicity? First, as a control of the hypoxic cell irradiation setup we showed that the photocytotoxicity of the photosensitizers Rose Bengal and  $[\text{Ru}(\text{Ph}_2\text{phen})_2(\text{bpy})]\text{Cl}_2$  is seriously impaired at 1%  $\text{O}_2$ . The low dioxygen concentration lowered the photo index (PI), *i.e.* the ratio of the  $\text{EC}_{50}$  value obtained in a dark control and that after light irradiation, to 3.0 and 1.9, respectively, compared to the much higher values observed under normoxia (>400 and 29, respectively). Using the same set up, the cytotoxicity of the supposed PACT

complexes  $[\text{Ru}(\text{bpy})(\text{Ph}_2\text{phen})(\text{mtmp})](\text{PF}_6)_2$  and  $[\text{Ru}(\text{dmbpy})_2(\text{mtmp})]\text{Cl}_2$  was tested, which showed a clear cytotoxicity enhancement after green light irradiation under hypoxia. The cytotoxicity in the dark was too low to establish a PI, which for a true PACT agent should be in the same range under normoxia and hypoxia.<sup>2</sup> Overall, the hypoxic conditions appear to be interesting for testing whether photosubstitutionally active compounds are indeed true, oxygen-independent PACT compounds, or weak but targeted PDT agents.

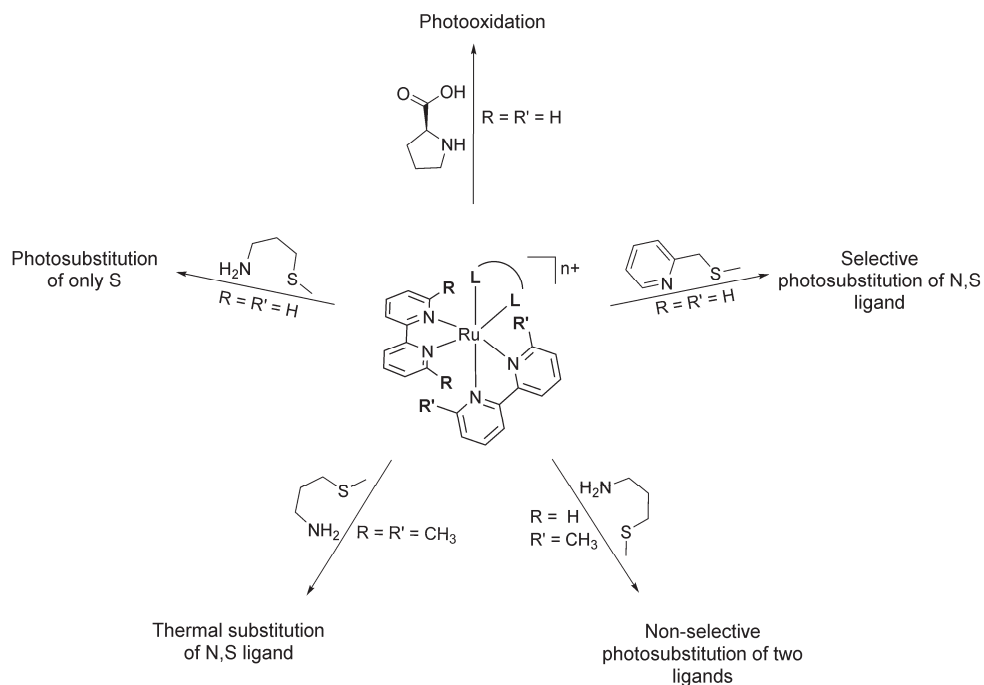
## 7.2 Discussion and conclusions

### 7.2.1 How to design a ruthenium complex capable of photosubstituting a bidentate ligand?

In the last decade, the photoreactivity of ruthenium polypyridyl complexes has been extensively studied. It is commonly accepted that thermal population of a triplet metal-centered state ( $^3\text{MC}$ ) following photochemical generation of a triplet metal-to-ligand charge transfer state ( $^3\text{MLCT}$ ) is the critical step to photosubstitute a ligand. Indeed, in the  $^3\text{MC}$  state the coordination bond between one of the photolabile ligand L and the ruthenium center elongates, thus becoming weaker and more prone to cleavage by substitution of the leaving ligand by an entering solvent molecule.<sup>3</sup> In phosphorescent complexes such as  $[\text{Ru}(\text{bpy})_3]^{2+}$ , the  $^3\text{MC}$  state is very high in energy, which prevents photosubstitution to occur. As mentioned in previous chapters, there are two methods to make the  $^3\text{MC}$  states more accessible. One is to distort the octahedral coordination sphere of the metal, upon which the crystal field splitting energy is decreased, making the thermal population of a metal-based  $e_g$  orbital from a half-filled ligand-based  $\pi^*$  orbital possible.<sup>4</sup> The other method is to tune the electronic structure of the complex by changing the nature of the ligand to be photosubstituted.<sup>5</sup>

In the research described in this thesis we have followed both approaches (Scheme 7.2). In absence of octahedral distortion, *i.e.* in a complex of the type  $[\text{Ru}(\text{bpy})_2(\text{L})]^{n+}$ , the nature of the coordinating atoms of ligand L has a great impact on photosubstitution. When L is L-proline, the complex  $[\text{Ru}(\text{bpy})_2(\text{L-proline})]^+$  does not photosubstitute any ligand due the strong  $\sigma$ -donor properties of the carboxylate moiety. However, when the negatively charged carboxylate group is substituted by a thioether donor group, photosubstitution of the sulfur donor atom by a solvent molecule does occur in water, as shown for  $[\text{Ru}(\text{bpy})_2(\text{mtpa})](\text{PF}_6)_2$ . Interestingly, upon light irradiation the photoproduct  $[\text{Ru}(\text{bpy})_2(\text{mtpa-}\kappa\text{N})(\text{OH}_2)]^{2+}$  was obtained in the steady state, *i.e.* full photosubstitution of mtpa by two water molecules did not occur. When

the primary amine of mtpa was replaced by pyridine as in mtmp, the bis-aqua species  $[\text{Ru}(\text{bpy})_2(\text{OH}_2)_2]^{2+}$  was obtained upon light irradiation of  $[\text{Ru}(\text{bpy})_2(\text{mtp})]^{2+}$  in water. Although sulfur is clearly a more photolabile donor atom than a negatively charged oxygen ligand, and pyridine leads to full photosubstitution compared to the monosubstitution of the primary amine-based mtpa, a second factor has to be considered: the chelate ring size. As shown in Chapter 6, the chelate ring size has a major impact on the photoreactivity of N,S-based cyclometalated ruthenium complexes. Thus, we would expect that the different photoreactivity of mtpa and mtmp is not only due to the nature of the nitrogen donor atom, but also due to the different chelate ring sizes. In order to definitively solve this question, complexes bearing pyridine-based ligands resulting in a six-membered ring (*i.e.*  $[\text{Ru}(\text{bpy})_2(\text{mtep})]^{2+}$ ) and primary amine-based ligands resulting in a five-membered ring ( $[\text{Ru}(\text{bpy})_2(\text{mtea})]^{2+}$ ) should be synthesized and their photochemistry investigated.



Scheme 7.2. The photoreaction taking place upon irradiation of a ruthenium(II) complex depends on the nature of the photolabile ligand and on the strain of the complex.

The effect of the distortion of the octahedral geometry was also thoroughly investigated. In Chapter 2 and Chapter 4 we used varying numbers of hindering ligands such as dmbpy. Although octahedral distortion has a positive impact on the photosubstitution rate, it also has a negative impact on the selectivity of the

photosubstitution reaction, or even on the thermal stability of the complex in the dark. For example,  $[\text{Ru}(\text{bpy})(\text{dmbpy})(\text{L-prolinate})]^+$  and  $[\text{Ru}(\text{bpy})(\text{dmbpy})(\text{mtpa})]^{2+}$  photosubstituted both dmbpy and L-proline or mtpa upon irradiation in  $\text{CH}_3\text{CN}$  and water, respectively, while  $[\text{Ru}(\text{dmbpy})_2(\text{mtpa})]^{2+}$  is unstable in the dark. Thus, tris-heteroleptic complexes with only one hindering dmbpy ligand were considered, as they bring more thermal stability while keeping efficient photosubstitution. These heteroleptic complexes are significantly more challenging to synthesize, all the more when dissymmetric N,S or N,O ligands are introduced. The selectivity of photosubstitution reactions can also become problematic as several reactions may occur in parallel. To our knowledge, the non-selectivity in the photosubstitution of a ruthenium(II) complex is unprecedented, as well as the solvent-dependent selectivity, as shown for  $[\text{Ru}(\text{dmbpy})_2(\text{mtmp})]^{2+}$  (Chapter 6). Indeed, understanding the fate of an excited state is not an easy task. Few groups have reported computational chemistry methods to predict and understand conical intersections, from where an excited complex in the  $^3\text{MLCT}$  can follow different reaction pathways.<sup>6-9</sup> For example, the case of the bis-sulfoxide complex  $[\text{Ru}(\text{bpy})_2(\text{OSSO})]^{2+}$  (OSSO = dimethylbis-(methylsulfanyl)methyl)silane), which generates a mixture of mono- and bis-isomerized S $\rightarrow$ O complexes upon light irradiation, has been thoroughly studied.<sup>10</sup> In the case of a photosubstitution reaction, studies performed to the date usually focus on the  $^3\text{MC}$ - $^3\text{MLCT}$  gap, assuming that the entering ligand reacts quickly with any pentacoordinated intermediate state. In this thesis we show that a more complete method involving the nature of the entering ligand and including the effect of the solvent would be necessary.

### 7.2.2 Photocytotoxicity of ruthenium complexes photosubstituting a ligand

Light irradiation of ruthenium polypyridyl complexes might lead to several photoproducts, each of which may have its own biological effect. As shown in Figure 7.1, the excited state may lead by photosubstitution to an aquated ruthenium(II) complex and the free ligand, by electron transfer to superoxide radicals ( $\text{O}_2^-$ ), and/or by energy transfer to singlet oxygen ( $^1\text{O}_2$ ). Depending on which photoproduct is responsible for cell death, the mode of action can be considered as a PACT (metal-based or ligand-based), PDT type I, or PDT type II, respectively. However, it is also possible that several of these processes occur at the same time, making the identification of the predominant mode of action quite difficult.

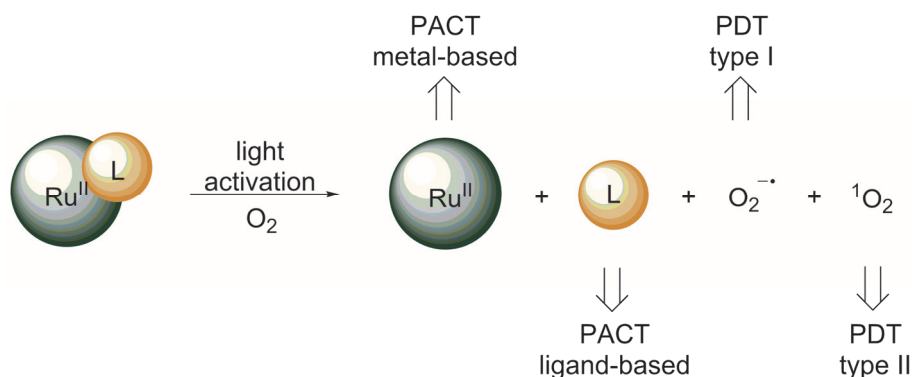


Figure 7.1. Possible photoproducts generated after light irradiation of a ruthenium(II) polypyridyl complex. Depending on which compound leads to cell death the mode of action will be associated to metal-based PACT, ligand-based PACT, PDT type I, or PDT type II.

In order to study specifically the photocytotoxicity of the metal center we first avoided the use of cytotoxic photolabile ligands and focused on L-proline, mtmp, and mtpa. Since dmbpy was found to be cytotoxic against A549 cells with an  $EC_{50}$  value of  $\sim 8 \mu\text{M}$  (Chapter 3), at least part of the cytotoxicity of all complexes partially releasing dmbpy may be attributed to the dissociated dmbpy. For Glazer's reference compound  $[\text{Ru}(\text{bpy})_2(\text{dmbpy})]\text{Cl}_2$  for example,<sup>1</sup> we demonstrated that the photocytotoxicity is caused by the photoreleased dmbpy, while  $[\text{Ru}(\text{bpy})_2(\text{OH}_2)_2]^{2+}$  appeared to be incapable of penetrating the cell and do any harm. Some ambiguity between metal-based and ligand-based photocytotoxicity was also found for  $[\text{Ru}(\text{bpy})(\text{dmbpy})(\text{mtpa})](\text{PF}_6)_2$  (Chapter 4) and  $[\text{Ru}(\text{dmbpy})_2(\text{mtmp})]\text{Cl}_2$  (Chapter 6), which can photosubstitute non-selectively both the N,S ligand and dmbpy.

For compounds in which the photocytotoxicity unambiguously comes from the metal center, distinguishing a PDT type II mechanism vs. a PACT mechanism led us to test our complexes under low dioxygen concentrations (1%), instead of the 21% typically used in the field. Even under 1%  $\text{O}_2$ , a complex like  $[\text{Ru}(\text{bpy})(\text{Ph}_2\text{phen})(\text{mtmp})]^{2+}$ , which photosubstitutes mtmp by solvent molecules, showed enhanced cytotoxicity upon light irradiation. Clearly, the obtained photocytotoxicity remained mild under such demanding testing conditions, which entail the performance of the whole cytotoxicity assay under hypoxic conditions using 2D cancer cell monolayers that have been passaged twice under hypoxia before the assay. However, the fact that some photocytotoxicity was observed at all is encouraging, and justifies future research with different compounds and possibly different cancer models, ultimately aiming at demonstrating photoactivated anticancer activity *in vivo*.

### 7.2.3 On lipophilicity and dark cytotoxicity

Next to photocytotoxicity and its relation to the photochemical properties of the ruthenium complex, studying the impact of the lipophilicity of the metal-containing prodrug on its dark cytotoxicity has been highlighted many times across this thesis. Generally, bis(bipyridine)-based complexes, with  $\log P$  values around  $-1.4$  are not lipophilic enough to cross cell membranes and be taken up passively (Chapter 3), which also explains why  $[\text{Ru}(\text{bpy})_3]\text{Cl}_2$  is a poor PDT agent *in vitro* in spite of its excellent singlet oxygen generation properties (*data not shown*). Increasing the lipophilicity of the ruthenium complex by adding several methyl or phenyl groups, usually results in higher cell uptake, as has been described previously.<sup>11</sup> It also leads to a higher dark cytotoxicity.  $[\text{Ru}(\text{dmbpy})_2(\text{mtpa})](\text{PF}_6)_2$  or  $[\text{Ru}(\text{bpy})(\text{Ph}_2\text{phen})(\text{mtmp})](\text{PF}_6)_2$  are two examples of more lipophilic complexes showing significant dark cytotoxicity. Although the reason for such general cytotoxicity is unknown, many reports show that positively charged lipophilic compounds localize in the mitochondria, destabilizing the mitochondrial membrane potential, thus suggesting a general mechanism for dark cytotoxicity.<sup>12</sup> Finally, when the ruthenium complexes are too lipophilic, like in  $[\text{Ru}(\text{Ph}_2\text{phen})_2(\text{mtmp})]\text{Cl}_2$  or the monocationic cyclometalated complex  $[\text{Ru}(\text{bpy})(\text{phpy})(\text{mtep})]\text{PF}_6$ , the cytotoxicity observed in the dark is too high to be significantly improved by light irradiation, thus leading to overall disappointing photo indexes. In conclusion, the best metal-based PACT compounds require intermediate lipophilicity using tris-heteroleptic complexes and dissymmetric non-toxic protecting ligands, leading to stereochemically challenging chemical structures and interesting, solvent-dependent selectivity issues under light irradiation.

### 7.3 References

1. B. S. Howerton, D. K. Heidary and E. C. Glazer, *J. Am. Chem. Soc.*, **2012**, 134, 8324-8327.
2. L. N. Lameijer, D. Ernst, S. L. Hopkins, M. S. Meijer, S. H. C. Askes, S. E. Le Dévédec and S. Bonnet, *Angew. Chem., Int. Ed.*, **2017**, 56, 11549-11553.
3. A. J. Göttle, F. Alary, M. Boggio-Pasqua, I. M. Dixon, J.-L. Heully, A. Bahreman, S. H. C. Askes and S. Bonnet, *Inorg. Chem.*, **2016**, 55, 4448-4456.
4. A.-C. Laemmel, J.-P. Collin and J.-P. Sauvage, *Eur. J. Inorg. Chem.*, **1999**, 383-386.
5. R. N. Garner, L. E. Joyce and C. Turro, *Inorg. Chem.*, **2011**, 50, 4384-4391.
6. F. Alary, M. Boggio-Pasqua, J.-L. Heully, C. J. Marsden and P. Vicendo, *Inorg. Chem.*, **2008**, 47, 5259-5266.
7. V. I. Baranovskii, D. A. Mal'tsev and O. V. Sizova, *Russ. Chem. Bull.*, **2012**, 61, 973-979.
8. B. A. McClure, N. V. Mockus, D. P. Butcher Jr, D. A. Lutterman, C. Turro, J. L. Petersen and J. J. Rack, *Inorg. Chem.*, **2009**, 48, 8084-8091.
9. S. E. Greenough, G. M. Roberts, N. A. Smith, M. D. Horbury, R. G. McKinlay, J. M. Žurek, M. J. Paterson, P. J. Sadler and V. G. Stavros, *Phys. Chem. Chem. Phys.*, **2014**, 16, 19141-19155.
10. K. Garg, A. W. King and J. J. Rack, *J. Am. Chem. Soc.*, **2014**, 136, 1856-1863.
11. C. A. Puckett and J. K. Barton, *J. Am. Chem. Soc.*, **2007**, 129, 46-47.

## Chapter 7

12. M. Dickerson, Y. Sun, B. Howerton and E. C. Glazer, *Inorg. Chem.*, **2014**, 53, 10370-10377.

# APPENDIX I: GENERAL PHOTOCHEMISTRY METHODS

---

## AI.1 Irradiation with a Xe lamp

A LOT Xenon 1000 W lamp was used for the irradiation of NMR tubes and preparative scale photoreaction cells. Depending on the experiment, either IR short pass, >400 nm long pass, and/or 450 nm blue light (450FS10-50 from Andover Corporation) filters were mounted on the lamp. Figure AI.1 shows the transmission spectra of the filters.

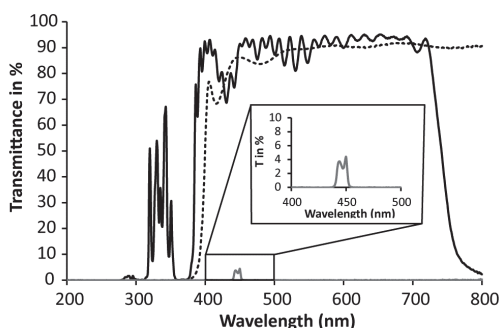


Figure AI.1. Transmittance curves of the IR filter (continuous black), the >400 nm long pass filter (dashes), and the 450 nm band pass filter (grey).

For the photoreactions performed in preparative scale, a 100 mL cylindrical photoreaction cell (d = 5 cm, l = 5 cm) equipped with a water-cooling system was used. Figure AI.2 shows the irradiation setup.



Figure AI.2. Irradiation setup for a preparative scale photoreaction under Ar.

## AI.2 Use of Glotaran software for the calculation of the photosubstitution quantum yield.

Upon light irradiation, a complex RuL converts into a complex RuY by photosubstitution of a ligand (L) by a solvent molecule (Y). Considering that both metal complexes are thermally stable, the quantum yield of the photosubstitution reaction  $\Phi_{PR}$  can be calculated by monitoring the photoreaction with UV-vis spectroscopy. As explained in detail by Bahreman and Bonnet,<sup>1</sup> when the irradiation is performed at a wavelength that is not an isosbestic point, the  $\Phi_{PR}$  can be obtained from the slope of a plot of the number of mol of RuL ( $n_{RuL}$ ) vs. the total number of mol of photons absorbed by RuL from  $t_0$  till  $t_i$  ( $Q_i$ ).  $Q_i$  is calculated according to Equation AI.1:

$$Q_i(t) = \sum_{t=0}^i q_i$$

Equation AI.1

where  $q_i$  is the moles of photons absorbed by RuL between two consecutive UV-vis measurements at  $t_{i+1}$  and  $t_i$  ( $\Delta t = t_{i+1} - t_i$ ).  $q_i$  is calculated according to Equation AI.2:

$$q_i = \left( \frac{(A_{RuL})_{ave}}{(A_e)_{ave}} \right)_i \cdot (1 - 10^{-3 \cdot (A_e)_{ave}}) \cdot \varphi \cdot \Delta t$$

Equation AI.2

where  $(A_{RuL})_{ave}$  is the average of the absorbance due to RuL between two consecutive UV-vis measurements,  $(A_e)_{ave}$  is the average of the absorbance of the solution at the irradiation wavelength between two consecutive UV-vis measurements,  $(1 - 10^{-3 \cdot (A_e)_{ave}})$  is the probability of absorption of a photon when the irradiation comes from the top and goes through 3 cm pathlength, while all absorbances are measured through a 1 cm pathlength, and  $\varphi$  is the photon flux of the irradiation source at the irradiation wavelength.

The value of  $(A_{RuL})_{ave}$ , and by extension  $n_{RuL}$ , is generally calculated by the two-wavelength method, where the time evolution of the concentrations of the two absorbing species (the reagent and photoproduct) is obtained by following the time evolution of the absorbance at two different wavelengths.<sup>1</sup> However, this method cannot be always used. In some cases the molar extinction coefficient of the photoproduct is unknown, or two sequential photoreactions may take place. In the latter case, the molar extinction coefficients of the intermediate, which cannot be

isolated, is often unknown. In such cases, modelling the evolution of the UV-vis spectra vs. time is convenient. In this thesis, we have used Glotaran software for doing this, thus we fitted the time-dependent evolution of the UV-vis spectroscopy data to a kinetic model based on first-order laws, obtaining two output data sets that can be used for the calculation of  $\Phi_{PR}$ . The first dataset is a collection of globally fitted absorption spectra of the starting complex, the photoproduct, and the intermediate (if any), which makes possible the calculation of the molar extinction coefficient of all the species from that of the starting reagent (Figure AI.3a). The second dataset is the modelled evolution of the relative fractions of the two or three ruthenium species vs. irradiation time, here as well according to global fitting (Figure AI.3b). From the time evolution of these fractions and the molar absorption coefficient of all species, the time evolution of  $n_{RuL}$  can be calculated, as well as  $Q_i$ . The slope of the plot of  $n_{RuL}$  vs.  $Q_i$  (Figure AI.3c) gives the quantum yield of the reaction.

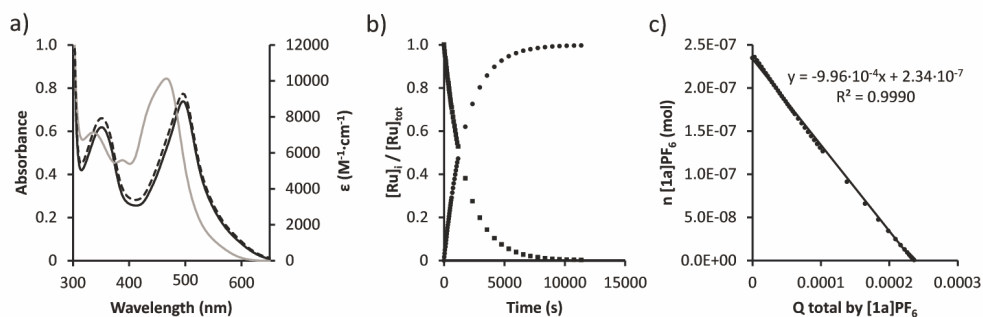


Figure AI.3. Typical example of Glotaran global fitting of a one-step photochemical reaction, here for the time evolution of the absorbance of a solution of  $A\text{-[Ru(bpy)}_2\text{(L- prol)]PF}_6$  ( $[1a]PF_6$ ) irradiated in PBS under air, leading to photooxidation (Chapter 2). a) Left axis: globally fitted absorption spectra of  $[1a]PF_6$  (black) and  $A\text{-[Ru(bpy)}_2\text{(L- prol - 2H)]PF}_6$  ( $[7]PF_6$ ) (grey). Right axis: experimental spectrum of  $[1a]PF_6$ . b) Modelled evolution of the relative concentrations of  $[1a]PF_6$  (squares) and  $[7]PF_6$  (circles) vs. irradiation time according to global fitting. c) Plot of the amount of  $[1a]PF_6$  (mol) vs. total amount of photons absorbed by  $[1a]PF_6$  (mol). The slope of the obtained line is the opposite of the photooxidation quantum yield. Conditions: 0.078 mM solution of  $[1a]PF_6$  in PBS irradiated at 298 K in air using a 493 nm LED at  $1.61 \cdot 10^{-7} \text{ mol} \cdot \text{s}^{-1}$ .

### AI.3 Singlet Oxygen quantum yield measurement

The quantum yield of singlet oxygen generation was determined in a custom-built setup (Figure AI.4), in which both UV-vis absorption and infrared emission spectroscopy could be performed. All optical parts were connected with optical fibers from Avantes (Apeldoorn, The Netherlands), with a diameter of 200-600  $\mu\text{m}$ . For each measurement, 500  $\mu\text{L}$  of sample, consisting of the compound in deuterated methanol ( $A_{450} \leq 0.1$  for 4.0 mm pathlength), was placed in a stirred 104F-OS semi-micro

fluorescence cuvette (Hellma Analytics, Müllheim, Germany) in a CUV-UV/VIS-TC temperature-controlled cuvette holder from Avantes. The sample was allowed to equilibrate at 293 K for 5 min. Emission spectroscopy was performed with a 450 nm fiber-coupled laser (Laser system LRD-0450; Laserglow, Toronto, Canada), at 50 mW optical power (4 mm beam diameter;  $0.4 \text{ W}\cdot\text{cm}^{-2}$ ) at a  $90^\circ$  angle with respect to the spectrometer. The excitation power was measured using a S310C thermal sensor connected to a PM100USB power meter (Thorlabs, Dachau, Germany). Infrared emission spectra were measured from 1000 nm to 1400 nm using an Avantes NIR256-1.7TEC spectrometer. The infrared emission spectrum was acquired within 9 s, after which the laser was turned off directly. UV-vis absorption spectra before and after emission spectroscopy were measured using an Avalight-DHc halogen-deuterium lamp (Avantes) as light source (turned off during emission spectroscopy) and an Avantes 2048L StarLine UV-vis spectrometer as detector, both connected to the cuvette holder at a  $180^\circ$  angle. No difference in UV-vis absorption spectrum was found due to exposure to the blue laser, showing that the singlet oxygen emission is that of the starting compound. All spectra were recorded with Avasoft 8.5 software from Avantes and further processed with Microsoft Office Excel 2010 and Origin Pro 9.1 software.

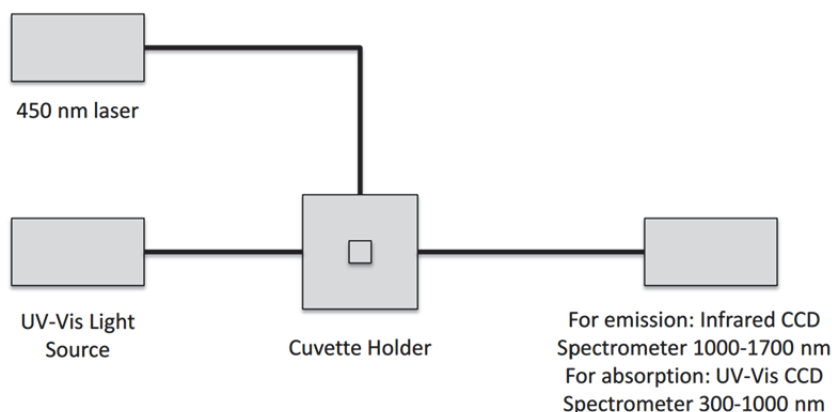


Figure AI.4. Setup for  $^1\text{O}_2$  quantum yield measurement.

The quantum yield of singlet oxygen production was calculated using the relative method with  $[\text{Ru}(\text{bpy})_3]\text{Cl}_2$  as the standard ( $\Phi_A = 0.73$  in  $\text{CD}_3\text{OD}$ ),<sup>2</sup> according to Equation 7.1:

$$\Phi_{\Delta,sam} = \Phi_{\Delta,std} \times \frac{A_{450,std}}{A_{450,sam}} \times \frac{E_{sam}}{E_{std}}$$

Equation 7.1

where  $\Phi_{\Delta}$  is the quantum yield of singlet oxygen generation,  $A_{450}$  is the absorbance at 450 nm, E is the integrated emission peak of singlet oxygen at 1274 nm, and *sam* and *std* denote the sample and standard, respectively.

## AI.4 References

1. A. Bahreman, J.-A. Cuello-Garibo and S. Bonnet, *Dalton Trans.*, **2014**, 43, 4494-4505.
2. D. Garcia-Fresnadillo, Y. Georgiadou, G. Orellana, A. M. Braun and E. Oliveros, *Helv. Chim. Acta*, **1996**, 79, 1222-1238.



# APPENDIX II: CELL CULTURE AND (PHOTO)CYTOTOXICITY STUDIES

---

## **AII.1 General:**

Human cancer cell line A549 (human lung carcinoma) was distributed by the European Collection of Cell Cultures (ECACC), and purchased from Sigma Aldrich. Dulbecco's Modified Eagle Medium (DMEM, with and without phenol red, without glutamine), Glutamine-S (GM;200 mg/ml), trichloroacetic acid (TCA), glacial acetic acid, sulforhodamine B (SRB), and tris(hydroxymethyl)aminomethane (Trisbase) were purchased from Sigma Aldrich. Fetal calf serum (FCS) was purchased from Hyclone. Penicillin and streptomycin were purchased from Duchefa and were diluted to a 100 mg/mL penicillin/streptomycin solution (P/S). Trypsin and OptiMEM (without phenol red) were purchased from Gibco Life Technologies. Trypan blue (0.4% in 0.81% sodium chloride and 0.06% potassium phosphate dibasic solution) was purchased from BioRad. Plastic disposable flasks and 96-well plates were purchased from Sarstedt. Cells were counted by using a BioRad TC10 automated cell counter with Biorad cell-counting slides. UV-vis measurements for analysis of 96-well plates were performed with a M1000 Tecan Reader. Cells were inspected with an Olympus IX81 microscope.

## **AII.2 Cell culture**

Cells were cultured in Dulbecco's Modified Eagle Medium containing phenol red, supplemented with 8.0% v/v FCS, 0.2% v/v P/S and 0.9% v/v glutamax. Cells were incubated at 37 °C at 7.0% CO<sub>2</sub> in 75 cm<sup>2</sup> T-flasks and splitted once a week at 80-90% confluency. Cells were cultured for a maximum of 8 weeks for all biological experiment, and passaged at least twice after being thawed.

## **AII.3 Cell-irradiation setup**

The cell-irradiation system consisted of a Ditabis thermostat (980923001) fitted with two flat-bottomed micro-plate thermoblocks (800010600) and a 96-LED array fitted to a standard 96-well plate. The 454 nm LED (OVL-3324), 520 nm LED (OVL-3324), fans (40 mm, 24 VDC, 9714839), and power supply (EA-PS 2042-06B) were obtained from Farnell. See Hopkins *et al.* for a full description.<sup>1</sup>

## AII.4 Cytotoxicity assays

A549 cells were seeded at  $t = 0$  in 96-well plates at a density of 5000 cells/well (100  $\mu\text{L}$ ) in OptiMEM supplemented with 2.4% v/v FCS, 0.2% v/v P/S, and 1.0% v/v glutamax (called OptiMEM complete) and incubated for 24 h at 37 °C and 7.0%  $\text{CO}_2$ . After this period, aliquots (100  $\mu\text{L}$ ) of six different concentrations of freshly prepared stock solutions of the compounds in OptiMEM were added to the wells in triplicate (see plate design in Figure AII.1). Sterilized dimethylsulfoxide (DMSO) was used to dissolve the compounds in such amounts that the maximum v/v% of DMSO per well did not exceed 0.5%. For every irradiated plate a parallel control plate was prepared and treated identically, but without irradiation. Plates were incubated in the dark for an additional time. After this period, half of the plates were irradiated and the other half were kept in the dark. After irradiation, all the plates were incubated in the dark until a total time of 96 h after seeding (see the respective Experimental Section for the details). The cells were fixated by adding cold TCA (10 % w/v; 100  $\mu\text{L}$ ) in each well and the plates were stored at 4 °C for at least 4 h as part of the sulforhodamine B (SRB) assay that was adapted from Vichai *et al.*<sup>2</sup> In short, after fixation, TCA medium mixture was removed from the wells, rinsed with demineralized water three times, and air dried. Then, each well was stained with 100  $\mu\text{L}$  SRB (0.6% w/v in 1% v/v acetic acid) for 30 min, the SRB was removed by washing with acetic acid (1 % v/v), and air dried. The SRB dye was solubilized with Tris base (10 mM; 200  $\mu\text{L}$ ), and the absorbance in each well was read at  $\lambda = 510$  nm by using a M1000Tecan Reader.

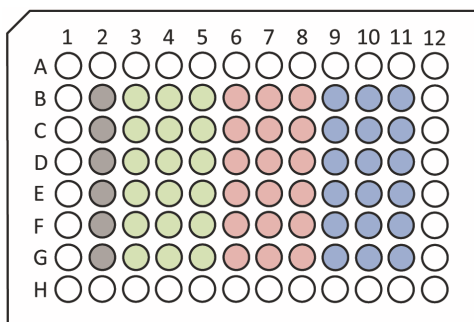


Figure AII.1. Design of a 96-well plate used in the cytotoxicity assays. Grey: non-treated cells ( $n_i = 6$ ); green: cells treated with compound A with six different concentrations (one per row) per triplicate ( $n_i = 3$ ); red: cells treated with compound B with six different concentrations (one per row) per triplicate ( $n_i = 3$ ); blue: cells treated with compound C with six different concentrations (one per row) per triplicate ( $n_i = 3$ ).

The SRB absorbance data per compound per concentration was averaged over three identical wells (technical replicates,  $n_t = 3$ ) in Excel and made suitable for use in GraphPad Prism. Relative cell populations were calculated by dividing the average absorbance of the treated wells by the average absorbance of the untreated wells. In any case, it was checked that the cell viability of the untreated cells of the samples irradiated were similar (maximum difference of 10%) to the non-irradiated samples to make sure no harm was done by light alone. The data from three independent biological replications was plotted versus log(concentration in  $\mu\text{M}$ ). The resulting dose-response curve for each compound under dark and irradiated conditions was fitted to a non-linear regression function with fixed  $y$  maximum (100%) and minimum (0%) (relative cell viability) and a variable Hill slope, to obtain the effective concentration ( $\text{EC}_{50}$  in  $\mu\text{M}$ ). The simplified two-parameter Hill-slope equation used for the fitting is shown in Equation AII.1:

$$\frac{100}{(1 + 10^{((\log_{10}\text{EC}_{50}-X) \cdot \text{Hill slope}))}}$$

*Equation AII.1*

Photo indices (PI) reported in Table 3.1, Table 4.3, and Table 6.3 were calculated, for each compound, by dividing the  $\text{EC}_{50}$  value obtained in the dark by the  $\text{EC}_{50}$  value determined under light irradiation.

## **AII.5. References**

1. S. L. Hopkins, B. Siewert, S. H. C. Askes, P. Veldhuizen, R. Zwier, M. Heger and S. Bonnet, *Photochem. Photobiol. Sci.*, **2016**, 15, 644-653.
2. V. Vichai and K. Kirtikara, *Nat. Protocols*, **2006**, 1, 1112-1116.



## APPENDIX III SUPPORTING INFORMATION FOR CHAPTER 2

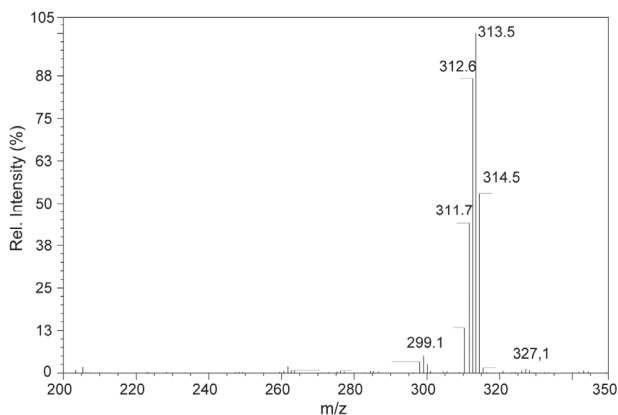


Figure AIII.1. Mass spectrum of complex  $[5]^{2+}$  with a calcd  $m/z = 313.1$ .  $[Ru(dmbpy)_3]^{2+}$  and  $[Ru(bpy)_2(dmbpy)]^{2+}$  resulting from limited ligand scrambling are present with calcd  $m/z = 327.1$  and 299.1, respectively.

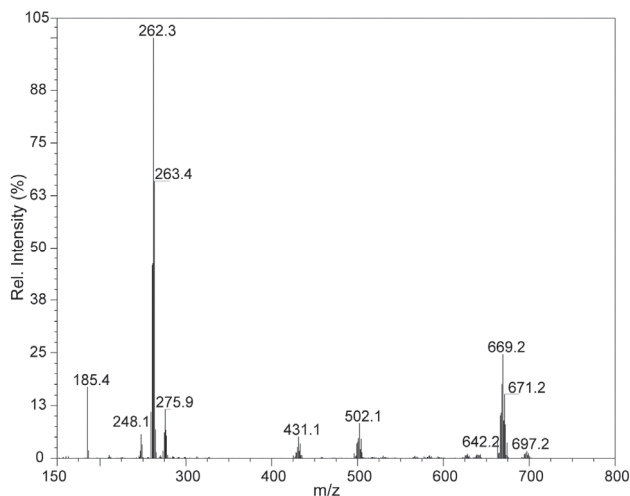


Figure AIII.2. Mass spectrum after photolysis of a  $CH_3CN$  solution of  $[5]PF_6$  under  $Ar$  and at  $25\text{ }^\circ C$  with peaks corresponding to the free ligand  $\{dmbpy + H\}^+$  (calcd  $m/z = 185.2$ ),  $[Ru(bpy)(dmbpy)(CH_3CN)_2]^{2+}$  (calcd  $m/z = 262.1$ ),  $[Ru(bpy)_2(CH_3CN)_2]^{2+}$  (calcd  $m/z = 248.1$ ),  $[Ru(dmbpy)_2(CH_3CN)_2]^{2+}$  (calcd  $m/z = 276.1$ ),  $\{[Ru(bpy)_2(CH_3CN)_2]PF_6\}^+$  (calcd  $m/z = 642.1$ ),  $\{[Ru(bpy)(dmbpy)(CH_3CN)_2]PF_6\}^+$  (calcd  $m/z = 669.1$ ), and  $\{[Ru(dmbpy)_2(CH_3CN)_2]PF_6\}^+$  (calcd  $m/z = 697.1$ ).

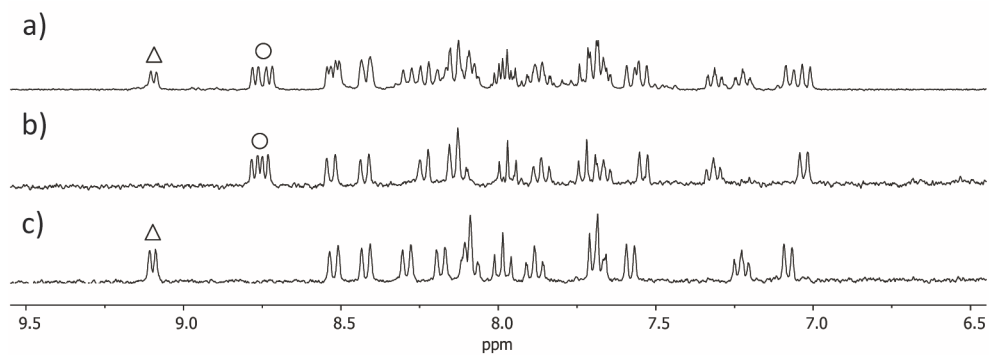


Figure AIII.3.  $^1\text{H}$  NMR spectra (region 6.5 – 9.5 ppm) in  $\text{D}_2\text{O}$  of a) the crude reaction mixture containing  $[\mathbf{2a}]\text{PF}_6$  and  $[\mathbf{2b}]\text{PF}_6$ ; b) fraction A of the chromatography column on alumina containing complex  $[\mathbf{2a}]\text{PF}_6$  (round); and c) fraction B containing complex  $[\mathbf{2b}]\text{PF}_6$  (triangle).

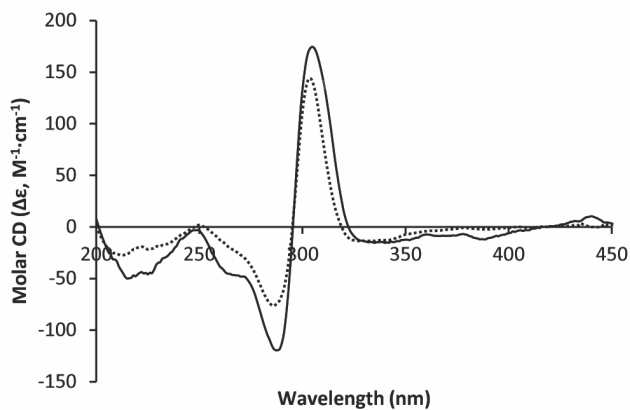


Figure AIII.4. Circular dichroism spectra of a solution of  $[\mathbf{2a}]\text{PF}_6$  (continuous) and  $[\mathbf{2b}]\text{PF}_6$  (dashed) in water with concentrations of  $3.27\cdot 10^{-5}\text{ M}$  and  $6.50\cdot 10^{-5}\text{ M}$ , respectively, in a 0.1 cm path length cuvette.

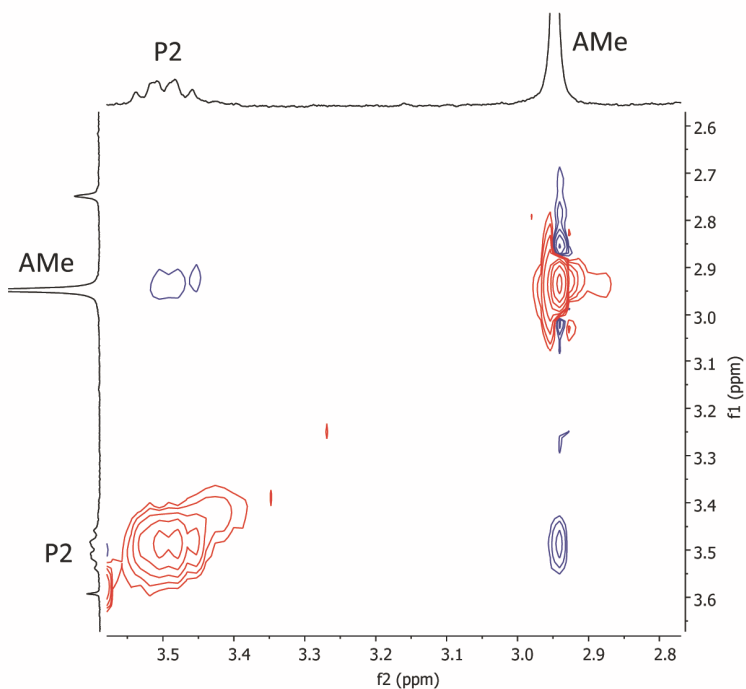


Figure AIII.5. NOESY NMR spectrum of a solution of  $[2a]PF_6$  in  $D_2O$  showing an off-diagonal peak between the  $\alpha$  proton P2 and the methyl peak AMe of dmbpy.

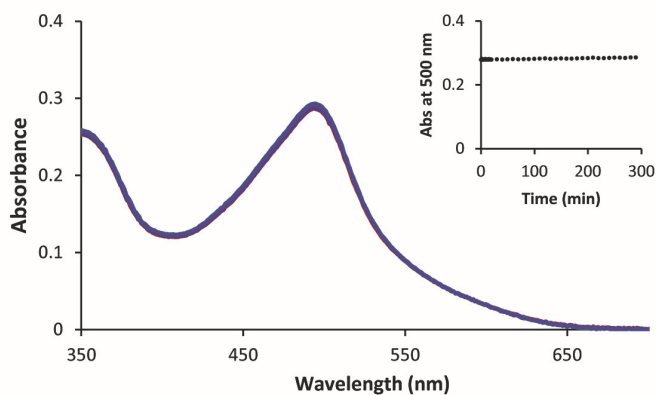


Figure AIII.6. Evolution of the UV-vis spectra (region 350 – 700 nm) of a solution of  $[1a]PF_6$  in PBS (0.035 mM) in the dark at 310 K under air.

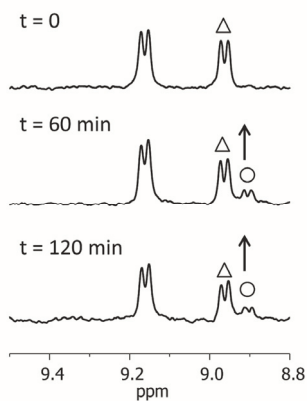


Figure AIII.7. Evolution of the  $^1\text{H}$  NMR spectra (region 8.5 – 9.5 ppm) of the irradiation of  $[\mathbf{1a}]\text{PF}_6$  at 310 K in deuterated PBS (pD=7.8) under Ar. The doublet at 9.16 ppm (triangle) corresponds to the  $\text{H}_6$  proton on the bpy for complex  $[\mathbf{1a}]^+$  and the arising doublet at 8.90 ppm corresponds to the  $\text{H}_6$  proton on the bpy for the delta isomer. Concentration of  $[\mathbf{1a}]\text{PF}_6 = 0.45$  mM.

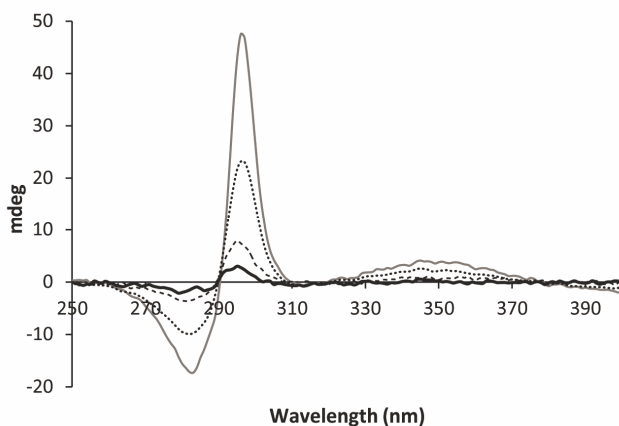


Figure AIII.8. Circular dichroism spectra (region 250 – 400 nm) of a solution of  $[\mathbf{1a}]\text{PF}_6$  in PBS in a 0.1 cm cuvette before (grey continuous) and after irradiation with a 493 nm LED in the following conditions. Dots: under Ar; dashed: under air with 5 mM GSH; black continuous: under air. Detailed conditions of the photo reactions are given in Table AIII.1.

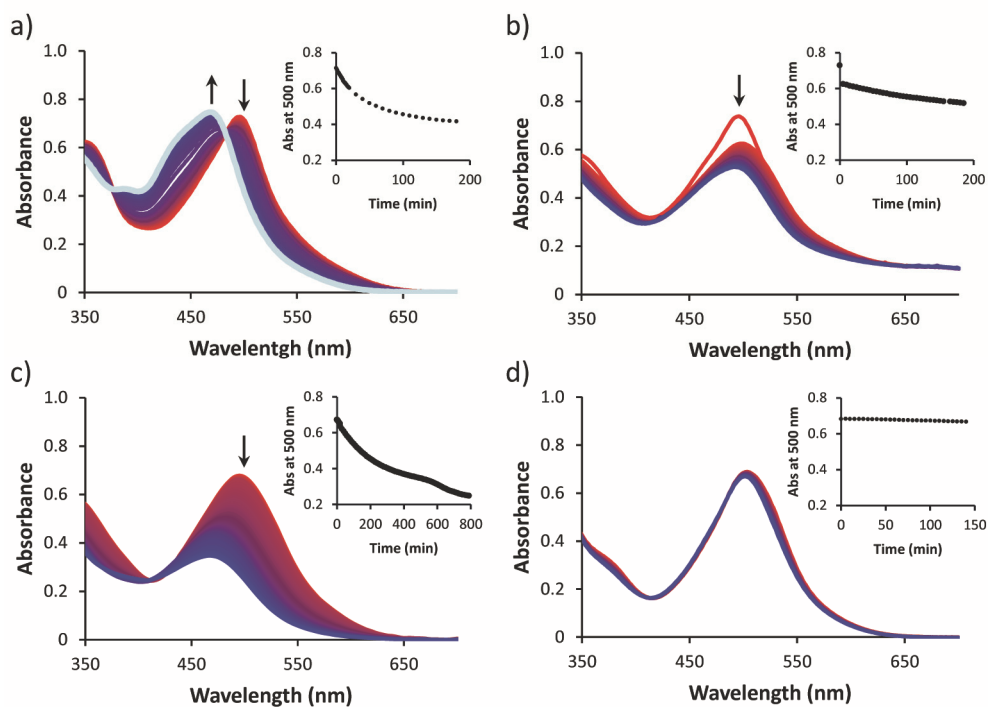


Figure AIII.9. Evolution of the UV-vis spectra (region 350 – 700 nm) of an irradiated solution of a)  $[1a]PF_6$  (0.078 mM) with 5mM of GSH, b)  $[2a]PF_6$  (0.032 mM), c)  $[2b]PF_6$  (0.087 mM), and d)  $[3a]PF_6$  (0.077 mM) in PBS at 298 K under air. Conditions are detailed in Table AIII.1.

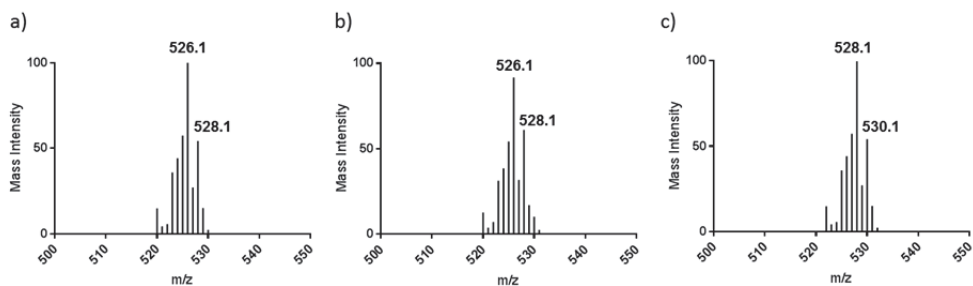


Figure AIII.10. Calculated isotope pattern of a)  $[7]^+$ , b) a mixture 7:3 of  $[1]^+:[7]^+$ , and c)  $[1]^+$ .

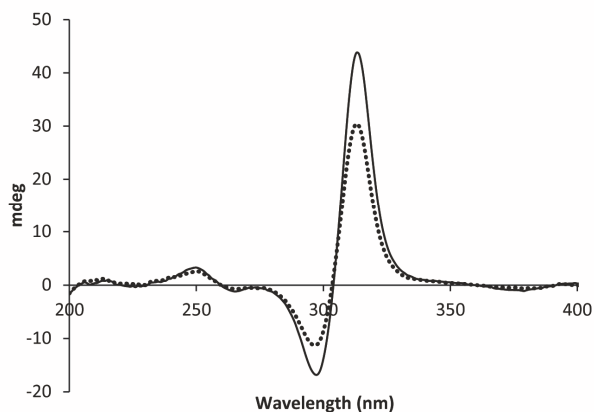


Figure AIII.11. Circular dichroism spectra (region 200 – 400 nm) of a solution of  $[3a]PF_6$  in PBS before (continuous) and after 140 min light irradiation (dotted) using a 493 nm LED under air. Conditions are detailed in Table AIII.1.

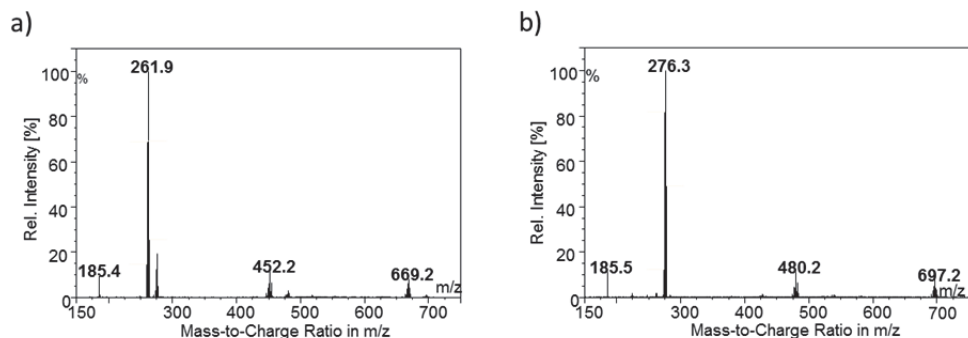


Figure AIII.12. Mass spectrum of acetonitrile solutions of (a)  $[2a]PF_6$  and (b)  $[3a]PF_6$  after the irradiation with a 493 LED. a) Peaks corresponding to  $\{dmbpy + H\}^+$  (calcd  $m/z = 185.2$ ),  $[Ru(bpy)(dmbpy)(CH_3CN)_2]^{2+}$  (calcd  $m/z = 262.1$ ),  $[Ru(bpy)(L-Prol - 2H)(CH_3CN)_2]^+$  (calcd  $m/z = 452.1$ ), and  $\{[Ru(bpy)(dmbpy)(CH_3CN)_2]PF_6\}^+$  (calcd  $m/z = 669.1$ ). b) Peaks corresponding to  $\{dmbpy + H\}^+$  (calcd  $m/z = 185.2$ ),  $[Ru(dmbpy)_2(CH_3CN)_2]^{2+}$  (calcd  $m/z = 276.1$ ),  $[Ru(dmbpy)(L-Prol - 2H)(CH_3CN)_2]^+$  (calcd  $m/z = 480.1$ ), and  $[Ru(dmbpy)_2(CH_3CN)_2]PF_6\}^+$  (calcd  $m/z = 697.1$ ). Conditions are detailed in Table AIII.1.

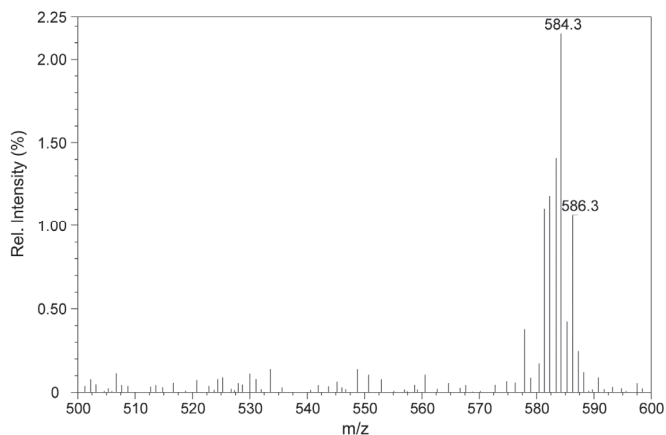


Figure AIII.13. Mass spectrum after 140 min irradiation with a 493 nm LED of a solution of  $[3a]PF_6$  in PBS (0.077 mM) under air with a peak corresponding to  $[3a]^+$  (calcd  $m/z = 584.1$ ). Conditions of the irradiation are detailed in Table AIII.1.

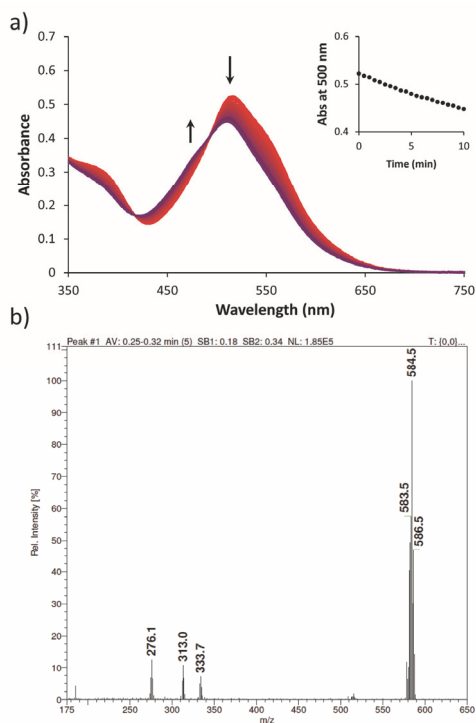


Figure AIII.14. a) Evolution of the UV-vis spectra of a solution of  $[3a]PF_6$  (0.062 mM) in  $CH_3CN$  upon irradiation for 10 min under Ar with a 493 nm LED with a photon flux of  $1.61 \cdot 10^{-8} \text{ mol} \cdot \text{s}^{-1}$ . b) Mass spectrum after 10 min irradiation of solution in (a) with peaks corresponding to  $[Ru(dmbpy)_2(CH_3CN)_2]^{2+}$  (calcd  $m/z = 276.1$ ),  $[Ru(dmbpy)_2(L-Hprol)(CH_3CN)]^{2+}$  (calcd  $m/z = 313.1$ ),  $[Ru(dmbpy)_2(L-Hprol)(CH_3CN)_2]^{2+}$  (calcd  $m/z = 333.6$ ), and  $[Ru(dmbpy)_2(L-prol)]^+$  (calcd  $m/z = 584.2$ ).

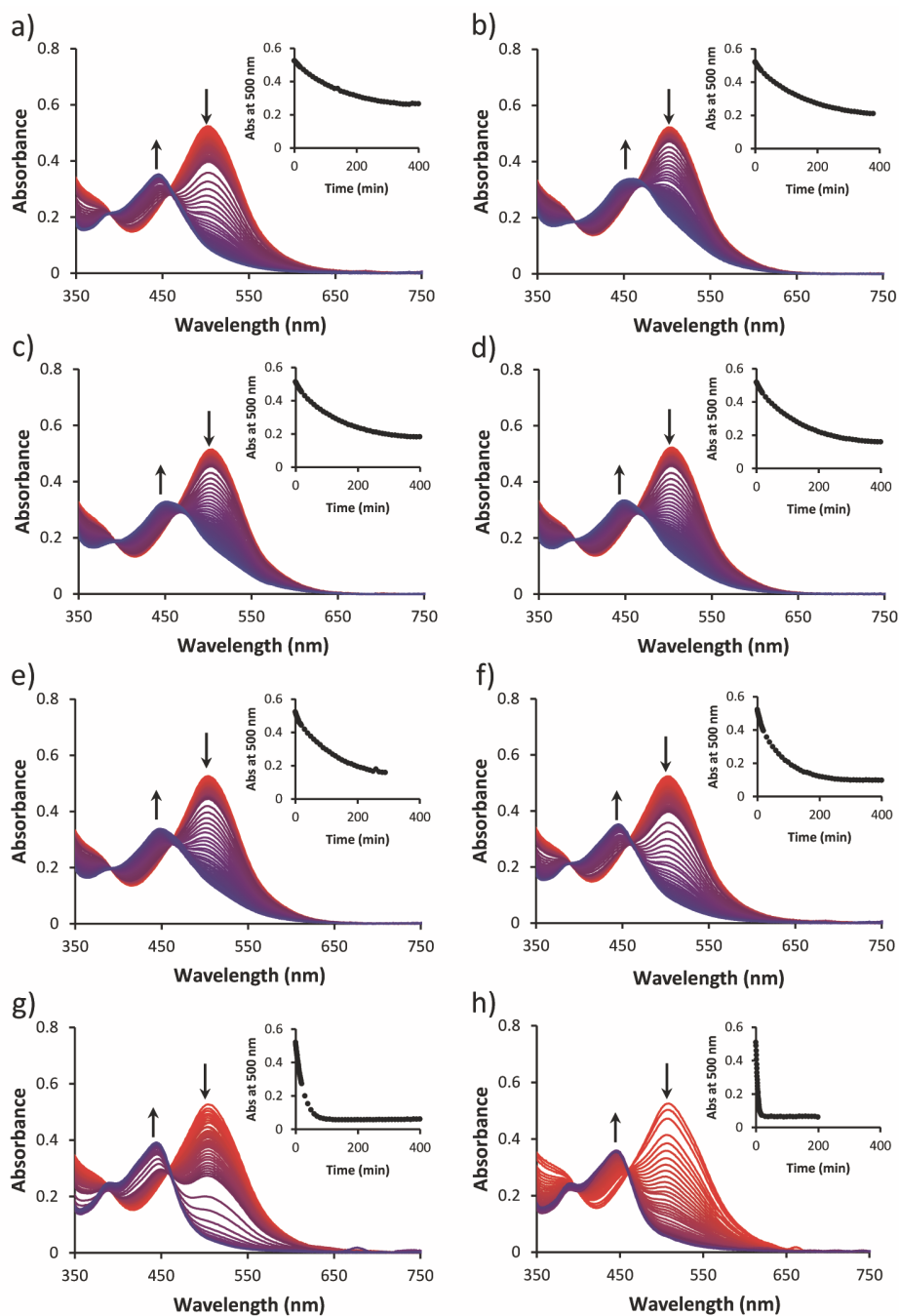


Figure AIII.15. Evolution of the UV-Vis spectra of a solution of  $[3a]PF_6$  (0.062 mM) in water with a) 1%  $CH_3CN$ , b) 2%  $CH_3CN$ , c) 3%  $CH_3CN$ , d) 4%  $CH_3CN$ , e) 5%  $CH_3CN$ , f) 10%  $CH_3CN$ , g) 30%  $CH_3CN$ , and h) 80%  $CH_3CN$  upon irradiation under Ar with a 493 nm LED with a photon flux of  $1.13 \cdot 10^{-7} - 1.16 \cdot 10^{-7} \text{ mol} \cdot \text{s}^{-1}$ .

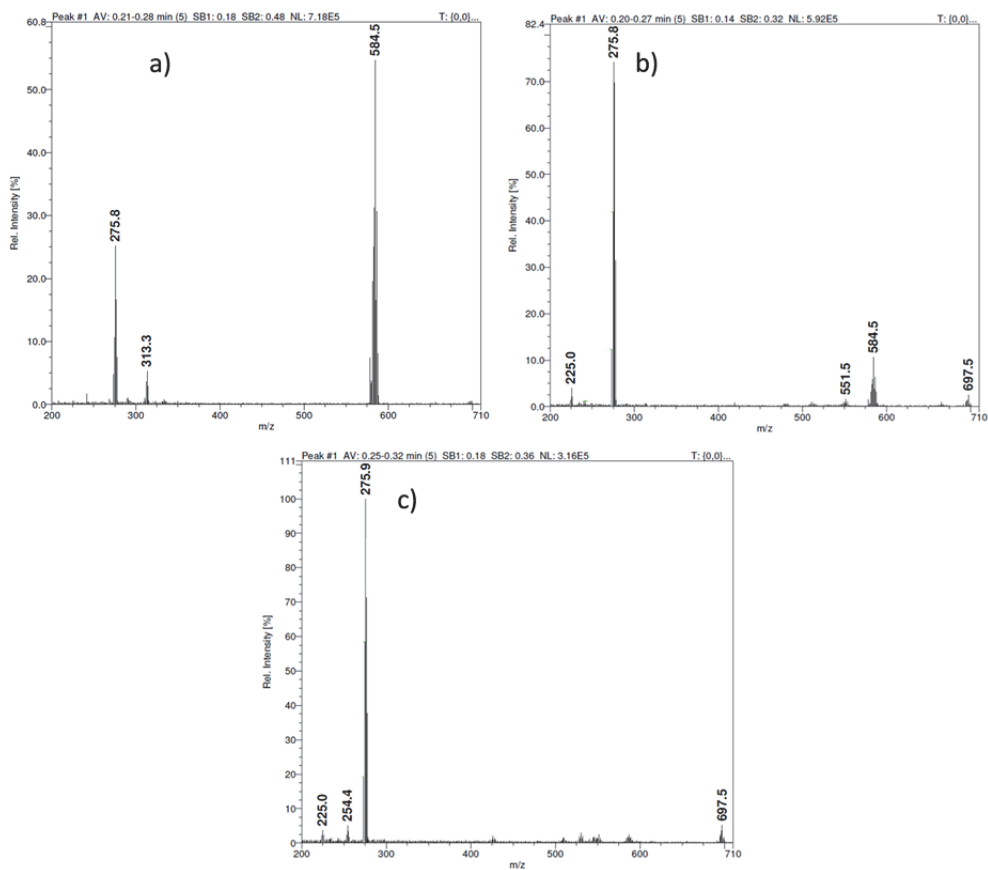


Figure AIII.16. Mass spectra of a solution of  $[3a]PF_6$  (0.062 mM) in water with a) 2%  $CH_3CN$ , b) 2%  $CH_3CN$ , and c) 80%  $CH_3CN$  after 15, 300, and 55 min irradiation, respectively, under Ar with a 493 nm LED with a photon flux of  $1.13 \cdot 10^{-7} - 1.16 \cdot 10^{-7} \text{ mol} \cdot \text{s}^{-1}$  with peaks corresponding to  $[Ru(dmbpy)_2(CH_3CN)_2]^{2+}$  (calcd  $m/z = 276.1$ ),  $\{[Ru(dmbpy)_2(L\text{-}prol)(CH_3CN)] + H\}^{2+}$  (calcd  $m/z = 313.1$ ),  $[Ru(dmbpy)_2(L\text{-}prol)]^+$  (calcd  $m/z = 584.2$ ),  $\{[Ru(dmbpy)_2(CH_3CN)_2]PF_6\}^+$  (calcd  $m/z = 697.1$ ).

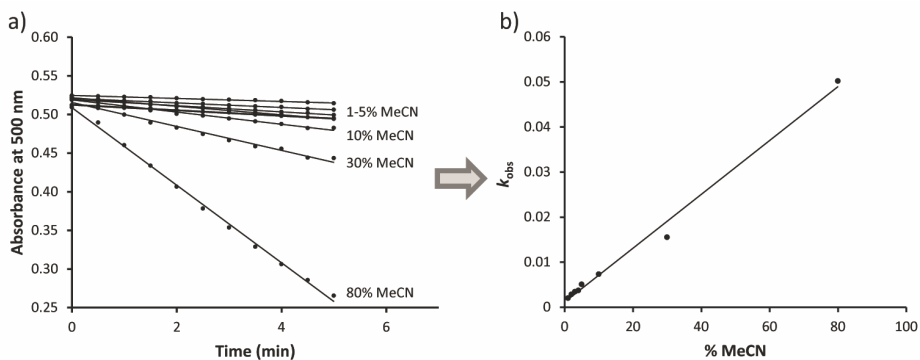


Figure AIII.17. a) Plot of the evolution of the absorbance at 500 nm vs. time (first 5 min) during light irradiation of  $[3a]PF_6$  in water containing different  $CH_3CN$  concentrations. Conditions: ruthenium concentration 0.062 mM, water contains 1, 2, 3, 4, 5, 10, 30, or 80 vol%  $CH_3CN$ , irradiation under Ar, light source is a 493 nm LED with a photon flux of  $1.13 \cdot 10^{-7} - 1.16 \cdot 10^{-7} \text{ mol} \cdot \text{s}^{-1}$ . The negative slope of these curves is  $-k_{obs}$ . b) Evolution of  $k_{obs}$  vs.  $CH_3CN$  concentration (in vol%) in water. All the numerical values of  $k_{obs}$  are given in Table AIII.2.

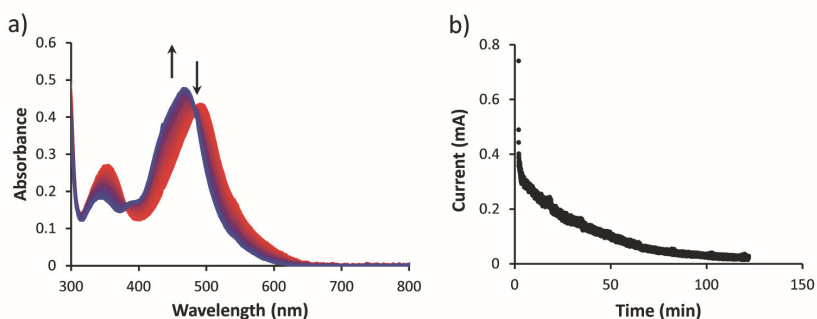


Figure AIII.18. a) Evolution of the UV-vis spectra (region 350 – 650 nm) and b) current measured on the working electrode associated with the oxidation process vs. time during the electrochemical oxidation of a solution of  $[1a]PF_6$  in PBS. Conditions: 0.1 mM  $[1a]PF_6$  in PBS, carbon sponge working and counter electrodes, and Ag/AgCl reference electrode. Chronoamperometry was performed at +0.645 V and compartments were separated by a nafion membrane.

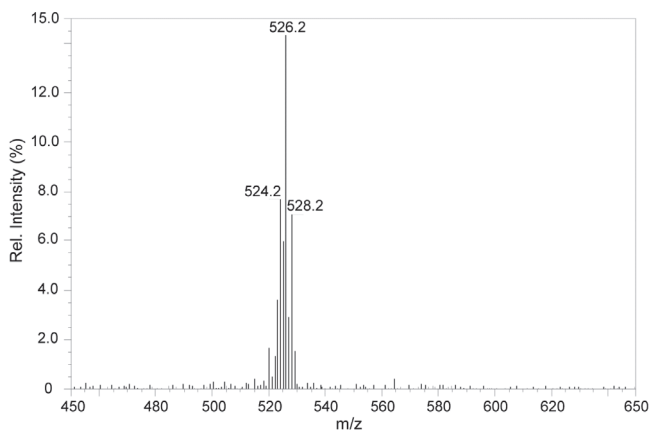


Figure AIII.19. Mass spectrum after chronoamperometry of  $[1a]PF_6$  in PBS with a peak corresponding to  $[7]^+$  (calcd  $m/z = 526.1$ ). Conditions: solution of  $[1a]PF_6$  in PBS (0.1 mM), using carbon sponge as working and counter electrodes, and Ag/AgCl as a reference electrode. The experiment was performed at +0.645 V and compartments were separated by a nafion membrane.

Table AIII.1. Conditions of the photoreactions monitored with MS, UV-vis, and CD.

Complex	Solvent	Stock solution			Working sol. (mM)	Photon flux 493 nm LED ( $mol \cdot s^{-1}$ )	Time (min)	Air /Ar
		w (mg)	V (mL)	M (mM)				
$[1a]PF_6$	PBS					$1.61 \cdot 10^{-7}$	180	Air
	PBS + 5 mM GSH	1.57	5	0.467	0.0178	$1.61 \cdot 10^{-7}$	180	Air
$[2a]PF_6$	PBS					$1.61 \cdot 10^{-7}$	150	Ar
$[2a]PF_6$	PBS	1.03	10	0.147	0.032	$1.19 \cdot 10^{-7}$	180	Air
$[2b]PF_6$	PBS	0.92	10	0.131	0.087	$1.09 \cdot 10^{-7}$	790	Air
$[3a]PF_6$	PBS	1.40	25	0.077	0.077	$1.48 \cdot 10^{-7}$	140	Air
$[1a]PF_6$	$CH_3CN$	0.96	10	0.142	0.071	$1.10 \cdot 10^{-7}$	90	Ar
$[2a]PF_6$	$CH_3CN$	1.29	10	0.184	0.092	$1.12 \cdot 10^{-7}$	80	Ar
$[2b]PF_6$	$CH_3CN$	1.28	10	0.182	0.121	$1.05 \cdot 10^{-7}$	70	Ar
$[3a]PF_6$	$CH_3CN$	1.08	10	0.148	0.074	$1.12 \cdot 10^{-7}$	180	Ar

### Appendix III

Table AIII.2. Observed rate constants ( $k_{obs}$ ) for the formation of  $[Ru(dmbpy)_2(CH_3CN)_2]^{2+}$  at different concentrations of  $CH_3CN$ . Conditions: solution of  $[3a]PF_6$  (0.062 mM) in water with 1%, 2%, 3%, 4%, 5%, 10%, 30%, and 80%  $CH_3CN$  upon irradiation under Ar with a 493 nm LED with a photon flux of  $1.13 \cdot 10^{-7} - 1.16 \cdot 10^{-7} \text{ mol} \cdot \text{s}^{-1}$ .

vol% $CH_3CN$	$k_{obs}$
1	$2.03 \cdot 10^{-3}$
2	$2.86 \cdot 10^{-3}$
3	$3.43 \cdot 10^{-3}$
4	$3.72 \cdot 10^{-3}$
5	$5.08 \cdot 10^{-3}$
10	$7.34 \cdot 10^{-3}$
30	$1.55 \cdot 10^{-2}$
80	$5.02 \cdot 10^{-2}$

Table AIII.3. Absolute and relative energies in water (COSMO) and dipole moments ( $D$ ) of the isomers of  $[1a]^+$ ,  $[2b]^+$ , and  $[3a]^+$  optimized by DFT/PBE0/TZP.

Isomer	Absolute energy in water (Hartree)	Relative energy $\Delta E$ in water ( $\text{kJ} \cdot \text{mol}^{-1}$ )	Dipole moment in water (debye)
$[1a]^+$	-16.77848092	0.0	37.8
$[1b]^+$	-16.77581705	6.9	52.5
$[2a]^+$	-18.22296593	1.9	11.1
$[2b]^+$	-18.22368686	0.0	35.8
$[2c]^+$	-18.21391701	25.7	73.1
$[2d]^+$	-18.22284318	2.2	53.7
$[3a]^+$	-19.67189354	0.0	34.7
$[3b]^+$	-19.66442602	19.6	52.0

Table AIII.4. Calculated bond lengths ( $\text{\AA}$ ), angles ( $^\circ$ ), and structural distortion parameters in the DFT-minimized geometry of complexes  $[\mathbf{1a}]^+$ ,  $[\mathbf{2b}]^+$ , and  $[\mathbf{3a}]^+$ . Atom numbering is indicated in Figure AIII.20.

Atoms	$[\mathbf{1a}]^+$	$[\mathbf{2b}]^+$	$[\mathbf{3a}]^+$
<b>Ru7-N15</b>	2.1067	2.1080	2.1243
<b>Ru7-N8</b>	2.0802	2.0700	2.1035
<b>Ru7-N21</b>	2.0728	2.1268	2.1098
<b>Ru7-N4</b>	2.0798	2.1304	2.1175
<b>Ru7-N34/N62</b>	2.1650	2.1811	2.2111
<b>Ru7-O48</b>	2.1094	2.1055	2.1086
<b>N4-Ru7-N21</b>	78.39	78.49	78.29
<b>N15-Ru7-N8</b>	78.22	78.36	78.27
<b>N34/62-Ru7-O48</b>	80.21	79.84	78.02
<b>N21-Ru7-N8</b>	90.89	94.18	98.21
<b>N4-Ru7-N8</b>	95.21	95.36	101.4
<b>N21-Ru7-N15</b>	97.25	103.5	101.9
<b>N21-Ru7-N34/62</b>	96.86	94.43	97.92
<b>N4-Ru7-N34/62</b>	91.81	92.22	86.92
<b>N4-Ru7-O48</b>	94.55	99.05	98.26
<b>N8-Ru7-O48</b>	92.78	91.79	86.14
<b>N15-Ru7-O48</b>	90.11	79.57	81.58
<b>N15-Ru7-N34/62</b>	95.21	93.79	93.36
<sup>a</sup> $\sigma^2$	50.5	75.7	90.4
<sup>b</sup> $\lambda$	2.21	2.50	3.06

<sup>a</sup>The bond angle variance is  $\sigma^2 = \frac{1}{11} \sum_{n=1,12} (\theta_n - 90)^2$ , where  $\theta_n$  is one of the twelve angles in Table AIII.4. <sup>b</sup>The mean quadratic elongation is  $\lambda = \frac{1}{6} \sum_{n=1,6} \left[ \frac{d_n - \langle d \rangle}{\langle d \rangle} \right]^2$ , where  $d_n$  is one of the bond length in Table AIII.4 and  $\langle d \rangle$  is the mean of those bond lengths.

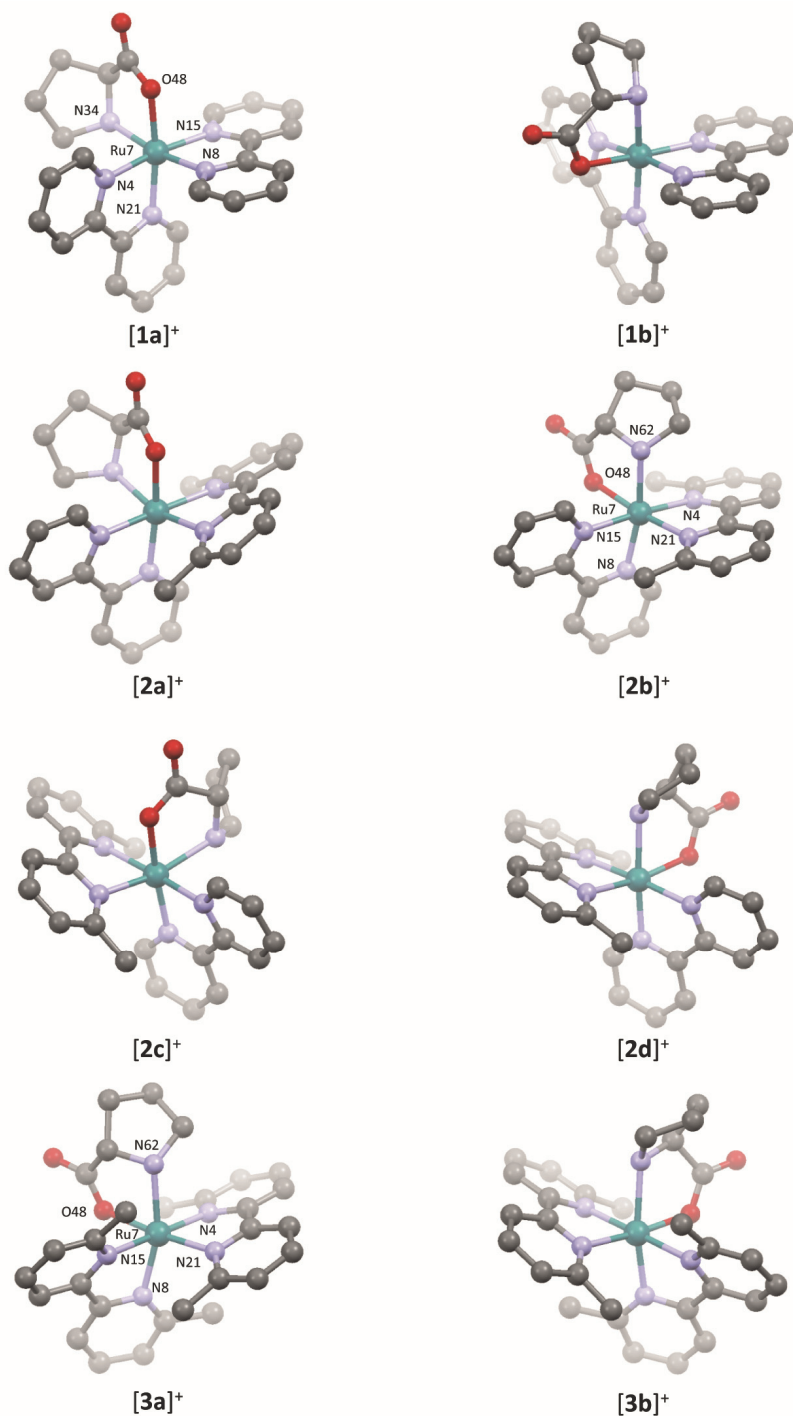


Figure AIII.20. Structures of [1a]<sup>+</sup>, [1b]<sup>+</sup>, [2a]<sup>+</sup>, [2b]<sup>+</sup>, [2c]<sup>+</sup>, [2d]<sup>+</sup>, [3a]<sup>+</sup>, and [3b]<sup>+</sup> optimized by DFT in water (COSMO).

# APPENDIX IV: SUPPORTING INFORMATION FOR CHAPTER 3

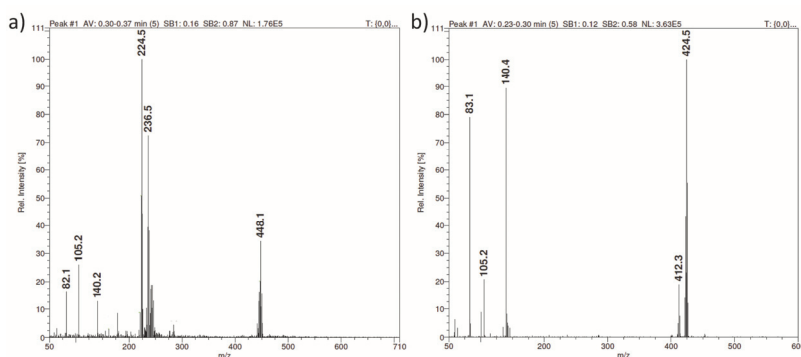


Figure AIV.1. Mass spectrum of water solutions of (a)  $[2]Cl_2$  and (b)  $[3]Cl_2$  after 80 min irradiation with a 445 nm LED. a) Peaks corresponding to  $\{mtmp + H\}^+$  (calcd  $m/z = 140.2$ ),  $[Ru(bpy)_2(OH)_2]^{2+}$  (calcd  $m/z = 225.0$ ),  $[Ru(bpy)_2(OH_2)(OH)]^+$  (calcd  $m/z = 448.5$ ). b) Peaks corresponding to  $\{mtmp + H\}^+$  (calcd  $m/z = 140.2$ ) and  $[Ru(Ph_2phen)_2(CH_3CN)_2]^{2+}$  (calcd  $m/z = 424.1$ ). Conditions are detailed in Figure 3.1.

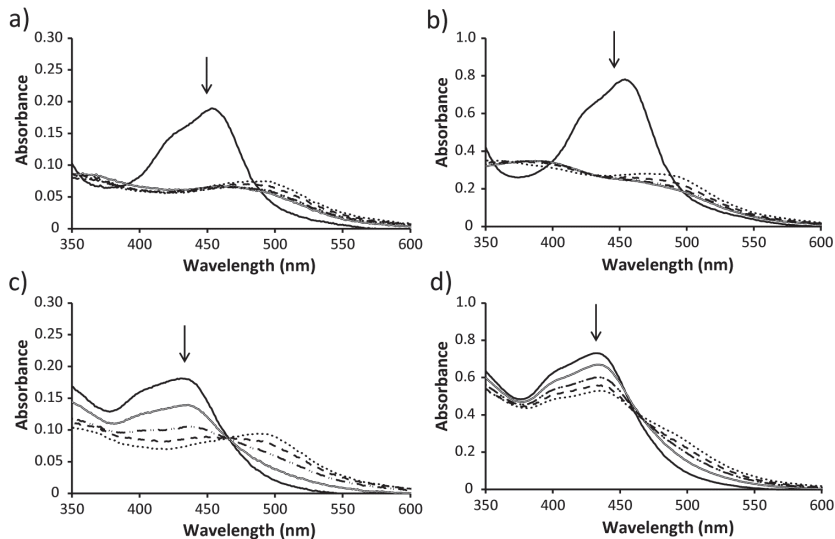


Figure AIV.2. Evolution of the UV-vis spectrum of a well in a 96-well plate containing compound (a)  $[1]Cl_2$  ( $40 \mu M$ ), (b)  $[1]Cl_2$  ( $200 \mu M$ ), (c)  $[2]Cl_2$  ( $40 \mu M$ ), and (d)  $[2]Cl_2$  ( $200 \mu M$ ) in OptiMEM complete, under blue light irradiation (310 K) at 0 min (—), 2 min (=), 5 min (---), 8 min (- - -), 10 min (···). Under such conditions, 10 min irradiation correspond to a light dose of  $6.5 J \cdot cm^{-2}$

## Appendix IV

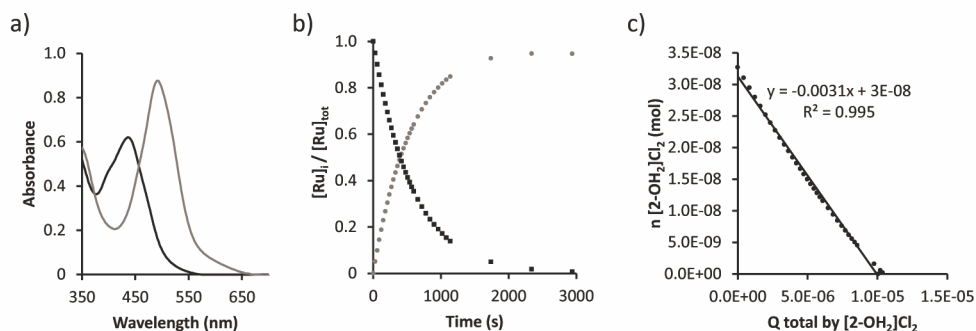


Figure AIV.3. Kinetic data for the second step of the photosubstitution of  $[2]Cl_2$  in water under  $N_2$ . a) Globally fitted absorption spectra of the mono-aqua intermediate  $[Ru(bpy)_2(\eta^1\text{-mtmp})(OH_2)]Cl_2$  ( $[2-OH_2]Cl_2$ , black) and  $[Ru(bpy)_2(OH_2)_2]Cl_2$  (grey) according to modelling using the Glotaran software. b) Modelled evolution of the relative concentrations of  $[2-OH_2]Cl_2$  (squares) and  $[Ru(bpy)_2(OH_2)_2]Cl_2$  (circles) vs. irradiation time according to global fitting using Glotaran. c) Plot of the amount of  $[2-OH_2]Cl_2$  (mol) vs. total amount of photons absorbed by  $[2-OH_2]Cl_2$  (mol). The slope of the obtained line is the opposite of the quantum yield of the formation of the bis-aqua complex. Conditions: 0.109 mM solution of  $[2-OH_2]Cl_2$  in demineralized water irradiated at 298 K under  $N_2$  using a 445 nm LED at  $1.49 \cdot 10^{-7} \text{ mol} \cdot \text{s}^{-1}$ .

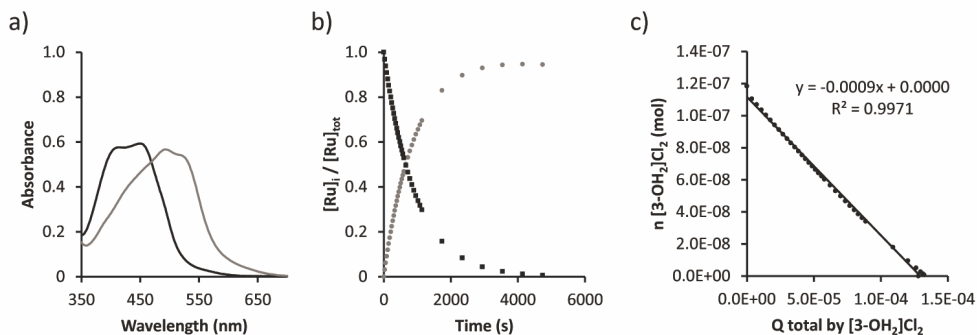


Figure AIV.4. Kinetic data for the second step of the photosubstitution of  $[3]Cl_2$  in water under  $N_2$ . a) Globally fitted absorption spectra of the mono-aqua intermediate  $[Ru(Ph_2phen)_2(\eta^1\text{-mtmp})(OH_2)]Cl_2$  ( $[3-OH_2]Cl_2$ , black) and  $[Ru(Ph_2phen)_2(OH_2)_2]Cl_2$  (grey) according to modelling using the Glotaran software. b) Modelled evolution of the relative concentrations of  $[3-OH_2]Cl_2$  (squares) and  $[Ru(Ph_2phen)_2(OH_2)_2]Cl_2$  (circles) vs. irradiation time according to global fitting using Glotaran. c) Plot of the amount of  $[3-OH_2]Cl_2$  (mol) vs. total amount of photons absorbed by  $[3-OH_2]Cl_2$  (mol). The slope of the obtained line is the opposite of the quantum yield of the formation of the bis-aqua complex. Conditions: 0.038 mM solution of  $[3-OH_2]Cl_2$  in demineralized water irradiated at 298 K under  $N_2$  using a 445 nm LED at  $1.31 \cdot 10^{-7} \text{ mol} \cdot \text{s}^{-1}$ .

# APPENDIX V: SUPPORTING INFORMATION FOR CHAPTER 4

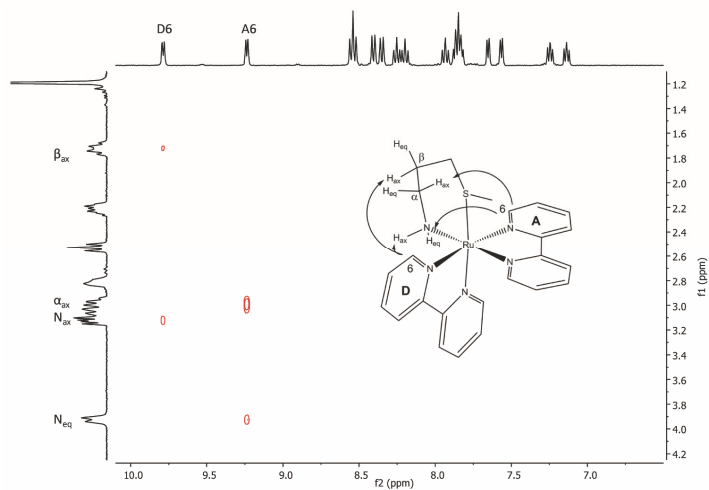


Figure AV.1. NOESY NMR spectrum of a solution of  $[1](PF_6)_2$  in  $D_2O$  showing off-diagonal peaks between the  $\alpha_{ax}$  proton and the A6 proton, the  $N_{eq}$  proton and the A6 proton, the  $\beta_{ax}$  proton and the D6 proton, and the  $N_{ax}$  proton and the D6 proton. This confirms that the isomer is  $\Lambda$ -(S)-eq- $[1]^{2+}$ .

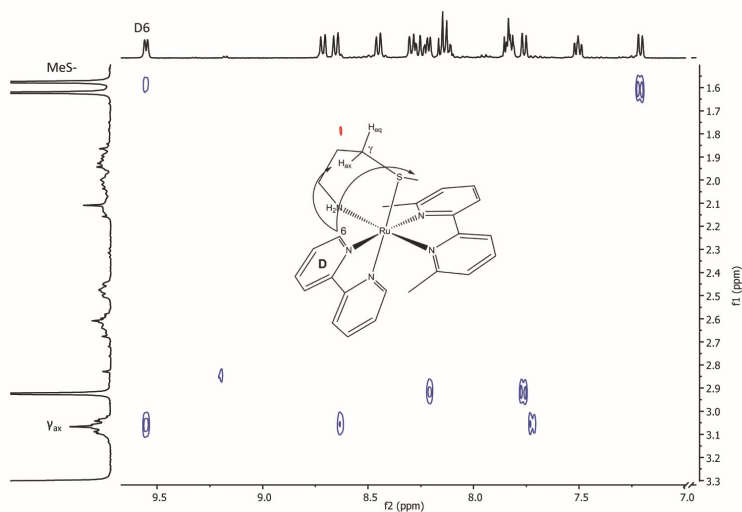


Figure AV.2. NOESY NMR spectrum of a solution of  $[2](PF_6)_2$  in  $CD_3OD$  showing off-diagonal peaks between the  $\gamma_{ax}$  proton and the D6 proton, and the methyl thioether group and the D6 proton. This confirms that the isomer is  $\Lambda$ -(R)-eq- $[2a]^{2+}$ .

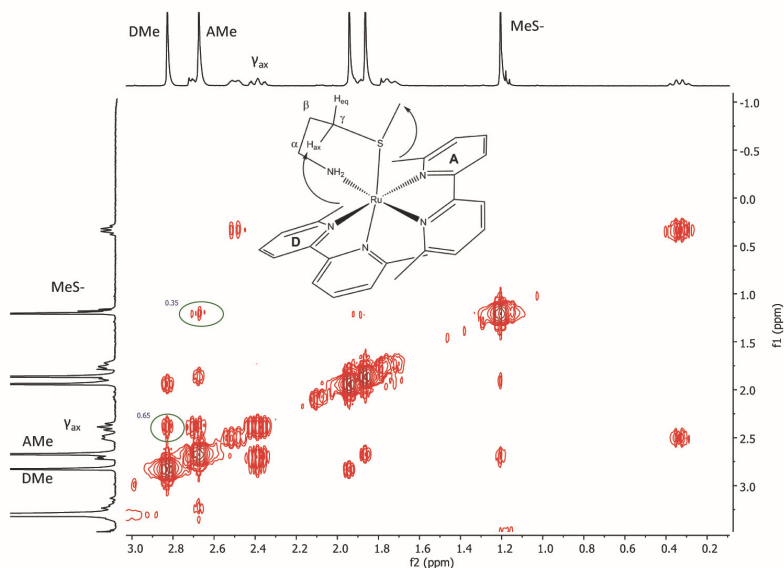


Figure AV.3. NOESY NMR spectrum of a solution of  $[3](PF_6)_2$  in  $CD_3OD$  showing off-diagonal peaks between the  $\gamma_{ax}$  proton and the DMe substituent, and the methyl thioether group and the AMe substituent, with relative intensities of 65% and 35% respectively. This confirms that the isomer is  $A(S)\text{-ax-}[3]^{2+}$ .

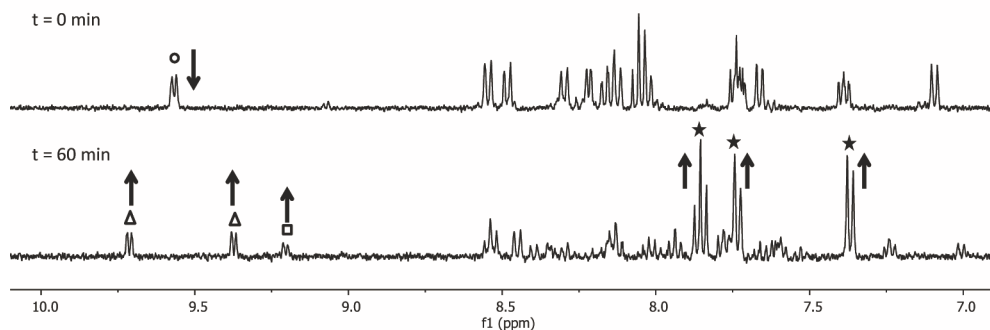


Figure AV.4. Evolution of the  $^1H$  NMR spectra (region 10 – 7 ppm) of a solution of  $[2](PF_6)_2$  in  $D_2O$  irradiated under  $N_2$  with a Xe lamp at 298 K. The doublet at 9.57 ppm (triangle) corresponds to the  $H_6$  proton on the bpy for complex  $[2]^{2+}$  (circle) and the rising doublets at 9.72, 9.38, and 9.21 ppm correspond to the  $H_6$  proton on the bpy of two new complexes (triangles and square). The arising peaks at 7.86, 7.74, and 7.37 ppm correspond to free dmbpy (star). Concentration of  $[2](PF_6)_2 = 1.99$  mM.

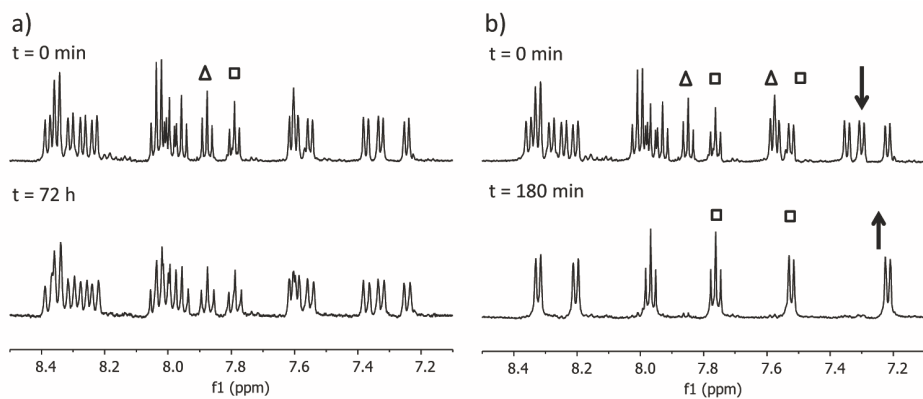


Figure AV.5. a) Evolution of the  $^1\text{H}$  NMR spectra (region 8.5 – 7.2 ppm) of a solution of  $[\mathbf{3}](\text{PF}_6)_2$  at 298 K in  $\text{D}_2\text{O}$  under  $\text{N}_2$  in the dark. No change in the spectra is observed. b) Evolution of the  $^1\text{H}$  NMR spectra (region 8.5 – 7.2 ppm) of a solution of  $[\mathbf{3}](\text{PF}_6)_2$  in  $\text{D}_2\text{O}$  irradiated under  $\text{N}_2$  with a Xe lamp at 298 K. Peaks with a triangle corresponds to  $[\mathbf{3}](\text{PF}_6)_2$  and peaks with a square correspond to  $[\text{Ru}(\text{dmbpy})_2(\text{OH}_2)]^{2+}$ . Concentration of  $[\mathbf{3}](\text{PF}_6)_2 = 2.61 \text{ mM}$ .

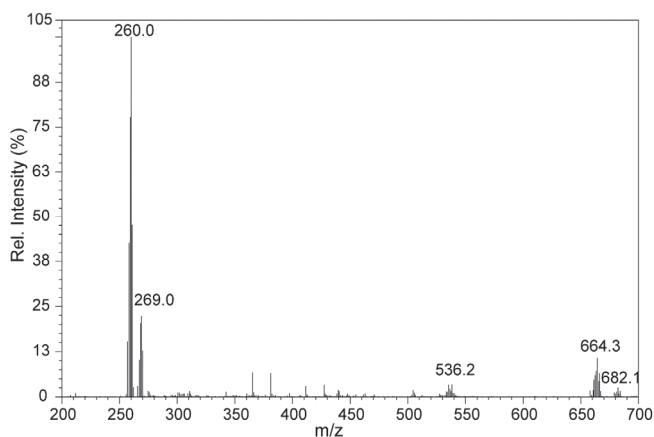


Figure AV.6. Mass spectrum of a 0.145 mM solution of  $[\mathbf{I}](\text{PF}_6)_2$  in water after 6 min of light irradiation at 298 K with a 445 nm LED with a photon flux of  $2.98 \cdot 10^{-8} \text{ mol} \cdot \text{s}^{-1}$  under  $\text{N}_2$  with peaks corresponding to  $[\text{Ru}(\text{bpy})_2(\text{mtpa})]^{2+}$  (calcd  $m/z = 259.6$ ),  $[\text{Ru}(\text{bpy})_2(\text{mtpa})(\text{OH}_2)]^{2+}$  (calcd  $m/z = 268.6$ ), and  $[\text{Ru}(\text{bpy})_2(\text{mtpa})(\text{OH})]^+$  (calcd  $m/z = 536.1$ ). Conditions are detailed in Table 4.5.

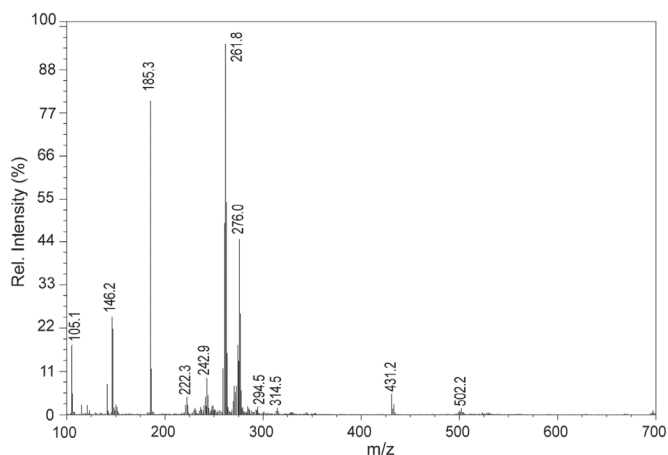


Figure AV.7. Mass spectrum of a 0.101 mM solution of  $[2](PF_6)_2$  in water after 60 min of light irradiation at 298 K with a 445 nm LED with a photon flux of  $2.92 \cdot 10^{-8} \text{ mol} \cdot \text{s}^{-1}$  under  $N_2$  with peaks corresponding to  $\{mtpa + H\}^+$  (calcd.  $m/z = 106.1$ ),  $\{dmbpy + H\}$  (calcd.  $m/z = 185.2$ ),  $[Ru(dmbpy)(bpy)(CH_3CN)_2]^{2+}$  (calcd.  $m/z = 262.1$ ), and  $[Ru(bpy)(mtpa)(CH_3CN)_2]^{2+}$  (calc.  $m/z = 222.5$ ). Conditions are detailed in Table 4.5.

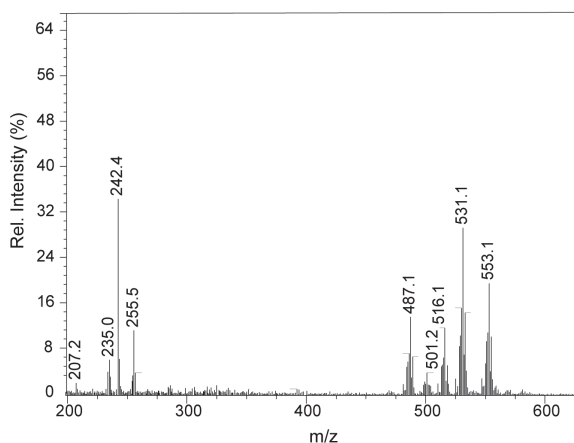


Figure AV.8. Mass spectrum of a 0.123 mM solution of  $[3](PF_6)_2$  in water after light irradiation at 298 K with a 445 nm LED with a photon flux of  $2.79 \cdot 10^{-7} \text{ mol} \cdot \text{s}^{-1}$  under  $N_2$  with no peaks corresponding to the starting  $[3](PF_6)_2$ . Conditions are detailed in Table 4.5.

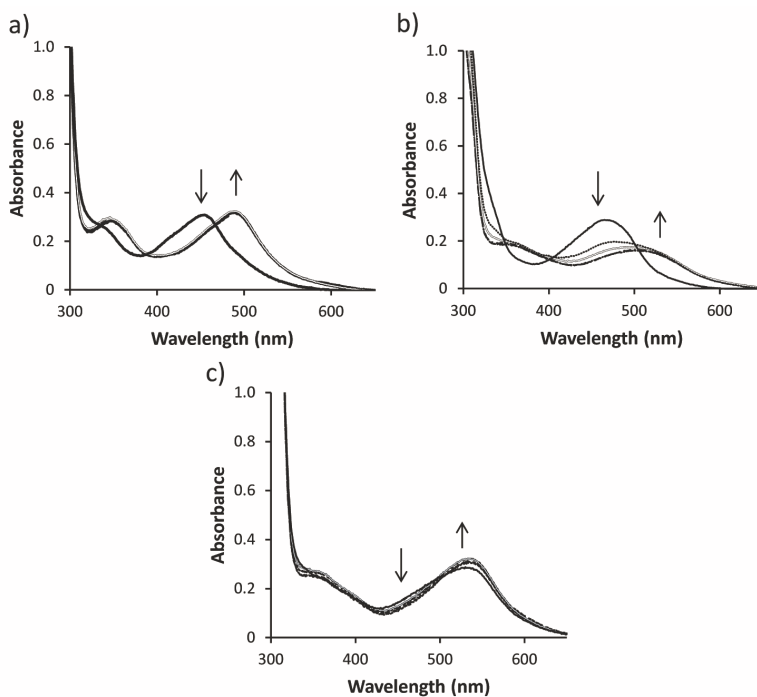


Figure AV.9. Evolution of the UV-vis spectra of a well in a 96-well plate containing compound (a) [1] ( $PF_{\phi_2}$ ) ( $86 \mu M$ ), (b) [2] ( $PF_{\phi_2}$ ) ( $86 \mu M$ ), or (c) [3] ( $PF_{\phi_2}$ ) ( $86 \mu M$ ) in OptiMEM complete under blue light irradiation ( $37^\circ C$ ) at 0 min (—), 2 min (⋯), 5 min (=), 10 min (- - -), or 15 min (—⋯—).

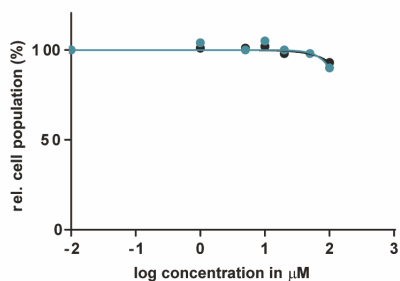


Figure AV.10. Dose-response curves for A549 cells in presence of mtpa irradiated with blue light ( $454 \text{ nm}$ ,  $6.35 \text{ J}\cdot\text{cm}^{-2}$ ) 6 h after treatment (blue data points) or left in the dark (black data points). Photocytotoxicity assay outline: cells seeded at  $5\cdot 10^3$  cells/well at  $t = 0 \text{ h}$ , treated with mtpa at  $t = 24 \text{ h}$ , irradiated at  $t = 30 \text{ h}$ , and SRB cell-counting assay performed at  $t = 96 \text{ h}$ . Incubation conditions:  $37^\circ C$  and  $7\% \text{ CO}_2$ .

Table AV.1. Calculated bond lengths ( $\text{\AA}$ ), angles ( $^\circ$ ), and structural distortion parameters in the DFT-minimized geometry of complexes  $[1]^{2+}$ ,  $[2]^{2+}$ , and  $[3]^{2+}$ .

Atoms	$\Lambda$ -(R)- eq-[1] <sup>2+</sup>	$\Lambda$ -(S)- eq-[1] <sup>2+</sup>	$\Lambda$ -(R)- eq-[2a] <sup>2+</sup>	$\Lambda$ -(S)- eq-[2a] <sup>2+</sup>	$\Lambda$ -(R)- eq-[2b] <sup>2+</sup>	$\Lambda$ -(S)- eq-[2b] <sup>2+</sup>	$\Lambda$ -(R)- eq-[3] <sup>2+</sup>	$\Lambda$ -(S)- eq-[3] <sup>2+</sup>	$\Lambda$ -(S)- ax-[3] <sup>2+</sup>
Ru13-N12	2.106	2.102	2.156	2.162	2.104	2.109	2.155	2.194	2.144
Ru13-N3	2.093	2.093	2.148	2.154	2.104	2.164	2.129	2.146	2.129
Ru13-N21	2.098	2.107	2.088	2.086	2.16	2.101	2.125	2.156	2.130
Ru13-N14	2.111	2.115	2.109	2.101	2.187	2.181	2.136	2.201	2.144
Ru13-N26	2.169	2.181	2.177	2.174	2.172	2.183	2.194	2.207	2.186
Ru13-S30	2.384	2.368	2.407	2.414	2.397	2.372	2.438	2.366	2.427
N12-Ru13-N3	77.92	77.93	77.48	77.54	77.8	77.48	77.44	76.67	77.51
N21-Ru13-N14	77.73	77.78	77.89	77.91	76.94	77.13	77.50	76.34	77.35
N26-Ru13-S30	90.31	91.54	89	91.02	93.04	90.99	81.74	91.17	86.78
N12-Ru13-N21	95.12	94.6	96.62	96.07	94.45	95.48	100.67	89.22	100.46
N3-Ru13-N21	89.39	89.69	93.95	94.68	86.59	87.48	96.70	86.06	97.03
N3-Ru13-N14	95.79	96.24	102.24	101.25	92.09	91.87	101.67	90.33	100.86
N3-Ru13-S30	92.6	91.47	87.64	86.27	88.6	91.29	94.90	91.59	89.26
N12-Ru13-S30	83.6	93.76	83.06	90.75	79.33	88.83	77.89	93.39	84.51
N12-Ru13-N26	98.82	99.29	99.69	99.77	98.42	101.86	98.70	107.51	98.98
N14-Ru13-S30	103.79	93.84	102.45	95.26	108.56	90.31	104.12	100.46	97.84
N14-Ru13-N26	87.03	86.13	80.88	81.72	91.32	88.51	82.28	84.89	82.80
N21-Ru13-N26	87.61	87.71	89.38	88.34	91.39	98.23	86.45	90.93	87.15
<sup>a</sup> $\sigma^2$	62.4	45.0	81.8	63.3	81.8	52.5	108.6	76.3	76.0
<sup>b</sup> $\lambda$	0.0022	0.0020	0.0023	0.0025	0.0021	0.0017	0.0029	0.0017	0.0027

<sup>a</sup>The bond angle variance is  $\sigma^2 = \frac{1}{11} \sum_{n=1,12} (\theta_n - 90)^2$ , where  $\theta_n$  is one of the twelve angles in Table AV.1. <sup>b</sup>The mean quadratic elongation is  $\lambda = \frac{1}{6} \sum_{n=1,6} \left[ \frac{d_n - \langle d \rangle}{\langle d \rangle} \right]^2$ , where  $d_n$  is one of the bond length in Table AV.1 and  $\langle d \rangle$  is the mean of those bond lengths.

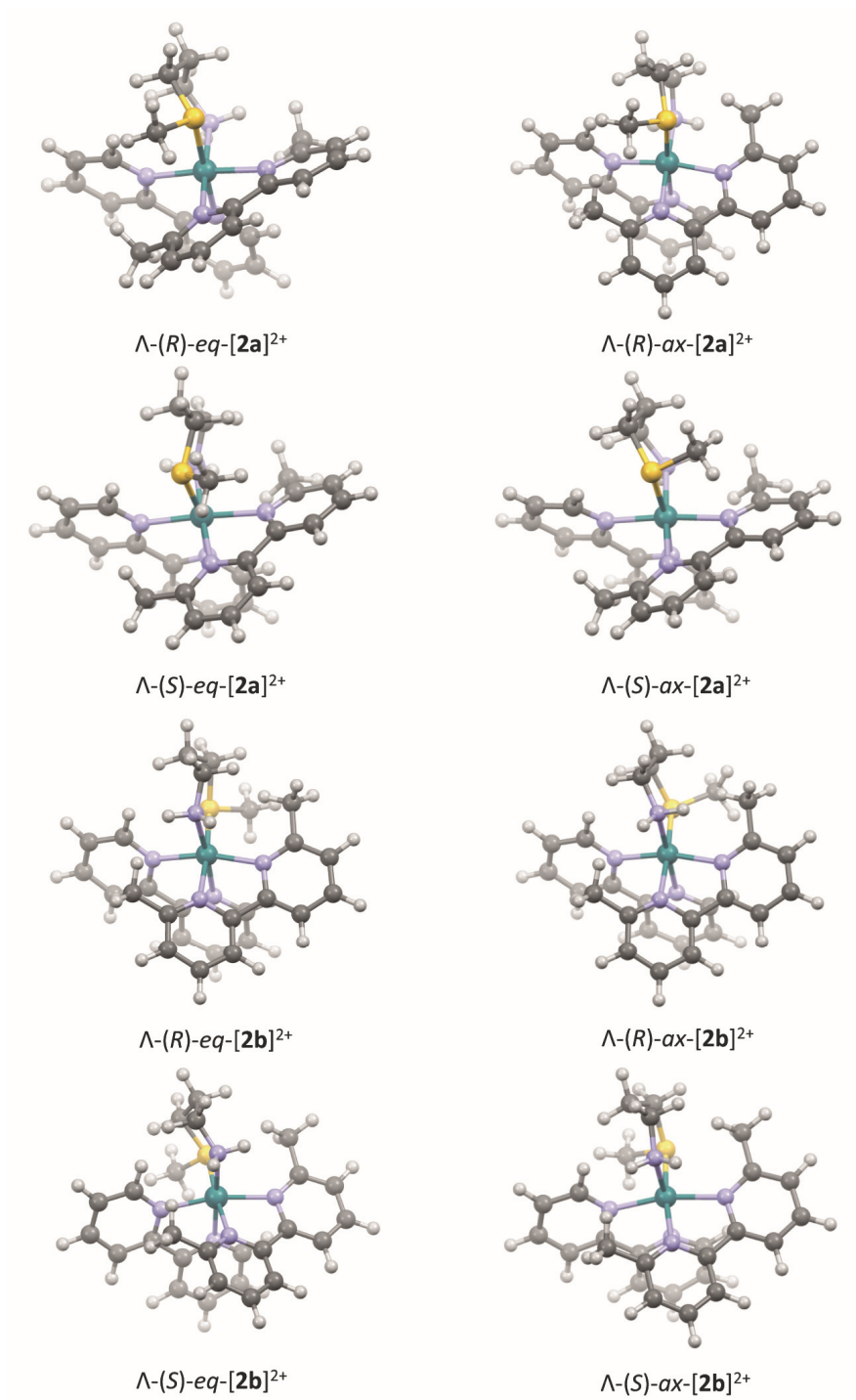


Figure AV.11. Structures of the isomers of [2]<sup>2+</sup> optimized by DFT in water (COSMO).

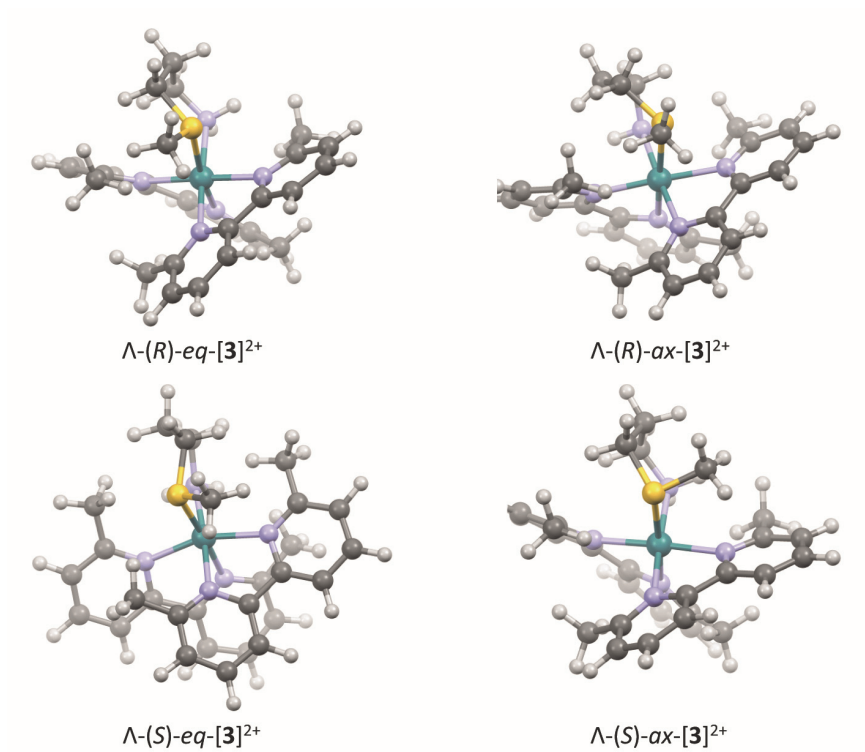


Figure AV.12. Structures of the isomers of  $[3]^{2+}$  optimized by DFT in water (COSMO).

## APPENDIX VI: SUPPORTING INFORMATION FOR CHAPTER 5

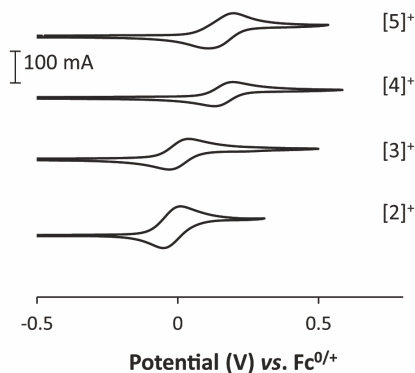


Figure AVI.1. Cyclic voltammograms of 1 mM solutions of  $[2]PF_6$ ,  $[3]PF_6$ ,  $[4]PF_6$ , and  $[5]PF_6$  in 0.1 M  $Bu_4NPF_6/CH_3CN$  ( $\nu = 100 \text{ mV}\cdot\text{s}^{-1}$ ).

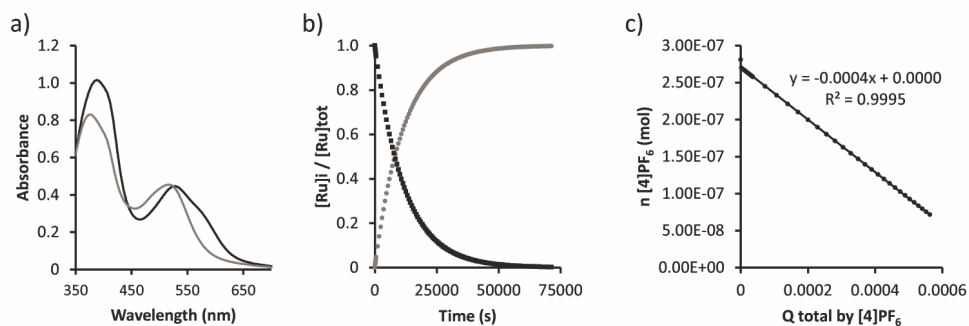


Figure AVI.2. Kinetic data for the photosubstitution of  $[4]PF_6$  in  $CH_3CN$  under  $N_2$ . a) Left axis: globally fitted absorption spectra of  $[4]PF_6$  (black) and  $[Ru(bpy)(phpy)(CH_3CN)_2]PF_6$  (grey) according to modelling using the Glotaran software. b) Modelled evolution of the relative concentrations of  $[4]PF_6$  (squares) and  $[Ru(bpy)(phpy)(CH_3CN)_2]PF_6$  (circles) vs. irradiation time according to global fitting using Glotaran. c) Plot of the amount of  $[4]PF_6$  (mol) vs. total amount of photons absorbed by  $[4]PF_6$  (mol). The slope of the obtained line is the opposite of the quantum yield of the formation of the bis-acetonitrile complex. Conditions: 0.094 mM solution of  $[4]PF_6$  in  $CH_3CN$  irradiated at 298 K under  $N_2$  using a 521 nm LED at  $6.80 \cdot 10^{-8} \text{ mol}\cdot\text{s}^{-1}$ .

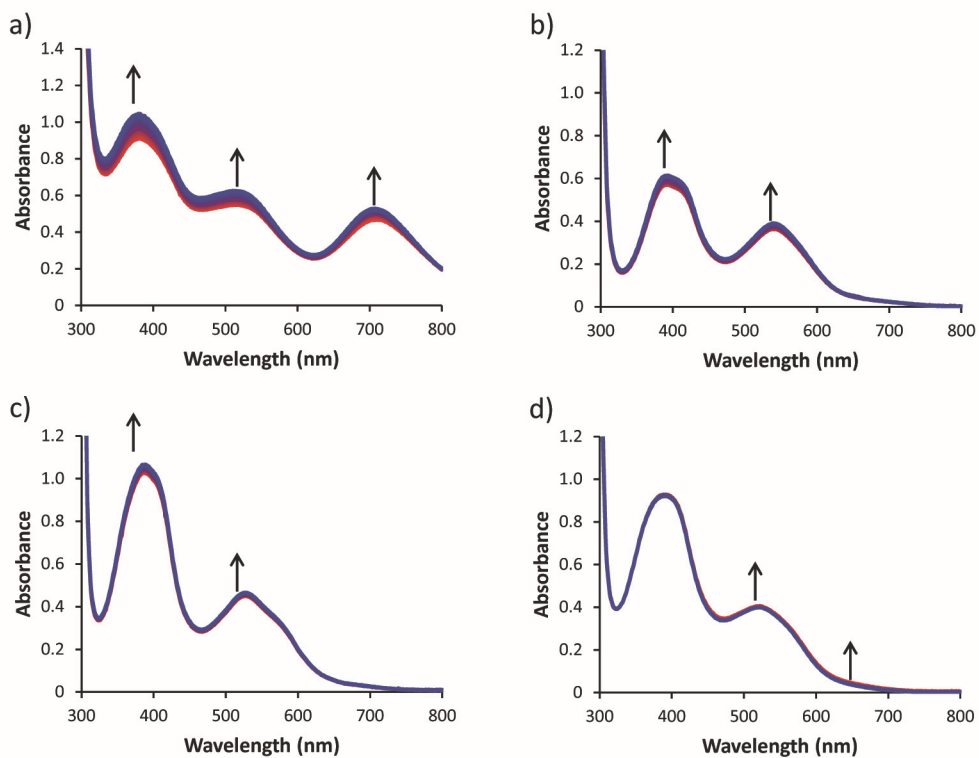


Figure AVI.3. Evolution of the UV-vis spectra over 10 h in the dark at room temperature and under air of acetonitrile solutions of a) [2]PF<sub>6</sub>, b) [3]PF<sub>6</sub>, c) [4]PF<sub>6</sub>, and d) [5]PF<sub>6</sub>.

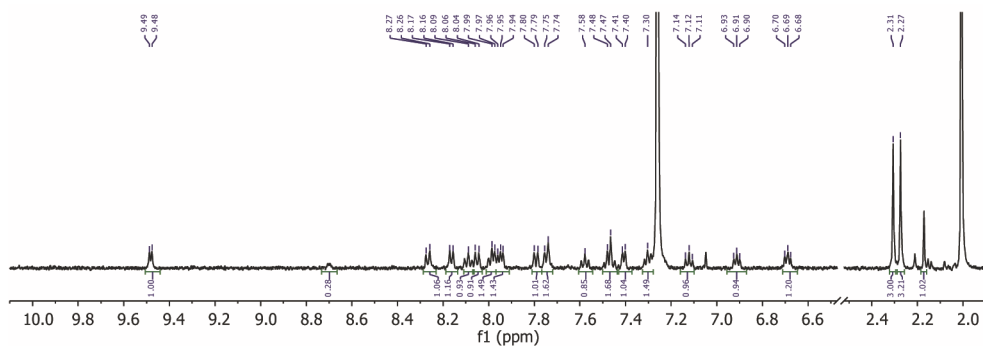


Figure AVI.4. <sup>1</sup>H NMR of a solution of [1b]PF<sub>6</sub> in CDCl<sub>3</sub>. After irradiation of [1a]PF<sub>6</sub> in CH<sub>3</sub>CN with a Xe lamp mounted with a <400 nm filter and an IR filter, the solvent was evaporated and the photoproduct was redissolved in CDCl<sub>3</sub>.

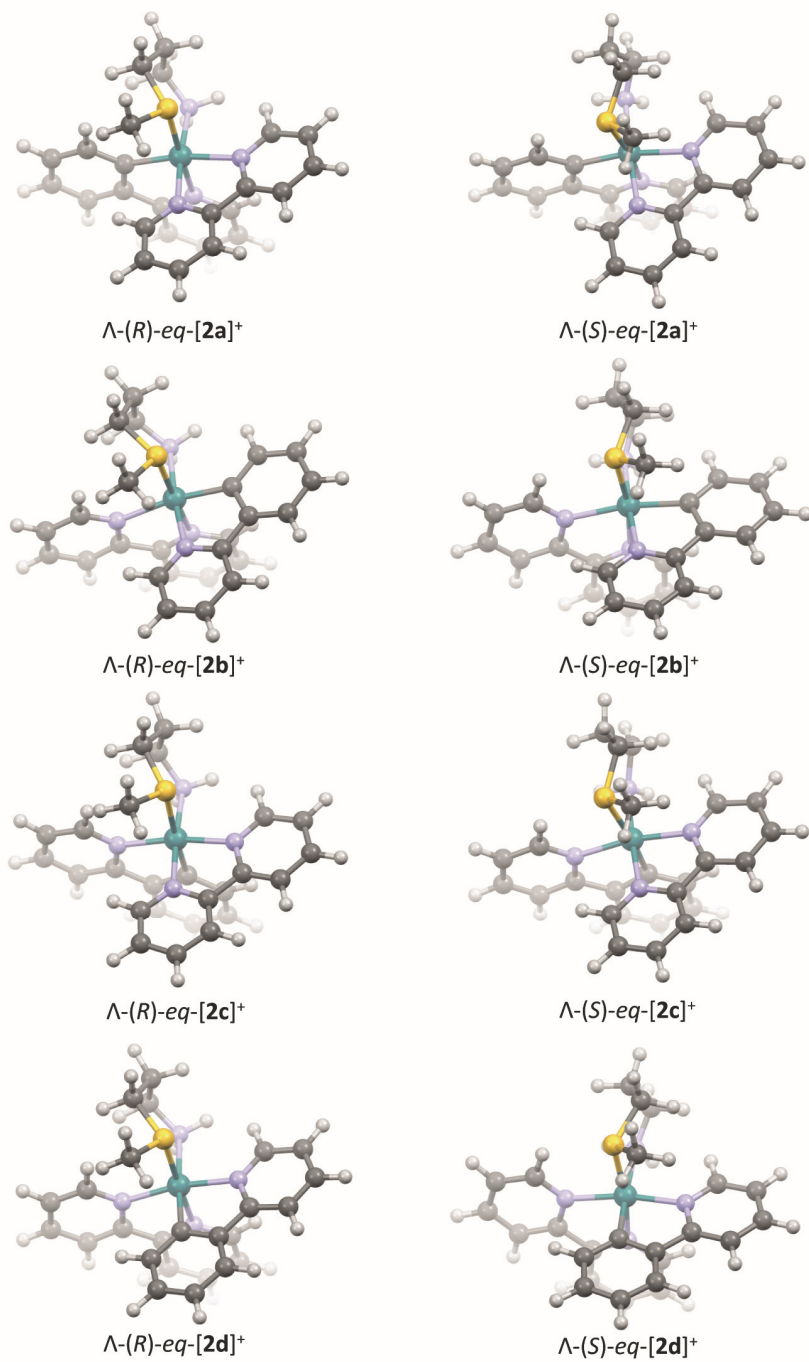


Figure AVI.5. Structures of isomers  $\Lambda$ -(R)-eq and  $\Lambda$ -(S)-eq of [2a]<sup>+</sup>, [2b]<sup>+</sup>, [2c]<sup>+</sup>, and [2d]<sup>+</sup> optimized by DFT in water (COSMO).

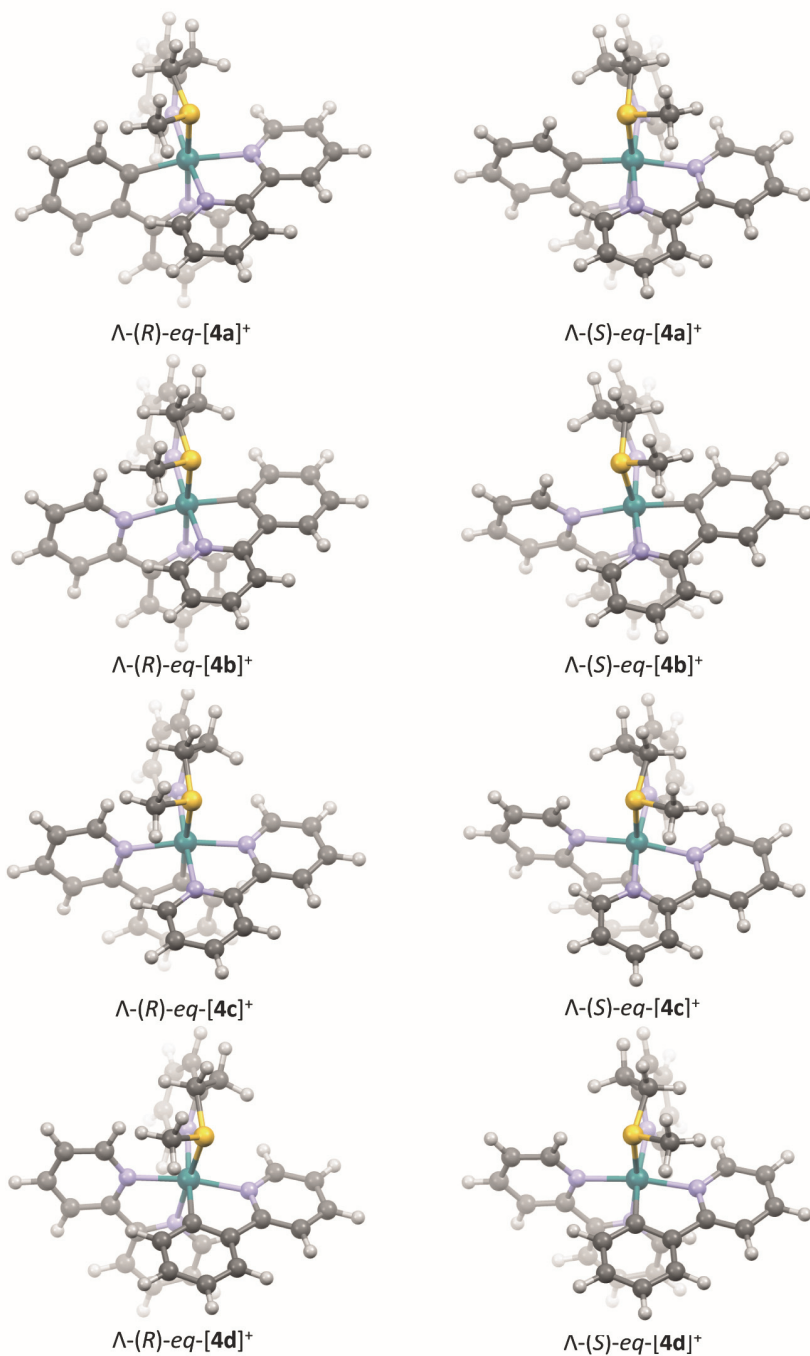


Figure AVI.6. Structures of isomers  $\Lambda$ -(R)-eq and  $\Lambda$ -(S)-eq of [4a]<sup>+</sup>, [4b]<sup>+</sup>, [4c]<sup>+</sup>, and [4d]<sup>+</sup> optimized by DFT in water (COSMO).

## APPENDIX VII: SUPPORTING INFORMATION OF CHAPTER 6

---

### AVII.1 Comments on the synthesis

Due to the dissymmetry of mtmp, two different coordination isomers were obtained for  $[\text{Ru}(\text{Ph}_2\text{phen})(\text{mtmp})(\text{ox})]$  (**[8]**): one with the sulfur donor *trans* to  $\text{Ph}_2\text{phen}$ , and another one with the sulfur donor atom *trans* to  $\text{ox}^{2-}$ . These two isomers can be separated by column chromatography on alumina using a mixture  $\text{CH}_2\text{Cl}_2:\text{CH}_3\text{OH}$  as eluent. However, when working with a pure isomer, further replacement of the  $\text{ox}^{2-}$  by bpy yielded a mixture of two isomers of *cis*- $[\text{Ru}(\text{Ph}_2\text{phen})(\text{bpy})(\text{mtmp})](\text{PF}_6)_2$  (**[2](PF<sub>6</sub>)<sub>2</sub>**) that probably have the sulfur atom either *trans* to  $\text{Ph}_2\text{phen}$  or to bpy. As isomerization occurred as well in this last step, the isolation of pure isomers of **[8]** was later avoided, keeping a single separation step after coordination of the third ligand, *i.e.* after **[2]<sup>2+</sup>** was obtained.

Full characterization of **[2b]<sup>2+</sup>** was attempted using 2D NMR (NOESY) spectroscopy in  $\text{CD}_3\text{CN}$ . Off-diagonal correlations were observed between one of the  $\text{H}_\beta$  protons and B6, and between the other  $\text{H}_\beta$  and P1 (Figure AVII.1). Thus, these signals are not conclusive and may correspond either to the isomer with the sulfur donor *trans* to bpy or the isomer with the sulfur donor *trans* to  $\text{Ph}_2\text{phen}$ . Unfortunately, no other off-diagonal correlation peak involving the thiomethyl group was observed, which prevents from unambiguously assigning **[2b]<sup>2+</sup>** as the isomer with S *trans* to bpy or to  $\text{Ph}_2\text{phen}$ . Probably, the methyl group sits above the middle of both the bpy or the  $\text{Ph}_2\text{phen}$  ligands, as shown in Chapter 4 for similar complexes. Unfortunately, single crystals suitable for X-Ray crystallography could not be obtained.

## Appendix VII

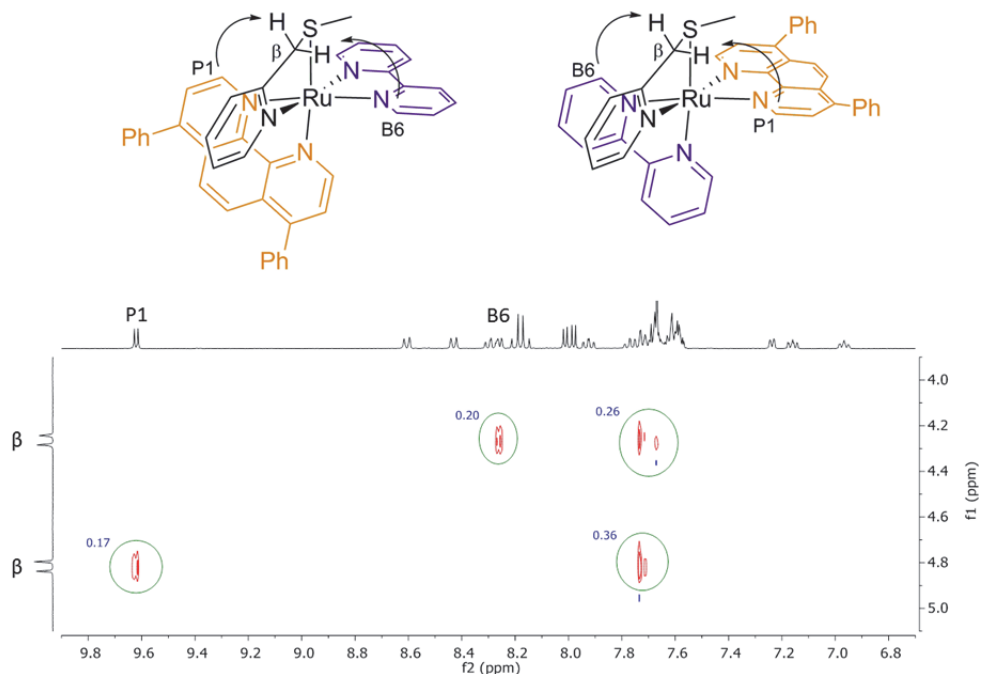


Figure AVII.1. NOESY NMR spectrum of a solution of a purified isomer of  $[2](PF_6)_2$ , called  $[2b](PF_6)_2$ , in  $CD_3CN$ . Off-diagonal peaks between one of the  $H_\beta$  of *mtmp* and B6 and between the other  $H_\beta$  and P1 can be seen, with relative intensities of 20% and 17%, respectively. The other interaction (36% and 26%) corresponds to off-diagonal correlations correspond to intraligand NOESY interactions.

Table AVII.1. Selected bond length ( $\text{\AA}$ ) and angles ( $^\circ$ ) for  $\Lambda$ -(S)/ $\Delta$ -(R)- $[Ru(dmbpy)_2(mtmp-\kappa N, \kappa S)]Cl_2 \cdot CH_3OH \cdot H_2O$ .

	$\Lambda$ -(S)-[3]Cl <sub>2</sub>
Ru1-S1	2.3709(4)
Ru1-N1	2.1254(12)
Ru1-N2	2.0928(12)
Ru1-N3	2.0934(12)
Ru1-N4	2.1000(12)
Ru1-C5	2.1362(12)
S1-C30-C29-N5	-26.36(16)

## AVII.2 Photochemistry

Due to the different solubility in water of the four complexes, their photochemistry was described either in water or in acetonitrile. In Chapter 2 we already highlighted the importance of the solvent on photosubstitution reactions. In order to assess whether

photosubstitution would happen during photocytotoxicity assays, solutions of [1]Cl<sub>2</sub>, [2](PF<sub>6</sub>)<sub>2</sub>, [3]Cl<sub>2</sub>, [4]PF<sub>6</sub>, and [5]Cl<sub>2</sub> in the cell culture media containing less than 0.5% DMSO were irradiated with green light (520 nm) in a 96-well plate using the irradiation setup of the cell assay.

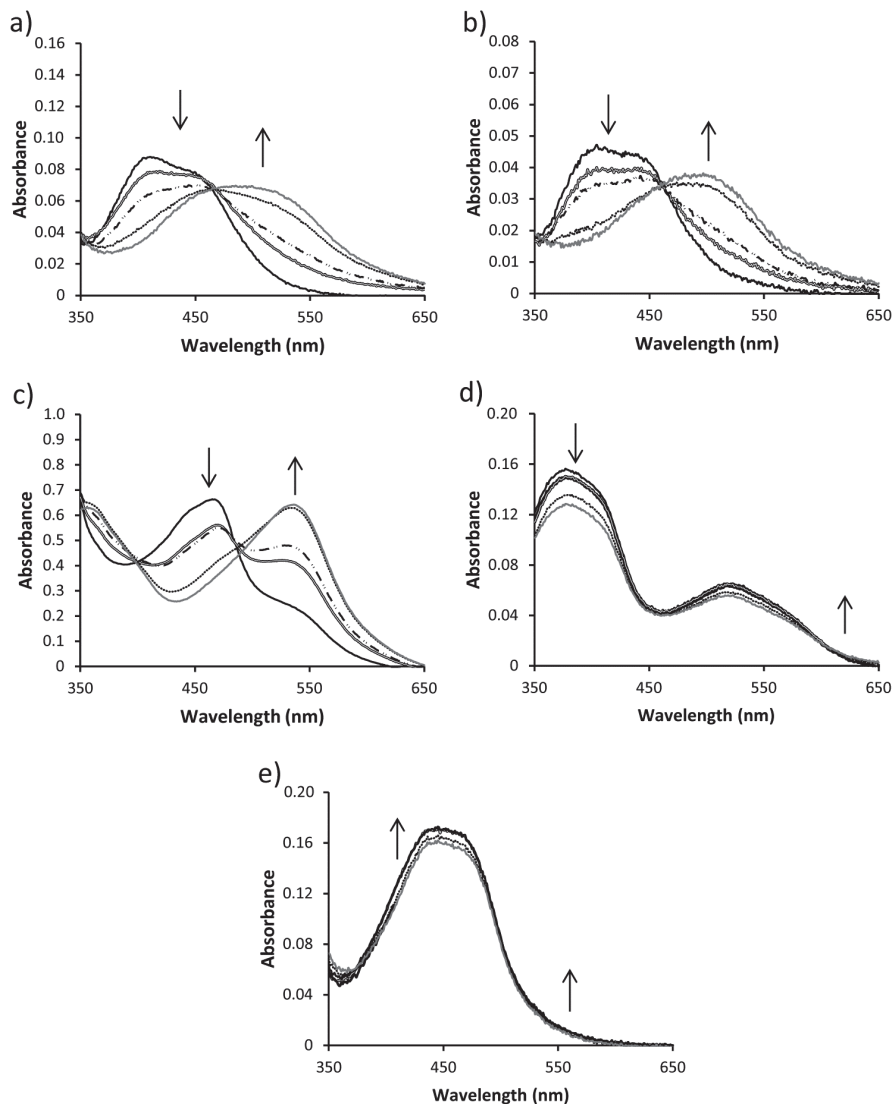


Figure AVII.2. Evolution of the UV-vis spectrum of a well in a 96-well plate containing compound (a) [1]Cl<sub>2</sub> (20 μM), (b) [2](PF<sub>6</sub>)<sub>2</sub> (20 μM), (c) [3]Cl<sub>2</sub> (200 μM), (d) [4]PF<sub>6</sub> (10 μM), and (e) [5]Cl<sub>2</sub> (20 μM) in OptiMEM complete, under green light irradiation (37 °C) at 0 min (continuous black), 2 min (=), 5 min (- · - · -), 15 min (- · -), and 30 min (continuous grey). In such conditions, 15 min irradiation correspond to a light dose of 18.8 J.cm<sup>-2</sup>.

## Appendix VII

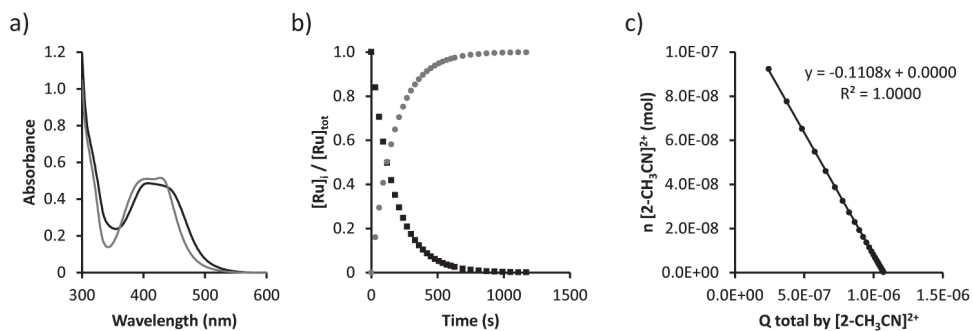


Figure AVII.3. Kinetic data for the second step of the photosubstitution of  $[2](PF_6)_2$  in  $CH_3CN$  under  $N_2$ . a) Globally fitted absorption spectra of the mono-aqua intermediate  $[Ru(bpy)(Ph_2phen)(\eta^1\text{-mtmp})(CH_3CN)]^{2+}$  ( $[2-CH_3CN]^{2+}$ , black) and  $[Ru(Ph_2phen)_2(CH_3CN)_2]^{2+}$  (grey) according to modelling using the Glotaran software. b) Modelled evolution of the relative concentrations of  $[2-CH_3CN]^{2+}$  (squares) and  $[Ru(Ph_2phen)_2(CH_3CN)_2]^{2+}$  (circles) vs. irradiation time according to global fitting using Glotaran. c) Plot of the amount of  $[2-CH_3CN]^{2+}$  (mol) vs. total amount of photons absorbed by  $[2-CH_3CN]^{2+}$  (mol). The slope of the obtained line is the opposite of the quantum yield of the formation of the bis-aqua complex. Conditions: 0.036 mM solution of  $[2](PF_6)_2$  in  $CH_3CN$  irradiated at 298 K under  $N_2$  using a 521 nm LED at  $6.21 \cdot 10^{-8} \text{ mol} \cdot \text{s}^{-1}$ .

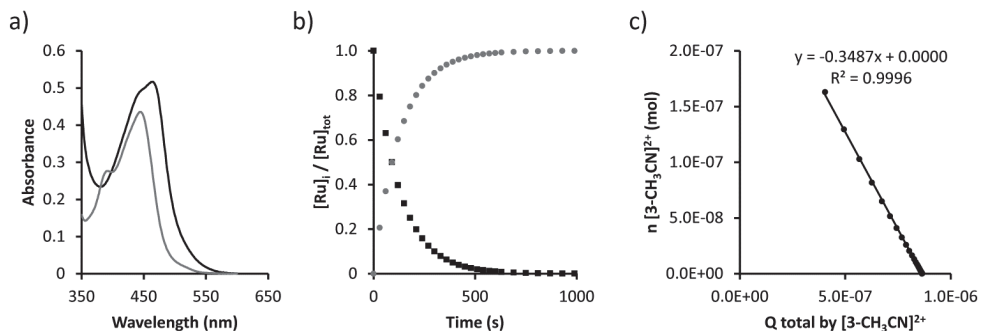


Figure AVII.4. Kinetic data for the second step of the photosubstitution of  $[3]Cl_2$  in  $CH_3CN$  under  $N_2$ . a) Globally fitted absorption spectra of the mono-aqua intermediate  $[Ru(dmbpy)(\eta^1\text{-mtmp})(CH_3CN)]^{2+}$  ( $[3-CH_3CN]^{2+}$ , black) and  $[Ru(dmbpy)_2(CH_3CN)_2]^{2+}$  (grey) according to modelling using the Glotaran software. b) Modelled evolution of the relative concentrations of  $[3-CH_3CN]^{2+}$  (squares) and  $[Ru(dmbpy)_2(CH_3CN)_2]^{2+}$  (circles) vs. irradiation time according to global fitting using Glotaran. c) Plot of the amount of  $[3-CH_3CN]^{2+}$  (mol) vs. total amount of photons absorbed by  $[3-CH_3CN]^{2+}$  (mol). The slope of the obtained line is the opposite of the quantum yield of the formation of the bis-aqua complex. Conditions: 0.088 mM solution of  $[3]Cl_2$  in  $CH_3CN$  irradiated at 298 K under  $N_2$  using a 521 nm LED at  $6.25 \cdot 10^{-8} \text{ mol} \cdot \text{s}^{-1}$ .

### AVII.3 Cell growth curves

The growth curves of the two cancer cells under normoxia (21%) or hypoxia (1%  $O_2$ ) were investigated by seeding the cells at  $t = 0$  and incubating them in the dark. Cells were fixed using TCA at 4, 24, 48, 72, and 96 h after seeding, and then stained with SRB in a cell viability assay. Two biological replicates ( $nb = 2$ ) were performed to

discard any different impact of the hypoxia depending on the passage number. As shown in Figure AVII.5, under normoxia the two cell lines showed a characteristic exponential growth, with doubling times between 20 and 40 h during the first 72h (Figure AVII.5c). Under hypoxia PC3pro4 cells showed an exponential growth and A549 cells show a less acute exponential growth than under normoxia, with doubling times closer to 40 h. Further incubation to 96 h show differences in the growth depending on the cell line. As shown in Figure AVII.5, cells under normoxia grew faster in the last 24 h of the protocol, whereas under hypoxia this growth stabilized, leading to lower cell confluences.

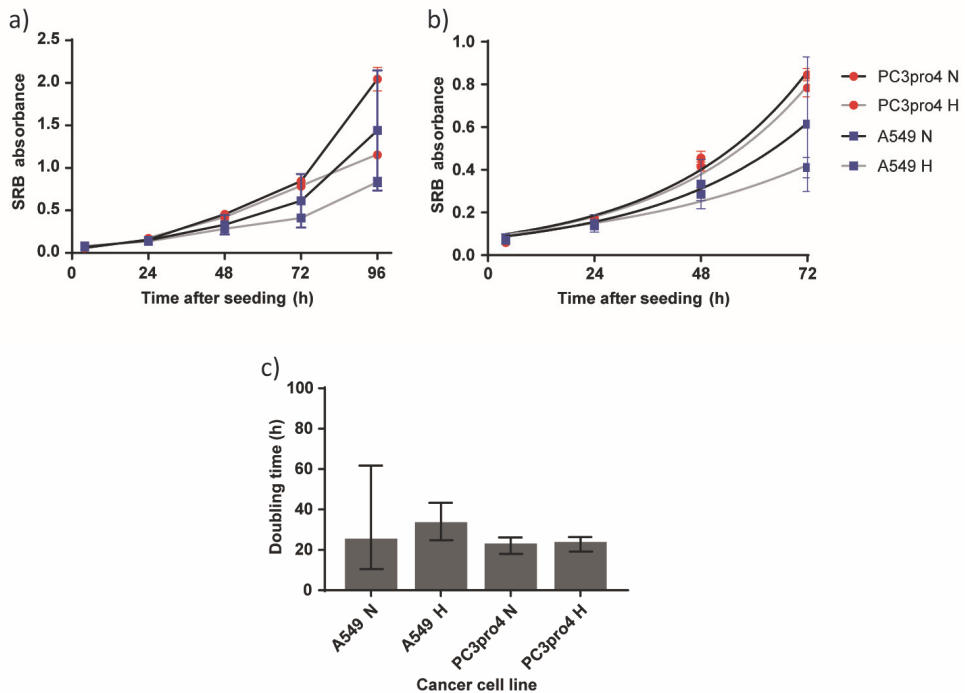
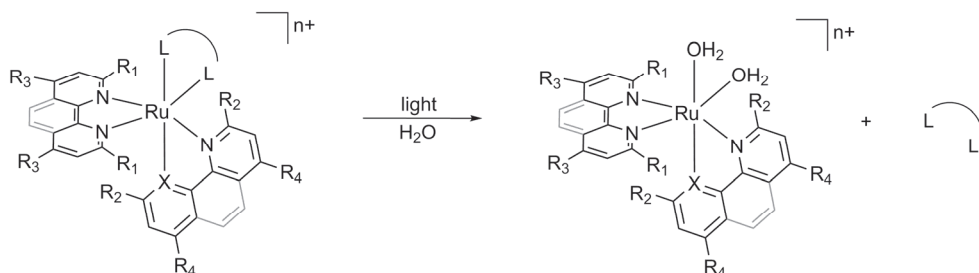


Figure AVII.5. Growth curve (a), fitted exponential growth curves (b), and doubling times with 95% confidence interval (c) for A549 (blue squares) and PC3pro4 (red circles) cancer cell lines under normoxia (N, black line) and hypoxia (H, grey line). Conditions: cells were seeded at time 0 in a 96-well plate using OptiMEM complete and incubated at 37 °C and either 21% O<sub>2</sub> (normoxia) or 1% O<sub>2</sub> (hypoxia) (A549 N = 5.000 cells/well, A549 H = 6.000 cells/well, PC3pro4 N = 4.000 cells/well, and PC3pro4 H = 4.000 cells/well). Cells were fixed using TCA at 4, 24, 48, 72, and 96 h after seeding and then stained with SRB. The SRB absorbance of ten technical replicates (nt = 10) was averaged for one experiment; two biological replicates were performed (nb = 2).



# SAMENVATTING

Het hoofddoel van het onderzoek beschreven in dit proefschrift was de ontwikkeling van nieuwe fotoactiveerbare chemotherapie (PACT), gebaseerd op van ruthenium(II)-complexen die een atoxisch, fotolabel ligand bevatten. De geschiktheid van het lichaamseigen aminozuur L-proline als beschermend ligand is beschreven in Hoofdstuk 2 in een serie complexen van het type  $[\text{Ru}(\text{N},\text{N})_2(\text{L-prolinaat})]\text{PF}_6$ . Het aantal sterisch gehinderde methylgroepen in deze serie is geleidelijk verhoogd van nul in  $[\text{Ru}(\text{bpy})_2(\text{L-prolinaat})]\text{PF}_6$  (**[1]** $\text{PF}_6$ , bpy = 2,2'-bipyridine) tot twee in  $[\text{Ru}(\text{bpy})(\text{dmbpy})(\text{L-prolinaat})]\text{PF}_6$  (**[2]** $\text{PF}_6$ , dmbpy = 6,6'-dimethyl-2,2'-bipyridine) tot vier in  $[\text{Ru}(\text{dmbpy})_2(\text{L-prolinaat})]\text{PF}_6$  (**[3]** $\text{PF}_6$ ). Er is geconstateerd dat de fotoreactiviteit van dit type complexen afhankelijk is van het oplosmiddel: terwijl in waterige oplossing geen van de bovengenoemde complexen substitutie vertonen onder bestraling met licht, fotosubstitueren de sterisch gehinderde complexen **[2]** $\text{PF}_6$  en **[3]** $\text{PF}_6$  in acetonitril op het ligand L-proline of dmbpy, óf beiden in parallel. Interessant is verder dat **[1]** $\text{PF}_6$  in aanwezigheid van zuurstof twee waterstofatomen verliest na lichtbestraling in water, en daarmee tot het iminocomplex  $[\text{Ru}(\text{bpy})_2(\text{L-prolinaat} - 2\text{H})]\text{PF}_6$  foto-oxideert. De aanwezigheid van elektrondonerende methylgroepen in **[2]** $\text{PF}_6$  en **[3]** $\text{PF}_6$  verlaagt de zuurgraad van het amine, en voorkomt zo de oxidatie tot imine. Gezien de stabiliteit van het ruthenium-prolinaatcomplex in water en de niet-selectieve fotosubstitutie in acetonitril werd het gebruik van het negatief geladen L-prolinaat als beschermiligand verworpen en in het verlengde daarvan ook alle andere natuurlijke aminozuren met een *N,O*-coördinatie.



Schema 1. Fotosubstitutie van een bidentaalligand in een ruthenium(II)-polypyridylcomplex veroorzaakt door lichtbestraling in water. In het onderzoek bescreven in dit proefschrift zijn de octaëdrische verstoring en lipofiliteit van de complexen gevarieërd door de functionele groepen  $R_1$ ,  $R_2$ ,  $R_3$ , en  $R_4$  aan te passen.  $X = \text{N}$  of  $\text{C}$ .

## Samenvatting

Glazer *et al.* heeft de fotocytotoxiciteit van  $[\text{Ru}(\text{bpy})_2(\text{dmbpy})]\text{Cl}_2$  op longkanker cellen (A549-cellen) gerapporteerd, en heeft deze toxiciteit, analoog aan de werking van cisplatina, toegeschreven aan het fotogegeneerde complex  $\text{cis-}[\text{Ru}(\text{bpy})_2(\text{OH}_2)_2]^{2+}$ .<sup>1</sup> In hoofdstuk 3 laten we echter zien dat het ligand dmbpy, dat ook vrijkomt bij de fotoreactie, op zichzelf ook giftig is. Daarom rees de vraag: is  $[\text{Ru}(\text{bpy})_2(\text{OH}_2)_2]^{2+}$  cytotoxisch? Kan een PDT-effect worden uitgesloten? Om de rol van  $[\text{Ru}(\text{bpy})_2(\text{OH}_2)_2]^{2+}$  te onderzoeken hebben we de fototoxiciteit van  $[\text{Ru}(\text{bpy})_2(\text{dmbpy})]\text{Cl}_2$  vergeleken met die van  $[\text{Ru}(\text{bpy})_2(\text{mtmp})]\text{Cl}_2$  (mtmp = 2-(methylthio)methylpyridine), met een neutraal, zwavel-bevattend bidentaats ligand. De complexen zijn vergelijkbaar in hun reactiviteit: ze produceren  $[\text{Ru}(\text{bpy})_2(\text{OH}_2)_2]^{2+}$  onder bestraling met licht, ze hebben een lage quantumopbrengst voor de productie van singletzuurstof, en ze hebben een vergelijkbare lipofiliteit en een lage celopname. Het verschil tussen de twee complexen is dat het vrijkomende ligand mtmp zelf niet cytotoxisch is. Als A549-cellen met  $[\text{Ru}(\text{bpy})_2(\text{mtmp})]\text{Cl}_2$  behandeld worden, wordt er geen cytotoxisch effect waargenomen worden, noch in het donker noch na bestraling met licht. Derhalve hebben we geconcludeerd, dat het fotogegeneerde  $[\text{Ru}(\text{bpy})_2(\text{OH}_2)_2]^{2+}$  niet cytotoxisch is, en dat de cytotoxiciteit, die na bestraling van  $[\text{Ru}(\text{bpy})_2(\text{dmbpy})]\text{Cl}_2$  met licht wordt waargenomen, veroorzaakt wordt door het vrijgekomen dmbpy. Echter, het lipofielere complex  $[\text{Ru}(\text{Ph}_2\text{phen})_2(\text{mtmp})]\text{Cl}_2$  ( $\text{Ph}_2\text{phen}$  = 4,7-difenyl-1,10-fenantroline) laat na bestraling met licht verhoogde cytotoxiciteit zien. Op basis van de bevindingen kan worden geconcludeerd dat, een rutheniumcomplex zelf cytotoxisch kan zijn, maar het complex moet dan wel lipofiel genoeg zijn om te worden opgenomen door kankercellen.

De geschiktheid van *N,S*-moleculen als beschermende liganden, en het belang van een bepaalde mate van lipofiliteit die nodig is om cytotoxische activiteit te bereiken, heeft tot de synthese van een nieuwe serie van complexen geleid die het *N,S*-ligand 3-(methylthio)propylamine (mtpa) bevatten, hetgeen in Hoofdstuk 4 beschreven staat. In deze serie wordt de octaëdrische verstoring en lipofiliteit van het complex verhoogd door het toevoegen van methylgroepen op 6- en 6'-positie van het bpy-ligand, zoals in Hoofdstuk 2 voor L-prolinaatcomplexen beschreven is. Het aantal methylgroepen in de verbindingen heeft een cruciaal effect op de fotochemie en cytotoxische activiteit van deze complexen. Terwijl het sterisch ongehinderde complex  $[\text{Ru}(\text{bpy})_2(\text{mtpa})](\text{PF}_6)_2$  mtpa niet volledig fotosubstitueert en dus niet fototoxisch voor A549-cellen is, laat het meer sterisch gehinderde complex  $[\text{Ru}(\text{bpy})(\text{dmbpy})(\text{mtpa})](\text{PF}_6)_2$  efficiënte mtpa-fotosubstitutie zien onder bestraling met blauw licht, hetgeen dan ook tot fotocytotoxiciteit leidt. Wanneer het complex echter te sterisch gehinderd is, zoals in

[Ru(dmbpy)<sub>2</sub>(mtpa)](PF<sub>6</sub>)<sub>2</sub>, wordt het ook thermisch in het donker geactiveerd en verliest daardoor zijn selectieve fotoactiviteit. De karakterisatie van deze complexen was niet triviaal. Naast de chiraliteit van de octaëder ( $\Delta$  of  $\Lambda$ ) zijn er nog twee bronnen van isomerie aanwezig in deze complexen: de configuratie (*S* of *R*) van het gecoördineerde zwavelatoom, en de stoelinversie van de zesring die resulteert uit de coördinatie van het *N,S*-chelende ligand aan het rutheniumion. De laatste vorm van isomerie transformeert een axiale thioethermethylgroep (*ax*) in een equatoriale groep (*eq*) en *vice versa*. Dit leidt tot een totaal van vier isomeren voor [Ru(bpy)<sub>2</sub>(mtpa)](PF<sub>6</sub>)<sub>2</sub> en [Ru(dmbpy)<sub>2</sub>(mtpa)](PF<sub>6</sub>)<sub>2</sub>, en acht isomeren voor [Ru(bpy)(dmbpy)(mtpa)](PF<sub>6</sub>)<sub>2</sub>, in het laatste geval mede veroorzaakt doordat het zwavelatoom van mtpa zowel *trans* ten opzichte van de bpy als de dmbpy kan staan. Ondanks de complexiteit van de stereochemische identificatie van deze complexen, zijn ze allemaal volledig gekarakteriseerd door een combinatie van 2D-NMR spectroscopie en DFT-berekeningen. De interligand-interactie tussen de waterstofatomen in de axiale positie van de mtpa-stoelconformatie en de substituenten op positie 6 van het bpy-ligand bleken de drijvende kracht in de stereoselectiviteit van de synthese te zijn.

Aangezien *N,S*-liganden beter blijken te zijn dan *N,O*-liganden voor toepassing in PACT rutheniumcomplexen, door hun selectieve fotosubstitutie, zijn deze liganden ook geselecteerd voor de synthese van fotoactiveerbare gecyclometaleerde rutheniumcomplexen van het type [Ru(bpy)(phpy)(*N,S*)]PF<sub>6</sub> (phpy = 2-fenylpyridine) (Hoofdstuk 5). Het effect van de grootte van de chelaat ring van het *N,S*-ligand op het rutheniumion (vijfring *vs.* zesring) en de aard van het stikstofdonoratoom (primaire amine *vs.* pyridine) is systematisch onderzocht. Coördinatie van 2-(2-methylthioethyl)pyridine (mtep) of mtpa aan het ruthenium(II)ion resulteert in een zesring met stoelconformatie en leidt tot één van acht mogelijke isomeren. Maar als het *N,S*-ligand tot een chelende vijfring leidt (bij 2-methylthioethylamine (mtea) of mtmp), werden twee of drie isomeren verkregen, die moeilijk van elkaar te isoleren scheiden waren. De grootte van de chelaatring van het *N,S*-chelende ligand kan dus gebruikt worden om de stereoselectiviteit van de reactie te sturen. Bovendien leiden complexen met *N,S*-liganden die in een zesring coördineren tot een snellere fotosubstitutie in acetonitril, dan hun analogen met een vijfring chelaat. Waarschijnlijk is re-chelatie in het laatste geval sneller, waardoor de gehele fotosubstitutiesnelheid verlaagd wordt. Tenslotte, als het stikstofdonoratoom van het *N,S*-ligand een pyridine is, bleek het complex minder gevoelig voor oxidatie te zijn dan wanneer het een primaire amine betreft. We schrijven dit effect toe aan de *trans*-positie van het  $\pi$ -

## Samenvatting

accepterende pyridineligand ten opzichte van het koolstofdonoratoom, waarmee de hoge elektronendichtheid in het rutheniumion, veroorzaakt door de cyclometallering, gestabiliseerd wordt. Het complex  $[\text{Ru}(\text{bpy})(\text{phpy})(\text{mtep})]\text{PF}_6$ , dat een op pyridine gebaseerd *N,S*-ligand bevat dat een zesring chelaat vormt, vervult alle criteria om een veelbelovend PACT medicijn te worden: het kan op een stereoselectieve manier gesynthetiseerd worden, is stabiel onder zuurstofrijke condities in het donker en het niet-toxische *N,S*-ligand wordt effectief gefotosubstitueerd onder bestraling met groen licht.

In het laatste hoofdstuk vroegen we ons af of de rutheniumcomplexen die in dit proefschrift beschreven staan, échte PACT medicijnen zijn. In andere woorden: kan het lage quantumrendement voor de productie van singletzuurstof ( $\Phi_d$ ) de waargenomen cytotoxiciteit verklaren? Ten eerste hebben we, als controle voor de hypoxische belichtingsopstelling, laten zien dat de fotocytotoxiciteit van de fotosensibilisators Rose Bengal en  $[\text{Ru}(\text{Ph}_2\text{phen})_2(\text{bpy})]\text{Cl}_2$  sterk gereduceerd wordt bij 1%  $\text{O}_2$ . De lage zuurstofconcentratie reduceert de fotoindex (PI), d.w.z. de verhouding tussen de  $\text{EC}_{50}$  waarden verkregen bij behandeling in het donker met die verkregen na lichtbestraling, naar respectievelijk 3.0 en 1.9, vergeleken met de veel hogere gemeten waarden bij normoxia (respectievelijk >400 en 29). Dezelfde opstelling werd gebruikt om de cytotoxiciteit van de vermeende PACT-complexen  $[\text{Ru}(\text{bpy})(\text{Ph}_2\text{phen})(\text{mtmp})](\text{PF}_6)_2$  en  $[\text{Ru}(\text{dmbpy})_2(\text{mtmp})]\text{Cl}_2$  te testen, welke een duidelijke toxiciteitverhoging na bestraling met groen licht in hypoxische condities lieten zien. De cytotoxiciteit in het donker was te laag om een PI te bepalen, die voor een écht PACT medicijn voor normoxische en hypoxische condities in hetzelfde gebied zou moeten liggen.<sup>2</sup> Samenvattend kan gezegd worden dat het gebruik van hypoxische condities erg interessant is om te testen of een fotosubstituerend complex ook daadwerkelijk een echte, zuurstofonafhankelijke PACT-verbinding is, of een zwak, doch gericht PDT medicijn.

## References

1. B. S. Howerton, D. K. Heidary and E. C. Glazer, *J. Am. Chem. Soc.*, **2012**, 134, 8324-8327.
2. L. N. Lameijer, D. Ernst, S. L. Hopkins, M. S. Meijer, S. H. C. Askes, S. E. Le Dévédec and S. Bonnet, *Angew. Chem., Int. Ed.*, **2017**, 56, 11549-11553.

# LIST OF PUBLICATIONS

---

A. Bahreman, **J. A. Cuello-Garibo**, and S. Bonnet, “Yellow-light sensitization of a ligand photosubstitution reaction in a ruthenium polypyridyl complex covalently bound to a Rhodamine dye”, *Dalton Trans.*, **2014**, 43, 4494-4505.

**J. A. Cuello-Garibo**, E. Pérez-Gallent, L. van der Boon, M. A. Siegler, and S. Bonnet, “Influence of the steric bulk and solvent on the photoreactivity of ruthenium polypyridyl complexes coordinated to L-proline”, *Inorg. Chem.*, **2017**, 56, 4818-4828.

**J. A. Cuello-Garibo**, M. S. Meijer, and S. Bonnet, “To cage or to be caged? The cytotoxic species in ruthenium-based photoactivated chemotherapy is not always the metal”, *Chem. Commun.*, **2017**, 53, 6768-6771.

**J. A. Cuello-Garibo**, C. James, M. A. Siegler, and S. Bonnet, “Ruthenium-based PACT compounds based on an N,S non-toxic ligand: a delicate balance between photoactivation and thermal stability”, *Chem<sup>2</sup>*, **2017**, *in press*.

**J. A. Cuello-Garibo**, C. James, S. L. Hopkins, M. A. Siegler, and S. Bonnet, “Tuning the stereoselectivity, photoreactivity, and redox potential of cycloruthenated complexes by small changes in the N,S ligand”, *manuscript in preparation*.

**J. A. Cuello-Garibo**, S. Bronkhorst, Y. Batsuin, V. H. S. van Rixel, C. Schmidt, I. Ott, M. A. Siegler, and S. Bonnet, “PACT or PDT: are ruthenium(II) complexes photosubstituting a non-toxic ligand also phototoxic under hypoxic conditions?”, *manuscript in preparation*.



# CURRICULUM VITAE

---

Jordi-Amat Cuello-Garibo was born in Puçol, País Valencià (Spain) on 9 April 1989. In 2007, he graduated from the Puçol High School. In that year, he started his BSc studies in Chemistry at the Universitat de València. During his studies, he visited Leiden University within the Erasmus Exchange Program for his Master Thesis, which was performed under the supervision of Dr. Sylvestre Bonnet with the title “*Fluorescent labeling of photoreactive ruthenium polypyridyl complexes: probing molecular motion at the surface of a lipid bilayer*”. In 2013, he received the *Licenciatura* degree (equivalent to Master of Science) in Chemistry at Universitat de València.

After a short experience in the industry (Octoplus B.V.), he started his PhD studies under the supervision of Dr. Sylvestre Bonnet and Prof. dr. Bouwman in the research group ‘Metals in Catalysis, Biomimetics, and Inorganic Materials’ (MCBIM) of the Leiden Institute of Chemistry, Leiden University. During his PhD studies he collaborated with Prof. dr. Snaar-Jagalska (Leiden University) and Prof. dr. I. Ott (TU Braunschweig). He supervised three BSc students and three MSc students from Ukraine, France, United Kingdom, and The Netherlands.

Parts of the results reported in this thesis were presented at the following meetings and conferences:

- Holland Research School of Molecular Chemistry (HRSMC) Symposiums, in Amsterdam and Leiden, The Netherlands, in 2015 (poster) and 2016 (oral), respectively.
- HRSMC Photochemistry Summer School in Maastricht, The Netherlands, 2016 (poster award).
- HRSMC Advanced Metal-Organic Chemistry and Catalysis Summer School in Eindhoven, The Netherlands, 2014 (poster).
- Chemistry as Innovating Science (CHAINS) in Veldhoven, The Netherlands, 2015 (poster) and 2016 (poster).
- 25<sup>th</sup> Lecture Conference on Photochemistry (GDCh) in Jena, Germany, 2016 (oral).



# ACKNOWLEDGEMENTS

---

The European Research Council is acknowledged for financially support this work. Prof. Dr. Ingo Ott and Dr. Claudia Schmidt (TU Braunschweig) are acknowledged for AAS measurements (Chapter 6). Prof. Dr. Ewa Snaar-Jagalska and Quanchi Chen (Leiden University) are acknowledged for their collaboration and work with zebra fish (not described in this thesis). Dr. Samantha Hopkins (Leiden University) is acknowledged for electrochemistry experiments (Chapter 5), scientific discussions on ruthenium chemistry, and, together with Dr. Bianka Siewert (Leiden University), for designing the (photo)cytotoxicity assay used throughout this thesis. Their assistance and biochemical training is invaluable. Dr. Bart Limburg (Leiden University) is acknowledged for the development of the UV-vis irradiation setup. Dr. Sven Askes and Michael Meijer are acknowledged for singlet oxygen emission experiments (Chapter 3 and Chapter 6). Elena Pérez-Gallent is acknowledged for her help with chronoamperometry experiments (Chapter 2). Crystallographer Dr. Maxime Siegler (Johns Hopkins University) is kindly acknowledged for X-ray crystallography. John van Dijk, Jos van Brussel, and Anne-Geert Volbeda (Leiden University) are kindly acknowledged for MS and ICP-OES measurements. Dr. Karthick Sai Sankar Gupta and Fons Lefeber (Leiden University) are gratefully acknowledged for their assistance with NMR measurements. Gerwin Spijksma (Leiden University) is acknowledged for HRMS measurements. Dr. Vincent van Rixel (Leiden University) is acknowledged for his assistance on crystal growing (Chapter 6), general scientific discussions, and support. Anja Busemann (Leiden University) is acknowledged for her contribution to this thesis (corrections and Samenvatting) and support. Lucien Lameijer (Leiden University) is acknowledged for all scientific discussions. Victorio Sáez-Talens (Leiden University), Juan Julio Domínguez-Pardo (Utrecht University), Dr. Guillem Paniagua Soriano (CNIO, Madrid), and Dr. Oskar González Mendia (University of the Basque Country) are kindly acknowledged for exchange of ideas and support during this PhD research. Supervised students, namely Mélanie Hilf, Lennard van der Boon (Chapter 2), Catriona James (Chapter 4 and Chapter 5), Vlad Mints, Yevhen Batsuin (Chapter 6), and Sharon Bronkhorst (Chapter 6) are all acknowledged for their contributions to this thesis.

